UNIVERSIDADE DE SÃO PAULO
INSTITUTO DE FÍSICA

Coerência de spin fotoinduzida em EuTe e em ilhas quânticas de (In,Ga)As

Alexander Raul Naupa Roque

Orientador: Prof. Dr. André Bohomoletz Henriques

Tese apresentada ao Programa de Pós-Graduação em Física da Universidade de São Paulo como requisito parcial para a obtenção do título de Doutor em Ciências.

Banca examinadora:

Prof. Dr. André Bohomoletz Henriques - IFUSP
Prof. Dr. Alexandre Levine - IFUSP
Prof. Dr. Eduardo Campos Valadares - UFMG
Prof. Dr. Marcelo Maialle - UNICAMP
Prof. Dr. Marcos Henrique Degani – UNICAMP

São Paulo

2019

FICHA CATALOGRÁFICA
Preparada pelo Serviço de Biblioteca e Informação
do Instituto de Física da Universidade de São Paulo

Naupa Roque, Alexander Raul

Coerência de spins fotoinduzida em EuTe e em ilhas quânticas de (In,Ga)As. São Paulo, 2019.

Tese (Doutorado) – Universidade de São Paulo. Instituto de Física, Depto. de Física dos Materiais e Mecânica

Orientador: Prof. Dr. André Bohomoletz Henriques
Área de Concentração: Física

Unitermos: 1. Spintrônica; 2. Óptica não linear; 3. Magnetismo.

USP/IF/SBI-098/2019

UNIVERSITY OF SÃO PAULO
PHYSIC'S INSTITUTE

Photo-induced spin coherence in EuTe and in (In,Ga)As quantum dots

Alexander Raul Naupa Roque

Adviser: Prof. Dr. André Bohomoletz Henriques

Thesis submitted to the Physics Institute of the University of São Paulo in partial fulfillment of the requirements for the degree of Doctor of Science.

Thesis Defence Committee:

Prof. Dr. André Bohomoletz Henriques - IFUSP
Prof. Dr. Alexandre Levine - IFUSP
Prof. Dr. Eduardo Campos Valadares - UFMG
Prof. Dr. Marcelo Maialle - UNICAMP
Prof. Dr. Marcos Henrique Degani – UNICAMP

São Paulo

2019

Dedicado a mis padres

Acknowledgements

I would like to express my gratitude to Prof. Andre Henriques for the supervision and several lessons which contributed to my professional and personal development and for the opportunity to work in his laboratory.

To Prof. Dr. Paul Koenraad, Prof. Dr. Pavel Usachev and Prof. Dr. Giovanni Galgano for the given support to this work.

I am grateful to the members of my qualification exam and thesis defese: Prof. Dr. Valmir Antonio Chitta, Prof. Dr. Alexandre Levine, Prof. Dr. Antonio Domingues dos Santos, Prof. Dr. Eduardo Campos Valadares (UFMG), Prof. Dr. Marcelo Maialle (UNICAMP), Prof. Dr. Marcos Henrique Degani (UNICAMP) and Prof. Dr. Alain André Quivy for their valuable remarks and suggestion that encouraged me advancing this thesis.

This study was financed in part by the Coordenação de Aperfeiçoamento de Pessoal de Nível Superior - Brasil (CAPES) - Finance Code 001.

To the employees of the DFMT: Olímpio Ribeiro da Fonseca Neto, Xavier Pierre Marie Gratens, Gilberto Francisco dos Santos, Vagner Aparecido Braghim, Rossana Gimenes and specially to Francisco de Paula Oliveira "Paulinho", admirable worker and better person who remains in the memory of those who knew him.

To my brothers and sister and rest of family and in totally random order to the colleagues during the years in the DFMT, Eduard Levinson, Bruno de Abreu Silva, Carlos Gonzales, Heyner Lopes, Gustavo Acosta, Erick Piranha, Thales Garcia, Julio Nunes Villa, Maritim Landau, Edy Edy, Italo Alberto, Saeed Ullah, José Condori, Abel Condori, Alembert Lino, Allyson Ferreira Moraes, Julio Delgado, Amitesh Kumar, Rolando Ramirez, Carolina Rivadeneyra, Alvaro Torres Baptista, Pablo Badilla, Royer Ticse, Frank Taipe, Artinésio Widnesse, Rodrigo Calle, Juan Rivero, Franz Suxo Mamani, Cohen Corstjens, Fernando Aliaga, Flavio Moraes, Sjoerd van Kooten, Fabian Nima, Maria dos Santos, Mirla Bazan, Juancito Valdivia, to my football teams members: the "H.o.b.b.i.t.s" F.C. and Piratas F.C. through different seasons.

And to all that in some way have contributed to the realization of this thesis.

Abstract

This thesis is divided into three parts. In the first part, we attempted to measure the lifetime of a photo-generated trion (two electrons and a hole) in quantum dots (QD) containing a single trapped electron, by using time-resolved Faraday rotation (TRFR). The trion lifetime is a crucial parameter in QD spin dynamics, and it is usually measured by time-resolved photoluminescence (TRPL). However, the PL of a QD ensemble contains many overlapping bands, due to excitons excited simultaneously, which hamper precise measurements of the trion lifetime. The advantage of our method is that the TRFR associated with trions can be detected as a separate signal, which is not polluted by other simultaneous excitations. Using the TRFR method we find the trion lifetime to be $\tau = 0.15 \pm 0.05$ ns.

In the second part, we investigated the generation of photo-induced giant spin polarons in EuTe, which were recently discovered by our research group. In the vicinity of the Néel temperature, the photo-induced spin polaron magnetic moment reached nearly 700 Bohr magnetons, meaning that a single photon imposes spin coherence over 700 electrons. When the excitation light intensity is increased, the total induced magnetic moment of the illuminated region increases sublinearly. We attribute the sublinear increase to the presence of low-density defects in the crystal, which anchor the spin polarons, and limit the maximum achievable concentration of spin polarons in EuTe. We estimate the density of these defects to be of the order of 4.5×10^{15} cm^{-3}. These defects are plausibly generated during the growth process due to a deviation from stoichiometry. We find that the excitation light also causes a small heating of the illuminated region, which is undesirable because it favors spin disorder, but unavoidable. The temperature dependence of the spin polaron magnetic moment is well described by the Curie-Weiss law. In EuTe spin polarons can be generated efficiently at temperatures as high as 100 K, which is ten times the critical Néel temperature. Above 100 K, photoinduced spin polarons are thermally quenched with an activation energy of 11 meV.

In the third part, we present a simple, didactic and general semiclassical model, which allows to convert Faraday rotation (FR) into magnetization in magnetic semiconductors. Previously existing models are based on complex quantum mechanical calculations that are limited to the composition and electronic structure of each material investigated. In contrast, our model requires only a semiclassical conception of spin, and of the charge polarization effects light has in a solid. Our model is not tied on any specific electronic energy structure for the magnetic semiconductor. The model is used to demonstrate that in europium chalcogenides, for photon energies below the band gap, FR is directly proportional to the magnetization, independently of the magnetic phase, temperature, or magnetic field. Furthermore, we show that for EuX, the proportionality constant between FR and magnetization is dependent only on the photon energy and the band gap of the semiconductor. The model is validated by experimental measurements of FR and magnetization, using a EuSe sample.

Keywords: InGa/GaAs quantum dots, Polarons, EuTe, Faraday rotation.

Resumo

Esta tese está dividida em três partes. Na primeira parte, tentamos medir o tempo de vida de um trion (dois elétrons e um buraco) foto-gerado em ilhas quânticas (QD) contendo um elétron aprisionado, usando rotação de Faraday resolvida no tempo (TRFR). O tempo de vida do trion é um parâmetro crucial na dinâmica dos spins dos QDs e geralmente é medido por fotoluminescência (PL) resolvida no tempo. No entanto, a PL de um conjunto de QDs contém muitas bandas sobrepostas, devido a excitons excitados simultaneamente, o que dificulta medições precisas do tempo de vida do trion. A vantagem do nosso método é que a TRFR associado aos trions pode ser detectada como um sinal separado não poluído por outras excitações simultâneas. Usando o método TRFR, obtivemos um tempo de vida de $\tau = 0,15 \pm 0,05$ ns.

Na segunda parte, investigamos a foto-geração de polarons magnéticos gigantes no EuTe. Nas proximidades da temperatura de Néel, o momento magnético do polaron fotoinduzido atingiu quase 700 magnetons de Bohr. Quando a intensidade da luz de excitação é aumentada, o momento magnético total induzido da região iluminada aumenta sub-linearmente. Atribuímos o aumento sublinear à presença de defeitos de baixa densidade no cristal, que ancoram os polarons e limitam a concentração máxima alcançável de polarons no EuTe. Estimamos que a densidade desses defeitos seja 4.5×10^{15} cm^{-3}. Estes defeitos são plausivelmente gerados durante o processo de crescimento, devido a desvios da estequiometria. Descobrimos que a luz de excitação também causa um pequeno aquecimento da região iluminada, o que é indesejável porque favorece a desordem dos spins. A dependência da temperatura do momento magnético do polaron é descrita pela lei de Curie-Weiss. No EuTe, os polarons magnéticos podem ser gerados com eficiência em temperaturas de até 100 K, dez vezes superior a temperatura crítica de Néel do EuTe. Acima de 100 K, os polarons fotoinduzidos são termicamente extintos com uma energia de ativação de 11 meV.

Na terceira parte, apresentamos um modelo semiclássico simples, que permite converter a rotação de Faraday (FR) em magnetização nos semicondutores magnéticos. Modelos anteriores são baseados em cálculos complexos da mecânica quântica, limitados à composição e à estrutura eletrônica de cada material em particular. Em contraste, nosso modelo requer apenas uma concepção semiclássica do spin e dos efeitos de polarização de carga que a luz induz em um sólido. Nosso modelo não depende de nenhuma estrutura de energia eletrônica específica para o semicondutor magnético. O modelo é usado para demonstrar que nos calcogenos de európio, para energias de fótons abaixo do gap, a FR é diretamente proporcional à magnetização, independentemente da fase magnética, temperatura ou campo magnético. Além disso, mostramos que, para o EuX, a constante de proporcionalidade entre FR e magnetização depende apenas da energia do fóton e do band-gap do semicondutor. O modelo é validado por medições experimentais de FR e magnetização, usando uma amostra EuSe.

Palavras chave: Ilhas quânticas, Polarons, EuTe, Rotação de Faraday.

List of Figures

Contents

Chapter 1

Introduction

The first scientist to investigate the phenomenon of magnetism was William Gilbert (1540-1603), who introduced most of the modern terminology as "electricity" and the concept of "magnetic poles" in magnetic materials. He also discovered that the Earth itself is a weak magnet, by making an analogy between the way in which a suspended metal needle was oriented as it was moved over a round piece of magnetite (Lodestone), similar to the movement exhibited by compass needles along the surface of the Earth [1]. Despite his achievements and that of other scientists, the fundamental origin of magnetism could not be explained and remained as a mystery during the next three centuries. In the course of this period, in contrast, the study of the light was fruitful. René Déscartes (1596-1650) and Pierre Fermat (1601-1651) provided the mathematical formalism for the *ray optics* which was, at the time, enough to explain most of the light characteristics, others as Willebroud Snel Van Royal (1580-1626) rediscovered the laws of light reflection and refraction (Snell law), Christian Huygens (1629-1695) proposed the wave theory of light, while Sir Isaac Newton (1643-1727) postulated the particle nature of light. The further discovery of the interference and diffraction phenomena allows the light science being firmly established. These motivated posterior discoveries with Fresnel (1788-1827), Brewster (1781-1868) and Malus (1775-1812), that showed that different materials as, Iceland spar, are able to split the light in different rays unless it traverses the crystal parallel to its crystallographic axis, discovering with this experience the polarization of the light, which was a very powerful tool to investigate the properties of transparent materials. So, in 1845, in the course of the experiments studying the effect of magnetic fields on glass and many other materials, that allows the discovery of the diamagnetism, Michael Faraday (1791-1867) already famous for his discovery of the relation between electricity and magnetism, he also observed a relationship between the magnetism and light. He realized that, when light passing through transparent materials is exposed to a magnetic field parallel to the direction of the light propagation, then, a rotation of the light polarization occurs, the rotation angle of the passing light was proportional to the applied magnetic field. This phenomenon which was called the **Faraday effect** was the proof that light was an electromagnetic

phenomenon in which Faraday firmly believed, but this explanation was not very well understood. Eighteen years later, James Clerk Maxwell, in a wonderful paper entitled *the electromagnetic theory* [2], generalized the results obtained by other scientists as Coulomb, Oersted, Ampere, Gauss, Biot, Savart, Faraday, etc. That was a major step in the search for explaining the electromagnetic, and magneto-optical phenomena. In particular, the Maxwell equations established the missing mathematical relationship between the electric and magnetic systems, by describing how the change of electric fields produce a magnetic field and vice-versa. Although magnetism and electricity could be expressed through the Maxwell equations, the origin of the *intrinsic magnetism* in magnetic materials as magnetite and the interaction of materials with light, could not be understood uniquely from the Maxwell equations. The understanding of the microscopic mechanisms responsible for the Faraday rotation and other magnetic properties was achieved only after the discovery of the electron and the development of atomic models, but principally in the first half of XX century with the rise of *quantum mechanics*, the molecular fields theories [3][4], the discovery of the lattice structure of crystalline solids and the discovery of the **electron spin**. Spin is a universal property of electrons in all states of matter at all temperatures and was postulated in 1925 in order to explain certain features of the optical spectra of hot gases, particularly gases subjected to magnetic fields (Zeeman effect), and it later found theoretical confirmation in quantum mechanics.

All these scientific discoveries stimulated the development of technological innovations as the vacuum tube amplifier, that motivates the invention of the solid state *transistor*, which creates a revolution in the incipient electronic field, establishing the multi-billionaire *semiconductor industry* that allowed the invention of diodes, laser [5], integrated circuits and the first computer (the digital age). Since then, semiconductor materials as silicon have been at the center of condensed matter physics research, and started a demand for new materials and technological advances in fabrication techniques, to create pure and compound semiconductor crystals fabricated and engineered for specific applications, which has led to a continuous competition for the fabrication of smaller and more efficient technological devices. This miniaturization trend followed what was called the *Moore's Law*, which stated that the number of transistors (packing density) on a circuit would roughly double every 18 months. That empirical law was properly valid until 1980 but could not be sustained much longer, this is because integrating more transistors on the same area of an integrated circuit poses new challenges when their dimensions become of nanometric size. One of the problems is the device heating, caused by the higher resistance of device due to a smaller size, which can make the device to failure. Also, the continuous shrinking of the transistor dimensions crosses the quantum size boundaries where the quantum mechanical phenomena become important, and the flow of electrons can no longer be controlled as in the classical way. Then, it was necessary to find alternative ways to overcome these fundamental limits. One alternative is to encode the

information using one quantum characteristic of the electron: its spin.

In 1998 appeared a new field of research called *spintronics* [6] which in addition to electron charge, it utilizes the electron spin. This field of research begun when Albert Fert and Peter Grunberg discovered, independently, the Giant Magnetoresistence (GMR), which exploited the influence of the orientation of the spin of the electrons on the electrical conduction of a multilayer sample composed of alternate ferromagnetic and nonmagnetic layers [7, 8].

In this context, the emergence of technologies that allows us to continue studying the spin behavior in matter is of extreme importance. The adoption of lasers as light sources, cryogenic facilities and improved methods for the fabrication of high-quality samples, constitutes fundamental tools for research in fields as optics, magnetism, and magneto-optics, which has enormous implications if used in technological devices [9], in particular, because of the intense search for more efficient ways to control the magnetization of ferromagnetic materials by means other than magnetic fields, which actually take place on the order of nanoseconds, the *laser induced magnetization* [10].

1.1 Laser induced magnetization

The performance of digital data storage devices essentially depends on how fast we can store, write or read information. For example, the writing speed on a magnetic hard disc, where the information is stored in nanometric blocks of magnetized matter in one or the opposite direction (the 1 and 0 bites), is limited by how fast these blocks can be switched. Therefore, it is important to study the dynamics of the spins in ferromagnetic materials on the time scales where they change and how these spins are affected by external fields.

The simplest way of inducing a spin dynamic response in a magnetic material is by applying an external magnetic field to align the spins and induce a macroscopic magnetization. If we change the direction of the field, a reorientation of the spins is produced to realign the magnetization to the new direction of the magnetic field. This usually happens via a coherent damped precession of spins around an external field, as described by the Landau-Lifshitz-Gilbert equation [11, 12]. The re-orientation process can take several nanoseconds in ferromagnetic materials, depending on the damping efficiency mechanism in the material, provided electrons remain in equilibrium with each other during the precession. A completely different situation is observed if we induce magnetization on a magnetic material by a light pulse.

Besides its technological relevance, the physics behind such a light induced magnetization process is extremely interesting also from a fundamental perspective because it enables extraordinary spin dynamic studies.

Different systems have been studied using lasers. Particular examples are materials containing spatially confined electrons in quasi zero dimensional systems or intrinsic mag-

netic materials as europium chalcogenides.

1.2 Light induced magnetization in quasi-zero dimensional systems

One of the main obstacles to implement the electron spin in technological devices is the relatively short coherence time observed in semiconductor structures. The longer the spin coherence times of conduction electrons the more useful the device is because it makes possible to perform more operations (writing, reading) during which the coherence needs to be retained. In this sense, due to the extensive experience with bulk semiconductor, it is known that in order to enhance the spin coherence time, the electron spin should be isolated from the surrounding environment as much as possible, because the spin free-motion leads to a fast spin relaxation due to the interaction with the environment [13]. This isolation can be obtained e.g. by spin carrier localization at defect sites, or by an electric potential of metallic gates on the surface of the semiconductor or by spatially confining the carriers in a quasi-zero dimensional region, called a **quantum dot** (QD). The fascination with these structures stems from their strongly size-dependent physical and chemical properties intermediate between those of molecules and bulk solids. The systematic variation of properties with size follows simple scaling laws, and quantum dots are often described as artificial atoms.

In these artificial atoms, due to the heavy suppression of translational motion of the charge carriers (electron, holes, etc.), empirical evidence shows that coherence times at liquid helium temperatures can reach even the microsecond range [14], which are longer than coherence time normally obtained of picosecond order in bulk semiconductors where the spin-orbit is one of the major spin-flip mechanism. However, other spin-flip mechanisms become important in quantum dots such as the *hyperfine interaction* between the electrons and nuclear spins, and also the *exchange interaction* between the carriers, which leads as well to spin decoherence.

Studying spin dynamics in single QDs is possible but demanding due to the low signal to noise ratio. In this respect, it is common the study of systems containing an **ensemble of quantum dots**. In this case, the amplitude and direction of the effective nuclear field vary strongly from dot to dot. Thus, the average electron spin decays as a consequence of the random distribution of the local nuclear effective field [15], and a faster dephasing of electron spin coherence polarization occurs due to frequency precession dispersion about a magnetic field. For the III-V group semiconductor such as (In,Ga)As quantum dots, an ensemble spin dephasing time of a few nanoseconds at liquid helium temperature is commonly measured [16].

Additional to the requirement of long coherence time, is the comprehension of the mag-

netization process in semiconductors materials. In the case of singly negatively charged QD ensemble, the spins of the resident electrons are incoherent because they are uncorrelated, leading to an overall zero magnetization. However, by illuminating these QDs with light pulses, it is possible to generate a net magnetization. This process of light-induced magnetization was initially explained using a simple semi-classical model [17], by which the precession of the magnetic moment is field independent, which is in contradiction with experimental results. Recently, a new and more complete quantum mechanical model was developed [18], which describes the phase and amplitude of the photo-induced magnetization as a function of the applied magnetic field in accordance with experimental results.

1.3 Light induced magnetization in europium chalcogenides

Among all the intrinsically magnetic semiconductors, the family of europium chalcogenides EuX (X = O, S, Se, Te) has attracted many scientific studies since the 1960s [19]. The EuX peculiarities arise from their unusual coupling of the electronic, magnetic and optical properties, demonstrating that the control of its spin polarization can be used in magneto-optical devices [20][21][22][23][24][25].

In europium chalcogenides, all four compounds are semiconductors and exhibit a half-filled Eu 4f shell, giving rise to a large magnetic moment of 7 μ_B, producing large saturation magnetization, strong magneto-optic effects (Faraday or Kerr rotation), magnetoresistance, spin filtering effects, etc. The magnetic order of these moments depends on the chalcogen atom X. Below their critical temperatures, EuO and EuS are ferromagnetics (FM), EuTe is antiferromagnetic (AFM), while EuSe exhibits a complex pattern indicating a competition between FM and AFM order.

Initial models to explain the magneto-optical characteristics of europium chalcogenides as the *4f-5d transition model* was able to explain roughly the magnetic field dependence of absorption spectra of EuX [26][27]. Nevertheless, the poor quality of the manufactured samples at that time and the no total agreement with theory caused a decrease in the interest in the EuX compounds. However, with the rise of new growth techniques, such as molecular beam epitaxy (MBE), which allowed the fabrication of high purity and with excellent structural quality samples, the interest in EuX materials was renewed. As a consequence, it was possible to observe a rich and new magneto optical characteristic never seen before [28][29][30][31]. Also a re-examination of the *4f-5d* model with the inclusion of the *domain* formation, ignored until then, enabled for the first time a complete modeling of the absorption spectra of EuX as a function of the magnetic field, which showed a full agreement with the experimental results [32] and motivated researches on the correlation

between the incidence of light and magnetism in EuTe. These results also yield to the ability to detect magnetic states in EuTe through its optical spectra and the ability to create, through the incidence of light pulses, a region of polarized spins, the so-called **magnetic polaron**, which was confirmed by the results of EuTe photoluminescence [33]. The photo-induced creation of magnetic polarons had been predicted few decades ago in magnetic semiconductors by Kasuya and Nagaev [34][35], but the observation of the magnetic polarons and the determination of their characteristic parameters as electronic state which originates the polaron state, their magnetic moment, the polaron volume, lifetime or the dependence with temperature, were always a challenge, because the interpretation of experiments requires elaborate theories, as in the case of diluted magnetic semiconductors [36][37][38], and because the photo-induced EuTe polarons observed from photo-luminescence can be measured only at very low temperatures (below 25 K) [39] and quenched in magnetic fields [40]. Consequently, a new numerical approximation was proposed for intrinsic magnetic semiconductors in order to obtain the EuTe magnetic polaron parameters [41]. It was found that the magnetic polaron is constituted by the photo-excited electron and about 1000 spin-polarized atoms surrounding it, with polaron magnetic moment of $\sim 610\ \mu_B$ below the Néel temperature, and that these magnetic polarons should exist at even higher temperatures.

Because of the giant magnetic moment of these photo-induced polarons, a small magnetic field of a few tens of mT can produce a full alignment of the photo-induced polarons, which opens the prospect of using light to magnetize EuTe and use it for future applications, showing that researches in magnetization of EuX through the generation of magnetic polarons is still an unexplored and fascinating field.

1.4 Focus of this thesis

1. The first part of this thesis describes the photo-induced magnetization of a sample containing an ensemble of singly negatively doped (In,Ga)As/GaAs quantum dots. The investigation is based on a recent model which explains how a circularly polarized light pulse creates a *trion* state with characteristic recombination time τ, and describes the phase and amplitude of the photo-induced magnetization as a function of the applied magnetic field, having the trion recombination time as the one and only adjustable parameter in a fitting of the theory to the experiment, the trion recombination time is a key parameter both for fundamental and for practical applications [42]. However, there are limited data available, experimental and theoretical for the recombination time of the trions, which results very sensitive to the shape, size and composition of the quantum dots [43, 44, 45]. Measuring the trion recombination time with traditional methods involve complications during the measurement related to the contribution of other simultaneously excited states as excitons, dark excitons and technical complications separating exciting and emitted light in resonant excitation measurements. This is the reason for the search for new techniques for measuring the trion recombination time free of the mentioned difficulties. In this section, the central goal is revealing if the time resolving **Faraday rotation** represents a practical and reliable measuring method for the determination of the trion lifetime.

2. The second part of this thesis is set on the photo-induced magnetization of a thin film sample of EuTe by means of photo-created magnetic polarons. This is based on a recent paper where it was demonstrated that, in EuTe, it is possible to generate magnetic polarons with a magnetic moment of several hundred Bohr magnetons with a very long lifetime of 15 μs at T= 5 K. It is even possible to detect magnetic polarons at temperatures far above its critical temperature, at temperatures as high as 150 K [46], which can be detected using the pump-probe **Faraday rotation** technique. Thus, we use the pump-probe Faraday rotation technique to determine how efficiently this light induced magnetization mechanism can be exploited as a function of the pump intensity and temperature.

3. We present a new semi-classical approach to demonstrate that in europium chalcogenides (EuX), Faraday rotation in the transparency gap is proportional to the magnetization of the sample, the proportionality constant is dependent only on the photon energy and on the band gap of the semiconductor irrespective of the material's magnetic phase, temperature, or applied magnetic field.

1.5 Structure of this thesis

This thesis is structured in six chapters as follows: In chapter 2, we first introduce the theoretical concepts useful to describe the photo-induced magnetization process in magnetic materials as quantum charged quantum dots and europium chalcogenides. In chapter 3, we present an overview of the environment of cryogenic and optical measurements including the setups, techniques and the equipment we used for the study of the photo-induced magnetization. We also describe the characteristics of the sample used in the measurements. In chapter 4, we discuss the results about the light-induced magnetization where we divide this chapter in three parts, the first one is related to the photo-induced magnetization in an ensemble of quantum dots, the second is related to the photo-induced magnetization in a EuTe thin film and the third one is focused on the demonstration of the semi-classical Faraday effect formula and its experimental demonstration. Finally, the Appendix is devoted to the details of some topics and the proofs of the equations used in the main text.

Chapter 2

Fundamental concepts

In this chapter, we first discuss the general properties of magnetic materials which have the spin as the responsible for their macroscopic magnetic characteristics. We subdivide this chapter in three parts; the first includes an explanation of the general properties of magnetic materials, the second details the properties of optically active quantum dots, describing their properties as boxes for carriers and the optical selection rules that apply to the studied quantum dots in spectroscopy's experiments, and the third part is devoted to describing the fundamental properties of europium chalcogenides which is the material used to study the photo-creation of magnetic polarons.

2.1 Spin physics in magnetic materials

2.1.1 Magnetic moment of electrons and atoms

The magnetic properties of matter in which we are interested in are due entirely to the magnetic moment of the electrons. The nucleus also has a small magnetic moment, but it is insignificant compared to that of the electrons. The ordering of these magnetic moments in matter and the way they respond to magnetic fields allow us to classify the bulk magnetic properties of any substance as diamagnetic, paramagnetic, ferromagnetic, antiferromagnetic, etc. We will now examine the internal mechanisms responsible for the observed macroscopic magnetic behavior, particularly, we will be interested in the susceptibility of weakly magnetic substances and the saturation magnetization of strongly magnetic ones, paying attention to the variation of these properties with temperature, because this variation provides an important clue to the magnetic nature of the substance.

2.1.1.1 Magnetic moments of individual electrons

There are two kinds of electron motion, orbital and spin, and each one has a magnetic moment associated with it, and both can be thought as equivalent to a circulation of charge.

The magnetic moment of an electron, due to this orbital motion, may be calculated by

$$\mu_{orbital} = A\ I, \tag{2.1}$$

where A is the area of the loop of the current and I is the current produced by the electron in its motion (e = -1.6 $\times 10^{-19}$ C). Then, to evaluate $\mu_{orbital}$ we must know the size and shape of the orbit and the electron velocity. Following the original Bohr theory of the atom, the electron moving with velocity v in a circular orbit of radius r produces a magnetic moment equal to

$$\mu_{orbital} = (\pi r^2)(\frac{ev}{2\pi r}). \tag{2.2}$$

An additional postulate of the Bohr theory was that the orbital angular momentum of the electron must be an integer multiple of $\frac{h}{2\pi}$, where h is Planck's constant. Therefore

$$m_e v r = n(\frac{h}{2\pi}), \tag{2.3}$$

where n is an integer number and m_e is the mass of the electron. Combining these relations, we have for an electron in the first (n= 1) Bohr orbit,

$$\mu_{orbital} = \frac{eh}{4\pi m_e}. \tag{2.4}$$

Classically, the electron behaves as if it were in some sense spinning about its own axis, and associated with this spin exists a magnetic moment and an angular momentum. It is found experimentally and theoretically that the magnetic moment due to electron spin is equal to

$$\mu_{spin} = \frac{eh}{4\pi m_e}. \tag{2.5}$$

Thus, the magnetic moment due to spin and the one due to the orbital motion in the first Bohr orbit are exactly equal. This amount of magnetic moment is given a special symbol, μ_B, and a special name, the **Bohr magneton**. Thus, we define

$$\mu_B = \frac{eh}{4\pi m_e}. \tag{2.6}$$

It is a natural unit of magnetic moment and is extensively used in spin physics. How can the magnetic moment due to spin be understood physically if we do not know the shape of the electron or the way in which charge is distributed in it ?. We can assume an electron as a sphere with its charge homogeneously distributed over its surface, then, the rotation of this charge can produce an array of tiny current loops as is shown in figure 2.1(a), each of which has a magnetic moment directed along the rotation axis. But if

we calculate the resultant moment of all these loops, we would obtain a spin magnetic moment of $\frac{5}{6}\mu_B$ instead of μ_B. Then, the spin of the electron, and its associated magnetic moment, has to be accepted as a fact, consistent with wave mechanics and with a large number of experiments of various kinds, but with no basis in classical physics. The model of the spinning charge in Fig. 2.1(a) is therefore only an aid to visualization and it has no quantitative significance.

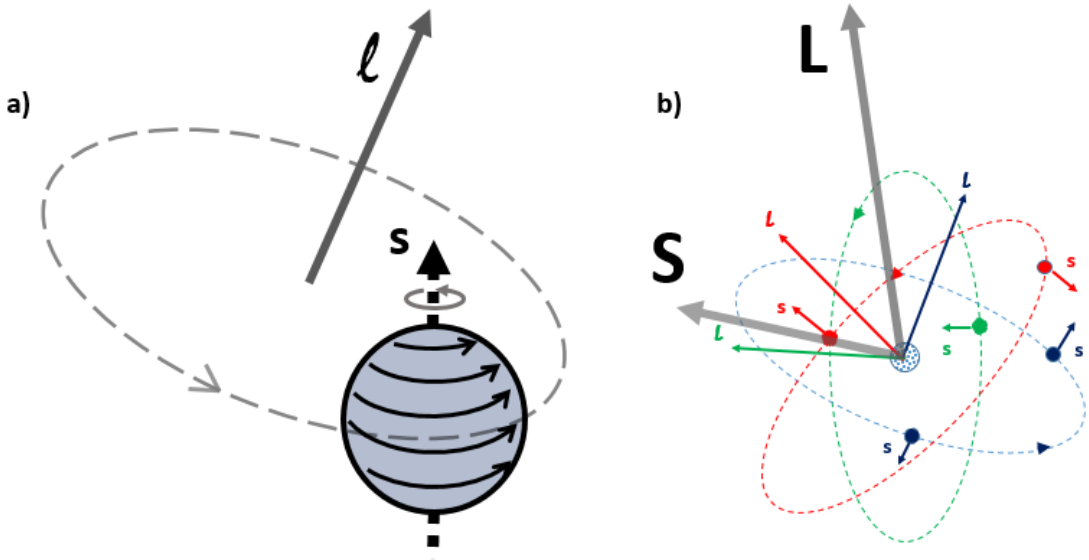

Figure 2.1: (a) Classical interpretation of the orbital (l) and spin (s) magnetic moment of a free electron as an orbiting and spinning charge. (b) Classical interpretation of magnetic moments of an individual atom in which exist a resultant magnetic moment (L) and (S).

2.1.1.2 Magnetic moments of individual atoms

In atoms that contain many electrons, each one spinning about its own axis with spin S and moving in its own orbit with orbital angular moment L, the magnetic moment associated with each kind of motion is a vector quantity, parallel to the axis of spin and normal to the plane of the orbit, respectively. The magnetic moment of the atom is the vector sum of all its electronic moments, and two possibilities arise:

1. The magnetic moments of all the electrons are so oriented that they cancel one another out, and the atom as a whole has no net magnetic moment. This condition leads to solids called *diamagnetics*.

2. The cancellation of electronic moments is only partial and the atom is left with a *net magnetic moment*. Such an atom is often referred to, for brevity, as a **magnetic atom** as is shown in figure 2.1(b).

To calculate the vector sum of the magnetic moments of all the electrons in any particular individual atom is a rather complex problem but solved in atomic physics books. The orbital and spin angular momenta can therefore combine in $(2L+1)(2S+1)$ ways.

This is the total number of choices of the z component of L (which is the number of terms in the series $-L, -L+1, \ \ldots \ , L-1, L$, i.e. $(2L+1)$) multiplied by the total number of choices of the z component of S (i.e. $(2S{+}1)$ by a similar argument). From all the possible values, the most important is the **ground state** which can be obtained by using the **Hund's rules**, which are based on the minimization of the energy of the electrons in the atom. The combination of angular momentum quantum numbers is used in order of importance, so that one first satisfies the first and then, having done this, attempts to satisfy the second, and so on for the third.

1. Arrange the electronic wave function so as to maximize S. In this way the Coulomb energy is minimized because of the Pauli exclusion principle, which prevents electrons with parallel spins being in the same place, and this reduces Coulomb repulsion between electrons.

2. The next step is, given the wave function determined by the first rule, to maximize L. This also minimizes the energy and can be understood by imagining that electrons in orbits rotating in the same direction can avoid each other more effectively and therefore reduce Coulomb repulsion.

3. Finally the value of J is found using $J = \mid L - S \mid$ if the shell is less than half full and $J = \mid L + S \mid$ if it is more than half full. This third rule arises from an attempt to minimize the spin-orbit energy.

One should note that the third rule is only applicable in certain circumstances. In many systems, atoms in a solid, transition metal ions being good examples, the spin-orbit energies are not as significant as some other energy term such as the crystal field so that Hund's third rule is disobeyed. However, for rare earth ions Hund's third rule works very well. The calculation from first principles of the net magnetic moment of an atom in a solid is, in general, not yet possible because of the presence of crystalline fields, and the exact net moment must be determined experimentally.

2.1.2 Magnetization due to non interacting magnetic moments

2.1.2.1 Classical theory of paramagnetism

Lets consider a unit volume of material containing N atoms, each one having a magnetic moment $\boldsymbol{\mu}$. Let the direction of each moment be represented by vectors drawn through the center of a sphere of unit radius. We wish to find the number dN of moments inclined at an angle between θ and $\theta{+}d\theta$ due the presence of an externally applied magnetic field $\boldsymbol{B}$ on the Z axis. In the absence of the field, the number of $\boldsymbol{\mu}$ vectors passing through unit area of the sphere surface is the same at any point on the sphere surface, and dN is proportional simply to the area dA, which is given, as is shown in figure 2.2, by $2\pi \sin\theta d\theta$. But when a field is applied, the $\boldsymbol{\mu}$ vectors shift toward the direction of the field. Each

atomic moment then has a certain potential energy E in the field, given by

$$E = -\boldsymbol{\mu} \cdot \boldsymbol{B} = -\mu B \cos\theta. \tag{2.7}$$

In a state of thermal equilibrium at temperature T, the probability of an atom having an energy E is proportional to the Boltzmann factor $e^{-E/k_B T}$, where k_B is the Boltzmann constant. Then, the number of moments between θ and $\theta + d\theta$ when the magnetic field is applied will now be proportional to dA, multiplied by the Boltzmann factor

$$dN = \aleph dA e^{-E/k_B T} = \aleph(2\pi \sin\theta d\theta) e^{\mu B \cos\theta / k_B T}, \tag{2.8}$$

where $\aleph$ is a proportionality constant, determined by

$$\int_0^N dN = N. \tag{2.9}$$

For brevity, we put $a = \mu B / k_B T$. Then, we have

$$\int_0^\pi \aleph(2\pi \sin\theta d\theta) e^{a\cos\theta} = N. \tag{2.10}$$

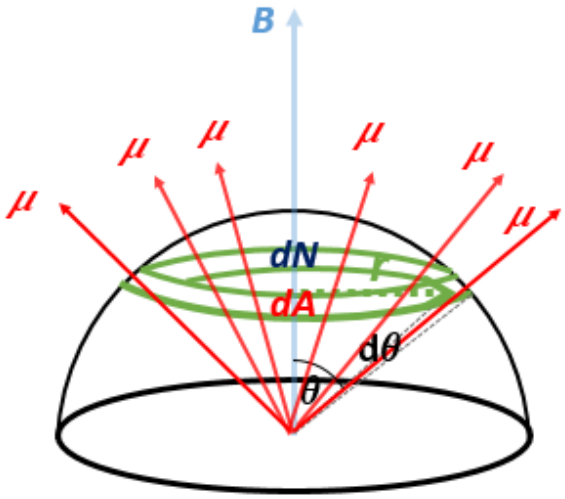

Figure 2.2: Classical interpretation of the magnetization due to an externally applied magnetic field B in a non interacting magnetic moment system.

The total magnetic moment $\boldsymbol{M}$ in the direction of the field (Z axis), acquired by the unit volume under consideration, is given by multiplying the number of atoms dN by the contribution $\mu\cos\theta$ of each atom in that direction and integrating over the total number of atoms

$$M = M_z = \int_0^N \mu \cos\theta dN. \tag{2.11}$$

Substituting equation 2.8 into 2.11, we have

$$M = \int_0^N \mu \cos\theta dN = \mu 2\pi \aleph \int_0^\pi e^{a\cos\theta} \sin\theta \cos\theta d\theta. \tag{2.12}$$

By solving we obtain

$$M = \frac{N\mu \int_0^\pi e^{a\cos\theta} \sin\theta\cos\theta d\theta}{\int_0^\pi e^{a\cos\theta}\sin\theta d\theta} = N\mu\left(\frac{e^a + e^{-a}}{e^a - e^{-a}} - \frac{1}{a}\right) = N\mu\left(coth(a) - \frac{1}{a}\right), \tag{2.13}$$

where we realized that $N\mu$ is the maximum possible moment which the material can have. It corresponds to perfect alignment of all the atomic magnets parallel to the field, which is a state of complete saturation. Calling this quantity M_0, we have

$$\frac{M}{M_0} = coth(a) - \frac{1}{a}. \tag{2.14}$$

The expression on the right is called the **Langevin function**, usually abbreviated to *L(a)*. Expressed as a series, it is

$$L(a) = coth(a) - \frac{1}{a} \quad = \quad \frac{a}{3} - \frac{a^3}{45} + \frac{2a^5}{945} - ..., \tag{2.15}$$

which is valid only for $a << 1$. *L(a)* as a function of a is plotted in figure 2.3. At large a values, *L(a)* tends to 1, and for a less than about 0.5, it is practically a straight line with slope of $1/3$, as seen in equation 2.15. The Langevin principal characteristics are:

1. Saturation will occur if $a = \frac{\mu B}{k_B T}$ is large enough. This makes good physical sense, because large $\boldsymbol{B}$ or low T, or both, is necessary if the aligning tendency of the field is going to overcome the disordering effect of thermal agitation.

2. At small a value, which is normally the case, the magnetization $\boldsymbol{M}$ varies linearly with $\boldsymbol{B}$, as is shown in figure 2.3.

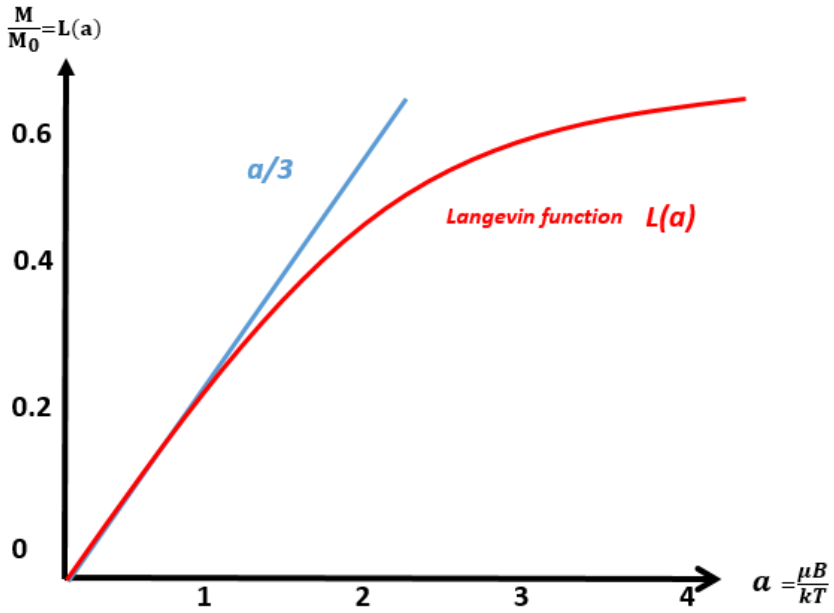

Figure 2.3: Langevin function (in red) as a function of the magnetic field and temperature. The straight line (in blue) is the approximation of the Langevin function for low values of a.

The Langevin theory leads for small a value to $L(a) \approx a/3$, and equation 2.14 becomes

$$M = N\mu\frac{a}{3} = \frac{N\mu^2 B}{3k_B T}. \tag{2.16}$$

Therefore, the susceptibility at constant volume, defined as

$$\chi_v = \lim_{H\to 0}\frac{M}{H} = \lim_{B\to 0}\frac{\mu_0 M}{B} \tag{2.17}$$

can also be written as

$$\chi_v = \frac{\mu_0 N\mu^2}{3k_B T} \qquad or \qquad \chi_v = \frac{C}{T}, \tag{2.18}$$

which is dimensionless in SI, or has units [emu cm^{-3} Oe^{-1}] in the cgs system. This is called the *Curie Law*, with Curie constant

$$C = \frac{\mu_0 N\mu^2}{3k_B}. \tag{2.19}$$

As we saw, the Langevin theory of paramagnetism, which leads to the Curie law, is based on the assumption that the individual carriers of magnetic moment (atoms or molecules) **do not interact** with one another, and react only to the applied magnetic field and thermal agitation. Many paramagnetics, however, do not obey this law; they obey instead the more general Curie–Weiss law, postulated in 1907 [47] which considers that the elementary moments do interact with one another. This interaction could be

expressed in terms of a fictitious field caused by the magnetization of the surrounding material which is called the **molecular field** $\boldsymbol{B_m}$ (at that time, it was thought that matter was composed of molecules instead of atoms) acting in addition to the applied field $\boldsymbol{B_0}$. Weiss assumed that the intensity of the molecular field was directly proportional to the amount of alignment already attained, the magnetization $\boldsymbol{M}$:

$$\boldsymbol{B_m} = \lambda \boldsymbol{M}, \tag{2.20}$$

where λ is called the molecular field constant. Therefore, the total field acting on the material is

$$\boldsymbol{B_t} = \boldsymbol{B_m} + \boldsymbol{B_0}. \tag{2.21}$$

Then, the Curie's law may be written as

$$\chi_v = \frac{\mu_0 M}{B_t} = \frac{C}{T}, \tag{2.22}$$

and using equation 2.21 we obtain

$$\chi_v = \frac{\mu_0 M}{B_0 + B_m} = \frac{\mu_0 M}{B_0 + \lambda M} = \frac{C}{T}. \tag{2.23}$$

Solving for $\mu_0 M$, we obtain

$$\mu_0 M = \frac{C B_0}{T - \lambda C/\mu_0}. \tag{2.24}$$

Therefore, the Curie-Weiss susceptibility is

$$\chi_v = \frac{\mu_0 M}{B_0} = \frac{C}{T - \lambda C/\mu_0} = \frac{C}{T - T_c}, \tag{2.25}$$

where

$$T_c = \frac{\lambda C}{\mu_0} = \frac{\lambda N \mu^2}{3 k_B}. \tag{2.26}$$

The Curie-Weiss temperature is a measure of the strength of the interaction because it is proportional to the molecular field constant λ.

For substances that obey Curie's law, figure 2.4 shows how χ_v varies with the temperature. If we plot $1/\chi_v$ versus temperature for the paramagnetic system, a straight line will result; this line will pass through the origin (Curie behavior) or intercept the temperature axis at $T = \theta$ (Curie–Weiss behavior). Both positive and negative values of θ are possible. A positive value of θ indicates that the molecular field is aiding the applied field and therefore tending to make the elementary magnetic moments parallel to one another and to the applied field, the susceptibility is then larger than it would be if the molecular field were absent. If θ is negative, the molecular field opposes the applied field and tends to decrease the susceptibility.

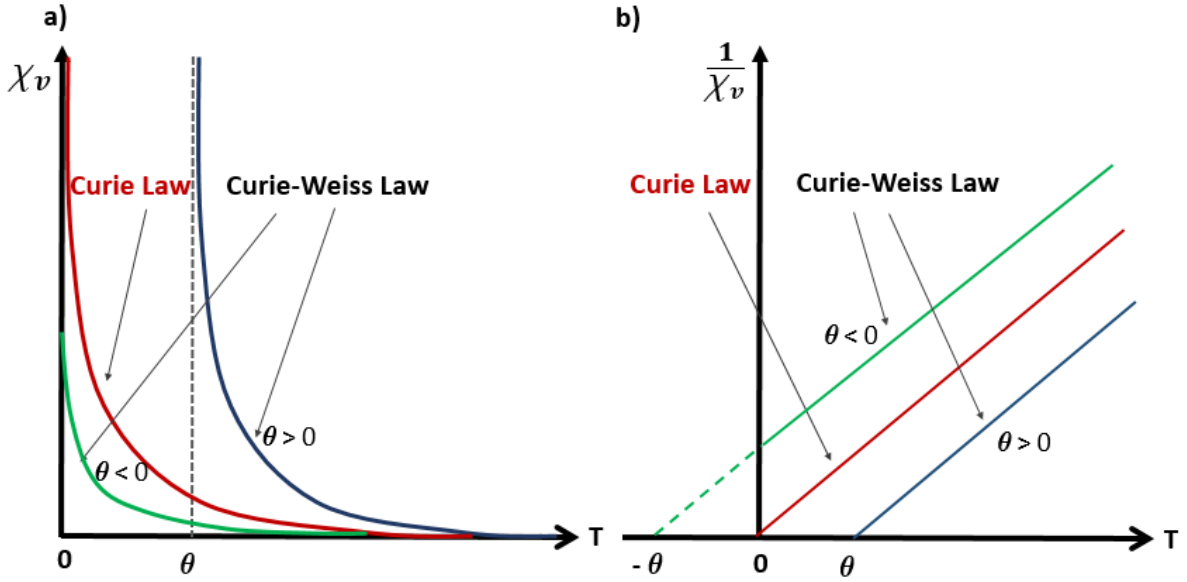

Figure 2.4: (a) Susceptibility and (b) inverse of susceptibility of a paramagnet following the Curie and Curie-Weiss behaviour as a function of temperature.

2.1.2.2 Quantum theory of paramagnetism

The central postulate of quantum mechanics is that the energy of a system is not a continuous variable. When it changes, it must change by discrete amounts, called quanta of energy. If the energy of a system is a function of an angle, then that angle can undergo only discontinuous stepwise changes. This is precisely the case in a paramagnetic substance, where the potential energy of each atomic moment $\boldsymbol{\mu}$ in a field $\boldsymbol{B}$ is given by $E = -\mu B \cos\theta$. In the classical theory, the energy, and hence θ, is regarded as a continuous variable, and $\boldsymbol{\mu}$ can lie at any angle θ to the field. In quantum theory, θ is restricted to certain definite values θ_1, θ_2, ... , and intermediate values are not allowed. This restriction is called space quantization. The classical case is shown in Fig. 2.5(a), where the moments can have any direction (angle θ) in the shaded area; Fig. 2.5(b) illustrates the quantum case, in which the moments are restricted to specific directions (angle θ_i).

The rules governing space quantization are usually expressed in terms of angular momentum rather than magnetic moment. We must therefore consider the relation between the orbital and the spin moments.

The orbital magnetic moment for an electron in the *first* Bohr orbit is given by equation 2.4

$$\mu_{orbital} = \frac{eh}{4\pi m_e}.$$

If we write its corresponding (n=1) orbital angular momentum $\frac{h}{2\pi}$ as $\boldsymbol{l}$, we have for the first orbital magnetic moment

$$\boldsymbol{\mu_{orbital}} = \frac{e}{2m_e}\boldsymbol{l}. \tag{2.27}$$

The intrinsic spin magnetic moment for an electron is given by equation 2.5,

$$\mu_{spin} = \frac{eh}{4\pi m_e}.$$

If we write its corresponding spin angular momentum ($\boldsymbol{s} = \pm\hbar/2 = \pm h/4\pi$), we have for the spin magnetic moment

$$\boldsymbol{\mu_{spin}} = \frac{e}{m_e}\boldsymbol{s}. \tag{2.28}$$

The equations 2.27 and 2.28 can be combined into one general relation between magnetic moment $\boldsymbol{\mu}$ and angular momentum $\boldsymbol{P}$ by introducing a quantity g_P:

$$\boldsymbol{\mu} = g_P \frac{e}{2m_e}(\boldsymbol{P}), \tag{2.29}$$

where $g_P = g_L = 1$ for orbital and $g_P = g_S = 2$ for spin, g is called the g factor and e=-1.6 $\times 10^{-19}$ C. Then,

$$\boldsymbol{\mu_{orbital}} = g_L \frac{e}{2m_e}(\boldsymbol{L}), \tag{2.30}$$

and

$$\boldsymbol{\mu_{spin}} = g_S \frac{e}{2m_e}(\boldsymbol{S}). \tag{2.31}$$

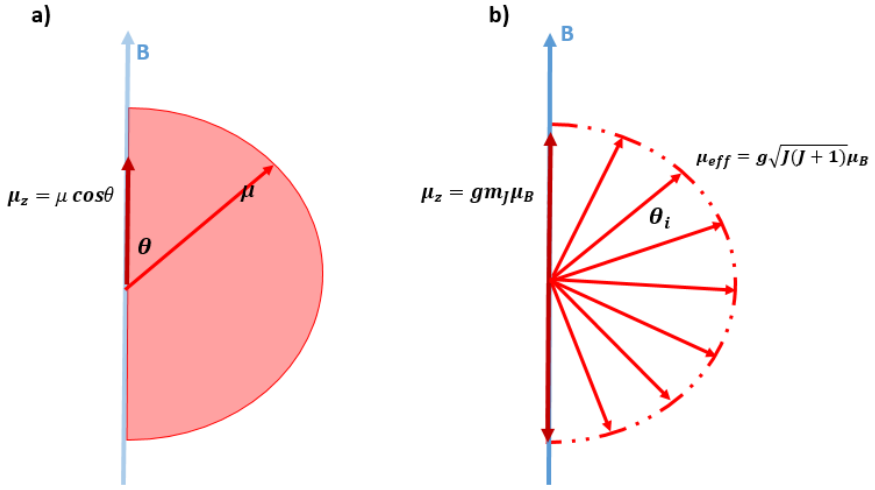

Figure 2.5: Possible orientation for the magnetic moments in a paramagnet system under an applied magnetic field in the classical case (a) and in the quantum case (b).

In an atom composed of many electrons, the angular momentum of the variously oriented orbits combine vectorially to give the resultant orbital angular momentum of the atom, which is characterized by the quantum number $L = \sum_{-l}^{+l} m_l$. Similarly, the individual electron spin momenta combine to give the resultant spin momentum, described by the quantum number $S = \sum_{-s}^{+s} m_s$. Finally, the orbital and spin momenta of the atom combine to give the total angular momentum of the atom $\boldsymbol{J}$, described by the quantum

number J with possible values $|L-S| \leq J \leq L+S$. Then **the net magnetic moment of the atom**, usually called the effective moment μ_{eff}, is given in terms of g and J, as we might expect by analogy with equation 2.29. The relation is

$$\boldsymbol{\mu_{eff}} = g\frac{e}{2m_e}\boldsymbol{J} = g\frac{e}{2m_e}\sqrt{J(J+1)}\frac{h}{2\pi} = g\sqrt{J(J+1)}\mu_B \quad [\text{A.m}^2]. \tag{2.32}$$

Because of the spatial quantization, the effective moment can point only at certain discrete angles θ_1, θ_2, ... to the field. Rather than specify these angles, we specify instead the possible values of $\boldsymbol{\mu_z}$, the component of $\boldsymbol{\mu_{eff}}$ in the direction of the applied field $\boldsymbol{B}$ (Z axis). These possible values are:

$$\mu_{eff} = gm_J\mu_B, \tag{2.33}$$

where m_J is the quantum number associated with $\boldsymbol{J_z}$. For an atom with a total angular momentum $\boldsymbol{J}$, the allowed values of m_J are integer numbers from $-J, -J+1, ... \leq m_j \leq ..., +J-1, +J$ and there are $(2J+1)$ numbers in this set. The μ_z and μ_{eff} are shown in figure 2.5(b).

The value of J for an atom may be an integer or a half-integer, and the possible values range from $J = 1/2$ to $J = \infty$. These extreme values have the following meanings:
$J = 1/2$: This corresponds to pure spin, with no orbital contribution ($L = 0$, $J = S = 1/2$), so that $g = 2$. Since the permissible values of m_J decrease from $+J$ to -J in steps of unity, these values are simply $+1/2$ and -1/2 for this case. The corresponding moments μ_z are then μ_B and -μ_B, parallel and antiparallel to the field, respectively.
$J = \infty$: Here there are an infinite number of J values, corresponding to an infinite number of moment orientations. This is equivalent to the classical distribution of Fig. 2.5(a)

To compute μ_z or μ_{eff} we must know g, as well as J, for the atom in question. The g factor is given by the Landé equation:

$$g = g_L\frac{J(J+1) - S(S+1) + L(L+1)}{2J(J+1)} + g_S\frac{J(J+1) + S(S+1) - L(L+1)}{2J(J+1)}. \tag{2.34}$$

If there is no net orbital contribution to the moment, $L = 0$ and $J = S$. Then equation 2.34 gives $g = 2$ whatever the value of J. On the other hand, if the spins cancel out, then $S = 0$, $J = L$, and $g = 1$. The g factors of most atoms lie between 1 and 2, but values outside this range are sometimes encountered.

The values of J, L, and S are known only for isolated atoms; it is, *in general, impossible to calculate μ for the atoms of a solid*, unless certain assumptions are made. One such assumption, valid for many substances, is that there is no orbital contribution to the moment, so that $J = S$. The orbital moment is, in such cases, said to be quenched. This condition results from the action of the electric field, called the **crystalline field**,

produced by the surrounding atoms or ions in the solid on the atom or ion considered. This field has the symmetry of the crystal involved. Thus, the electron *orbits* in a particular isolated atom might be circular, but when that atom forms part of a cubic crystal, the orbits might become elongated along three mutually perpendicular axes because of the electric fields created by the adjoining atoms located on these axes. In any case, the orbits are in a sense bound, or "coupled," rather strongly to the crystal lattice. The *spins*, on the other hand, are only *loosely coupled to the orbits*. Thus, when a magnetic field is applied along some arbitrary direction in the crystal, the strong orbit–lattice coupling often prevents the orbits, and their associated orbital magnetic moments, from turning toward the field direction, whereas the *spins are free to turn because of the relatively weak spin orbit coupling*. The result is that *only the spins contribute to the magnetization process* and the resultant magnetic moment of the specimen; the orbital moments act as though they were not there. Quenching may be complete or partial. Fortunately, it is possible to measure g for the atoms of a solid, and such measurements tell us what fraction of the total moment, which is also measurable, is contributed by spin and what fraction by orbital motion [48].

Assuming that g and J are known for the atoms involved, we can proceed to calculate the total magnetization of a specimen as a function of the field and temperature. The procedure is the same as that followed in deriving the classical (Langevin) law, except that:

1. The quantized component of magnetic moment in the field direction $\mu_z = gm_J\mu_B$ replaces the classical term $\mu\cos\theta$.

2. A summation over discrete moment orientations replaces an integration over a continuous range of orientations.

Then, the energy of each moment in the direction of the magnetic field $\boldsymbol{B}$ is

$$E = -\boldsymbol{\mu}\cdot\boldsymbol{B} = -gm_J\mu_B B. \tag{2.35}$$

According to Boltzmann statistics, the probability of an atom having an energy E is proportional to:

$$e^{-E/k_BT} = e^{gm_J\mu_B B/k_BT}. \tag{2.36}$$

If there are N atoms per unit volume, the magnetization M is given by the product of N and the average magnetic moment resolved in the direction of the field, or

$$M = N\frac{\sum gm_J\mu_B e^{gm_J\mu_B B/k_BT}}{\sum e^{gm_J\mu_B B/k_BT}}. \tag{2.37}$$

After considerable manipulation, this reduces to

$$M = NgJ\mu_B \left(\frac{2J+1}{2J} coth \left(\frac{2J+1}{2J} a' \right) - \frac{1}{2J} coth \left(\frac{a'}{2J} \right) \right), \tag{2.38}$$

where

$$a' = \frac{gJ\mu_B B}{k_B T} = \frac{\mu_z B}{k_B T}, \tag{2.39}$$

we recognize $NgJ\mu_B$=$N\mu_z$, which is the product of the number of atoms per unit volume and the maximum moment of each atom in the direction of the field. Therefore $N\mu_z = M_0$, the saturation magnetization, and we can write

$$\frac{M}{M_0} = \frac{2J+1}{2J} coth \left(\frac{2J+1}{2J} a' \right) - \frac{1}{2J} coth \left(\frac{a'}{2J} \right). \tag{2.40}$$

The expression on the right is called the **Brillouin function** obtained in 1927. It is abbreviated $\beta_J(J, a')$ and is shown in figure 2.6.

$$\frac{M}{M_0} = \beta_J(J, a'). \tag{2.41}$$

Evaluating when $J = \infty$, the classical distribution, the Brillouin function reduces to the Langevin function:

$$\frac{M}{M_0} = coth(a') - \frac{1}{a'}. \tag{2.42}$$

Evaluating when $J = 1/2$, so that the magnetic moment consists of one spin per atom, the Brillouin function reduces to,

$$\frac{M}{M_0} = tanh(a'). \tag{2.43}$$

The Brillouin function, like the Langevin, is zero for $a^{'}$ equal to zero and tends to unity as $a^{'}$ becomes large. However, the shape of the curve in between depends on the value of J for the atom involved. Moreover, the quantity a in the classical theory differs from the corresponding quantity $a^{'}$ in the quantum theory:

$$a = \frac{\mu B}{k_B T} \qquad \text{Classical,} \tag{2.44}$$

$$a' = \frac{\mu_z B}{k_B T} \qquad \text{Quantum.} \tag{2.45}$$

In the classical theory, μ is the net magnetic moment of the atom. The quantity which corresponds to this in quantum theory is the effective moment μ_{eff}, (and not its component μ_z along the field direction).

When a is small, the function *coth(a)* can be replaced by $(1/a + a/3)$. With this

substitution, the Brillouin function, for small $a^{'}$ reduces to:

$$\beta_J(J, a') \approx \frac{a'(J+1)}{3J}, \tag{2.46}$$

and from equations 2.43 and 2.46

$$M = M_0\beta_J(J, a') = (NgJ\mu_B)\beta_J(J, a') \approx NgJ\mu_B a' \frac{J+1}{3J}$$

$$= NgJ\mu_B(\frac{gJ\mu_B B}{k_B T})\frac{J+1}{3J} = \frac{Ng^2J(J+1)\mu_B^2 B}{3k_B T} = \frac{N\mu_{eff}^2 B}{3k_B T}. \tag{2.47}$$

As mentioned earlier, the quantum numbers J, L, and S are usually not known for an atom or molecule in a solid. Under these circumstances it is customary to compute the magnetic moment from the susceptibility measurements, on the assumption that the moment is due only to the spin component; then $L = 0$, $J = S$, and $g = 2$. The result is called the "spin only" moment. The value of J $(= S)$ is computed from the experimental value of the constant $\frac{N\mu_{eff}^2 B}{3k_B}$.

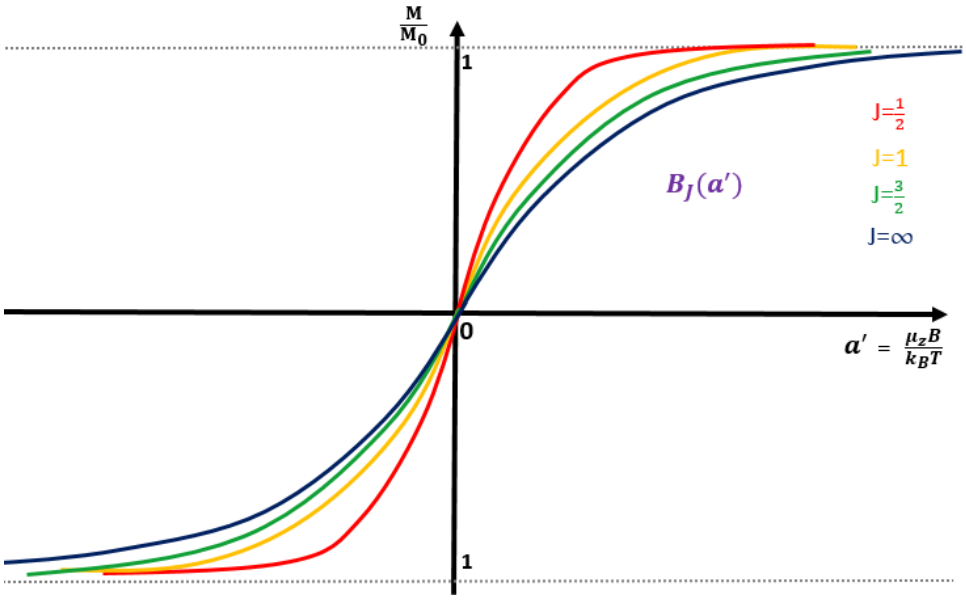

Figure 2.6: Brillouin function as a function of magnetic field and temperature for different J values.

2.1.3 Interacting magnetic moments: Spontaneous magnetic order

Now we will consider the different types of magnetic ground state which can be photo-induced by interactions operating between the magnetic moments in matter. The different

ground states include; ferromagnets, in which all the magnetic moments are in parallel alignment, antiferromagnets and ferrimagnets, in which adjacent magnetic moments lie in antiparallel alignment, spiral or helical structures in which the direction of the magnetic moment precesses around a cone or a circle as one moves from one site to the next, and spin glasses in which the magnetic moments lie in frozen random arrangements.

It is well known that the dipole-dipole interaction between magnetic moments is too much weak to explain the spin depending interaction in solids, then, we will see that exist stronger interaction forces that are responsible for the magnetic order in magnetic materials.

2.1.3.1 Ferromagnetism

We have seen how the Weiss hypothesis leads to the Curie–Weiss law, $\chi_v = \dfrac{C}{T - T_c}$, which many paramagnetic materials obey. We also saw that T_c is directly related to the molecular field $\boldsymbol{B_m}$, because $T_c = \lambda C/\mu_0$ and $B_m = \lambda M$, where λ is the molecular field coefficient. If T_c is positive, so is λ, it means that $\boldsymbol{B_m}$ and $\boldsymbol{M}$ are in the same direction or that the molecular field aids the applied field in magnetizing the material.

Above its Curie temperature T_c a ferromagnet becomes paramagnetic, and its susceptibility then follows the Curie –Weiss law, with an experimental value θ approximately equal to T_c.

The value of θ is therefore large and positive, and so is the molecular field coefficient. This fact led Weiss to make the assumption that a molecular field acts in a ferromagnetic substance below its Curie temperature as well as above, and that this field is so strong that it can magnetize the substance to saturation even in the absence of an applied magnetic field. The substance is then self-saturating, or "spontaneously magnetized." Before we consider how this can come about, we must note that the theory is, at this stage, incomplete. For if iron, for example, how can we explain the fact that it is quite easy to obtain a piece of iron in the un-magnetized condition?. Weiss answered this objection by making a second assumption: a ferromagnet in the demagnetized state is divided into a number of small regions called **domains**. Each domain is spontaneously magnetized to the saturation value M_s, but the directions of magnetization of the various domains are such that the specimen as a whole has no net magnetization. The process of magnetization is then one of converting the specimen from a multi-domain state into one in which it is a single domain magnetized in the same direction as the applied field. The Weiss theory therefore contains two essential postulates: spontaneous magnetization and division into domains.

In a ferromagnetic substance, all the magnetic moments lie along a single unique direction, and this effect is generally due to **exchange interactions** between the spins in the material.

For a ferromagnet in an applied magnetic field $\boldsymbol{B}$, the appropriate Hamiltonian, considering the exchange interaction and the energy of the spins in the magnetic field $\boldsymbol{B}$, is

$$E = -\sum_{ij} J_{ij} \boldsymbol{S}_i \cdot \boldsymbol{S}_j + g\mu_B \sum_j \boldsymbol{S}_j \cdot \boldsymbol{B}. \tag{2.48}$$

The *exchange constants* J_{ij} for nearest neighbours will be positive in this case, to ensure ferromagnetic alignment. The first term on the right is the Heisenberg exchange energy and the second term on the right is the Zeeman energy. To keep things simple to begin with, let us assume that we are dealing with a system in which there is no orbital angular momentum, so that $L = 0$ and $J = S$.

The molecular field is proportional to the magnetization, i.e,

$$\boldsymbol{B}_m = \lambda \boldsymbol{M}. \tag{2.49}$$

In the i-th site with spin $\boldsymbol{S_i}$, it exchange interacts with all the j-th neighboring sites, of spin $\boldsymbol{S_j}$, according to:

$$\boldsymbol{E}_i = -2\sum_j J_{ij} \boldsymbol{S}_i \cdot \boldsymbol{S}_j, \tag{2.50}$$

where J_{ij} is the exchange integral, a constant that depends on the wavefunctions of the interacting electrons. This interaction is equivalent to a Zeeman type interaction between the i-th site and the molecular field $\boldsymbol{B}_m$. The energy of this interaction is given by:

$$\boldsymbol{E}_i = -g\mu_B \boldsymbol{S}_i \cdot \boldsymbol{B}_m, \tag{2.51}$$

where the sign on the right side is taken as negative, so that the exchange interaction favors the alignment of the spins when $J_{ij} > 0$.

Equating the expressions 2.50 and 2.51, we obtain the molecular field acting on the site i as:

$$\boldsymbol{B}_m = \frac{2}{g\mu_B} \sum_j J_{ij} \boldsymbol{S}_j. \tag{2.52}$$

We can approximate this expression by replacing each spin $\boldsymbol{S}_j$ by an average $\langle \boldsymbol{S}_j \rangle$ which is parallel to the magnetization of the material, so that:

$$\boldsymbol{B}_m = \frac{2}{g\mu_B} \sum_j J_{ij} \langle \boldsymbol{S}_j \rangle. \tag{2.53}$$

Since the exchange integrals decrease with the distance between the spins, we can restrict ourselves to the **nearest neighbors approximation**, which is to limit the sum in equation 2.53 only to the closer sites. Assuming z nearest neighbor, whose exchange

interaction is described by J_{xc}, we obtain:

$$\boldsymbol{B}_m = \frac{2}{g\mu_B} z J_{xc} \langle \boldsymbol{S}_j . \rangle \tag{2.54}$$

Since all the magnetic atoms are identical and equivalent, the average value $\langle \boldsymbol{S}_j \rangle$ is related to the magnetization of the lattice through the relation

$$\boldsymbol{M} = N g \mu_B \langle \boldsymbol{S}_j \rangle, \tag{2.55}$$

which replaced in equation 2.54 results in

$$\boldsymbol{B}_m = \frac{2 z J_{xc}}{N g^2 \mu_B^2} \boldsymbol{M}. \tag{2.56}$$

From this equation, by comparison with equation 2.49, we obtain the constant λ as:

$$\lambda = \frac{2 z J_{xc}}{N g^2 \mu_B^2}. \tag{2.57}$$

The energy of the i-th atom in a magnetic material due the presence of an effective magnetic field $\boldsymbol{B} = \boldsymbol{B}_0 + \boldsymbol{B}_m$, where $\boldsymbol{B}_0$ is the applied field assuming that the magnetization is oriented toward the field direction, defined as the Z direction, can be written as

$$E = g\mu_B \boldsymbol{J} \cdot (\boldsymbol{B}_0 + \boldsymbol{B}_m). \tag{2.58}$$

Then,

$$E = g\mu_B J_z (B_0 + B_m). \tag{2.59}$$

This is equivalent to the energy of a paramagnet in a magnetic field $\boldsymbol{B} = \boldsymbol{B_0} + \boldsymbol{B_m}$. This allow us to use the result in equation 2.41, replacing B by $B_0 + B_m$ in order to get:

$$M(B_0, T) = M_0 \beta_J(a^{'}), \tag{2.60}$$

where

$$a^{'} = \frac{g\mu_B J (B_0 + \lambda M(B_0, T))}{k_B T}. \tag{2.61}$$

These two equations must be solved simultaneously, which can be done by the graphical method or numerically, looking at the intersection between the two magnetizations. These equations can be written as

$$M(a) = M_0 \beta_J(a), \tag{2.62}$$

and from equation 2.61,

$$M(a) = \frac{k_B T}{g\mu_B J \lambda} a - \frac{B_0}{\lambda}. \tag{2.63}$$

A plot of the above two curves is shown in figure 2.7 for different temperatures.

For $B_0 = 0$, it is shown that from temperatures higher than a critical temperature T_c, the Curie temperature, there is no intersection other than trivial and the magnetization is always zero (not ferromagnetic state). Below the Curie temperature, there are always two solutions, one positive and one negative and there is always a net magnetization. In the limit $T \to 0$ the magnetization amounts to M_0.

For $B_0 > 0$, there is always a solution (ferromagnetic state) with limit value $M_0 - B_0/\lambda$ at $T = 0$.

To find the ordering temperature, we equal the derivatives of the curves $M(a)$ and β_J for $a \to 0$. The limit for $a \to 0$ can be calculated through an expansion of $\beta_J(a)$ in a power series in a, resulting in,

$$\lim_{a\to 0} \beta_J^{'}(a) = \frac{J+1}{3J}. \tag{2.64}$$

So that, on one hand, from equations 2.62 and 2.64,

$$M'(a \to 0) = M_0 \frac{J+1}{3J}, \tag{2.65}$$

and, on the other one hand, from equation 2.63,

$$M'(a) = \frac{k_B T}{g\mu_B J\lambda}. \tag{2.66}$$

So that equating both equations which is valid at the critical temperature and when $a \to 0$, is possible to determine the Curie temperature as

$$M_0 \frac{J+1}{3J} = \frac{k_B T_c}{g\mu_B J\lambda}. \tag{2.67}$$

Then we have,

$$T_c = \frac{(J+1)g\mu_B \lambda M_0}{3k_B}, \tag{2.68}$$

or simply,

$$T_c = C\lambda, \tag{2.69}$$

where $C = \dfrac{(J+1)g\mu_B M_0}{3k_B}$, with $M_0 = Ng\mu_B J$. Then, we can write

$$C = \frac{J(J+1)g^2\mu_B^2 N}{3k_B}, \tag{2.70}$$

which is the same Curie temperature of paramagnetic materials.

At high temperatures, when $a << 1$, the Brillouin function can be approximated by

$B_J(a) = \dfrac{(J+1)}{3J}a$ so that the magnetization becomes

$$M(B_0,T) = M_0\frac{J+1}{3J}\frac{g\mu_B JM(B_0,T)}{k_BT} = C\frac{(B_0+\lambda M(B_0,T))}{k_BT}. \tag{2.71}$$

Solving by $M(B_0,T)$, we obtain:

$$M(B_0,T) = \frac{C}{T-T_c}B_0. \tag{2.72}$$

So the the susceptibility becomes,

$$\chi_v = \frac{\mu_0 C}{T-T_c}, \tag{2.73}$$

which has the shape of the Curie-Weiss law, which is valid in the region $T > T_c$.

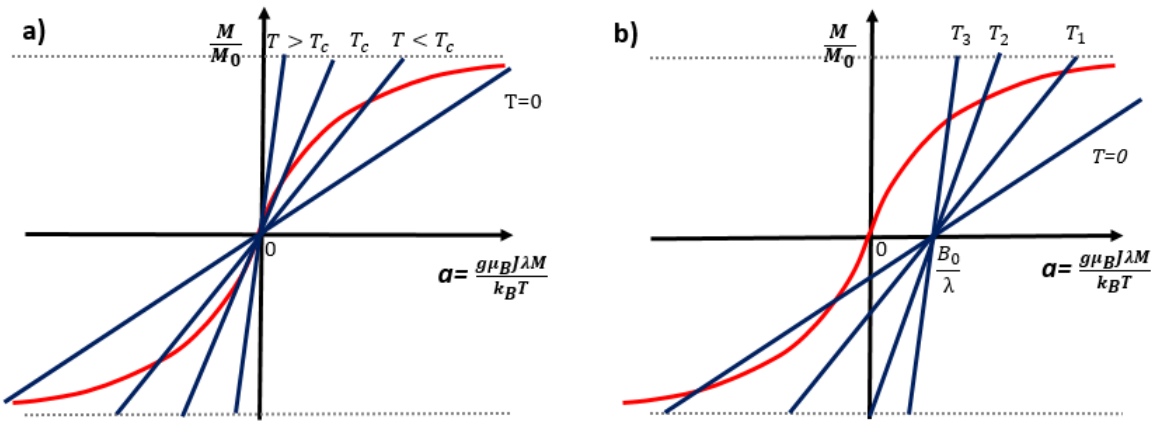

Figure 2.7: Graphic solution for the magnetization equations $M(a)$ and $\beta_J(a)$ for the cases $B_0 = 0$ (a) and for $B_0 > 0$ (b). When we have an intercept (a solution) then a net magnetic order is possible.

2.1.3.2 Antiferromagnetism

Antiferromagnetic substances have the characteristics that they have a small positive susceptibility at all temperatures. The way in which the susceptibility of an antiferromagnetic varies with temperature is shown in figure 2.8(a). The substance is paramagnetic above its critical temperature called the Néel temperature T_N and antiferromagnetic below it. As the temperature decreases, χ_v increases but goes through a maximum at T_N.

The molecular field $\boldsymbol{B_m}$, in the paramagnetic region, is opposed to the applied field $\boldsymbol{B_0}$; whereas $\boldsymbol{B_0}$ acts to align the magnetic moments, $\boldsymbol{B_m}$ acts to dis-align them. If we now think of the molecular field on a very localized scale, the result is that any tendency of a particular magnetic moment to point in one direction is immediately counteracted

by a tendency for the moment on an adjacent magnetic moment to point in the opposite direction. In other words, *the exchange force is negative*, contrary to the ferromagnetic case.

Below the critical temperature T_N, this tendency toward an antiparallel alignment of moments is strong enough to act even in the absence of an applied field, because the randomizing effect of thermal energy is so low. The lattice of magnetic ions in the crystal then *breaks up into two sublattices*, designated A and B, having moments more or less opposed. The tendency toward antiparallelism becomes stronger as the temperature is lowered below T_N, until at 0 K the antiparallel arrangement is perfect.

We now see that an antiferromagnetic at 0 K consists of two interpenetrating and identical sublattices of magnetic ions, each spontaneously magnetized to saturation in zero applied field, but in opposite directions, just as the single lattice of a ferromagnetic is spontaneously magnetized. Evidently, an antiferromagnetic has no net spontaneous moment and can acquire a moment only when a strong field is applied to it.

We will apply the molecular field theory to the simplest possible case, namely, one for which the lattice of magnetic ions can be divided into two identical sublattices, A and B, such that any A ion has only B ions as nearest neighbors, and vice versa. *We assume that the only interaction is between nearest neighbors (AB) and ignore the possibility of interactions between second-nearest neighbors (AA and BB).*

We now have two molecular fields to deal with. The molecular field $\boldsymbol{B_{mA}}$ acting on the A ions is proportional and in the opposite direction to the magnetization of the B sublattice:

$$\boldsymbol{B_{mA}} = -\lambda \boldsymbol{M_B}, \tag{2.74}$$

where λ is the molecular field coefficient, taken as positive. Similarly,

$$\boldsymbol{B_{mB}} = -\lambda \boldsymbol{M_A}. \tag{2.75}$$

These two equations are valid both above and below T_N. We will consider the two cases in turn.

$T > T_N$, the paramagnetic state

In the paramagnetic region, we can find an equation for the susceptibility. Assuming a Curie-law behavior, we have,

$$\chi_v = \frac{\mu_0 M}{B} = \frac{C}{T}, \tag{2.76}$$

or

$$\mu_0 MT = CB, \tag{2.77}$$

where B is the total field, applied and molecular, acting on the material.

We now write equation 2.77 for each sublattice,

$$\mu_0 M_A T = C_a(B_0 - \lambda M_B), \tag{2.78}$$

$$\mu_0 M_B T = C_a(B_0 - \lambda M_A), \tag{2.79}$$

where C_a is the antiferromagnetic Curie constant of each sublattice and $\boldsymbol{B_0}$ is the applied field. By adding these two equations we can find the total magnetization $\boldsymbol{M}$ produced by the field and hence the susceptibility:

$$\mu_0(M_A + M_B)T = C_a(2B_0 - \lambda(M_A + M_B)), \tag{2.80}$$

$$\mu_0 MT = C_a(2B_0 - \lambda M). \tag{2.81}$$

Solving for the spontaneous M,

$$M(\mu_0 T + \lambda C_a) = 2C_a B_0. \tag{2.82}$$

Then, the antiferromagnetic susceptibility is

$$\chi_v = \frac{\mu_0 M}{B_0} = \frac{2C_a}{T + \lambda C/\mu_0} = \frac{C}{T + T_N}, \tag{2.83}$$

where

$$C = 2C_a \qquad and \qquad T_N = \lambda C_a/\mu_0. \tag{2.84}$$

Note that, when a field is applied above T_N, each sublattice becomes magnetized in the same direction as the field, but each sublattice then sets up a molecular field in the opposite direction to the applied field, tending to reduce both $\boldsymbol{M_A}$ and $\boldsymbol{M_B}$. The result is that the susceptibility χ_v is smaller, and $1/\chi_v$ larger, than that of an ideal paramagnetic in which the molecular field is zero. The two are compared graphically in Fig. 2.8, which also shows how χ_v varies with temperature in a material with a large positive molecular field, such as a ferromagnetic above its Curie point.

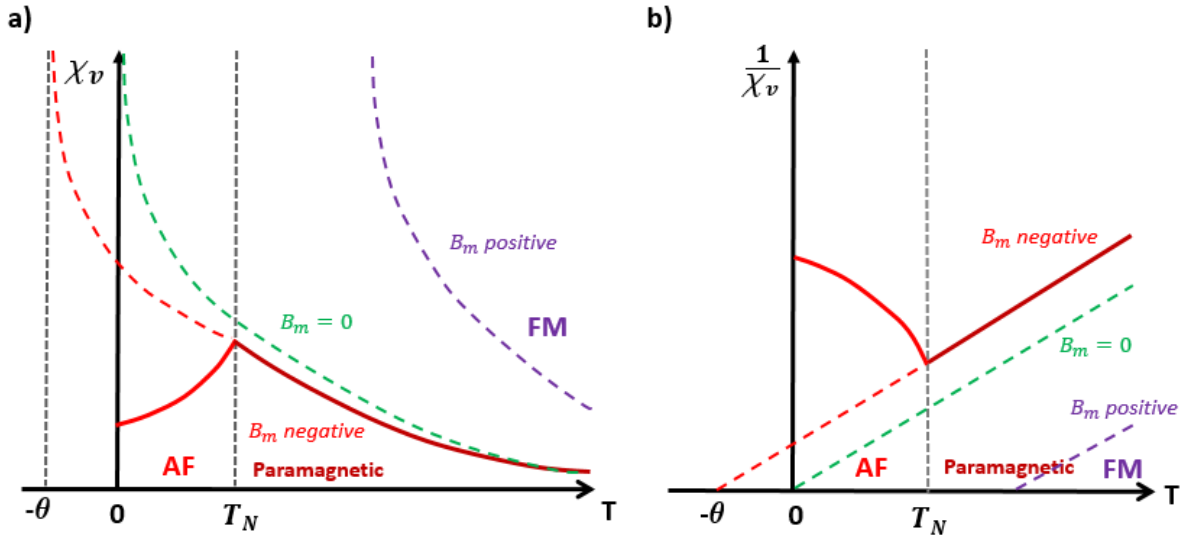

Figure 2.8: (a) Antiferromagnetic susceptibility and (b) inverse of susceptibility as a function of the temperature in a antiferromagnetic material. A comparison with a Curie paramagnetic material with $B_m = 0$ and a ferromagnetic material with $B_m > 0$ is also shown.

$T < T_N$ Antiferromagnetic state

In the antiferromagnetic region, each sublattice is spontaneously magnetized, in zero applied field, by the molecular field created by the other sublattice and the total magnetization is zero,

$$\boldsymbol{M} = \boldsymbol{M_A} + \boldsymbol{M_B} = 0. \tag{2.85}$$

Then,

$$\boldsymbol{M_A} = -\boldsymbol{M_B}. \tag{2.86}$$

Below T_N, each sublattice is spontaneously magnetized to saturation just as a ferromagnetic is, and we can compute its magnetization in the same way:

$$M_A = M_{0A}\beta_J(J, a') = M_{0A}\beta_J(J, \frac{\mu_z B}{k_B T}), \tag{2.87}$$

B is the total field acting on the A sublattice. Since we are computing the spontaneous magnetization, the applied field is zero ($B = B_m$), and we include only the molecular field due to the B sublattice

$$\boldsymbol{B_{mA}} = -\lambda \boldsymbol{M_B} = +\lambda \boldsymbol{M_A}. \tag{2.88}$$

Therefore, the spontaneous magnetization of the A sublattice is given by

$$M_A = M_{0A}\beta_J(J, \frac{\mu_z \lambda M_A}{k_B T}), \tag{2.89}$$

with a similar expression for the B sublattice. This equation can be solved graphically as in the ferromagnetic case.

Although the net spontaneous magnetization is zero below T_N, an applied field B_0 can produce a small magnetization. The resulting susceptibility is found to depend on the angle α which the applied field makes with the axis of antiparallelism (AFM axis) in Fig. 2.9, an axis which usually coincides with an important crystallographic direction in the crystal. For brevity, we will call this the antiferromagnetic axis. Then, we can consider two limiting cases.

$T < T_N$ and magnetic field perpendicular to the AFM Axis.
The effect of the applied field $\boldsymbol{B_0}$ is to turn each sublattice magnetization away from the AFM axis as shown in Fig. 2.9(a), where the vectors representing the magnetizations of the two sublattices are drawn from one point. This rotation immediately creates a magnetization $\boldsymbol{M}$ in the direction of the field and sets up an unbalanced molecular field B_m in the opposite direction. The spins will rotate until $\boldsymbol{B_m}$ equals $\boldsymbol{B}$,

$$2B_{mA}\cos\alpha = B_0, \tag{2.90}$$

or

$$2\lambda M_A \cos\alpha = B_0. \tag{2.91}$$

Also

$$M_\perp = 2M_A\cos\alpha, \tag{2.92}$$

Then, we have $\lambda M_\perp = B_\perp$, and using equation 2.84 we can define

$$\chi_\perp = \frac{\mu_0 M_\perp}{B_\perp} = \frac{\mu_0}{\lambda} = \frac{C}{2T_N}. \tag{2.93}$$

We note from equation 2.93 that the susceptibility perpendicular to the AFM axis is inversely proportional to the molecular field constant, as might be expected, and it is independent of the temperature.

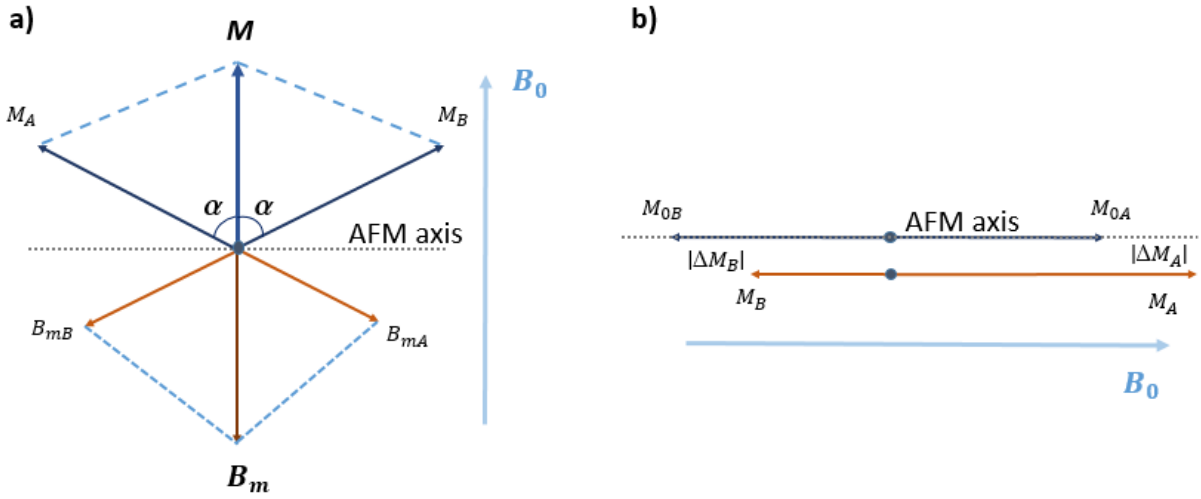

Figure 2.9: (a) In an antiferromagnetic material below the Néel temperature at $T = 0$ K, an applied magnetic field perpendicular to the AFM axis turns the spins in the B direction. (b) Applied magnetic field oriented parallel to the AFM axis makes to increase the magnetization in one sublattice but decrease the magnetization in the opposite direction.

$T < T_N$ and magnetic field parallel to AFM Axis.

Suppose the field is applied in the direction of the antiferromagnetic A sublattice. Then, the effect of the field is to increase the zero-field value of the A sublattice magnetization $\boldsymbol{M_A}$ by an amount ΔM_A and decrease the corresponding value M_B of the B sublattice by an amount ΔM_B, as shown in Fig. 2.9(b). The balance between the two sublattices is upset, and a net magnetization in the direction of the field is produced:

$$\boldsymbol{M = (M_{0A} + \Delta M_A) - (M_{0B} - \Delta M_B)} = \mid \Delta M_A \mid + \mid \Delta M_B \mid . \tag{2.94}$$

At $T = 0$ K, the sublattices are saturated and there is nothing that the field can do, then $\chi_{||} = 0$. When the temperature increases, thermal fluctuations reduce the molecular field and the field will be able to align a portion of the spins to its direction and this portions increases as the temperature increases, so that $\chi_{||}$ smoothly increases with temperature until $T = T_N$.

If the applied field B_0 makes an angle θ with the AFM axis of a particular crystal, then the magnetizations acquired by that crystal, parallel and perpendicular to the AFM axis, are

$$M_{||} = \chi_{||} B \cos\theta, \tag{2.95}$$

$$M_{\perp} = \chi_{\perp} B \sin\theta. \tag{2.96}$$

The magnetization in the direction of the field is then

$$M = M_{||}\cos\theta + M_{\perp}\sin\theta = \chi_{||}H\cos\theta^2 + \chi_{\perp}H\sin\theta^2 \tag{2.97}$$

or

$$\chi = \frac{\mu_0 M}{B} = \chi_{||}\cos\theta^2 + \chi_{\perp}\sin\theta^2. \tag{2.98}$$

In a powder specimen or a random polycrystal, in which there is no preferred orientation of the grains, the AFM axis takes on all possible orientations with respect to the applied field. To find the susceptibility of a powder we must therefore average over all orientations. This susceptibility of one crystal must then be averaged over all possible values of θ to give the susceptibility of the powder:

$$\chi = \frac{\mu_0 M}{B} = \chi_{||}\frac{1}{3} + \chi_{\perp}\frac{2}{3}. \tag{2.99}$$

A plot of the temperature variation of the powder susceptibility is included in Fig. 2.10

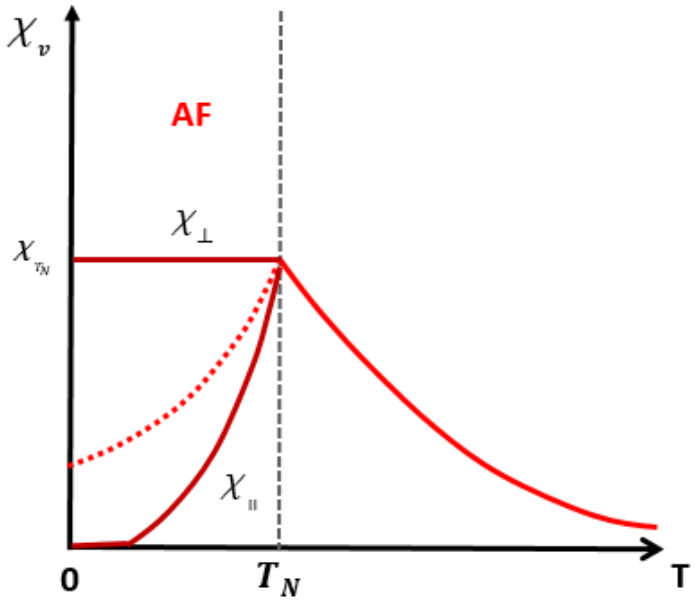

Figure 2.10: Susceptibility parallel and perpendicular to the AFM axis in an antiferromagnetic material as a function of the temperature. The effective susceptibility in a polycrystal $\chi = \chi_{||}\frac{1}{3} + \chi_{\perp}\frac{2}{3}$ below the critical temperature is shown as a dotted line.

2.1.4 Magnetic anisotropy

This term means that the magnetic properties, for example, the magnetization (M vs B, M vs T curves, etc.) depend on the direction in which they are measured. The most common magnetic anisotropy are: crystal anisotropy, formally called magnetocrystalline anisotropy, which is intrinsic to the material, other as shape anisotropy or stress anisotropy are extrinsic or "induced."

To clarify crystal anisotropy, lets suppose a single crystal with cubic structure cut in the form of a disk parallel to a plane $(1\bar{1}0)$. This specimen will then have directions of the form $< 001 >$, $< 110 >$, and $< 111 >$ as diameters, as shown in Fig. 2.11. Measurements of magnetization curves along these diameters, in the plane of the disk, will then give information about the three important crystallographic directions.

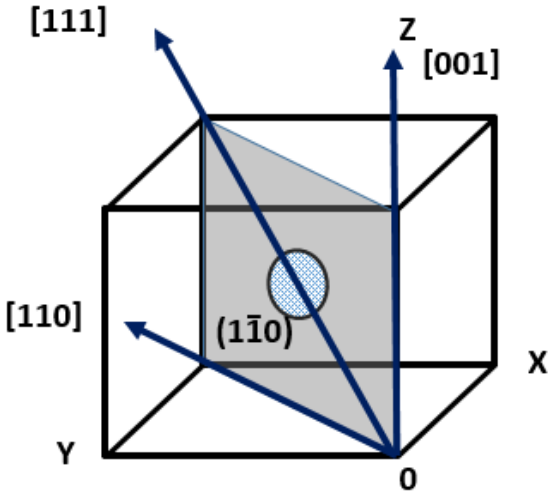

Figure 2.11: The three principal crystallographic directions in the $(1\bar{1}0)$ plane of a cubic material.

The results for a body-centered cubic structure (BCC), are shown in Fig. 2.12(a), and those for face-centered cubic (FCC) in Fig. 2.12(b). For BCC these measurements show that saturation can be achieved with low fields, in the $< 100 >$ direction, which is accordingly called the **easy direction** of magnetization. This tells us something about domains in BCC in the demagnetized state. As will become clear later, a domain wall separating two domains in a crystal can be moved by a small applied field. If we assume that domains in demagnetized BCC are spontaneously magnetized to saturation in directions of the form $< 100 >$, $< 010 >$, $< 0\bar{1}0 >$, and $< \bar{1}00 >$, then a possible domain structure for a demagnetized crystal disk cut parallel to (001) would be that shown in Fig. 2.13(a). It has four kinds of domains, magnetized parallel to four of the six possible easy directions, namely, [010], [100], [$0\bar{1}0$], and [$\bar{1}00$], the other two [001] and [$00\bar{1}$] are orthogonal to the 2D disk.

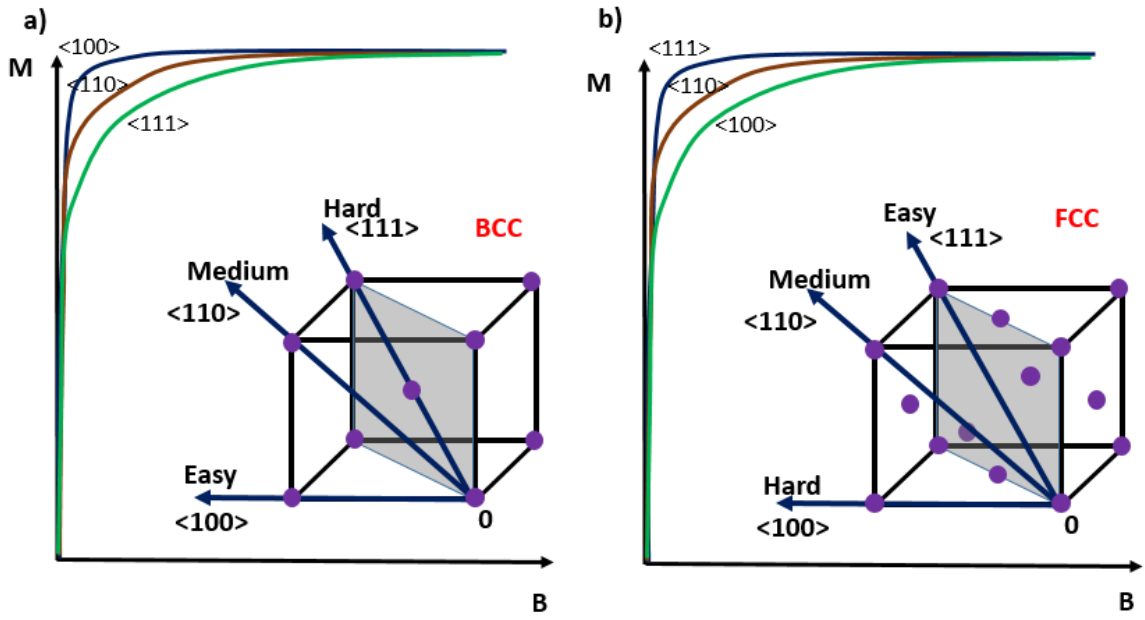

Figure 2.12: Magnetization as a function of an applied magnetic field curves for single crystals of the BCC (a) and FCC (b) structures.

Actually, our crystal disk, for example of 1 mm^2 contains tens or hundreds of domains, rather than the four shown in Fig. 2.13(a). However, all these domains are of only four types, namely, those with M_s vectors in the [010], [100], [0$\bar{1}$0], and [$\bar{1}$00] directions. If a field B is now applied in the [010] direction, the [010] domain will grow in volume by the mechanism of domain-wall motion, as indicated in Fig. 2.13(a). It is because the magnetic potential energy of the crystal is thereby lowered; The energy of a [010] domain in the field is -M_sB per unit volume, for a [0$\bar{1}$0] domain is +M_sB, and for a [100] or [$\bar{1}$00] domain is zero. Continued application of the field eliminates all but the favored domain, until the crystal is saturated. Since experiment shows that only a low field is needed to saturate BCC in a $< 100 >$ direction, we conclude that our postulated domain structure is basically correct and, more generally, *that the direction of easy magnetization of a crystal is the direction of spontaneous domain magnetization in the demagnetized state*.

In FCC, figure 2.12(b) shows that the direction of easy magnetization is of the form $< 111 >$, the body diagonal of the unit cell.

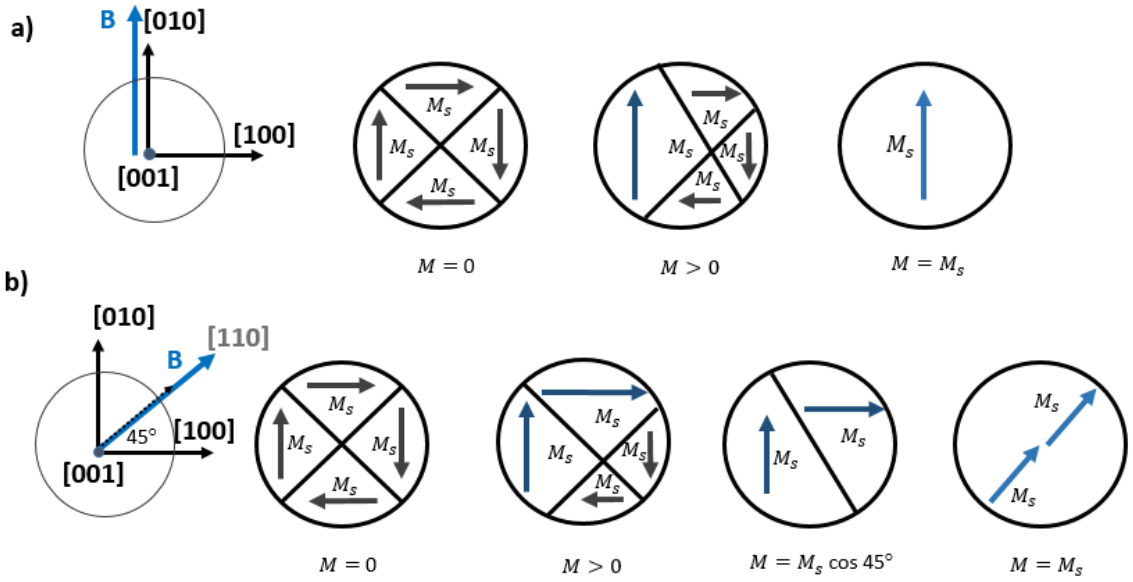

Figure 2.13: Domain structures in a BCC substance if one magnetic field is applied parallel (a) or not parallel (b) to some AFM axis.

Figure 2.12(a) shows that fairly high fields are needed to saturate BCC in a $< 110 >$ direction. For this orientation of the field, the domain structure changes as in Fig. 2.13(b). Domain wall motion, in a low field, occurs until there are only two domains left, each with the same potential energy. The only way in which the magnetization can increase further is by rotation of the M_s vector of each domain until it is parallel with the applied field. This process is called *domain rotation*. Domain rotation occurs only in fairly high fields, because the field is then *acting against the force of crystal anisotropy* which is usually fairly strong. Crystal anisotropy may therefore be regarded as a force which tends to hold the magnetization in certain equivalent crystallographic directions in a crystal. When the rotation process is complete, the domain wall disappears, and the crystal is saturated.

Because the applied field must do work against the anisotropy force to turn the magnetization vector away from an easy direction, there must be energy stored in any crystal in which M_s point in a non easy direction. This is called the **crystal anisotropy energy** E. This energy can be expressed in terms of a series expansion of the direction cosines of M_s relative to the crystal axes. In a cubic crystal, let M_s pointing to a non easy directions make angles α, β, θ with the crystal axes. Then,

$$E = K_0 + K_1(\cos\alpha^2 \cos\beta^2 + \cos\beta^2 \cos\theta^2 + \cos\alpha^2 \cos\theta^2) + K_2(\cos\alpha^2 \cos\beta^2 \cos\theta^2 + ...), \tag{2.100}$$

where K_0, K_1, K_2, ... are constants for a particular material at a particular temperature and are expressed in J/m^3 (SI). Higher powers are generally not needed, and sometimes K_2 is so small that the term involving it can be neglected. The first term, K_0, is independent of angle and is usually ignored, because normally we are interested only in the

change in the energy E when the M_s vector rotates from one direction to another.

When K_2 is zero, the direction of easy magnetization is determined by the sign of K_1. If K_1 is positive, then $E_{100} < E_{110} < E_{111}$, and $< 100 >$ is the easy direction, because E is a minimum when M_s is in that direction. If K_1 is negative, $E_{111} < E_{110} < E_{100}$, and $< 111 >$ is the easy direction. When K_2 is not zero, the easy direction depends on the values of both K_1 and K_2.

Physical origin of the crystal anisotropy: spin-orbit coupling

It is known that the exchange energy is isotropic, depending only on the angle between adjacent spins and not on the direction of the spin axis relative to the crystal lattice, then, this spin–spin interaction do not contribute to the crystal anisotropy. There is also a coupling between the spin and the orbital motion of each electron. When an external field tries to reorient the spin of an electron, the orbit of that electron also tends to be reoriented. But the orbit is strongly coupled to the lattice and therefore resists the attempt to rotate the spin axis. In most materials, the orbital magnetic moments are almost entirely quenched. This means that the orientations of the orbits are fixed very strongly to the lattice due to the strong orbit-lattice coupling, meaning that even large fields cannot change them. The energy required to rotate the spin system of a domain away from the easy direction, which we call the **anisotropy energy**, *is just the energy required to overcome the spin–orbit coupling*. This coupling is relatively weak, because fields of a few hundred Oersteds or a few tens of kiloamps per meter are usually strong enough to rotate the spins. We can also speak of a spin–lattice coupling ("lattice" consists of a number of atomic nuclei arranged in space, each with its surrounding cloud of orbital electrons) and conclude that it too is weak.

The strength of the anisotropy in any particular crystal is measured by the magnitude of the anisotropy constants K_1, K_2, etc. Although there seems to be no doubt that crystal anisotropy is due primarily to spin-orbit coupling, the details are not clear, and it is generally not possible to calculate the values of the anisotropy constants in a particular material from first principles.

Nor is there any simple relationship between the easy, or hard, direction of magnetization and the way atoms are arranged in the crystal structure. Thus, in iron, which is BCC, the direction of greatest atomic density, i.e., the direction in which the atoms are most closely packed, is $< 111 >$, and this is the hard axis. But in nickel (FCC), the direction of greatest atomic density is $< 110 >$, which is an axis of medium hard magnetization. When iron is added to nickel to form a series of face-centered cubic solid solutions, the easy axis changes from $< 111 >$ to $< 100 >$ depending on the percentage of iron [48].

Anisotropy in antiferromagnetics

In antiferromagnets, in zero magnetic field, the spins of the two sublattices are parallel, to an important crystallographic axis. When a field is applied perpendicular to the AFM axis, the sublattice magnetizations rotate away from this axis, as shown in Fig. 2.10(a), until the reverse molecular field equals the applied field. Actually, there is another force tending to resist the rotation of the spins, and that is the crystal anisotropy which tends to bind the spin directions to the AFM-axis. Inclusion of an anisotropy term does not alter the main conclusions reached before, but anisotropy forces are responsible for the **spin flopping**. When a substance of susceptibility χ_v is magnetized by a field $\boldsymbol{B}$, its magnetization $\boldsymbol{M}$ is $\chi_v B/\mu_0$ and its potential energy in the field is $-\chi_v B^2/\mu_0$. In an antiferromagnetic below the Néel temperature, $\chi_\perp$ is greater than $\chi_{||}$. This means that the state with spins perpendicular to $\boldsymbol{B}$ is of lower energy than that in which spins are parallel and antiparallel to $\boldsymbol{B}$. Thus, when $\boldsymbol{B}$ is parallel to the spin directions and the AFM-axis, as in Fig. 2.14(a), there is a tendency for the spin directions to rotate into orientation perpendicular to AFM axis, counteracting the binding of the spin to the AFM-axis direction by the crystal anisotropy forces. As the field increases, a critical value will be reached when these forces are overcome at magnetic field B_1. The magnetization for the antiferromagnet parallel magnetic field is shown in Fig. 2.14(a). There is no effect until the **spin-flop** transition at magnetic field B_1, above this field the magnetization increases steadily until saturation is reached at magnetic field B_2. If the anisotropy effect is very strong, another effect can occur. In this case, no spin-flop occurs. Instead we get a **spin-flip** transition, i.e. the magnetization of one sublattice suddenly reverses when the magnetic field reaches a critical value B_3 , and the system moves in a single step to the ferromagnetic state [49]. This is illustrated in Fig. 2.14(b).

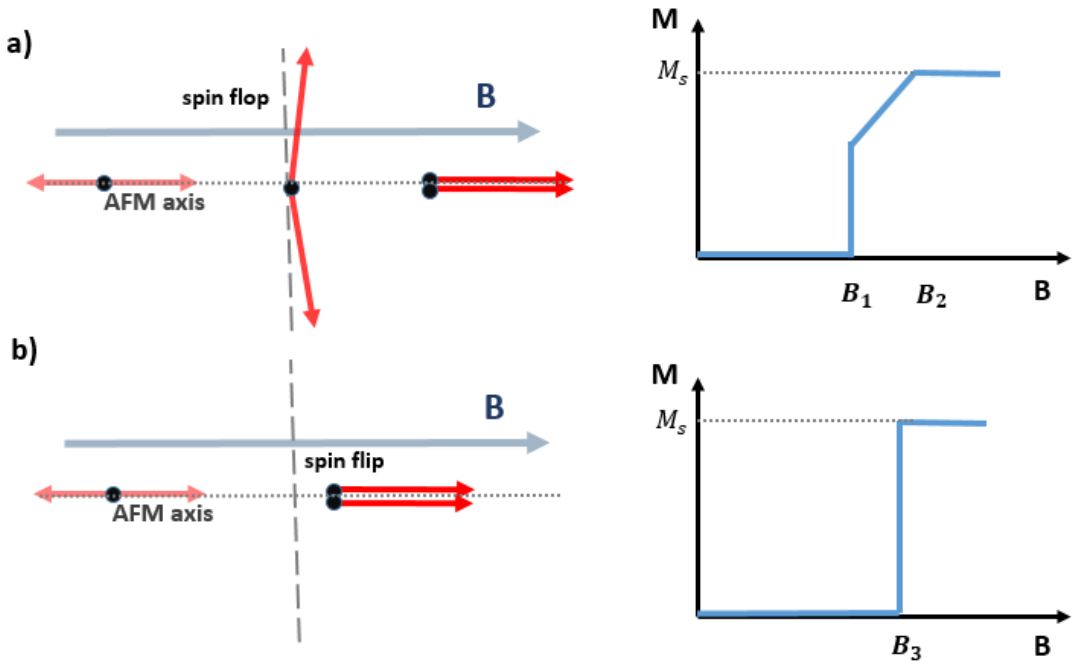

Figure 2.14: (a) Magnetization for applying magnetic field parallel to an antiferromagnet axis. Initially nothing happens but then there is a spin-flop transition to a spin-flop phase at B_1. The magnetic field then rotates the moments until saturation is achieved at the field B_2. (b) If there is a strong preference for the spins to lie along the parallel direction, there is a spin-flip transition at B_3. Both figures show the expected curves for absolute zero. Finite temperature will round off the sharp corners. This is also known as a metamagnetic transition.

2.2 Spin physics in semiconductor quantum dots

2.2.1 Semiconductor quantum dots

Semiconductor QDs are quasi-zero-dimensional nano-crystals, with carriers confined in all three dimensions. This happens when the dimensions of typically direct band-gap semiconductor hetero-structures are reduced to the order of 2-100 nm. In this situation, the energy of the confined carriers can not be obtained, as normally, from the periodic potential of the crystal, the Bloch waves, that extent over an entire crystal. For quantum dots, the energy of the carriers depends on the potential energy due to the *confinement*, which is not periodic, and the periodic potential can be considered as a perturbation. The approximate solution for the energy of the carriers in this system shows that the confinement leads the characteristic continuous conduction and valence bands, typically observed in bulk semiconductors to be replaced by **discrete energy levels**, with a density of states resembling a sequence of delta functions. For this reason, quantum dots are also called *artificial atoms*. These discrete energy levels are closely related to the shape, size, surrounding materials, and external fields applied to the QDs.

2.2.2 Spin-orbit interaction in quantum dots

In the classical electrodynamics, any moving particle as an electron orbiting its nucleus in an atom, will be affected by the electric field produced by its positively charged nucleus and will also experience a magnetic field. This is because in the electron rest frame, the charged nucleus is seen to circle around it, which creates a current accompanied by its surrounding magnetic field $\boldsymbol{B}$ that interacts with the spin of the electron with magnetic moment $\boldsymbol{\mu_S}$ in the form,

$$E = -\boldsymbol{\mu_S} \cdot \boldsymbol{B}. \tag{2.101}$$

This magnetic field is parallel and proportional to the electron orbital angular momentum $\boldsymbol{L}$,

$$\boldsymbol{B} = \frac{1}{m_e e c^2} \frac{1}{r} \frac{\partial U(r)}{\partial r} \boldsymbol{L}, \tag{2.102}$$

where m_e is the electron mass, e is the electron charge, c is the light velocity and $U(r)$ is the potential energy of the electron in the central field which depends on the particular orbit that the electron is in. The electron angular momentum is proportional to the electron spin magnetic moment $\boldsymbol{S}$ (Eq. 2.31),

$$\boldsymbol{\mu_s} = g_S \frac{e}{2m_e} \boldsymbol{S} \quad = \quad g_S \frac{\mu_B}{\hbar} \boldsymbol{S}, \tag{2.103}$$

where $e = -1.6 \times 10^{-19}$ C. Then, following equations 2.102 and 2.103, the interaction between the magnetic field and the spin magnetic moment can be written as

$$E = \alpha \boldsymbol{L} \cdot \boldsymbol{S}, \tag{2.104}$$

where the proportionality constant $\alpha = \dfrac{1}{m_e e c^2} \dfrac{1}{r} \dfrac{\partial U(r)}{\partial r} g_S \dfrac{\mu_B}{\hbar}$ can be written as depending on the quantum numbers n and l.

When two or more kinds of angular momentum interact with each other, the total angular momentum can be transferred from one to the other. Then, due the spin-orbit coupling, the angular momentum can be transferred between $\boldsymbol{L}$ and $\boldsymbol{S}$, but only the total angular momentum $\boldsymbol{J} = \boldsymbol{L} + \boldsymbol{S}$ is conserved. As an example, in an atom with two electrons, each has its own angular momentum $\boldsymbol{J_1}$ and $\boldsymbol{J_2}$, but only the total angular momentum $\boldsymbol{J_t} = \boldsymbol{J_1} + \boldsymbol{J_2}$ is conserved. Then, the spin-orbit interaction energy couples the previously separate terms for $\boldsymbol{L}$ and $\boldsymbol{S}$, resulting in that these two are no longer conserved separately, but only the total angular momentum $\boldsymbol{J}$ is conserved.

The coupling of spin and orbital angular momentum, and its resulting energy splitting, is what finally enables optical orientation of carrier spins in semiconductors, as the photon does not couple to the carrier spins directly. The photon interacts with the orbital state where the electron is in. However, as pure spin states are no longer the eigenstates of the Hamiltonian, the spin-orbit coupling is also responsible for many spin relaxation mechanisms.

2.2.3 Energy levels in quantum dots from the III-V group

In particular, the quantum dots based on the III-V group cover a huge range of different electronic properties, among them, for the case of (In,Ga)As QDs, it is known that they have a direct gap, which means that in the energy (E)-momentum (k) space the minimum of the conduction band lies exactly above the maximum of the valence band, which makes them suitable for optical studies at the Γ-point ($k = 0$). At this point, the energy difference between the top of the valence band and the minimum of the conduction band is the band gap energy E_g. In the III-V group compounds, the states in the conduction energy level have properties equivalent to **s-type atomic orbitals** and the valence energy level have properties equivalent to **p-type atomic orbitals**. So the electrons at the conduction band minimum have zero orbital angular moment (l=0) since they occupy an s-like orbital. In contrast, holes at the top of the valence energy levels have orbital angular moment (l=1) because they occupy a p-like orbital.

Due to the spin-orbit interaction, the energy states for the electron (s=1/2) must be studied considering the total angular momentum $\boldsymbol{J} = \boldsymbol{L} + \boldsymbol{S}$ with quantum numbers j,

l and s, respectively, and their quantum numbers for their projections on one axis (Z axis) J_z, m_l and m_s, respectively. From the angular momentum addition theory in the Appendix, the values for the quantum number j are integer or semi-integer numbers given by:

$$|l-s|,\ \ |l-s|+1, ... \leq j \leq ..., l+s-1,\ \ l+s, \tag{2.105}$$

and the values for the quantum number m_j are given by,

$$-j, -j+1, ... \leq m_j \leq ..., +j-1, +j. \tag{2.106}$$

Then, we can affirm:

For the conduction energy levels (l=0, s=1/2), the possible values for the total angular momentum are given by $|0-1/2| \leq j \leq |0+1/2|$. That is $j = 1/2$, and then the projection of its angular momentum are $m_j = \pm 1/2$. This is a doubly degenerate sub-band.

For the valence energy levels (l=1, s=1/2), the possible values for the total angular momentum are given by $|1 - 1/2| \leq j \leq |1 + 1/2|$. that is j=(1/2, 3/2). For j=1/2, the corresponding projections along the Z axis are $m_j = \pm 1/2$ resulting in a doubly degenerate band which are split from the j=3/2 states by the spin-orbit interaction. The two j=1/2 states referred to as *split-off bands* and are typically a few hundreds of meVs above j=3/2 states ($\Delta_{so} \approx 0.3$ eV in GaAs). When $j = 3/2$ holds, four possibles values for the projections exists $m_j = \pm 1/2$ and $\pm 3/2$ and can be separated into the **light-hole** (lh) band for ($m_j = \pm 1/2$) and the**heavy-hole** (hh) band for ($m_j = \pm 3/2$). The light hole states are typically tens of meVs below the heavy hole states. Thus, the hole ground state is composed of the doubly degenerated states $m_j = +3/2$, originating from $m_l = +1$ and $m_s = +1/2$, and m_j = -3/2, originating from m_l = -1 and m_s = -1/2.

In bulk semiconductors, the heavy hole and the light hole bands are degenerated at k=0 as is shown in Fig 2.15(a). Near the Γ-point, in the E vs k space, the bulk dispersion relation of the band structure is parabolic in the effective mass approximation and the energy bands for the conduction, heavy hole valence, light hole valence and split off band valence, can be written as:

$$E_c(k) = E_g + \frac{\hbar^2 k^2}{2m_e^*}, \tag{2.107}$$

$$E_{hh}(k) = -\frac{\hbar^2 k^2}{2m_{hh}^*}, \tag{2.108}$$

$$E_{lh}(k) = -\frac{\hbar^2 k^2}{2m_{lh}^*}, \tag{2.109}$$

$$E_{so}(k) = -\Delta_{so} - \frac{\hbar^2 k^2}{2m_{so}^*}, \tag{2.110}$$

where m_e^* is the electron effective mass, m_{hh}^* is the heavy hole effective mass, m_{lh}^* is the light hole effective mass and m_{so}^* is the effective split-off hole mass. But in QDs, both strain and quantum confinement split the remaining degeneracy of the *hh* and *lh* with a energy Δ_s as is shown in figure 2.15 (b) producing quantized states for carriers in these levels [50].

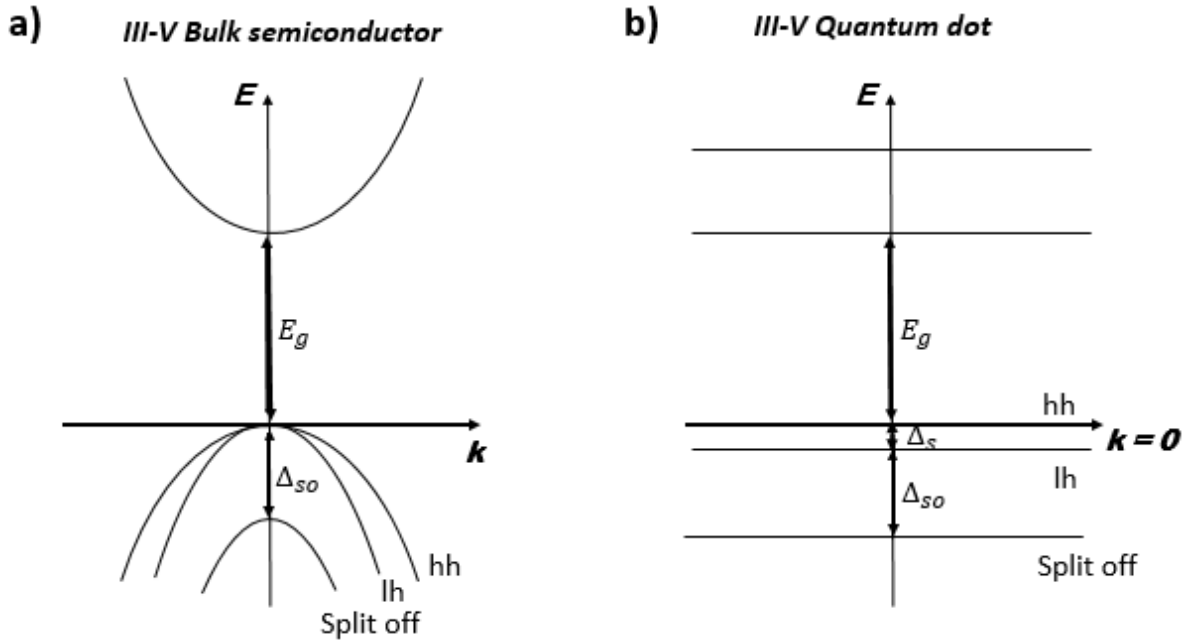

Figure 2.15: Energy levels under the effective mass approximation in (a) III-V group bulk semiconductor and in (b) III-V group semiconductor QD, where the degeneracy between the hh and lh levels disappears.

2.2.4 Interaction of III-V group quantum dots with light: Excitons

The optical excitation consists in transferring, by means of photons, an electron from a confined state in the valence band to a confined state in the conduction band, leaving a hole in the valence band. Due the confinement in a quantum dot, the pair electron-hole remain bounded and a large Coulomb energy is induced producing what is called a (neutral) **exciton state X^0** (lh-exciton or hh-exciton, depending on the kind of hole involved in the optical excitation).

In a III-V group quantum dot, as the (In,Ga)As QDs, the *hole ground state* in the valence band is the doubly degenerated heavy hole state with $j_z = +3/2$ and $j_z = -3/2$. Then, including the two possible spin states of an electron in the conduction band, four spin combinations are possible for a photo-excited hh exciton: $\uparrow\Uparrow, \downarrow\Uparrow, \uparrow\Downarrow$ and $\downarrow\Downarrow$, where $\downarrow$ ($\uparrow$) represents an spin down (up) electron with total angular momentum projection

-$\hbar/2$ ($+\hbar/2$) and $\Downarrow$ ($\Uparrow$) represent an spin down (up) hole with total angular momentum projection -$3\hbar/2$ ($+3\hbar/2$). The total projection of the angular momentum on the Z axis J_{tz} of these four possible combinations are $\boldsymbol{J_{tz} = J_z^e + J_z^{hh}}$ = +2,+1,-1,-2 in units of $\hbar$ respectively, conventionally denoted by: $|+2>$, $|-2>$, $|+1>$ and $|-1>$.

Circularly polarized photons of right or left polarizations have angular momentum on the direction of their propagation equal to +1 or -1 (in units of $\hbar$) and have zero spin. Thus, when optical excitation is due to a circularly polarized photon, its angular momentum is distributed between the photo-induced electron in the conduction band and the hole in the valence band according to the **angular momentum conservation principle** determined by the band structure of the semiconductor. Then, the following selection rules should be obeyed for an optical transition between two electronic states,

$$\Delta j = \pm 1 \qquad \Delta m_j = \pm 1 \qquad and \qquad \Delta s = 0. \tag{2.111}$$

These constraints distinguish the **bright exciton** states $|+1\rangle = |-1/2\rangle^e - |-3/2\rangle^{hh}$ and $|-1\rangle = |+1/2\rangle^e - |+3/2\rangle^{hh}$ from the **dark exciton** states $|+2\rangle = |+1/2\rangle^e - |-3/2\rangle^{hh}$ and $|-2\rangle = |-1/2\rangle^e - |+3/2\rangle^{hh}$. We call bright the excitons states in which an optical recombination by radiatively emission of a photon is possible and dark those that can not decay optically due to their larger angular momentum. These transitions are depicted in figure 2.16.

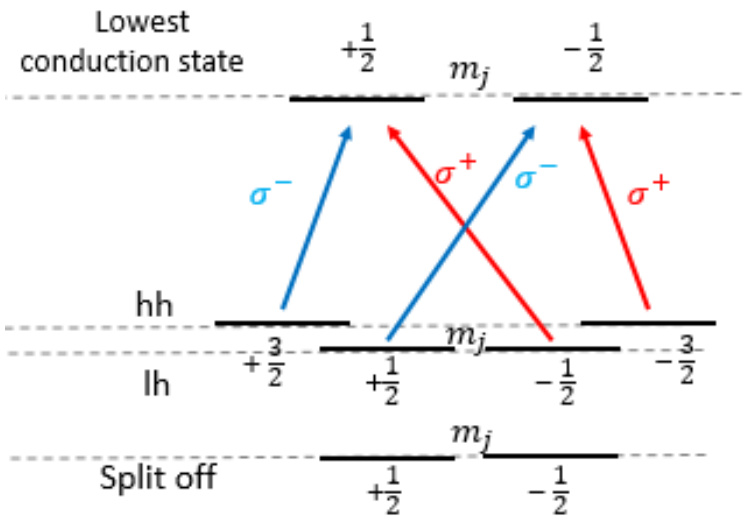

Figure 2.16: Selection rule allowed transitions in a III-V group QD due to a photon with $\pm$ $\hbar$ angular momentum.

2.2.5 Charged excitons in III-V group quantum dots: Trions

The quantum dot ground state may already be populated by a **resident electron** in the lowest conduction energy level or a resident hole on the top of the valence band, due to either residual or intentional dopant carriers, which modify the original energy levels. Thus, after a generation of an electron-hole pair in a charged quantum dot, the new discrete levels can be populated by two electrons in the same energy level with opposite spin states, due to Pauli exclusion principle, in **singlet configuration** or with high energy excitation by two electrons in different energy levels in **triplet configuration** or **singlet configuration**, giving rise in addition to the holes to multiple charged excitons states. The state consisting of either two electrons and a hole is called a **negative trion** (X^-), and the state consisting of two holes and one electron is called a **positive trion** (X^+). The lowest energy levels for the neutral and charged excitons are depicted in figure 2.17.

In contrast to neutral excitons, the charged excitons in doped QDs with resident electrons or holes provide an experimental tool for investigating the spin dynamics of electrons or holes separately, because in trions, the spins of both the two electrons or the two holes are aligned antiparallel (singlet), and thus, there is no net electron-hole exchange interaction in a (singlet) trion.

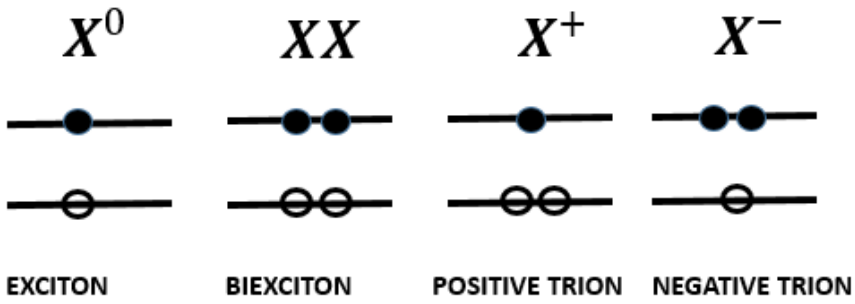

Figure 2.17: Lowest energy levels for the neutral exciton and charged excitons. A biexciton is a composite of two electrons and two holes.

For a *singly negatively charged quantum dot*, the ground state is occupied by one electron in the lowest energy level of the conduction band, the state $\boldsymbol{e_S}$. An optical excitation in this case corresponds to a transition between a single electron state to a *negative trion state*, the state of two electrons and one hole confined in the QD, which can be the *trion ground state* $\boldsymbol{S_s}$ or higher energy states as $\boldsymbol{S_p}$ or $\boldsymbol{T_p}$, as is shown in figure 2.18. From the Pauli exclusion principle, it is clear that the trion ground state transition is possible only if the state which is going to be occupied by the photo-created electron is free. Hence, for the case of a *right circularly polarized* incident photon, a trion ground state may be created if the dot is initially occupied by a spin-up ($+1/2$) electron but not

if the electron in the dot is initially in the spin-down (-1/2) state. This suppressing of the optical transition depending on the spin of the electron in the QD is referred as *Pauli blocking*.

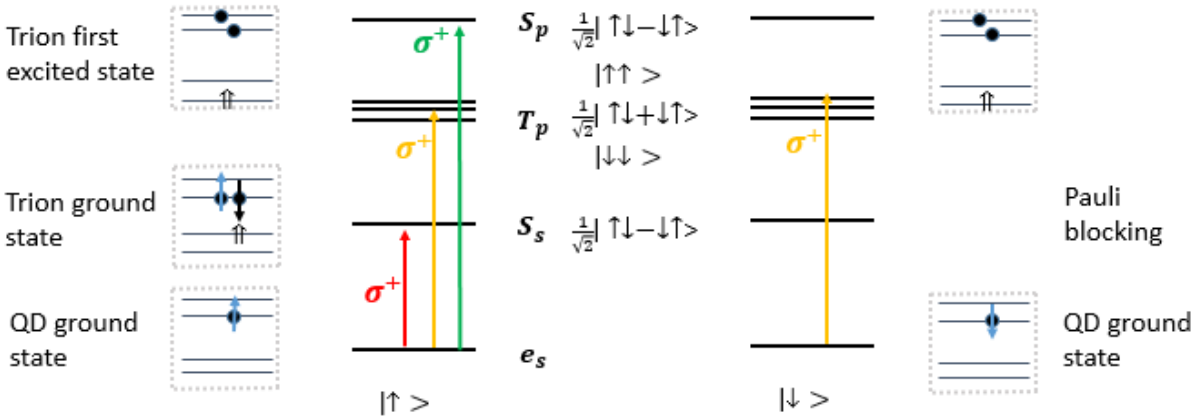

Figure 2.18: Possible transitions in a III-V group singly negatively doped quantum dot by light excitation using a right circularly polarized light. The trion ground state is the S_s state which is possible only if the QD ground state with resident electron is in the (+1/2) state.

2.2.6 Optical orientation of spins in a ensemble of negatively charged QDs.

Electron spin coherence can be generated in an ensemble of singly negatively charged quantum dots along one axis (Z-axis) if the dots are excited by light with energy at least resonant with band-gap of the quantum dots and able to transfer its angular moment. The absorbed light generates in each dot a superposition of a partially polarized **resident electron** and a trion consisting of two electrons (**resident** and photo-excited) and a hole. Even after the radiative recombination of the trion, the partially polarized resident electron spin (magnetic moment) oriented at an angle with respect to an externally applied magnetic field B normal to Z direction (along the Y-axis), feel a torque that tries to align it along the direction of the magnetic field. Consequently, the optically oriented electron spins precess in the X-Z plane about this field with a frequency given by $\omega_e = g_{e,y}\mu_B B/\hbar$, where $g_{e,y}$ is the electron g-factor along the field, producing an oscillating magnetization on the Z-axis component. The precession continues until scattering leads to reduction of this magnetization and the magnetic moment point on the magnetic field direction after a coherence time T_2 as is shown in Fig. 2.19(a). An example of the photo-induced magnetization profile obtained in this situation as a function of time is shown in Fig. 2.19(b). The evolution as function of the time can be modeled by an exponentially

damped harmonic oscillator function $M_z = e^{-t/T_2^*}\cos(\omega_e t)$.

In general, experimentally observed signals may look more complicated, as for example due in-homogeneous magnetic field or due to multiple carriers with different g-factor (precession frequencies) and dephasing times, leading to shorter dephasing times, referred as T_2^*.

For an ensemble of electron spins, this produce a *macroscopic magnetization* that can be measured using standard techniques.

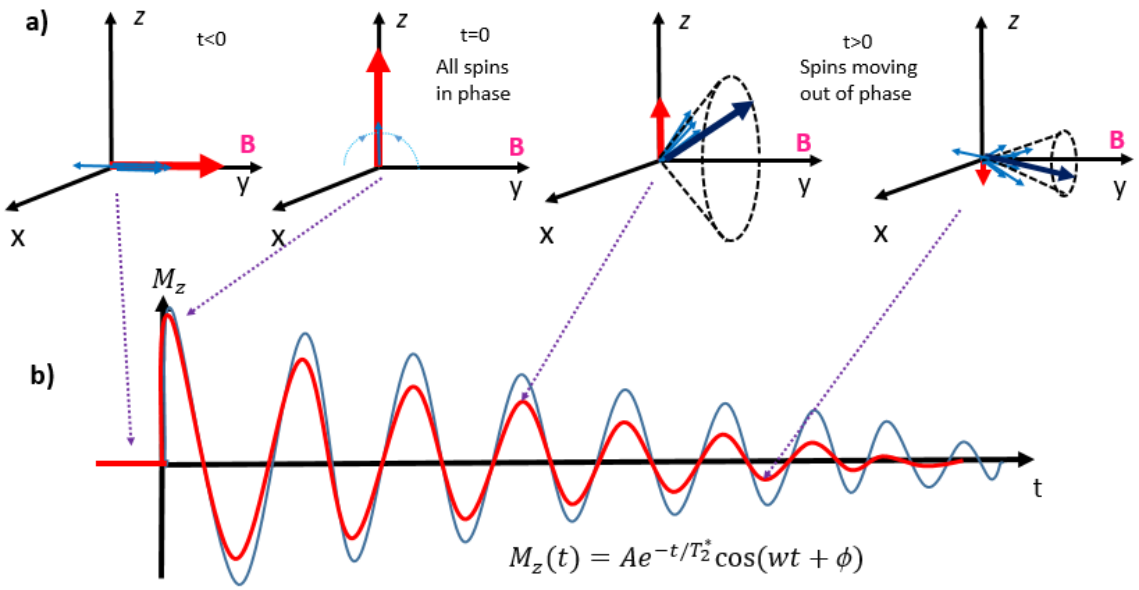

Figure 2.19: (a) Time evolution of the precession of the ensemble of spins about transverse magnetic field B (blue), the effective spin component on the Z axis is shown in red. (b) Magnetization profile on the Z axis produced by a single QD (blue), T_2 is the coherence time of a single quantum dot, for an ensemble of QDs (red), T_2^* is the coherence time.

2.2.7 Review of the model for light induced magnetization in n-doped QDs ensemble

Here the basic ideas of the most recent quantum mechanical model [18] for the process of photo-induced magnetization in a singly negatively doped ensemble of quantum dots are summarized.

We first consider a singly charged QD submitted to a magnetic field along the Y-axis. The electron's spin Hamiltonian will be described by:

$$H = -\boldsymbol{\mu} \cdot \boldsymbol{B} = -(-\frac{g}{\hbar}\mu_B S_y)B_y = \frac{g}{\hbar}\mu_B B_y S_y = \frac{1}{2}g\mu_B B_y \sigma_y = \frac{1}{2}\hbar\Omega\sigma_y, \tag{2.112}$$

where $\sigma_y = \begin{pmatrix} 0 & -i \\ i & 0 \end{pmatrix}$ is the y-Pauli matrix, $\Omega = \frac{geB}{2m_e}$ is the Larmor precession frequency, g is the g-factor, $e = +1.6 \times 10^{-19}$ C is the electron charge, B_y is the magnetic field on the Y axis, and m_e is the electron mass.

In equilibrium, *the electron spin will be polarized along the Y-axis*. Therefore, at a given instant before the arrival of the exciting light pulse, at t= 0, the QDs spin function will be given by:

$$\Psi(t < 0) = \frac{1}{\sqrt{2}}|\uparrow -i\downarrow\rangle. \tag{2.113}$$

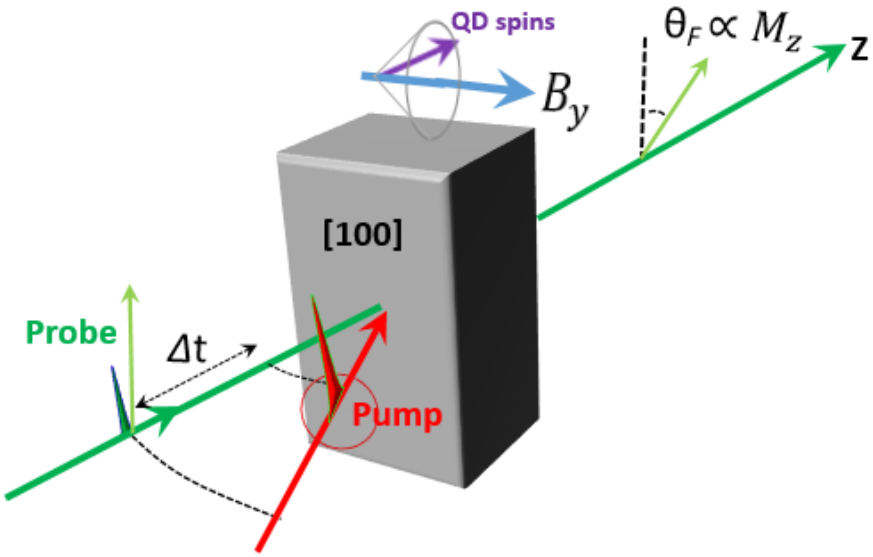

Figure 2.20: Pump-probe pulses with magnetic field perpendicular to the optical axis 100 (Voigt geometry) for photo-induced magnetization in a ensemble of QDs.

At t= 0, a right hand circularly polarized light σ^+ pulse resonant with the $e_S \rightarrow S_S$ or $e_S \rightarrow S_p$ (Singlet) transition energy travelling along the Z-axis hits the QD as is shown in figure 2.20, and instantaneously the QD spin function $\Psi(t < 0)$ change to:

$$\Psi(t = 0) = \frac{1}{\sqrt{2}}|\uparrow\downarrow \otimes \Uparrow -i\downarrow\rangle. \tag{2.114}$$

As the time progress, the paired electrons in the first spin wave function component do not precess (because $S = +\frac{1}{2} - \frac{1}{2} = 0$), but the hole, as well as the resident electron do precess, so the wave function $\Psi(t = 0)$ evolves in time to:

$$\Psi(0 < t < t_r) = \frac{1}{\sqrt{2}}|\uparrow\downarrow \otimes \chi_h(t) - i\chi_e(t)\rangle, \tag{2.115}$$

where $\chi_h(t)$ is the spin function of the precessing hole, and $\chi_e(t)$ is the spin function of

the precessing electron, which is obtained applying the time evolution operator ($e^{-\frac{iHt}{\hbar}}$) to $|\Uparrow\rangle$ and $|\downarrow\rangle$, respectively.

When the trion recombines at the recombination time $t = t_r$, different models use different consideration for this instant. Previous model assumes that the hole can recombine with *equal probability* either with the spin-up or the spin-down electron of the trion. However, in the present model [18], it is considered that the hole precess coherently, so in the moment of the recombination $t = t_r$, the hole spin will have an specific orientation. In consequence, *the recombination probabilities for the spin-up and spin-down electrons will be different* and depend on the hole precession dynamics. In the frame of this model, the simplest version considers that the hole spin do not precess and just the electron spin do precess. This simplification of the general model, called **static hole model**, conserve the essential physics of the process and is an excellent approximation of the general case and allow us working with concise expressions. Then, we consider that in the recombination instant $t = t_r$, the static hole captures *the same photo-excited electron which originate it*, this is, a spin-down electron, then the wavefunction is written as:

$$\Psi(t = t_r) = |\uparrow -i\chi_e(t)\rangle = \frac{1}{\sqrt{2}}|\uparrow -i\cos\frac{\Omega}{2}t_r\downarrow +i\sin\frac{\Omega}{2}t_r\uparrow\rangle. \tag{2.116}$$

The spin lifetime of photo-excited electrons is limited by the recombination process, but not in the case of the not excited resident electrons. After the recombination of the trion, the evolution of the $\Psi(t = t_r)$ state in time, after applying the time operator in $(t - t_r)$, can be written as:

$$\Psi(t > t_r) = \frac{1}{\sqrt{2}}\{[i\sin\frac{\Omega}{2}t + \cos\frac{\Omega}{2}(t - t_r)]|\uparrow\rangle + [-i\cos\frac{\Omega}{2}t + \sin\frac{\Omega}{2}(t - t_r)]|\downarrow\rangle\}. \tag{2.117}$$

Then, the expectation value of the time dependent photo-induced magnetic moment can be calculated as:

$$\langle\sigma(t > t_r)\rangle = \int \Psi^*(t > t_r)\sigma\Psi(t > t_r)d\tau. \tag{2.118}$$

When is considered the average of the recombination time for all the QDs in the ensemble.

$$\overline{\langle\sigma(t > t_r)\rangle} = \int \langle\sigma(t > t_r)\rangle dP(t_r), \tag{2.119}$$

where $\langle\sigma_z(t > t_r)\rangle$ is the z-component of $\langle\sigma(t > t_r)\rangle$ and $dP(t_r) = \frac{e^{-\frac{t_r}{\tau}}}{\tau}$ is the probability for recombination occurs at the interval t_r and t_r+dt_r, and τ is the trion recombination

time. Thus, finally we can obtain:

$$\overline{\langle\sigma(t > t_r)\rangle} = \frac{1}{2}\frac{\Omega\tau}{\sqrt{1+\Omega^2\tau^2}} e^{\frac{-t}{T_2^*}} \cos(\Omega\tau + (\frac{\pi}{2} - \arctan(\Omega\tau)). \tag{2.120}$$

Or

$$\overline{\langle\sigma(t > t_r)\rangle} = A e^{\frac{-t}{T_2^*}} \cos(\Omega\tau + \phi). \tag{2.121}$$

That is, the amplitude of the photo-induced magnetization is $A = \frac{1}{2}\frac{\Omega\tau}{\sqrt{1+\Omega^2\tau^2}}$ and the phase of the magnetization oscillations is $\phi = \frac{\pi}{2} - \arctan(\Omega\tau)$ as is shown in figure 2.21. These describe the precession movement of the photo-induced magnetic moment in the ensemble.

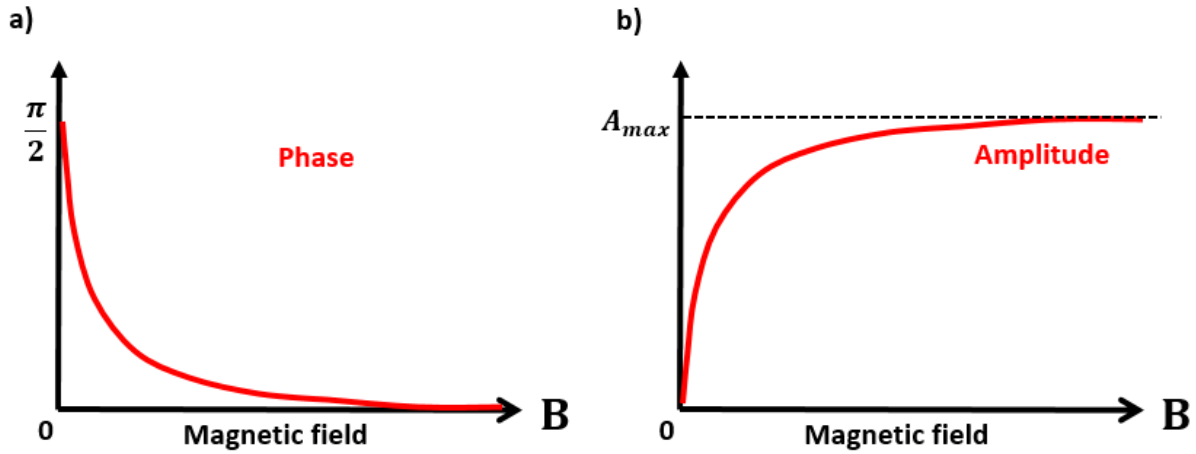

Figure 2.21: Phase (a) and amplitude (b) of the photo-induced magnetization in an ensemble of III-V group negatively doped QDs predicted by the quantum mechanical model presented in [18].

2.3 Spin physics in europium chalcogenides

2.3.1 Europium chalcogenides

Europium (Eu) belongs to the metallic elements known as rare earths, those comprising the lanthanide series and is the element of atomic number 63, which has the electronic distribution $[Eu] = [Xe]4f^7 6s^2$, where [Xe] represents the electronic distribution equivalent to a neutral Xenon atom, and can make an ionic bond with a chalcogen forming the binary compounds known as europium chalcogenides (EuX), where X= chalcogen. Chalcogens as O, Se, S, Te, Po, belong to 16 group of periodic table of elements and can bind with metallic elements giving rise to metallic chalcogenides. The common feature to all chalcogens is that they have six electrons in the valence shell, so they have a tendency to receive two electrons to fulfill its valence shells according to the Octet Rule. EuX are materials of great interest, mainly because of its magnetic properties associated with the Eu^{2+} ions, which have a large magnetic moment ($\mu \approx 8\ \mu_B$). The EuX ionic crystals are intrinsically magnetic and have a high density of Eu^{2+} ions in the lattice structure, giving to these materials one of the largest magnetic moments found in a semiconductor. Various properties of the EuX are related to their atomic structure and electronic energy levels. In EuX, the ionic bond takes place when the pair of valence electrons $6s^2$ from Eu atom migrate to chalcogens orbit so that the atoms become ionized and remain bonded by the attractive potential between the Eu^{2+} positive charges and the X^{2-} negative charges. The aggregation of these two elements in an ionic binary compound furnishes a crystalline solid of face centered cubic structure (FCC), as illustrated in figure 2.22.

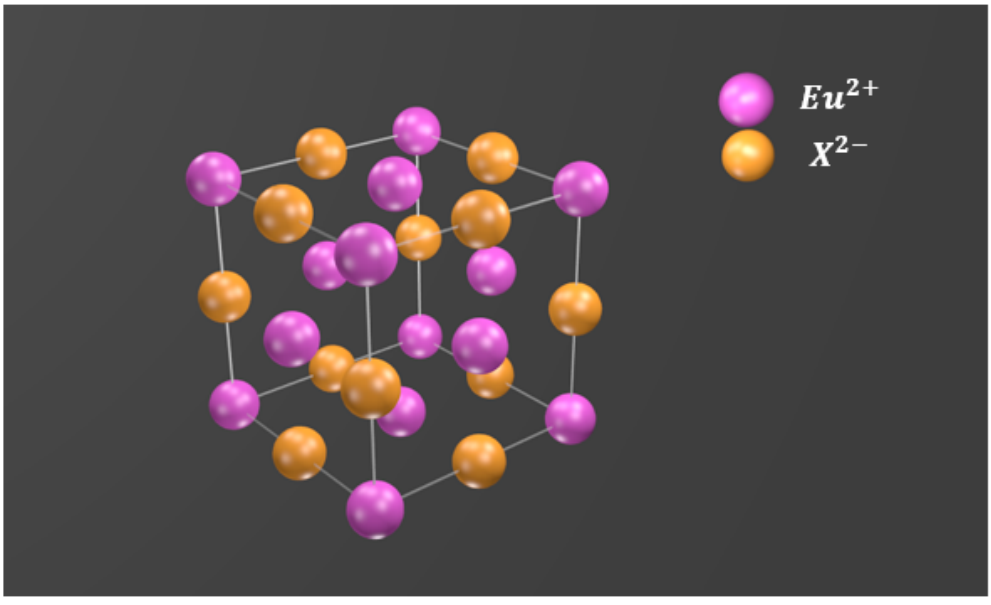

Figure 2.22: The face centered cubic structure in a europium chalcogenide EuX crystal.

The electronic distribution of the Eu^{2+} cation is $[Eu^{2+}]$=[Xe]$4f^7$. The seven remaining

electrons are distributed in a f orbital. In the ground state, the seven f-shell electrons are distributed according to Hund's rules. The first rule says that the individual spins, s_i, are distributed in a way to maximize the spin multiplicity, $2S + 1$, where $S = \sum_{i=1}^{7} m_{si}$ is the total spin of the atom. The higher multiplicity is obtained when the seven electrons have the same spin projection, $m_s = +1/2$, totaling $S = 7/2$. The orbital angular momentum L, of a subshell of quantum number is given by $L = \sum_{-l}^{+l} m_l$ where m_l is the projection on the Z-axis of the orbital angular momentum of each electron. As the f subshell can hold 14 electrons, it is half-filled. By the first Hund's rule, all seven electrons have the same spin projection and therefore each electron has a different projection m_l, so that the sum in L vanishes (L=0). The total angular momentum, $\boldsymbol{J = L + S}$, is given simply by the spin term, so Hund's first rule suffices to determine the ground state of Eu^{2+}.

The fact that all the spins in the subshell have the same m_s projections implies a high magnitude of the magnetic moment of Eu^{2+} ion, which classically is given by $\mu = g\mu_B S = 7\mu_B$ and in quantum theory is given by $\mu = g\mu_B\sqrt{S(S+1)} \sim 8\ \mu_B$. On the other hand, the X^{2+} anion has its valence shell filled with eight electrons, so that the chalcogens do not contribute to EuX magnetism.

The Eu^{2+} ions in EuX exchange interact with each other and when the energy of this interaction is higher than the thermal energy, the exchange interaction originates a magnetic ordering of Eu^{2+} spins. These ordering will be described through the mean field theory in the next section.

2.3.2 Magnetic order in EuX crystals

The mean field theory is a theoretical approximation that shows to be sufficient to explain most of the magnetic properties of EuX, as its magnetic order. In general, the exchange interaction has a limited reach and therefore it should not be significant on sites far away from each other. Thus, it will be considered interactions with the nearest, next-nearest and next-next nearest neighbors only. Any atom in a FCC lattice of size l possess 12 nearest neighbors (NN) located at a distance $l\sqrt{2}/2$ along the cubic diagonal, 6 next-nearest neighbors (NNN) at distance l along the cubic axis and 24 next-next nearest neighbor (NNNN) located at a distance $\sqrt{3}l/2$ as is shown in figure 2.23.

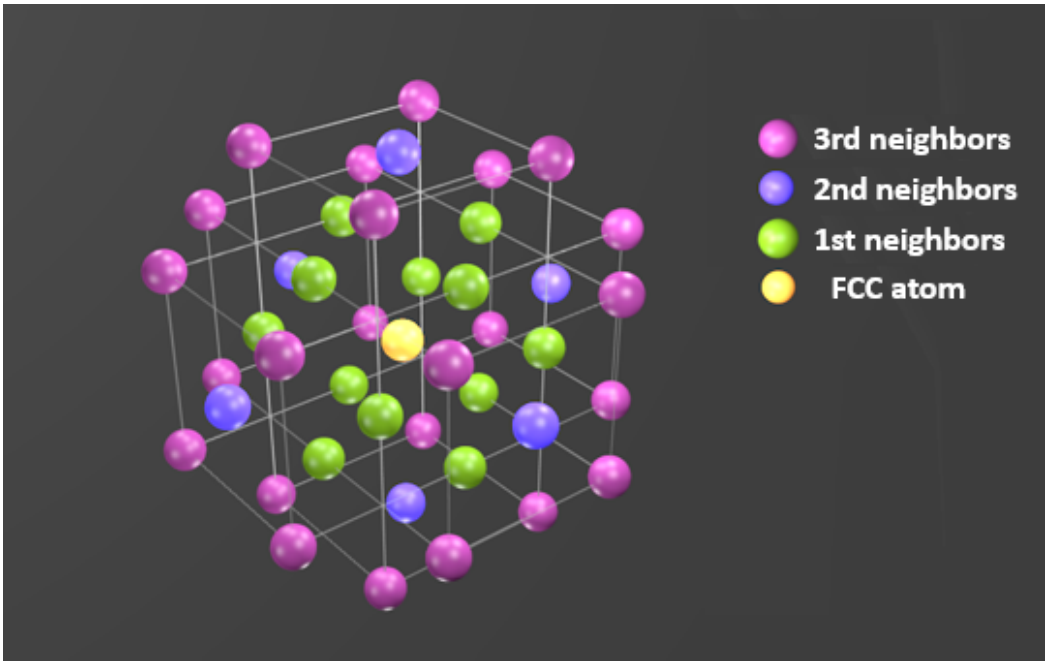

Figure 2.23: An Eu^{+2} atom within the face centered cubic structure, colored in yellow, has 12 nearest neighbors, colored in green, 6 next-nearest neighbors coloured in blue and 24 next-next nearest neighbor coloured in purple.

To implement the mean field approximation, it is necessary to divide the lattice into a number of sublattices that ensures that there are no interactions between elements in the same sublattice. In a face centered cubic lattice, this condition of non-intra-sublattice interactions can be achieved by dividing the lattice into eight inter-penetrating sublattices, so that each Eu^{2+} ion contained in a sublattice labeled as 1 of the material has two NN and 4 NNNN on sublattices labeled as 2,3,4,6,7 and 8. Also this ion has six NNN on another sublattice labeled as 5 as is shown in figure 2.24.

The effective field acting on an atom on the i-th sublattice is the composition of the molecular field due to exchange interactions with all neighboring sites. Then, the molecular field due to each sublattice is proportional to its magnetization, so that

$$B_i = B_0 + \sum_{j=1}^{8} \lambda_{ij} M_j, \tag{2.122}$$

where M_j is the magnetization of the j-th sublattice, B_0 is the external magnetic field and the molecular field constants are obtained from equation 2.57:

$$\lambda_{ij} = \frac{8(2z_{ij}J_{ij})}{Ng^2\mu_B^2}, \tag{2.123}$$

where z_{ij} is the number of equivalent spins surrounding the i-site (NN, NNN, NNNN, etc), and whose interactions with the j-th site are described by the same exchange constant

J_{ij}. The eight factor account for the number of sublattices, as discussed above, it grants that no intra-sublattice interactions are present, that is, $\lambda_{ii} = 0$. By symmetry $J_{ij} = J_{ji}$ and so $\lambda_{ij} = \lambda_{ji}$. The magnetization of each sublattice depends on the external field and on the molecular field due to the other sublattices.

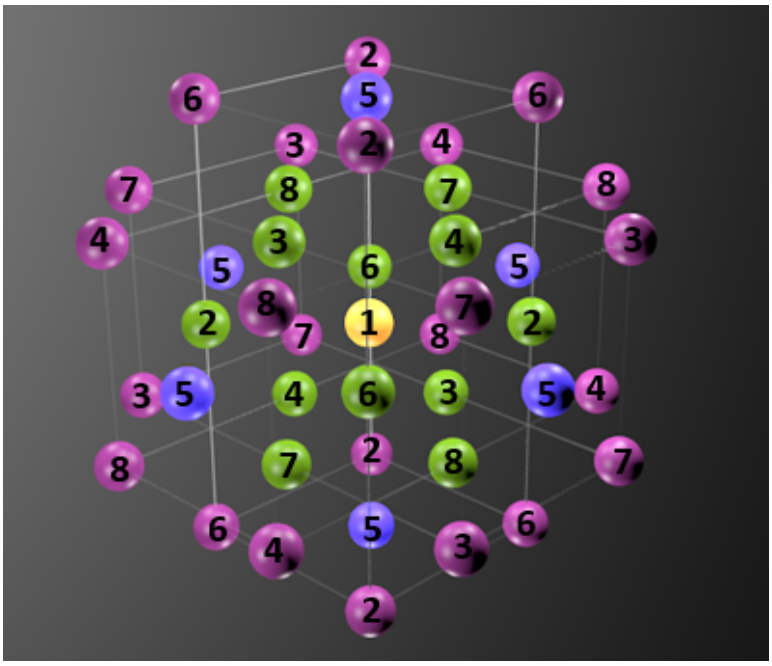

Figure 2.24: The eight sublattices in an Eu^{+2} atom within the face centered cubic structure.

In a system where the magnetizations of all sublattices point in the field direction, the result $M(B_0, T) = M_0\beta_J(y)$ with $y = \dfrac{g\mu_B J(B_0 + \lambda M(B_0, T))}{k_B T}$ [51] can be used (paramagnetic behavior), and the magnetization of the sublattice i, for a magnetic field oriented in the Z direction is given by

$$M_i = \frac{M_0}{8}\beta_J(\frac{g\mu_B J B_i}{k_B T}), \tag{2.124}$$

where M_0 was replaced by $M_0/8$ because every sublattice contains an eighth of the magnetic atoms of the crystal. As B_i depends on the magnetization of the other sublattices, equation 2.124 represents a system of eight coupled equations, whose analytical solution is quite complicated. However, in the high temperatures limit, even in a system with a magnetic anisotropy, the magnetizations of all sublattices point in the field direction. At this condition, in this temperature range we can use the first term of the power series expansion of Brillouin's function $\beta_J(x) \sim \dfrac{(J+1)}{3J}x$, simplifying the system to:

$$M_i = \frac{CB_i}{8T} \quad = \quad \frac{C(B_0 + \sum_{j=1}^{8}, \lambda_{ij} M_j)}{8T}, \tag{2.125}$$

where $C = \frac{g\mu_B(J+1)M_0}{3k_B}$ is the Curie constant. By adding the eight equations 2.125 we have:

$$\sum_{i=1}^{8} M_i = \sum_{i=1}^{8} \frac{CB_i}{8T} = \frac{C}{8T}\sum_{i=1}^{8}(B_0 + \sum_{j=1}^{8}\lambda_{ij}M_j), \tag{2.126}$$

and we can rewrite it as:

$$\sum_{i=1}^{8} M_i = \frac{CB_0}{T} + \sum_{i=1}^{8} M_i \frac{C}{8T}\sum_{j=1}^{8}\lambda_{ij} \quad \Rightarrow \quad \sum_{i=1}^{8} M_i(1 - \frac{C}{8T}\sum_{j=1}^{8}\lambda_{ij}) = \frac{CB_0}{T}. \tag{2.127}$$

The above expression in round brackets is independent of i due to translational equivalence of atoms in the lattice, that is, each atom has the same number and type of interaction of any other, so that the term in round brackets can be extracted from the summation:

$$(1 - \frac{C}{8T}\sum_{j=1}^{8}\lambda_j)M = \frac{CB_0}{T}, \tag{2.128}$$

where $M = \sum_{i=1}^{8} M_i$, that equation can be rewritten as

$$M = \frac{CB_0}{(1 - \frac{C}{8T}\sum_{j=1}^{8}\lambda_j)T}, \tag{2.129}$$

that provides exactly the Curie-Weiss law

$$\chi = \frac{C}{T - T_c} \quad with \quad T_c = \frac{C}{8}\sum_{j=1}^{8}\lambda_j. \tag{2.130}$$

The constant T_c is the Curie-Weiss temperature. Remembering equation 2.123 and using $M_0 = Ng\mu_B J$, we obtain that

$$T_c = \frac{2J(J+1)}{3k_B}\sum_{j=1}^{8} z_{ij}J_{ij}. \tag{2.131}$$

Thus, for a FCC lattice, by the eight-sublattices division, one Eu atom has two NN and 4 NNNN placed in the six neighbouring sublattices, and six NNN contained in the remaining sublattice, so that $\sum_{j=1}^{8} z_{ij}J_{ij} = 6 \times 2J_1 + 6 \times 4J_3 + 1 \times 6J_2$ where J_1, J_2 and J_3 are the exchange constants of an atom with its NN, NNN and NNNN, respectively. Thus the Weiss temperature for the EuX are given by:

$$T_c = \frac{2J(J+1)}{3k_B}(12J_1 + 6J_2 + 24J_3). \tag{2.132}$$

In general, the transition temperatures depend on the magnetic ordering of the spins, these

transitions are characterized by the temperature T_t, above of which the magnetization of each sublattice vanishes. To determine T_t, we go back to equation 2.125 and write explicitly the system of equation for (i=1,2,..., 8),

$$\begin{aligned} +M_1 - \frac{C}{8T}\lambda_{12}M_2 - \quad \cdots \quad \frac{C}{8T}\lambda_{18}M_8 \quad &= \quad \frac{C}{8T}B_0 \\ \vdots \qquad\qquad \ddots \qquad\qquad \vdots \qquad\qquad & \\ -\frac{C}{8T}\lambda_{81}M_1 - \frac{C}{8T}\lambda_{82}M_2 \quad \cdots \quad + M_8 \quad &= \quad \frac{C}{8T}B_0. \end{aligned} \tag{2.133}$$

The above system of equations only has nonzero solutions to M_i if and only if its characteristic determinant is zero, which defines an equation for the critical temperature.

We take the sublattice that contains 6 NNN of an atom in sublattice i= 1 as the one labelled as j=5. In this description:

$$\lambda_{15} = \frac{8(2\times(6J_2))}{Ng^2\mu_B^2} \qquad \text{and} \qquad \lambda_{1\neq 5} = \frac{8(2\times(2J_1+4J_3))}{Ng^2\mu_B^2}. \tag{2.134}$$

We can do the same for the other sublattices following a cyclic criteria, for example, for an atom in the sublattice i=2 the NNN are contained in the sublattice j=6 and we have:

$$\lambda_{26} = \frac{8(2\times(6J_2))}{Ng^2\mu_B^2} \qquad \text{and} \qquad \lambda_{2\neq 6} = \frac{8(2\times(2J_1+4J_3))}{Ng^2\mu_B^2}. \tag{2.135}$$

So we can define,

$$a_0 = \frac{8T}{C}, \qquad \lambda_0 = \frac{16}{Ng^2\mu_B^2}, \qquad a_1 = -\lambda_0(2J_1+4J_3) \qquad \text{and} \qquad a_2 = -\lambda_0(6J_2). \tag{2.136}$$

Then, we get the matrix

$$A = \begin{bmatrix} a_0 & a_1 & a_1 & a_1 & a_2 & a_1 & a_1 & a_1 \\ a_1 & a_0 & a_1 & a_1 & a_1 & a_2 & a_1 & a_1 \\ a_1 & a_1 & a_0 & a_1 & a_1 & a_1 & a_2 & a_1 \\ a_1 & a_1 & a_1 & a_0 & a_1 & a_1 & a_1 & a_2 \\ a_2 & a_1 & a_1 & a_1 & a_0 & a_1 & a_1 & a_1 \\ a_1 & a_2 & a_1 & a_1 & a_1 & a_0 & a_1 & a_1 \\ a_1 & a_1 & a_2 & a_1 & a_1 & a_1 & a_0 & a_1 \\ a_1 & a_1 & a_1 & a_2 & a_1 & a_1 & a_1 & a_0 \end{bmatrix}$$

Making det $A = 0$, we obtain three real solutions to the system, corresponding to,

$$(a) \quad a_0 = -6a_1 - a_2 \qquad \Rightarrow \quad T = C\lambda_0(12J_1 + 6J_2 + 24J_3)/8, \tag{2.137}$$

$$(b) \quad a_0 = 2a_1 - a_2 \qquad \Rightarrow \quad T = C\lambda_0(6J_2 - 4J_1 - 8J_3)/8, \tag{2.138}$$

$$(c) \quad a_0 = a_2 \qquad \Rightarrow \quad T = -C\lambda_0(6J_2)/8. \tag{2.139}$$

Each of these roots corresponds to a different system which is possible and indeterminate, that is, admits infinite solutions. However, it is possible to obtain relations between the magnetizations of each sublattice.
For the (a) root, the solutions imply

$$M_1 = M_2 = M_3 = M_4 = M_5 = M_6 = M_7 = M_8. \tag{2.140}$$

This corresponds to a **ferromagnetic** ordered system, where the magnetizations of all sublattices point in the same direction, and we can obtain a Curie's temperature

$$T_c = \frac{2J(J+1)(12J_1 + 6J_2 + 24J_3)}{3k_B} = \frac{63(2J_1 + J_2 + 4J_3)}{k_B}. \tag{2.141}$$

For the (b) root, the solutions have the form,

$$M_1 = M_5, \quad M_2 = M_6, \quad M_3 = M_7, \quad M_4 = M_8 = -(M_1 + M_2 + M_3). \tag{2.142}$$

These conditions can generate more than one kind of magnetic ordering, however, if one makes the choice $M_1 = M_2 = -M_3 = -M_4$, the obtained ordering is the so-called type-I **antiferromagnetic** order (AFMI), where the spins contained in the planes defined by the cubic axes (for example the X-Y planes) are ferromagnetically ordered between them, however the neighboring planes magnetizations point in opposite directions so that the whole material is antiferromagnetic. In this case, the Néel's temperature is

$$T_N^{AFMI} = \frac{2J(J+1)(6J_2 - 4J_1 - 8J_3)}{3k_B} = \frac{(-42J_1 + 63J_2 - 84J_3)}{k_B}. \tag{2.143}$$

For case (c) root, and using the restriction

$$M_1 = -M_5, \quad M_2 = -M_6, \quad M_3 = -M_7, \quad M_4 = -M_8. \tag{2.144}$$

We get the type-II **antiferromagnetic** arrangement (AFMII), where as well as in type-I AFM, the ferromagnetic planes are distributed alternately with reversed magnetizations. The difference is that in this case, the FM planes are the planes perpendicular the diag-

onals of the cube. At this condition, the ordering temperature is given by

$$T_N^{AFMII} = \frac{2J(J+1)(-6J_2)}{3k_B} = \frac{(-63J_2)}{k_B}. \tag{2.145}$$

We can note that in this case, the NN and NNNN exchange do not influence the Néel's temperature. Thus, through the simple Weiss effective field model, it was possible to reach the different magnetic orderings found in EuX at temperatures below the critical temperatures, which were determined in terms of the J_1, J_2 and J_3 exchange constants.

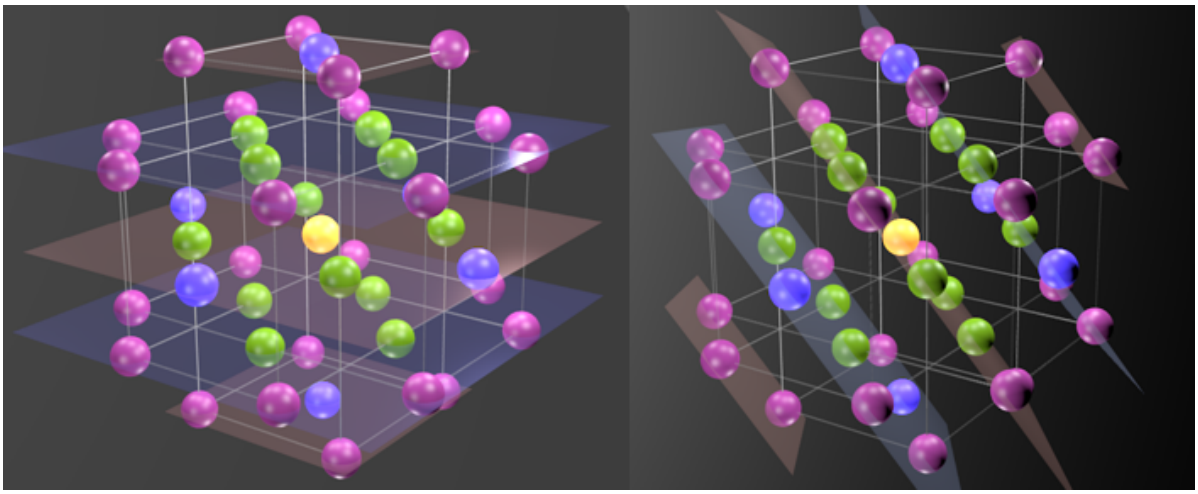

Figure 2.25: AFM type I ordering (left) and AFM type II ordering (right) in an FCC structure.

In figure 2.25 it is possible to see the FM planes composed of the NN, NNN and NNNN of a given lattice site in yellow. Using this theory is possible to predict the FM and the AFM type I and type II, where the magnetic state is then determined by the relative distribution of the total magnetization of these planes. In addition to the derived orderings from the choices made to solve the equations system, other magnetic orderings can be present in EuX, always formed by successive FM planes, which can be distributed in ↑↑↓↓ pattern [52] or even ferrimagnetic orderings ↑↑↓↑↑↓. However other theory needs to be applied.

By knowing the magnetic orderings that occur in each EuX, their respective critical temperatures and the spin's orientation evolution with applied magnetic field, it is possible to determine the value of the exchange constants in the mean field model.

2.3.3 Evidence of the formation of magnetic polarons in EuTe

2.3.3.1 Absorption spectra of EuTe vs magnetic field

The basic idea of the model for the absorption spectrum consists in the transition of one electron from a $4f$ valence level to a $5d$ conduction band built from Eu atomic levels [53].

The absorption dependence on the magnetic field is determined by the *d-f* exchange interaction characterized by the exchange integral J_{df}, between the electron in the excited $5d_{t2g}$ state and the magnetic field-oriented $4f^7$ lattice spins. Above the spin-flop field of 0.08 T, the crystal contains a single domain described by two magnetic sublattices, oriented at an angle θ with respect to the magnetic field direction as is shown in the top right-hand side inset of Fig. 2.26.

The angle θ can be obtained by *minimizing the molecular field energy of the i-th lattice spin* in the FCC structure [54],

$$E_i = -g_S \mu_B S B \cos\theta - 6J_1 S^2 - 6(J_1 + J_2) S^2 \cos 2\theta. \tag{2.146}$$

Thus,

$$\cos\theta = \begin{cases} \frac{B}{B_{SAT}}, & if \quad B < B_{SAT} \\ 1, & if \quad B \geq B_{SAT}, \end{cases} \tag{2.147}$$

where $B_{SAT} = -\frac{24(J_1+J_2)S}{g_S \mu_B}$, $J_1 = 0.04 \pm 0.01$ K and $J_2 = -0.15 \pm 0.01$ K are the nearest neighbor and next-nearest neighbor exchange constants, $g_S = 2$, and μ_B is the Bohr magneton.

Henceforward, we use the experimental value $B_{SAT} = 7.2$ T (Ref. [55]) (This internal field is achieved when the applied field is 8.3 T due to the demagnetization effect). Due to spin conservation in the electric-dipole absorption process, immediately after excitation, the electron spin is oriented along the spin of a magnetic sublattice; moreover, following the Franck-Condon principle, the electronic transition takes place at fixed spatial and spin coordinates of the lattice; hence, the magnetic field dependence of the exchange energy of the absorbing state will be given by the Heisenberg hamiltonian,

$$H_{df} = -2 \sum_{i}^{N} J(r - R_i) \boldsymbol{S_d} \cdot \boldsymbol{S_i}, \tag{2.148}$$

where $J(r - R_i)$ is the interaction constant associated with each lattice site. If we assume that the electron wavefunction is uniformly distributed in the N lattice sites with which it has appreciable overlap and is zero in the remaining sites, we can define the exchange constant, J_{df}, which characterizes the interaction of the photoexcited electron with any

of the N overlapped sites, so we can write,

$$H_{df} = -2\frac{J_{df}}{N}\sum_{i}^{N} \boldsymbol{S_d} \cdot \boldsymbol{S_i} \tag{2.149}$$

$$H_{df} = -2\frac{J_{df}}{N}(\frac{N}{2}\boldsymbol{S_d} \cdot \boldsymbol{S_1} + \frac{N}{2}\boldsymbol{S_d} \cdot \boldsymbol{S_2}) \tag{2.150}$$

$$H_{df} = -\frac{1}{2}J_{df}S(1 + \cos 2\theta) \tag{2.151}$$

where S_1 and S_2 are the spins in the sublattices 1 and 2, respectively, J_{df} is the exchange constant between the d and f states, $S_d = 1/2$ is the electron spin. Then, $\Delta h\nu_{abs} = \frac{1}{2}J_{df}S(1 + \cos 2\theta)$ which according to Eq. 2.147 gives the quadratic dependence on B shown by the dashed line in Fig. 2.26, in agreement with experiment.

$$\Delta h\nu_{abs} = -J_{df}S\cos^2\theta. \tag{2.152}$$

The maximum absorption redshift establishes $J_{df}S = 0.13$ eV.

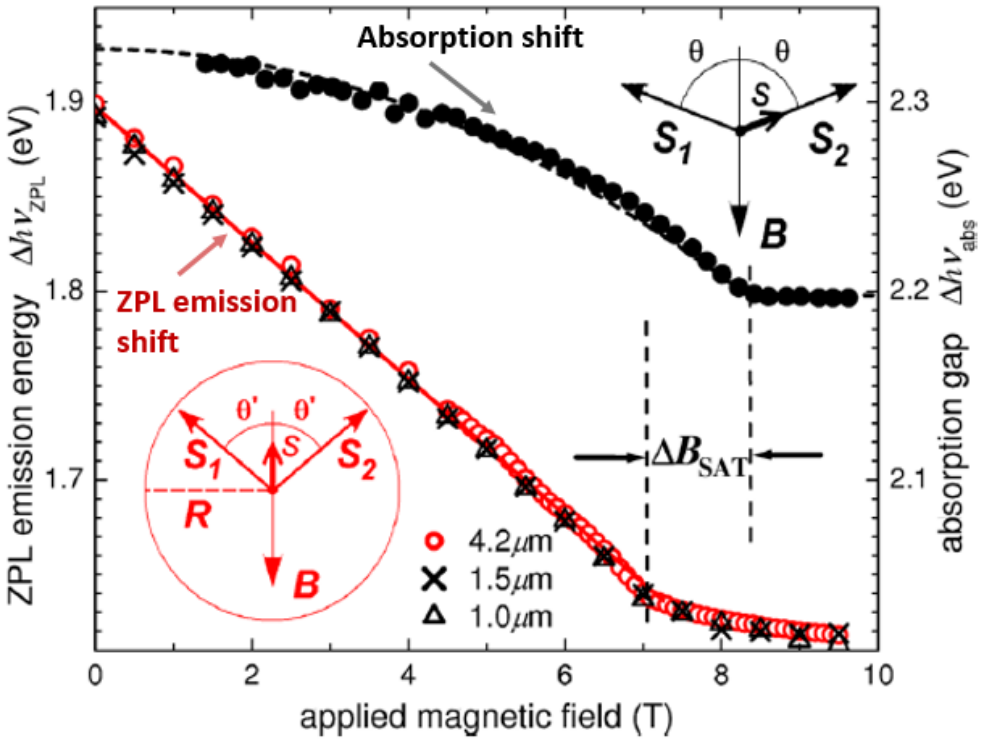

Figure 2.26: Absorption bandgap and zero phonon line (ZPL) peak position as a function of the applied magnetic field [51].

2.3.3.2 Emission spectra of EuTe vs magnetic field

A typical near-gap EuTe photo-luminescence (PL) spectra as a function of excitation power are shown in Fig. 2.27(a). At large excitation powers (20 W/cm^2), a narrow emission at 1.92 eV is seen (MX_1) and near 1.87 eV (MX_2), in agreement with Ref [56]. However, when the excitation power is reduced to 2 mW/cm^2, the PL develops an ensemble of equally spaced lines M_0, that combine into an emission band of total width 60 meV with a maximum at 1.88 eV at zero magnetic field. When a magnetic field B, is applied in the Faraday geometry, the MX_0 lines show a giant **redshift** of 37 meV/T, up to a saturation field.

Fig. 2.27(b) shows the MX_0 emission for samples of thickness 1, 1.5, and 4.2 μm, at B = 9.5 T. The spacing between the lines comprising the MX_0 luminescence is independent of the thickness of the epitaxial layer, demonstrating that the line structure is not related to Fabry-Perot interference causing modulation of the PL intensity of epitaxial EuTe grown on BaF_2 substrates [57]. The MX_0 lines are better resolved in thicker layers because they arise from luminescent regions that are further away from the BaF_2/EuTe interface, whose adjacency contains many structural defects due to the 6% lattice mismatch [58].

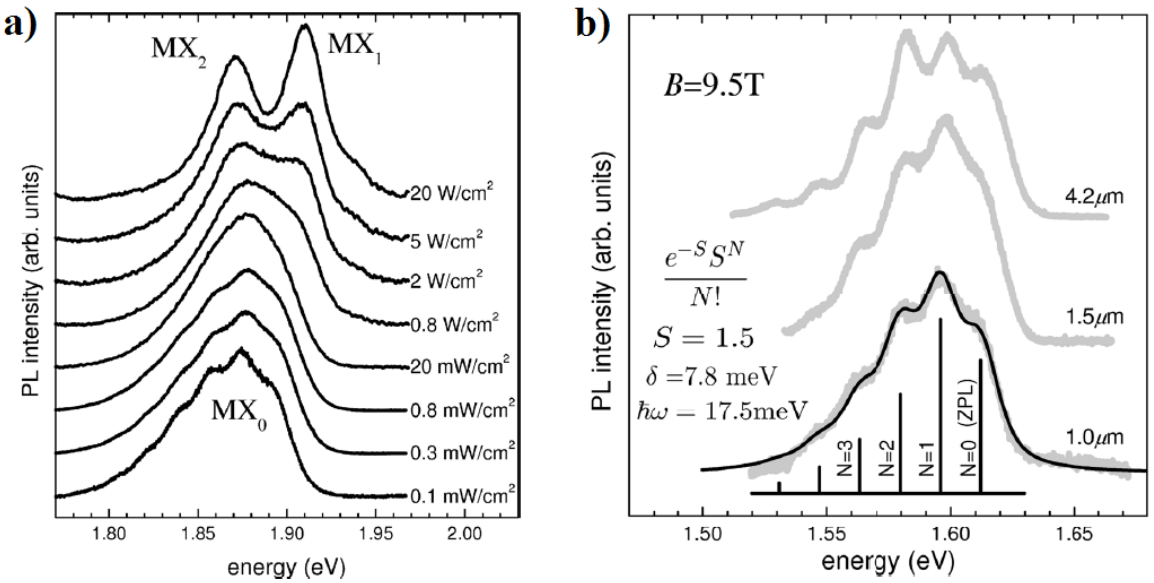

Figure 2.27: (a) PL spectra as a function of excitation power for an epitaxial EuTe layer of thickness 1.0 μm. (b) PL spectra for excitation power 1 mW/cm^2 [51] .

A Poisson distribution of intensities $\frac{e^{-S}S^N}{N!}$, N= 0,1,2,... , fit very well the MX_0 lineshape at all fields, as shown by the thin black line in Fig. 2.27(b) for B = 9.5 T, demonstrating that all MX_0 lines arise from the same electronic transition coupled to a vibrational mode [59]. *The fitting yields the energy position of the zero-phonon line (ZPL)* (N=0) as a function of B, the Huang-Rhys coupling strength S= 1.5, the half-width of the individual lines δ = 7.8 meV, and line spacing $h\nu$ =17.5 meV. The latter matches exactly

the energy of the LO-phonon in EuTe, [60] which identifies the vibrational mode involved in the MX_0 emission.

Before recombination, the photo-excited electron **relaxes** the exchange energy by flipping its spin towards a direction midway between the two sublattices, as shown schematically in the inset at the bottom left-hand side in Fig. 2.26. Then, the exchange energy of the photo-excited electron in the relaxed X-state with the lattice spins is,

$$H_{xf} = -2\frac{J_{xf}}{N}\sum_{i}^{N} \boldsymbol{S_x} \cdot \boldsymbol{S_i} \tag{2.153}$$

$$= -2\frac{J_{xf}}{N}(\frac{N}{2}\boldsymbol{S_x} \cdot \boldsymbol{S_1} + \frac{N}{2}\boldsymbol{S_x} \cdot \boldsymbol{S_2}), \tag{2.154}$$

where $S_x = 1/2$ represents the relaxed electron spin. We assume that the photo-excited electron spin makes an angle ϕ with the direction of the magnetic field B. Then,

$$H_{xf} = -J_{xf}S_xS\left(\cos(\theta-\phi)+\cos(\theta+\phi)\right). \tag{2.155}$$

By minimizing this expression as a function of ϕ in the equilibrium ($\frac{\partial H_{xf}}{\partial \phi} = 0$) we obtain $\phi = 0$ and then,

$$H_{xf} = -J_{xf}S\cos\theta. \tag{2.156}$$

Therefore, the magnetic field dependent shift of the ZPL will be given by

$$\Delta h\nu_{ZPL} = -J_{xf}S\cos\theta, \tag{2.157}$$

which from equation 2.147 gives a linear dependence on B as shown by the solid line in figure 2.26, in agreement with experiment which saturates at lower magnetic field. Here, another parameter, J_{xf}, was introduced to characterize the exchange interaction between the relaxed photo-excited electron and the lattice spins. The value of $J_{xf}S$ is determined by the maximum redshift of the ZPL prior to saturation, giving $J_{xf}S = 0.27$ eV.

2.3.3.3 Evidence of the formation of magnetic polarons

The exchange interaction energy between a *single i-th lattice spin* and the relaxed photo-excited electron given from equation 2.153 is equal to $\Delta_x = -|\psi_i^2|J_{xf}S\cos\theta$, where $|\psi_i^2|$ is the amplitude of the photo-excited electron wave function at the i-th lattice site. When a photo-excited electron is present, this energy must be added to the energy of the i-th lattice spin in non excited state,

$$E_i = -g_S\mu_B SB\cos\theta - 6J_1S^2 - 6(J_1+J_2)S^2\cos 2\theta - |\psi_i^2|J_{xf}S\cos\theta. \tag{2.158}$$

By minimizing this expression as a function of θ in the equilibrium ($\frac{\partial E_i}{\partial \theta} = 0$), we obtain

$$\cos\theta' = -\frac{g_S\mu_B SB + J_{xf}|\psi_i^2|}{24(J_1+J_2)S^2} = \frac{B+B_x}{B_{SAT}}, \tag{2.159}$$

where $B_x = \frac{J_{xf}|\psi_i^2|}{g_S\mu_B}$. Then, we can observed that the additional term Δ_x favors the alignment of the lattice spins with the spin of the photo-excited electron, to form a **magnetic polaron**, consisting of a conduction-band electron localized in space by a photo-excited hole and the attractive exchange field generated by the spins of the europium atoms within the range of the electronic wave function. Within a radius R around the electron, the tilt angle of the lattice spins is decreased from θ to θ' during the polaron lifetime (before recombination), as shown schematically in the bottom left-hand side inset in Fig. 2.26. When Δ_x is introduced into Eq. 2.146, the saturation field decreases by

$$\Delta B_{SAT} = \frac{J_{xf}}{g_S\mu_B}|\psi_i.|^2 \tag{2.160}$$

If we assume a *constant amplitude* of the electron wavefunction, as is shown in Fig. 2.28 (a), we can approximate $|\psi_i|^2 = \frac{1}{N}$, then $\Delta B_{SAT} = \frac{J_{xf}}{g_S\mu_B N}$ becomes a function of $J_{xf}S = 0.27$ eV. Then, using S=7/2 and the value $\Delta B_{SAT} = 1.2$ T (see Fig. 2.26), we can obtain,

$$1.2\ [T] = \frac{0.27\times(2/7)\quad [eV]}{N\times 2\times 5.78\times 10^{-5}\quad [eV/T^{-1}]} \qquad \rightarrow \qquad N \approx 500, \tag{2.161}$$

where $N = \frac{4}{3}\pi R^3\frac{4}{a^3}$ is the number of Europium atoms within the polaron radius R and $a = 6.6$ Å is the EuTe lattice parameter. Then we obtain $R \sim 3.6\ a$.

The tilt angle θ' of the lattice spins at $B = 0$, within the magnetic polaron radius, is determined by $\cos\theta' = \frac{\Delta B_{SAT}}{B_{SAT}}$ to give $\cos\theta' \sim 80°$. Using θ', the energy relaxation of the electron-lattice system due the magnetic polaron formation (the magnetic polaron binding energy, E_B) can be estimated, through $E_B = J_{xf}S\cos\theta' \sim 45$ meV. If we subtract E_B from the Stokes shift of 430 meV (see Fig. 2.26), the difference of 385 meV is too large to be attributed to an electron-hole Coulomb binding energy. This is indicative that the MX_0 luminescence arises from the de-excitation of an electronic state lying below the $5d_{t2g}$ conduction band, as also observed for the MX_1 luminescence. The absorbing and luminescent electronic states being different from one another also explains the numerical difference in the respective parameters $J_{df}S$ and $J_{xf}S$.

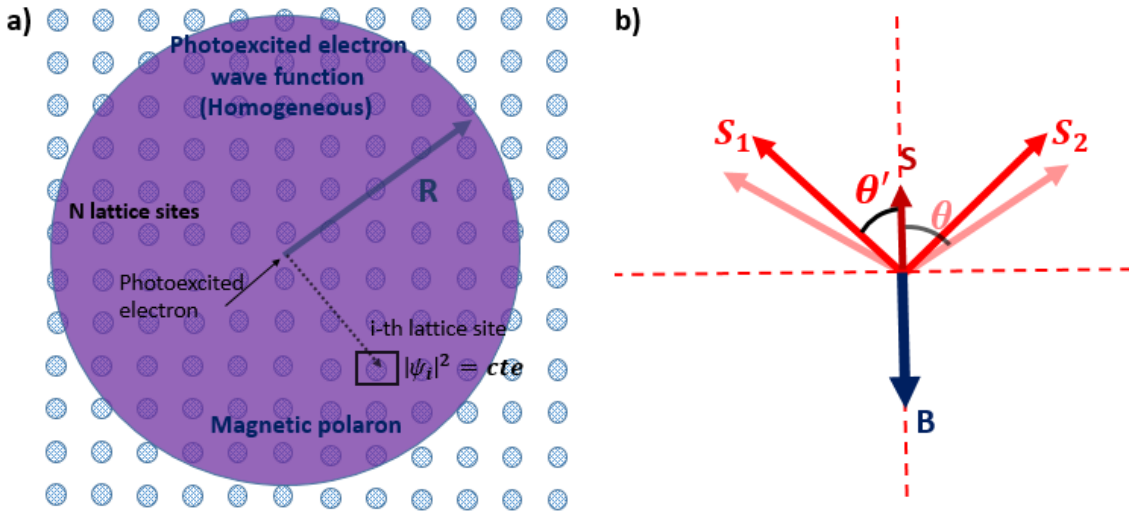

Figure 2.28: (a) Photo-excited electron wavefunction of constant amplitude inside the magnetic polaron. (b) The two antiferromagnetic sublattices are indicated by vectors S_1 and S_2, under the effect of the resultant magnetic field B, i.e., the superposition of an external field and the exchange field of the photo-excited electron, indicated by vector S. The lighter arrows indicate the sublattice spin orientation in the absence of a photo-excited electron. At any distance to the polaron center, both sublattices are tilted by the same angle θ' with respect to the perpendicular to their unperturbed equilibrium orientation indicated by the horizontal dashed line. The angle formed by the two sublattices due the applied magnetic field only at any distance is equal to θ.

2.3.4 Theoretical properties of magnetic polarons in EuTe

This section answer fundamental questions such as: what is the internal spin structure of the magnetic polarons, how can these polarons be generated efficiently, what is the polaron binding energy or how high temperature affect these polarons. This section answers these questions on the basis of a theoretical model and its confrontation with results of magneto-optical experiments. For this, a Schrodinger equation for the polaron was formulated and resolved by using both a variational and a self-consistent method.

To describe the localized photo-excited electron, the envelope-wave-function approach [61] is employed. In an isotropic crystal such as EuTe, the photo-excited electron is described by a spherically symmetric envelope wave function $\psi(r)$, where r is the distance to the center of the polaron as is shown in Fig. 2.29 (a).

The total energy of a photo-excited electron surrounded by a cloud of canted lattice spins (measured in respect to the energy of a free Bloch electron) is given by the sum:

$$E_{pol} = K + U_{Coul} + E_{xf} + E_{ff} + E_Z, \tag{2.162}$$

where K represents the kinetic energy of the photoexcited electron, U_{Coul} is its Coulomb energy in the field of the photoexcited hole, $E_{xf} = E_{xf}(J_{xf}, S, a, R_i, \phi(R_i))$ is the xf

exchange energy,

$$H_{xf} = -2\sum J_{xf}\boldsymbol{S_x}\cdot\boldsymbol{S_i} \tag{2.163}$$

$$= -2J_{xf}(\frac{1}{2})S\sum(\cos(\pi/2-\phi(R_i))+\cos(\pi/2-\phi(R_i)))\,\frac{a^3}{8}|\psi(R_i)|^2 \tag{2.164}$$

$$\rightarrow \quad H_{xf} = -J_{xf}S\sum\sin(\phi(R_i))\frac{a^3}{4}|\psi(R_i)|^2, \tag{2.165}$$

where J_{xf} is the constant for the exchange interaction between the photo-excited electron and the lattice spins, $S = 7/2$ is the spin of an Eu atom, a is the EuTe lattice parameter, R_i is the distance from the i-th lattice spin to the center of the polaron, $\phi(R_i)$ is the canting angle of the i-th lattice spin, and $\frac{a^3}{4}|\psi(R_i)|^2$ is the probability of the electron to be at the position R_i in the volume of one EuTe atom, as shown in Fig. 2.29 (b).

$E_{ff} = E_{ff}(J_1, J_2, S, B, R_i, \phi(R_i))$ is the change in the lattice *ff* energy induced by the photo-excited electron (E_{ff}(with polaron)-E_{ff}(without polaron)),

$$\sum -6J_1S^2 - 6(J_1+J_2)S^2\cos 2(\pi/2-\phi(R_i)) - \sum -6J_1S^2 - 6(J_1+J_2)S^2\cos 2\theta \tag{2.166}$$

$$\rightarrow \qquad E_{ff} = -\sum 12(J_1+J_2)S^2(\sin^2\phi(R_i) - \cos^2\theta), \tag{2.167}$$

where J_1 and J_2 are the first and second neighbor *ff* exchange constants, respectively. $E_Z = E_Z(B, S, R_i, \phi)$ is the change in the Zeeman energy of the lattice spins, induced by the photo-excited electron (E_z(with polaron)-E_z(without polaron)),

$$= \sum -(-g_S\mu_B S)B\cos(\pi/2+\phi(R_i)) - \sum -(-g_S\mu_B S)B\cos(\pi-\phi(R_i)) \tag{2.168}$$

$$\rightarrow \qquad E_z = -\sum g_S\mu_B SB(\sin\phi(R_i) - \cos\theta) \tag{2.169}$$

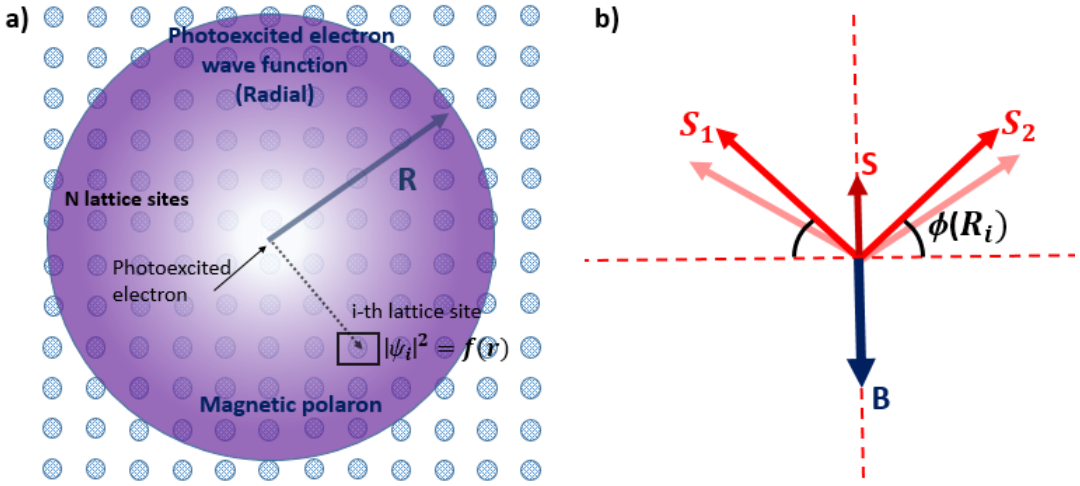

Figure 2.29: (a) Photo-excited wavefunction with radial dependence inside the magnetic polaron. (b) The two antiferromagnetic sublattices are indicated by vectors S_1 and S_2, under the effect of the resultant magnetic field B, i.e., the superposition of an external field and the exchange field of the photo-excited electron, indicated by vector S. The lighter arrows indicate the sublattice spin orientation in the absence of a photo-excited electron. At a given distance, R_i, to the polaron center, both sublattices are tilted by the same angle ϕ with respect to their unperturbed equilibrium orientation indicated by the horizontal dashed line.

By minimizing the total energy in respect to $\phi(R_i)$ we obtain

$$\sin\phi(R_i) = \begin{cases} 1, & if \quad A|\psi(r)|^2 + B/B_{SAT} > 1 \\ A|\psi(r)|^2 + B/B_{SAT}, & \text{otherwise} \end{cases}, \tag{2.170}$$

where $A = -\dfrac{J_{Xf}a^3}{96(J_1+J_2)S}$. Taking advantage of the continuum approximation [62], whereby the discrete distribution of Eu spins in the crystal lattice is replaced by a continuous one, with a density of spins equal to $4/a^3$ characteristic of the face-centered cubic lattice, the polaron problem can be formulated in terms of a very succinct writing the equation:

$$E_{xf} + E_{ff} + E_Z = \int_0^\infty |\psi(r)|^2 V_{pol} 4\pi r^2 dr, \tag{2.171}$$

here $V_{pol}(r)$ is the self energy which unifies $E_{Xf} + E_{ff} + E_Z$ with an specific value at the position r, which is not possible using the complicated original expression.

The hamiltonian operator is given by:

$$H_{pol} = -\frac{\hbar^2}{2m^* r^2}\frac{d}{dr}(r^2\frac{d}{dr}) - k\frac{e^2}{\varepsilon r} + V_{pol}(r). \tag{2.172}$$

And the polaron energy

$$E_{pol} = \int_0^\infty \psi^*(r) H_{pol} \psi(r) 4\pi r^2 dr. \tag{2.173}$$

The first term in Eq. 2.172 is the kinetic energy operator (m^* is the effective mass of the photo-excited electron), the second term is the Coulomb interaction operator between the electron and the photo-excited hole, which is screened by a dielectric constant ε, and $V_{pol}(r)$ is the self-energy term, which unites the *ff* , *xf*, and Zeeman energies in a single compact and concise expression.

Now we consider the polaron of radius R as composed of a core of ferromagnetic center of radius r_c and an external part of radius r such $r_c \leq r \leq R$.
For $r \leq r_c$,

we have $\sin\phi(R_i) = 1$, then $E_{xf} + E_{ff} + E_Z$ can be written as,

$$= J_{xf} S \sum \frac{a^3}{4} |\psi(R_i)|^2 + 12(J_1 + J_2) S^2 \sum \left(1 - (\frac{B}{B_{SAT}})^2\right) - g_S \mu_B S B \sum (1 - \frac{B}{B_{SAT}}). \tag{2.174}$$

By using

$$12(J_1 + J_2) = \frac{J_{xf} a^3}{8AS} \qquad \text{and} \qquad g_S \mu_B = \frac{J_{xf} a^3}{4AB_{SAT}} \tag{2.175}$$

Also the continuous approximation,

$$\sum f(R_i) \frac{a^3}{4} |\psi(rR_i)|^2 \quad \rightarrow \quad \int f(r) |\psi(r)|^2 4\pi r^2 dr, \tag{2.176}$$

we obtain

$$E_{xf} + E_{ff} + E_Z = -J_{xf} S \int_0^\infty \left(1 - \frac{(1 - (B/B_{SAT})^2)}{2A|\psi(r)|^2}\right) |\psi(r)|^2 4\pi r^2 dr. \tag{2.177}$$

Similarly, for $r > r_c$, $\sin\phi(R_i) = A|\psi(R_i)|^2 + \dfrac{B}{B_{SAT}}$ and we obtain

$$E_{xf} + E_{ff} + E_Z = -J_{xf} S \int_0^\infty \left(\frac{A}{2}|\psi(r)|^2 + B/B_{SAT}\right) |\psi(r)|^2 4\pi r^2 dr. \tag{2.178}$$

Then we can summarize,

$$V_{pol}(r) = -J_{xf} S \begin{cases} 1 - \dfrac{(1 - (B/B_{SAT})^2)}{2A|\psi(r)|^2}, & if \quad r \quad < \quad r_c \\ \dfrac{A}{2}|\psi(r)|^2 + B/B_{SAT}, & \text{otherwise} \end{cases}, \tag{2.179}$$

where r_c is the radius of the spherical ferromagnetic core at the center of the polaron and we have to note that is $\psi(r)$ dependent.

The ground state of the polaron is given by the minimum energy solution of the Schrodinger equation:

$$H_{pol}\psi(r) = E_{pol}\psi(r). \tag{2.180}$$

The Schrodinger equation must be solved by using the self-consistent method [63] because the confining potential V_{pol}(r) is dependent on the wave function, as Eq. 2.179 shows. Alternatively, an approximate solution can be found by using the variational method. Although less accurate, the variational method has the advantage of producing a fully analytical solution. A Bohr's wave function was here used $\psi(r, a_B) = \frac{e^{-r/a_B}}{\sqrt{\pi a_B^3}}$ and the effective Bohr radius a_B is the variational parameter.

It was used the numerical values of the parameters in Ref [41]. Figures 2.30 and 2.31(a) show the results of the calculations obtained both by the self-consistent and variational methods. The variational results found for $B = 0$ T is $a_B = 1.27$ a. Figure 2.30(a) shows the *polaron part* (the total is polaron part + Coulomb part) of the confining potential, V_{pol}(r), and the radial probability distribution associated with the envelope wave function of the confined electron for $B = 0$ T. The self-consistent V_{pol}(r) is less confining than the variational one and the self-consistent orbital is more extended. The energy of the photo-excited electron bound state is found to be -0.0942 eV for the variational method, and -0.0860 eV for the self-consistent one. Figure 2.30(b) shows the sine of the canting angle as a function of distance to the polaron center. The variational calculation produces a ferromagnetic core of radius $r_c = 0.95$ a, whereas the self-consistent result is $r_c = 0.47$ a. Given that the nearest neighbour distance in the face-centered cubic EuTe lattice is 0.71 a, then a small ferromagnetic core is predicted by the variational model, but no ferromagnetic core is expected in the self-consistent approximation.

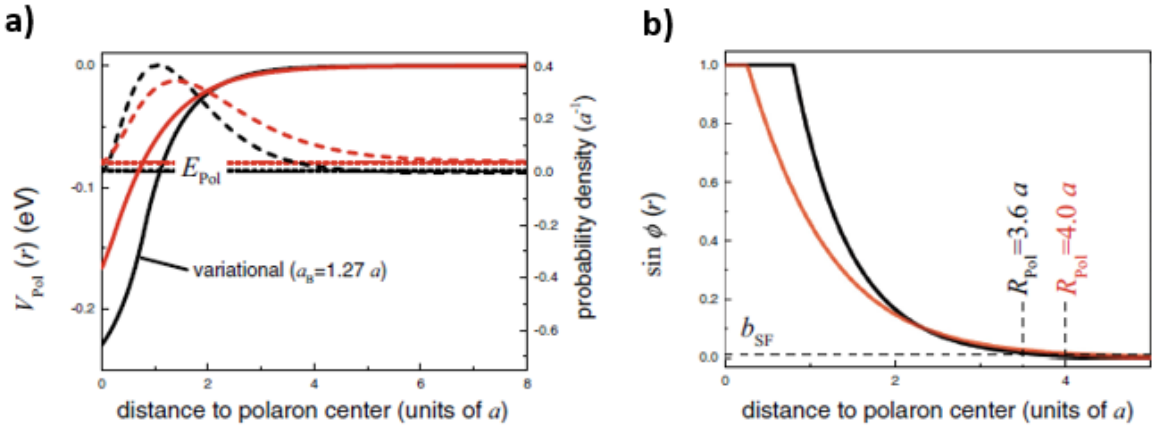

Figure 2.30: (a) Polaron ground state energy obtained by the self consistent method (red curves) and the variational method (black curves) at $B = 0$ T. V_{pol}(r) (solid line), probability density (dashed line), and energy of the ground state (dotted line). (b) Radial dependence of the canting angle, $b_{SF} = \frac{B_{SF}}{B_{SAT}}$.

In the idealized picture above, the photo-excited electron is allowed to polarize all lattice spins, no matter how distant they are from the polaron center. In reality, the polarization action of the photo-excited electron is limited to the region where the effective magnetic field generated by the photo-excited electron wins the competition with other sources of effective magnetic fields; for instance, the magnetic anisotropy [49], which is described by a spin-flop field of $B_{SF} \sim 0.1$ T [65]. Consequently, the polaron radius will be finite. The radius of the polaron can be estimated by taking the spin-flop field as a measure of the minimum effective field that the photo-excited electron must generate in order to have any effect on the lattice polarization. Then the polarization action of the photo-excited electron on the lattice spins, which is measured by how much this photo-excited electron changes the (sine of the) canting angle, which from Eq. 2.170 is given by $A|\psi(r)|^2 + 0$, must be greater than the change in $\sin\phi$ that would be caused by a magnetic field of magnitude B_{SF}, which is simply B_{SF}/B_{SAT} [39]. Thus the polaron volume is defined by the values of r that satisfy the inequality:

$$A|\psi(r)|^2 \geq B_{SF}/B_{SAT}. \tag{2.181}$$

The equality occurs at $r = R_{pol}$ and by using the Bohr's wave function $\psi(r, a_B) = \dfrac{e^{-r/a_B}}{\sqrt{\pi a_B^3}}$ produces an analytical expression for the polaron radius, if the variational approximation is used, it gives $R_{pol} = 3.6\ a$ for $B = 0$ T, and if the self-consistent approximation is used it gives $R_{pol} = 4.0\ a$ is found numerically from the equality of the condition in Eq. 2.181.

The average canting angle of the lattice spins within the polaron will be given by:

$$< \sin\phi >= \Omega_{pol}^{-1} \int_0^{R_{pol}} \sin\phi(r) 4\pi r^2 dr, \tag{2.182}$$

where $\Omega_{pol} = \dfrac{4}{3}\pi R_{pol}^3$ is the polaron volume, which gives $< \phi >= 7°$ for the variational model and $< \phi >= 5°$ for the self consistent one.

Thus, the total magnetic moment of a polaron can be estimated to be:

$$M_{pol} = \Omega_{pol} M_{SAT} \langle \sin\phi \rangle, \tag{2.183}$$

where $M_{SAT} = \dfrac{4 g_S \mu_B S}{a^3}$ is the saturation magnetization of the crystal, which gives $M_{pol} = 650\ \mu_B$ and $M_{pol} = 610\ \mu_B$ in the variational and self-consistent method, respectively. When the applied magnetic field intensity reaches B_{SAT}, the lattice spins attain complete ferromagnetic alignment, and the polaron potential becomes a constant, $V_{pol}(r) = -J_{xf} S$, as Eq. 2.179 shows. In this limit, the variational Bohr function becomes an exact solution of the polaron Hamiltonian. Indeed, the variational and self-consistent calculations converge to a single result as $B \to B_{SAT}$, as Fig. 2.31(a) shows. However,

the self consistent result, which is an exact solution of the polaron Schrodinger equation, produces a polaron radius that is almost independent of the magnetic field and varies by at most ~ 5 %, whereas the variational result for R_{pol} varies linearly with B, and can be increased by as much as 20 % by the application of a magnetic field.

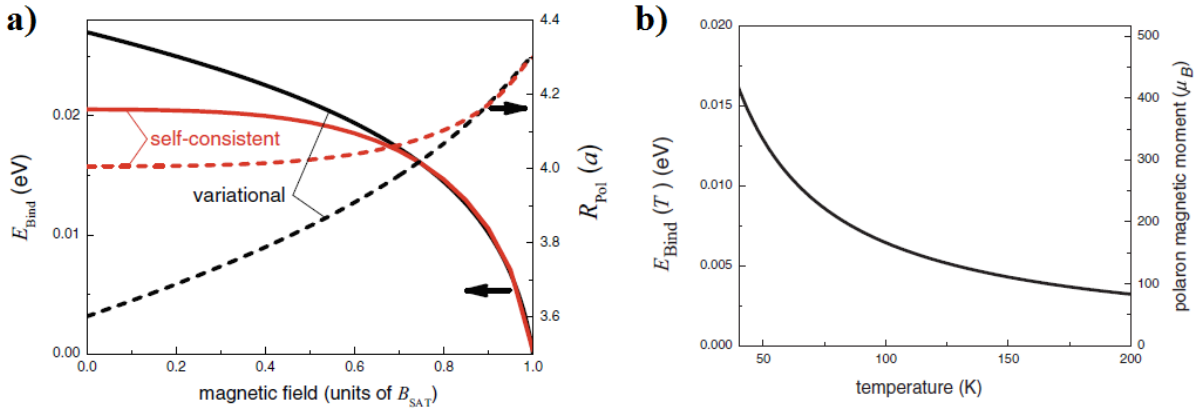

Figure 2.31: (a) Magnetic-field dependence of the polaron binding energy (solid lines) and of the polaron radius (dashed lines) obtained by the self-consistent (lighter curves) and the variational methods (darker curves). (b) Calculated magnetic polaron binding energy (left scale) and magnetic moment (right scale) as a function of temperature.

Based on the above theory, valid for $T = 0$ K, predictions can be made for polaron effects in the high-temperature limit, $T \gg T_N$, when the EuTe system approaches paramagnetic behavior. The magnetic moment of a polaron can also be estimated in the high-temperature limit, which can be observed in figure 2.31(b). It is deduced that, in EuTe, at 0 K, a polaron binding energy is 27 meV. However, this binding energy does not carry the usual meaning of thermal stability, because it decreases drastically when the sample is warmed up. For instance, at $T = 100$ K, the binding energy is already reduced to only 6 meV. The thermal destruction of a polaron is brought about by thermal fluctuations of the spin lattice that suppress the electron's self-energy. Photoluminescence excitation spectra of EuTe demonstrate that the photo-generation of polarons becomes increasingly inefficient when the energy of the pumping photon is increased above the band gap.

This theory is in good agreement with measurements of the zero phonon line as a function of magnetic field and temperature, and it could be applied to other polaronic systems.

Due to the high value of the binding energy, the polarons must exist at higher temperatures ($k_B T(300K) \approx 25$ meV). This motivates the search for experimental demonstration of these results.

2.3.5 Detection of photo-induced magnetic polarons by Faraday rotation technique

In this section it is demonstrated an experimental tool to measure photo-excited magnetic polarons in the europium chalcogenide Eute, which is achieved using a two-color pump-probe **photo-induced Faraday rotation** technique. This method can be used at any temperature and field, unlike photoluminescence studies reported before.

The energy of the pump photons is tuned at the EuTe band gap at 2.2 eV, whereas the probe photon energy was a value below the EuTe band gap (1.86 eV). A magnetic field is applied normal to the surface of the sample (Faraday geometry), which is parallel to the [111] crystalline direction of the sample [see Fig. 2.32(a)]. For optical excitation it be used a variety of monochromatic sources: A xenon lamp passing through a monochromator, a frequency-doubled Nd:YAG laser, or the frequency-doubled mode-locked Ti-sapphire tunable laser emitting pulses with the typical duration of 1.5 ps at a frequency of 76 MHz. The probe light source can be a semiconductor laser or the fundamental pulses of a mode-locked tunable Ti-sapphire laser. The excitation light is modulated at 2.33 kHz using a chopper or at 50 and 100 kHz using a photo-elastic modulator. The photoinduced Faraday rotation signal obtained result independent from the polarization of the optical excitation. For measuring the Faraday rotation angle of the linearly polarized probe beam, a **homodyne technique** based on **phase-sensitive balanced detection** can be used.

As seen in Fig. 2.33(b), the PFR shows a step-like increase when the energy of the pump photons resonates with the EuTe band gap, demonstrating that the PFR is provoked by photo-generated free conduction band carriers.

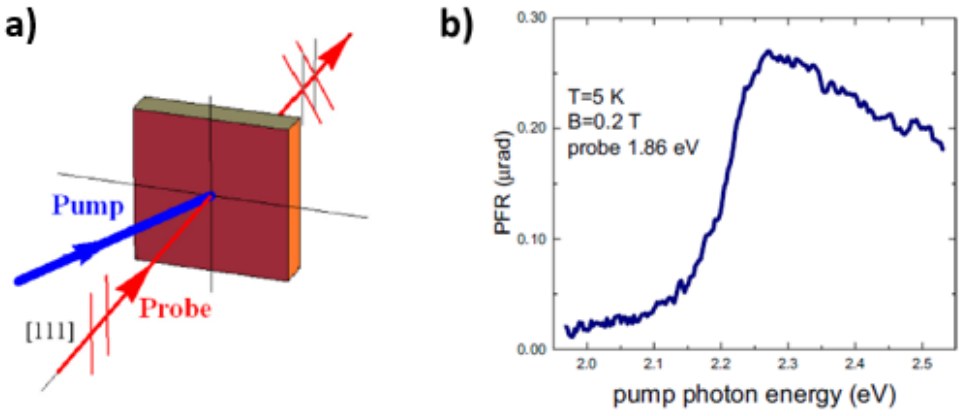

Figure 2.32: (a) Geometry of the pump-probe Faraday rotation experiment. The magnetic polarons in a longitudinal magnetic field are excited and probed by light. (b) PFR as a function of the pump energy at $T = 5$ K and $B = 0.2$ T [46].

By studying the shape of the measured PFR signal as a function of the magnetic field, and using the *linear relation between the Faraday rotation and the magnetization*,

a curve of the photo-induced magnetization is obtained. This curve has the remarkable characteristics:

1. Resonant at the pump energy of the EuTe band-gap.
2. Is zero at zero applied magnetic field.
3. PFR saturates rapidly as expected for magnetic polarons with huge magnetic moment.
4. PFR saturates at the expected theoretical value.

Then, the polarons can be considered as a paramagnetic system and the PFR curve can be described by a *Langevin function* and it is therefore sensitive to the temperature of the sample, whose shape determines the magnitude of the magnetic moment of an individual polaron, independently of the calibration of the measuring setup. Thus, the PFR signal is a direct measure of the photo-induced magnetization component along the probe wave vector [66]. Figure 2.32(b) shows the typical PFR signal obtained at $T = 5$ K, as a function of the magnetic field. Remarkably, the magnetic moment estimated using the Langevin function does not require any knowledge of the properties of an individual polaron, such as its lifetime, generation efficiency and circular birrefringence, which is needed if the polaron magnetic moment is estimated from the absolute value of the Faraday rotation angle.

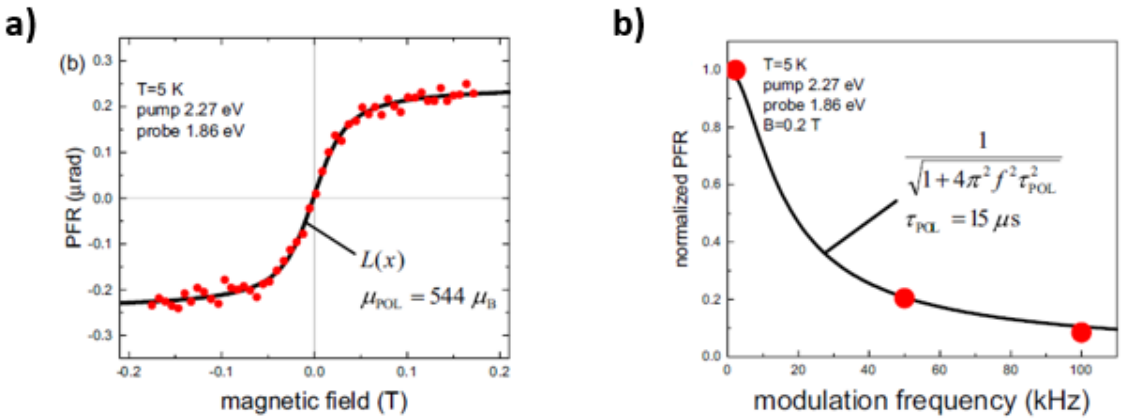

Figure 2.33: (a) Typical photo-induced Faraday rotation (PFR) signal as a function of the applied magnetic field at $T = 5$ K. (b) PFR as a function of the pump modulation frequency at $T = 5$ K and B =0.2 T [46].

Notice that the photo-generated hole is strongly localized in a Eu site, therefore it should not generate an effective exchange field, in contrast to the photo-excited electron. If we assume that the magnetic moment of a polaron is free to point in any direction except for the Zeeman interaction, the photo-induced magnetization will be described by

the Langevin formula (see, for instance, Ref. [66])

$$L(x) = coth(x) - \frac{1}{x} \qquad with \quad x = \frac{\mu_{pol} B}{k_B T}, \tag{2.184}$$

where μ_{pol} is the magnetic moment of an individual polaron. The S-like shape of the Langevin function dependence on field is determined by the one and only parameter, the magnetic moment of the individual particles forming a paramagnet. Therefore, it defines uniquely the magnitude of the polaron magnetic moment. Figure 2.33(a) shows that Eq. 2.184 provides an excellent fit of the experimental data, where the polaron magnetic moment best fit value is $\mu_{pol} = 544\ \mu_B$.

The polaron lifetime was investigated by examining the dependence of the intensity of the PFR signal on the modulation frequency of the pump light, which for a single exponential recombination kinetics is given by

$$\mathrm{PFR}(f) = \frac{\mathrm{PFR}(0)}{\sqrt{1 + 4\pi^2 f^2 \tau_{pol}^2}}. \tag{2.185}$$

Figure 2.33 (b) shows that Eq. 2.185 fits the experimental data very well and yields the polaron lifetime $\tau_{pol} = 15\ \mu s$. This result is in perfect agreement with the lifetime estimated using the absolute value of the PFR angle [see Fig. 2.33(b)] and the low-field Verdet constant for EuTe [67].

The paramagnetic behavior plus the large value of the magnetic moment of a polaron (540 μ_B at 5 K) suggests that the photo-excited magnetic polaron ensemble can be classified as superparamagnetic (non interacting and with large magnetic moment particles), if the concept defined by Bean [68] is used. To test this further, the measured PFR was plotted as a function of the dimensionless variable $x = \frac{\mu_{pol} B}{k_B T.}$, in which case all curves collapse into a single Langevin function as depicted in Fig. 2.33(a), confirming the legitimacy of the superparamagnetic polaron model.

Chapter 3

Materials and methods

The appropriate understanding of the operating principle of the equipment used during scientific experiments is fundamental for correct measurements and rigorous analysis of the data, allowing the experimentalist to obtain right conclusions of the physical phenomena of interest and avoiding erroneous results. Hence, in this chapter, we introduce the experimental environment for magneto-optical and cryogenic experiments and also the techniques utilized for the study of the ultrafast photo-induced magnetization measurements in this thesis. The techniques are the time-resolved Faraday rotation, the time-resolved differential transmission, photoluminescence, photo-induced Faraday rotation, bulk Faraday rotation, and superconducting quantum interference devices (SQUID) measurements. These methods rely on the optical determination of the magnetization via photo-induced excitation.

3.1 Environment in cryogenics experiments

The most relevant issues are: the cooling schemes, the vacuum technology, the cryostats and the superconducting magnets, which will be described in the following lines.

3.1.1 Cooling elements

A cryogenic experiment is dominated commonly by the need of getting a sample cold and keeping it cold, at temperatures below the boiling point of nitrogen N_2 (77.4 K) and around the boiling point of helium ^4He (4.2 K). The best way to achieve that, is by using liquefied gases, as liquid nitrogen (LN2) or liquid helium (LHe), which first provides cooling by interchanging heat with the sample and its surroundings, which absorbs the liquid latent heat maintaining the temperature at the boiling point, and then, warming up the liquid from the boiling point temperature evaporating the liquid to vapor.

For example, if we need to cool a system from room temperature down to 4 K, then, commonly first it is cooled to 77 K using liquid nitrogen and then liquid helium is used,

and not cooled using just liquid helium, since nitrogen is about a thousand times cheaper than helium per Joule of latent heat, and because the heat capacity of the components in a cryostat system drops sharply with temperature, so by the time it has reached 77 K, most of the heat has already been removed from the cryostat and too much less helium is needed.

Liquefied gases are normally stored and transported in a double-walled with vacuum isolated flask called *dewar*, in which, both walls join at their necks and the volume between the two walls is on a vacuum to minimize heat transfer by conduction or convection from the environment into the liquefied gas.

The properties of common liquefied gases are summarized in the next table and are compared with water.

Liquefied gas	boiling temperature	Freezing temperature	Latent heat
Water	373 K (+100.0° C)	273 K (0° C)	2265 kJ/kg
Nitrogen	77.4 K (-195.8° C)	63.2 K (-269° C)	200 kJ/kg
Helium	4.2 K (-268.9° C)	commonly not freezes at 1 atm.	21 kJ/kg

3.1.2 Vacuum pumps

Vacuum equipment is necessary for cryogenic experiments for many reasons. A vacuum barrier reduces conduction as heat loss mechanism between a cold system and its environment which is at higher temperature. Second, because vacuum pumps are needed to evacuate recipients with liquefied gases in order to reduce the vapor pressure, because an atmosphere with significant proportions of gas affects cooling power.

The most common vacuum pumps used in cryogenic experiments are the *mechanical vane pumps* which are oil-based vacuum pumps, that can be used to obtain, depending on the system, a pre-vacuum or even medium vacuum, achieving pressures of 10^{-2} or 10^{-3} mbar. The pumping mechanism is purely mechanical, consisting of a series of rotor and vanes in contact with oil in a chamber that force the gas we want to evacuate, for example, air, entering to the pump from the inlet to get trapped in the oil and be transported through the chamber with the help of vanes to the outlet, where the gas exits the system as the pump turns as is shown in figure 3.1. The oil acts as a lubricant and also allows the pumping of some corrosive gases, as it protects the metal to some degree.

In cryogenic experiments however, it is commonly necessary to reach pressures lower than those achievable by the mechanical rotary pump. Then, rotary pumps are often used as roughing pumps before a more sophisticated vacuum technology, as *turbo-molecular pumps*. Turbo-molecular pumps are capable of reaching pressures down to 10^{-8} mbar and must be backed with a mechanical rotary pump. In this pump, gas molecules can be given momentum in the desired direction by repeated collision with a moving solid surface, this is a rapidly spinning turbine rotor which "hits" gas molecules from the inlet of the pump

towards the exhaust in order to create or maintain a vacuum.

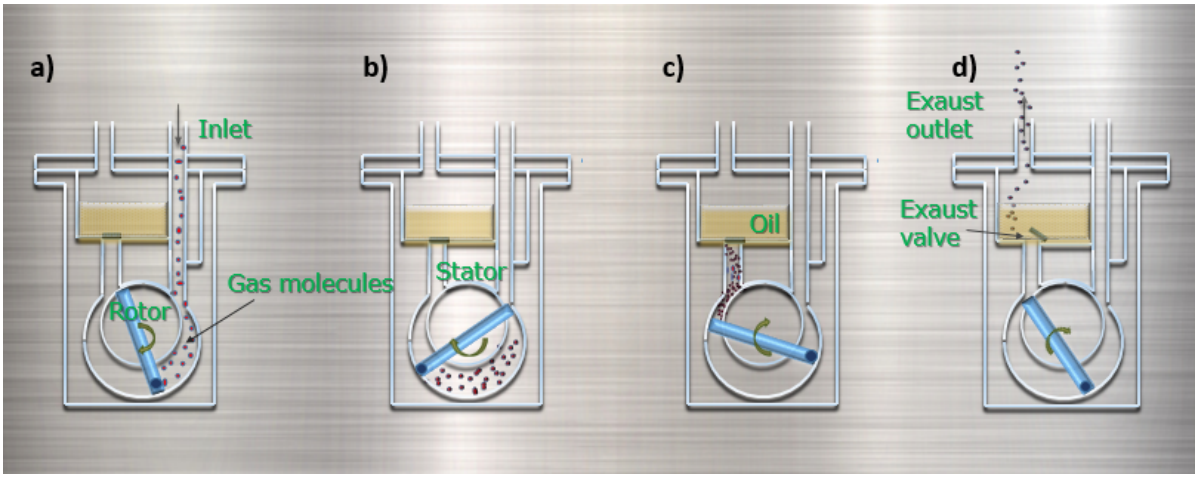

Figure 3.1: There are four stages of operation in a typical rotary vane pump. (a) Induction: the rotation of the rotor induces the gas into the pumping chamber. The volume occupied by the gas increases due to the crescent space created by the rotor. The gas pressure decreases in proportion to the increase in its volume (Boyle's law). This draws the gas into the pump and generates the required vacuum. (b) Isolation: the uppermost vane passes the inlet port, sealing it off from the gas being pumped. (c) Compression: further rotation compresses and heats the gas ahead of the lowermost vane, reducing its volume due to the decreasing space between the rotor and stator. (d) Exhaust: as the lowermost vane continues its rotation, the pressure in front of it increases sufficiently to force the exhaust valve open, discharging the gas at a pressure slightly above atmospheric.

3.1.3 Cryostat

Cryostat is the container where the sample at temperature experiment is in. The simplest cryostat configuration is the bath cryostat, which contains tens of liters of liquefied gas, commonly liquid helium and liquid nitrogen used to keep a sample at low temperature. Bath cryostats require substantial shielding to achieve the necessary thermal insulation for economical experiments. Shielding generally consists of vacuum barriers to insulated the internal cryostat temperature from room temperature, the vacuum barriers are obtained with pumps. The cryostat includes pressure control mechanisms and high-temperature control system to keep the system under the desired low temperature. Depending upon needs and availability, cryostat using liquid helium can be closed cycle recipients with complicated internal structures to permit a continuous flow to fill and recovery the evaporated cooling elements or can be filled with the liquefied gases using external dewars. The sample under study is normally located at the bottom and center of this cryostat in a variable temperature insert system (**VTI**) where the temperature is controlled at detail by balancing the effect of heating and cooling to provide a stable temperature in an area of interest by flowing liquid helium from the reservoir to the sample space through a capillary tube using a *needle valve* and heating the sample using an integrated *heater*

mounted close the sample as is shown in figure 3.2. The temperature can be decreased even below the liquid helium temperature by pumping the vapors above the liquid to reduce the pressure to its lowest possible level. In this way, it is achievable to reduce the temperatures down to 2.2 K (Lambda point). Cryostats commonly include two superconducting coils in the bottom of the cryostat used to apply magnetic fields in parallel or perpendicular direction to the surface of the sample if it is required and commonly includes also four glass windows, two parallel and two perpendicular to the axis of the coil, that allow to an external light source, like a laser, an access to the sample and make possible measurements with the reflected, transmitted or with the luminescence of the sample.

For our experiments, it was used a liquid helium (LHe) cooled Oxford cryostat, which operates in temperatures between 1.5 K and 300 K. The temperature was controlled with a LakeShore 340 controller, using Cernox temperature sensors positioned in the VTI inside the cryostat and at the sample holder which was specially designed to each measurement. In the data acquisition setup, a computer using a *Delphi* program was used to control devices as VTI system used to control the sample temperature, the mechanical delay line used to establish the time depending experiments, the power supply to set the magnetic fields (current-to-field system), the detection and amplification of the sample signals, etc.

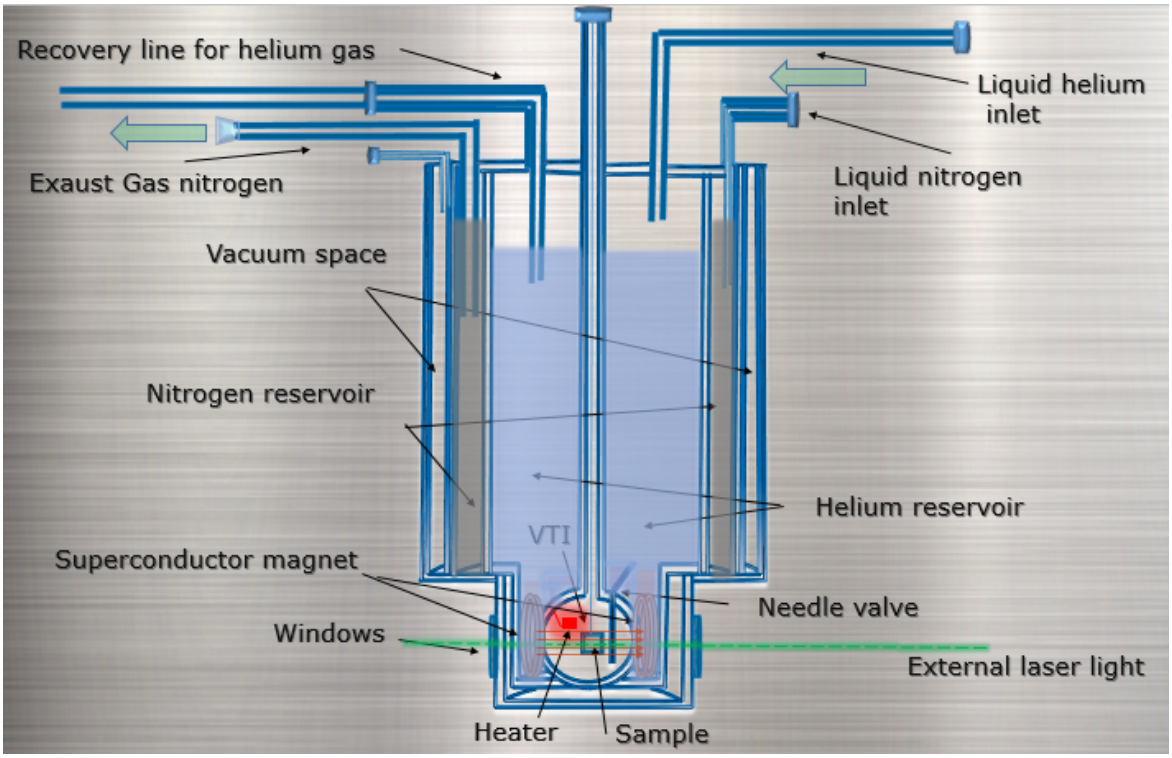

Figure 3.2: Basic internal structure of a bath cryostat used in our experiments.

3.1.4 Superconducting Magnets

Probably the highest impact application for superconductors is be used as a wire for superconducting magnets. Unlike resistive magnets, superconducting magnets do not require the application of an external voltage (current flow) to maintain the magnetic field. At the expense of refrigeration, this aspect is exploited in superconducting magnets to limit helium evaporation rate during operation by the use of the called **persistent magnet mode**. The persistent mode occurs when it is still super-current in the coils, but the external power supply (used to supply current to the magnet) has been turned off. To achieve the persistent mode, a superconducting switch is wired in parallel to the main coil windings, and a small *heater* is placed near this switch as is shown in figure 3.3. When ramping the magnet, heat is applied, causing the switch to go to resistive (no superconductor state) and therefore acting effectively as a broken wire in the circuit, dropping all applied voltage over the magnet coils. To establish the persistent mode, heat is removed from the superconducting switch (switch pass to superconducting state), thereby isolating the coils, so the external power supply can be removed, leaving a persistent supercurrent in the windings. It is important to remember that if the field needs to be changed or quit after entering to the persistent mode, then, it must be *slowly* ramped, it is, the power supply must be ramped to the correct voltage corresponding to the current in the magnet, and the superconducting switch must then be activated before any changes in the voltage across the magnet circuit can be made (to avoid going abruptly from the superconducting to the resistive state). Typical decay rates in persistent mode are some μT/min. Due to their small resistances and the huge amount of energy held within the circuit, of the order of a megajoule, superconducting coils are able to produce huge back EMF's when the current is ramped up or down. This inductance forces users to ramp at sufficiently slow rates to avoid transitioning the wires to the non-superconducting state dissipating the energy, thereby quenching the magnet with a plume of Helium from the magnet bath vent and potentially damaging the cryostat.

Superconducting magnets are capable of magnetic fields in the neighborhood of 20 T without the need for high voltage power supplies. The most common winding geometries for superconducting lab magnets are a continuous solenoid or split pair. Magnetic field homogeneity is always a concern, and standard superconducting solenoids have flat magnetic field profiles over a centimeter at the center field up to one part per thousand.

In our experiments, the cryostat is equipped with an LHe cooled superconducting coil to generate a uniform magnetic field at sample holder's position from up to 7 T, which can have its direction reversed by command of the Oxford power supply.

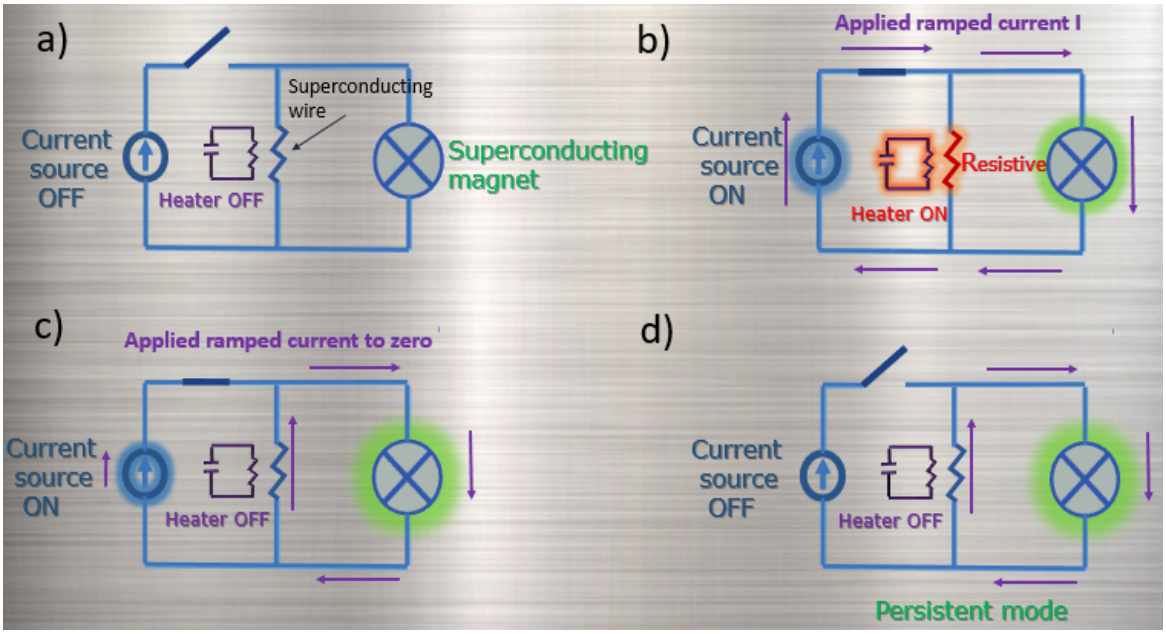

Figure 3.3: Basic operating principle for ramping a superconducting magnet from zero field to the persistent mode. (a) Initial state (zero field) (b) Slowly charging the magnet coupled to a heated superconducting wire. (c) In persistent mode, the magnet is short-circuited to the superconducting wire by turned-off the heater. (d) Current source can be turned off and experiments can be done.

3.2 Magneto-optical measurements

Among the existing magneto-optical methods to study the spin dynamic in magnetic materials, the ultrafast magneto optical techniques allow us to study fundamental processes in magnetism, such as short lived spin coherence, spin precession, photo-induced magnetization, spin-orbit and exchange interactions, etc. Phenomena that normally occur from the nanosecond to the femtosecond time scale.

To investigate and understand such ultrafast phenomena, the experiments commonly require to implement optical setups. It is important to know the characteristics of the devices used in these experiments, explained in this section. The main measurement techniques involved using optical setups are the time-resolved Faraday rotation (TRFR) and time-resolved differential transmission (TRDT) spectroscopy, which are used to measure spin and carrier relaxation dynamics, respectively. Other magneto-optical techniques which are used in this thesis include photoluminescence, photo-induced Faraday rotation and SQUID measurements, also explained in this section.

3.2.1 Optical setup

In this section, we are going to describe the optical components used in the optical setup we use to perform our magneto-optical experiments.

3.2.1.1 Laser light sources

Probably the most common laser used in scientific research is the **Ti:Sapphire laser**. Its preeminence is due to its *large gain bandwidth* or range of frequencies determined by Ti:Sapphire gain media (much larger than others as rare-earth-doped gain media). The maximum amplification gain and efficiency are obtained around 800 nm with possible tuning range between 650 nm to 1100 nm, which makes possible to generate ultrashort pulses in the femtosecond or picosecond domain.

Ti:sapphire lasers are normally **pumped** with a continuous-wave (CW) laser beam of several watts of pump power (sometimes even 20 W). For this, there is a wide range of possible pump wavelengths, which however are located in the green spectral region (with the absorption peak at $\approx$ 490 nm), where powerful laser diodes are not available. For example, 514 nm argon ion lasers, which are powerful, but very inefficient, expensive to operate and bulky. However, now is widely used the frequency-doubled solid-state lasers based on neodymium-doped gain media with wavelength typically of 532 nm, with a slightly reduced pump absorption efficiency (light that can be used for amplification) compared with 514 nm. Direct diode pumping at shorter wavelengths, e.g. at 455 nm with GaN-based laser diodes, is also possible, but with substantially reduced pump absorption.

Titanium-sapphire is especially suitable for pulsed lasers (**mode-locked**) since an ultrashort pulse inherently contains a wide spectrum of frequency components. This is due to the inverse relationship between the frequency bandwidth of a pulse and its time duration because they are conjugate variables. However, titanium-sapphire can also be used in continuous wave **CW** lasers with extremely narrow linewidths tunable over wide range frequencies in the visible and near-infrared region.

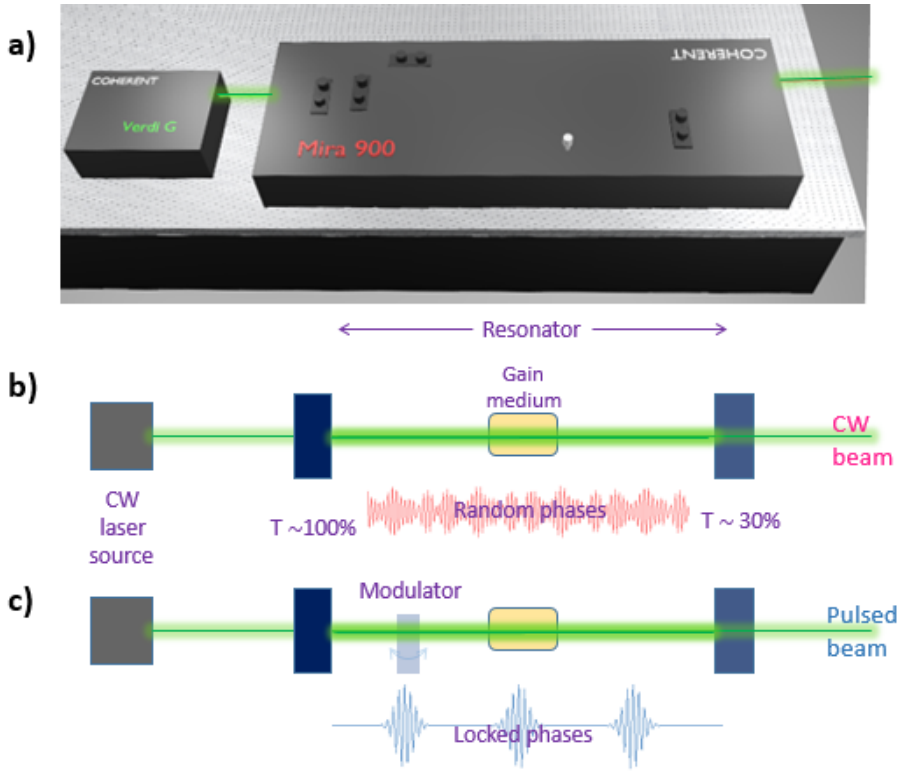

Figure 3.4: (a) Mira 900 model Ti:Sapphire ultrashort laser pumped with a continuous-wave Verdi G pump laser. (b) Simplification of the operating principle of a CW laser, the laser from the source bounce between the mirrors of the resonator leading to the formation of standing waves or modes with a discrete set of frequencies, known as the longitudinal modes of the particular cavity. Each of these modes oscillates independently, with no fixed relationship between each other. This modes are amplified in the resonator by the gain medium, the out-coming laser has random phases. (c) Pulsed lasers can be obtained in the resonator by using a modulator which introduce a well-defined and fixed phase relationship between the modes in the resonator. If the phases are *locked* then there is a constructive interference between the modes at an instant and a destructive interference at other times, the output will appear as (ultrafast) pulses.

In our experiments, the pump laser used was a Ti:Sapphire tunable and mode-lockable Mira 900 laser pumped by a CW semiconductor laser model Verdi G both supplied by Coherent as is shown in figure 3.4. The output wavelength for all reported experiments was tuned in detail for each experiment. In pulsed operation (mode-locked), the pulses in the near-infrared wavelength range were produced with a frequency of 75.6 MHz corresponding to a pulse period of 13.2 ns and with a pulse duration of near 2 ps (spectral width of near meV), significantly shorter than all characteristic relaxation times of the studied systems.

3.2.1.2 Beam-splitters

Non polarizing beam-splitter (BS) cubes: are optical devices used to divide an incident laser beam into two different beams while maintaining the incident light polar-

ization. The beam separation occurs at an interface within the cube, often made of two triangular glass prisms which are glued together with some transparent resin or cement. The thickness of that layer is used to adjust the power splitting ratio for a given wavelength, typically, half of the light incident is reflected and the other half is transmitted as is shown in figure 3.5 (a). Additionally, beam-splitters can be used in reverse to combine two different beams into a single one.

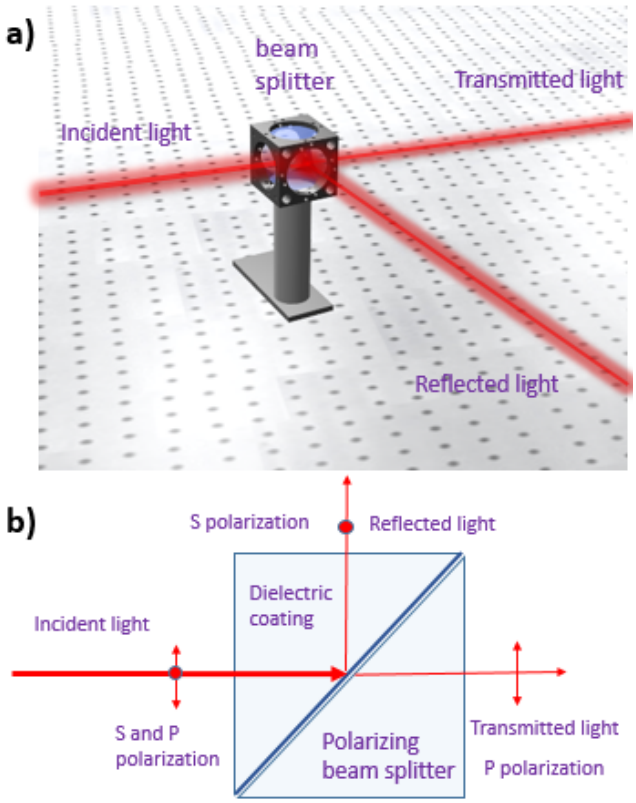

Figure 3.5: (a) Beam-splitter separates an incident beam into reflected and transmitted beams, the power ration between these beams for a wavelength range is normally 1:1. (b) Polarizing beam-splitters separates the reflected and transmitted beams into its S and P components.

Polarizing beam-splitters (PBS) cubes: in this device, instead of glass, is used a birefringent crystalline media or a resin with a dielectric coating, designed as either spectrally broadband or narrow-band to separate an incident unpolarized or polarized monochromatic beam into its components perpendicular and parallel to the plane of incidence, the S and P polarization components, respectively, as is shown in figure 3.5(b).

In our experiments was used a beam-splitter cube to divide the laser from the Coherent Mira 900 into the pump and probe beams. Also, we use a polarizing beam-splitter to obtain the reference and transmitted beams in the time-resolved differential transmission experiments.

3.2.1.3 Collimating and focusing lens

Collimating is the process of accurately aligning a light beam in a parallel fashion. For optical measurement, this ensures that the light has minimal spread as it propagates because of its natural tendency to diverge as it travels through an optical setup. For this, is common to use a set of optical lens (glass or polymer commonly with one curved surface to modify the wavefront curvature of the incident light to focus, defocus or collimate this beam) at appropriate focal distances. By the use of converging lens with manual steering location is also possible to focus a light beam with high precision onto specific spot positions.

In our experiments, we use collimating lens in different positions on the optical table. For the pump beam, it is very important because it goes through the delay line and for different positions of the delay line it travels different distances until the sample surface. This is, the delay scan causes a drift of the diameter of the Gaussian beam; as a result, the photon density changes. To minimize this unwanted effect, the beam is collimated in such a way that the neck of the Gaussian beam is kept in the middle of the delay line.

Also, after the pump and probe pulses are delayed with respect to each other, modulated and intensity tuned, they had to be focused on the sample position. With manual steering mirrors, lens and pin-holes, the pump and probe were aligned near parallel to each other (angle between them was $\approx 3°$) and directed normal to the entrance window of the cryostat. Both the pump and probe beams were then focused with precision on the same point (concentric on the sample surface position inside the cryostat) by adjusting mechanically the lens position. For time-resolved Faraday rotation analysis this spatial overlap is crucial. For this purpose, the pump spot size is adjusted so that it exceeds the probe spot size at the location of pump-probe overlap in the sample plane as is shown in figure 3.6. Such configuration guarantees that the signal will not change by small variations of the probe position or the probe spot size due to beam divergence while scanning the delay. Preliminary alignment of the spot overlapping is done by directing and focusing the beam on the sample and using an infrared video camera, which shows the position of spots on the sample.

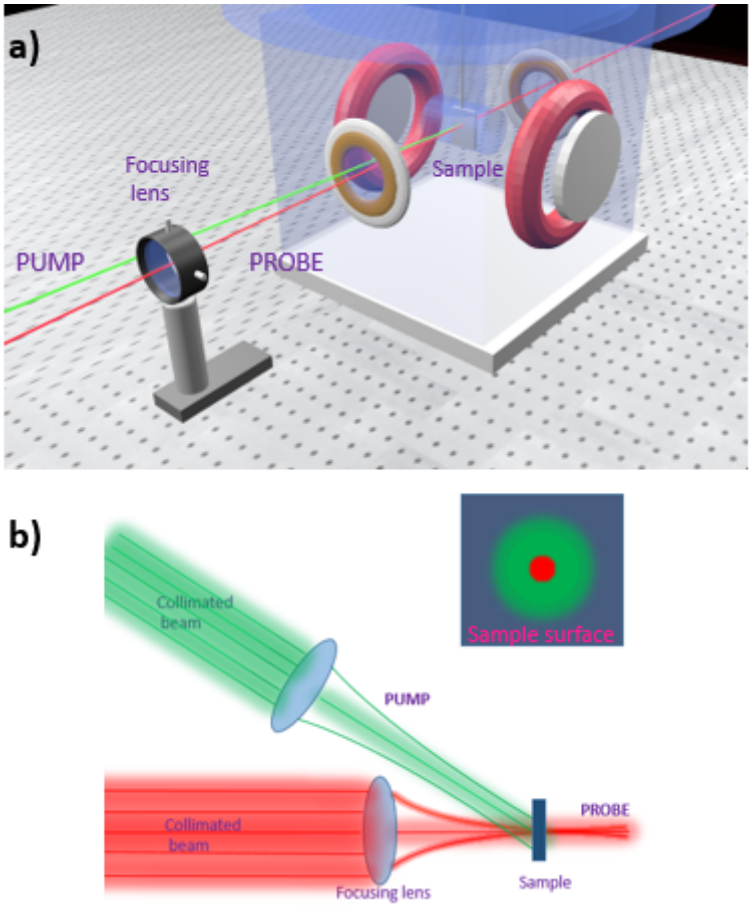

Figure 3.6: (a) Lens are used in our setup for collimating and focusing the light beams. For example, to focus the beams at the sample position inside the cryostat. (b) The pump and probe beams are concentric (inset) where the pump beam diameter is bigger than the probe diameter.

3.2.1.4 Delay line

In order to obtain temporal resolution in pump-probe experiments, the pump and probe are time delayed one relative to the other by making one of these beams travel through a computer-controlled mechanical delay line, based on a mobile retro-reflector (piece that reflects beams precisely back towards their source) mounted on a rail that induces the time delay between pump and probe beams, by changing the optical path length of the beam in it while the other has a fixed path.

Commonly, the pump beam is directed to the delay line because it is preferable to have a very stable beam path for the probe beam which is the beam later analyzed using the detectors. The probe beam is directed via a fixed and relatively simple path, to roughly equalize the optical path lengths of the pump beam, by successive reflections on a set of mirrors. The length of this path determines the range of the pump-probe delay time. To access to longer delay times, the beam could be aligned such that it passes twice the delay line.

In our experiments, the mechanical delay line used had 0.5 m, allowing time delays up to 3.33 ns for a single pass. The optical path was adjusted so that it allowed time delays between -0.75 ns and 3.5 ns with a precision below $\sim$ 50 fs.

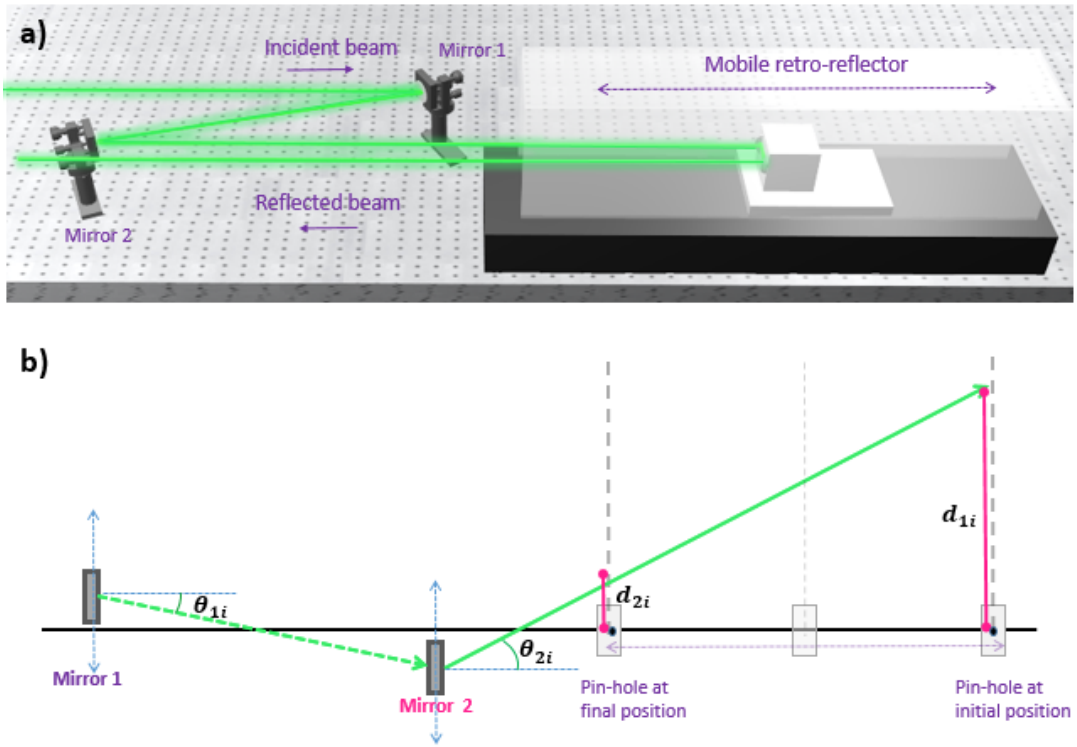

Figure 3.7: (a) The delay line makes possible time- resolved measurements by changing the path of an incident beam at each step of the moving retro-reflector. (b) Unidimentional "Walk the beam" process to align the beam in the delay line. The objective is to pass the beam through pin-holes 1 and 2 by changing the position of mirrors 1 and 2. This iterative process start by making $d_{2i} = 0$ using mirror 2 (beam pass through pinhole 1) and then making $d_{1i} = 0$ by using mirror 1 (beam pass through pinhole 2) at this point d_{2i} is not zero again but closer than before, the process start again until convergence.

3.2.1.5 Optical modulation

An optical modulator is a device which can be used for manipulating a property of a laser beam. Depending on which property of light is controlled, modulators are called intensity modulators, phase modulators, polarization modulators, frequency modulators, etc.

A photo-elastic modulator (PEM) is an optical device used to modulate the polarization of incident light. It is based on the photo-elastic effect, in which a transducer, mechanically, due stretching and compressing stress, change the birefringence (refractive indexes) of the transparent plate of the PEM, exhibiting a birefringence proportional to the strain which changes periodically at the frequency of the modulator f_M. For example, a linearly polarized monochromatic light impinging at 45 degrees to the PEM optical axis can be thought of as the sum of two components, one parallel and one perpendicular

to the optical axis of the PEM. The birefringence introduced in the plate retard one of these components more than the other, that is the PEM acts as a tunable wave plate. Typically it is adjusted to be either a quarter wave or half wave plate at the peak of the oscillation. For the quarter wave plate case, the amplitude of oscillation is adjusted so that at the given wavelength one component is alternately retarded and advanced 90 degrees relative to the other, so that the exiting light is alternately right-hand and left-hand circularly polarized at the peaks. The periodicity of these polarizations are normally from a modulator oscillator at frequency f_M and is used to drive a phase-sensitive detection, the *demodulation*.

In our experiments, to create non-equilibrium spin polarization in time resolved Faraday rotation in a sample with charged quantum dots, circularly polarized light is needed. For that reason, the pump pulse after being delayed is passed through a photo-elastic modulator. The transmitted beam oscillates from left to right circular polarization at 50 kHz. For photo-induced Faraday rotation measurements in the EuTe sample, modulation was obtained by using a mechanical chopper at frequency modulation of 2.33 khz.

3.2.1.6 Intensity tuning line

The pump and the probe beams intensities were controlled by using an intensity controller line composed of an optical pin-hole (small circular hole through which light can be transmitted), and a $\lambda/2$ wave-plate followed by a linear polarized aligned at 45 degrees of the PEM optical axis to regulate the light intensity through this array. The power ratio of the pump and probe was about 20 mW (pump) to 10 mW (probe) for time-resolved Faraday rotation measurements.

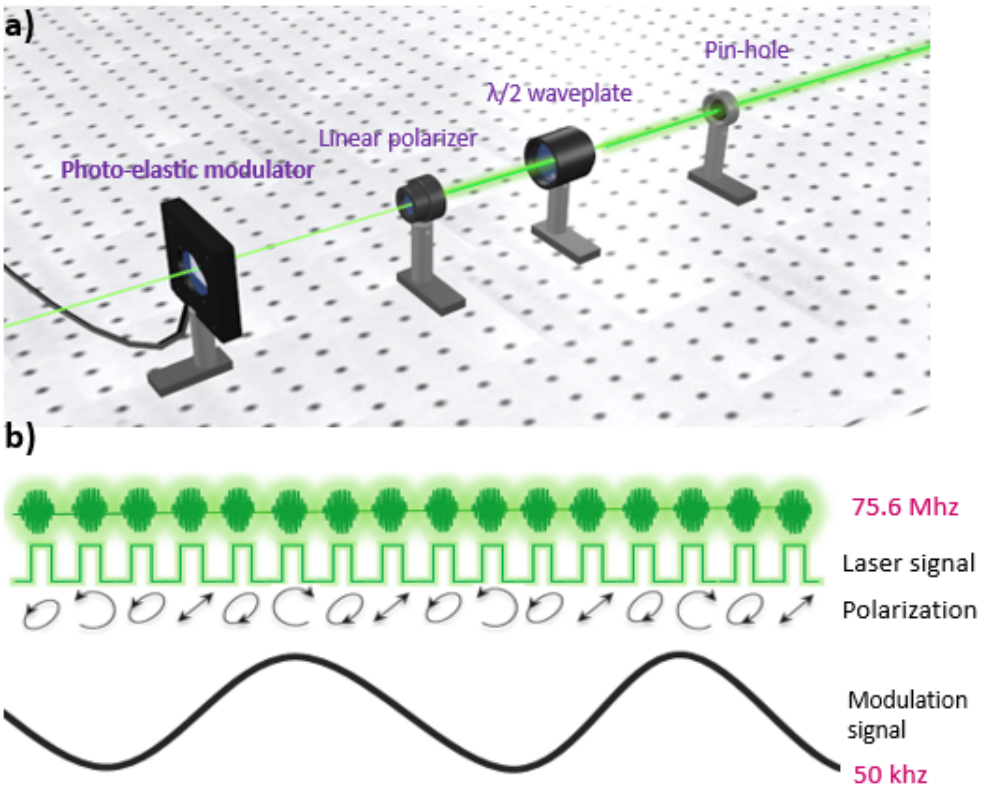

Figure 3.8: (a) Intensity tuning line to control the intensity of the pump and probe beams. (b) Pulsed beam can be represented as a periodical signal (commonly at 75.6 MHz), the polarization of this signal can be modulated with the frequency of the modulator (commonly at 50 kHz) to produce a periodical circularly polarized light signal.

3.2.1.7 Homodyne detection: frequency demodulation

In general, optical radiation can be measured by direct detection of the intensity falling on a photo-detector. However, the performance on direct detection can be limited by extreme low signals or due to the presence of unavoidable noise currents in the detector, which reduce the signal to noise ratio. Hence, it may be advantageous in certain circumstances to use improved detection techniques as the heterodyne detection method or the homodyne detection method.

Homodyne detection: Is a detection method for extracting information encoded in an oscillating signal of interest called "data signal" modulated in frequency and/or phase, by comparing this signal with a reference strong oscillation that would not modify if the data signal did not carry information. Homodyne signifies that the reference frequency (i.e. modulator or chopper frequency) equals the data signal frequency (i.e. virtually derived from the same source). The fundamental concept behind the homodyne detection is to improve the signal to noise ratio, for this, a **lock-in amplifier** synchronized with the reference frequency is used to efficiently reject the background noise due to pump scatter, laboratory lights, etc., by isolating and amplifying the data signal, commonly, the probe

signal, which carries all the information in the experiments.

Homodyne balanced detection: A remaining problem of homodyne detection is that excess noise of the reference oscillator directly affects the signal. This is avoided with a balanced setup where a beam-splitter separate the data signal into two signal directed to the photo-detector. With an electronic circuit, it is possible to obtain the difference between the two photo-currents. That difference is to first order not influenced by noise of the reference oscillator.

In our experiments, we used a balanced homodyne detection system to suppress background signals or low-frequency noise and to monitor the Faraday rotation. To improve the sensitivity of the experiment, the pump beam was modulated with the frequency modulator $f_M \approx 100$ kHz, that modulates the periodic pump excitation. After passing through the sample, the probe beam was splitted for in orthogonal polarization components to arriving at an auto-balanced Nirvana photo-detector supplied by Newport interfaced with the lock-in amplifier as is shown in figure 3.9. For more details see the Appendix section.

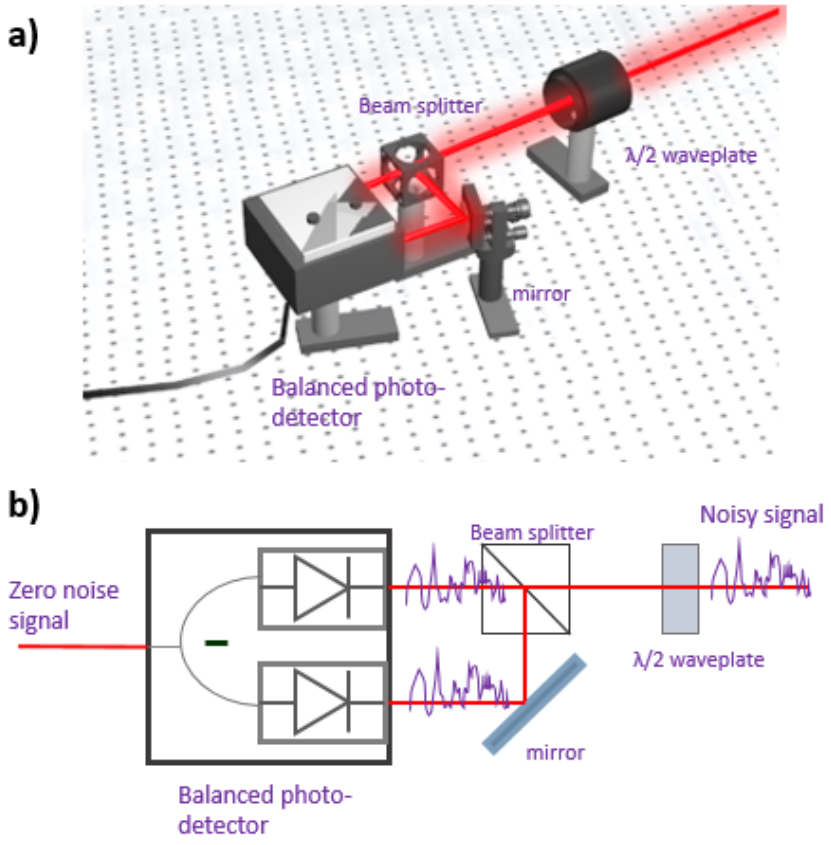

Figure 3.9: (a) After passing through the sample, the probe beam passed through a $\lambda/2$ plate in order to regulate the intensity of its two orthogonal polarization components arriving to a balanced detector. (b) Balanced detection is based on the subtraction of the noise common to both channels of the photo-detector.

3.2.2 Time-resolved Faraday rotation

It has been proven to be the most reliable tool to detect the optically induced spin dynamics in a semiconductor nanostructure and monitor its temporal decay. The operating principle of this magneto-optical technique is the following: the sample is exposed to a homogeneous magnetic field, typically oriented perpendicular to the sample optical axis (Voigt geometry) chosen to coincide with the growth direction of the sample, or parallel to the sample optical axis (Faraday geometry). Then, an intense ultrafast laser pulse which can be manipulated in energy, intensity, polarization and duration called **pump pulse**, is used to excite the sample electrons and temporally re-orient the sample electron spins, therefore, creating a macroscopic spin polarization. This polarization is probed by a subsequent linearly polarized weaker in energy laser pulse called *probe pulse*, which rotate their polarization plane in $\Delta\theta_F$ (**Faraday rotation effect**) after propagation through the sample which is spin-polarized due the pump, this rotation is proportional to the magnetization ΔM in the optical axis direction. The probe pulse is time delayed relative to the pump pulse by using a *delay line*. Therefore, is possible to measure the sample Faraday rotation which is a measure of the spin polarization along the optical axis as a function on time, this is done typically over times shorter than the repetition period of the pump pulse, commonly 13.2 ns.

More details of the measurement technique are explained in the Appendix section A.2.

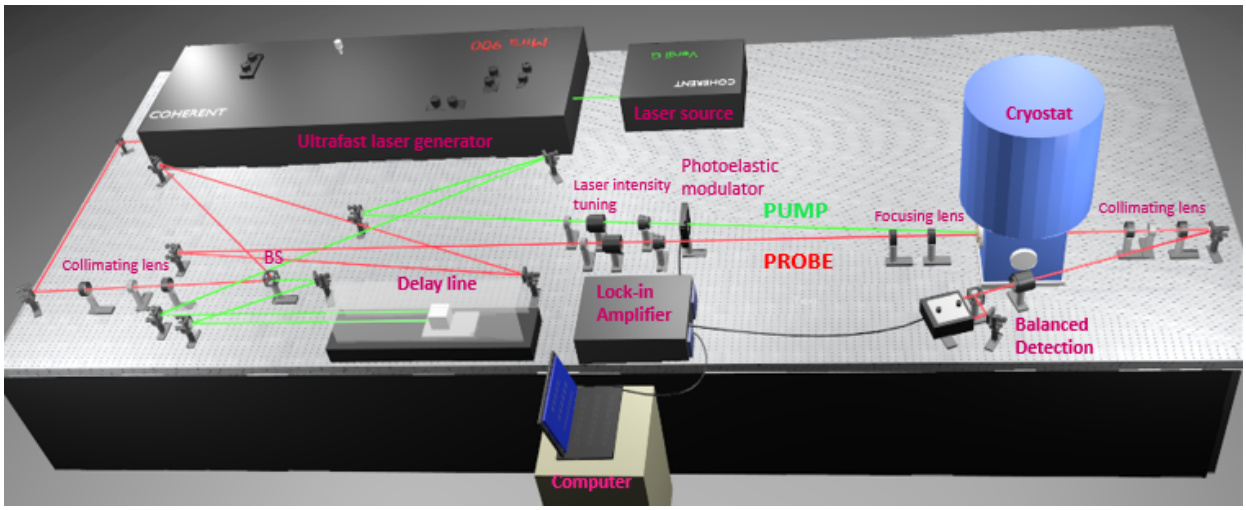

Figure 3.10: Setup for the time-resolved Faraday rotation experiments. The obtained signal $\Delta\theta_F(t)$ (Faraday rotation) is proportional to the magnetization $\Delta M(t)$ in the optical axis direction.

3.2.3 Time-resolved differential transmission

The experiment is a pump-probe technique used to inquire the dynamics of the carriers by probing the temporal evolution of the relaxation of photo-excited carriers in which,

the pump light produces a small variation ΔT in the amount of probe light that crosses the sample, because part of the light is absorbed by the sample and used to excited the carriers. Then, the following time-delayed probe pulses (which arrives much before the recombination of the photo-excited electron) have more probability to cross the sample because part of the carriers is already excited by the pump. Thus, the temporal evolution of ΔT has a continuously decreasing behavior, commonly an exponential decreasing behaviour.

In our experiments, the laser used was a Ti:Sapphire tunable and mode-lockable Mira 900 laser supplied by Coherent with a spectral width of 1 meV, corresponding to a pulse duration of about 2 ps. The output wavelength for all reported experiments was $\lambda = 880$ nm. In pulsed operation, pulses of a few picoseconds in duration were produced with a frequency of 76 MHz, corresponding to a pulse period of 13.2 ns. These pump and probe pulses are typically taken from the same laser source and are used to measure the differential transmission $\frac{\Delta T(t)}{T(0)}$, which is defined as,

$$\frac{\Delta T}{T} = \frac{T(t) - T(0)}{T(0)}, \qquad \text{with} \qquad T(t) = \frac{I(t)}{I(0)} \tag{3.1}$$

where $T(0)$ is the probe transmittance at t=0 when the pump light hits the sample and $T(t)$ is the probe transmittance at time t, where t is the delay time after excitation.

More details of the measurement technique are explained in the Appendix section A.3.

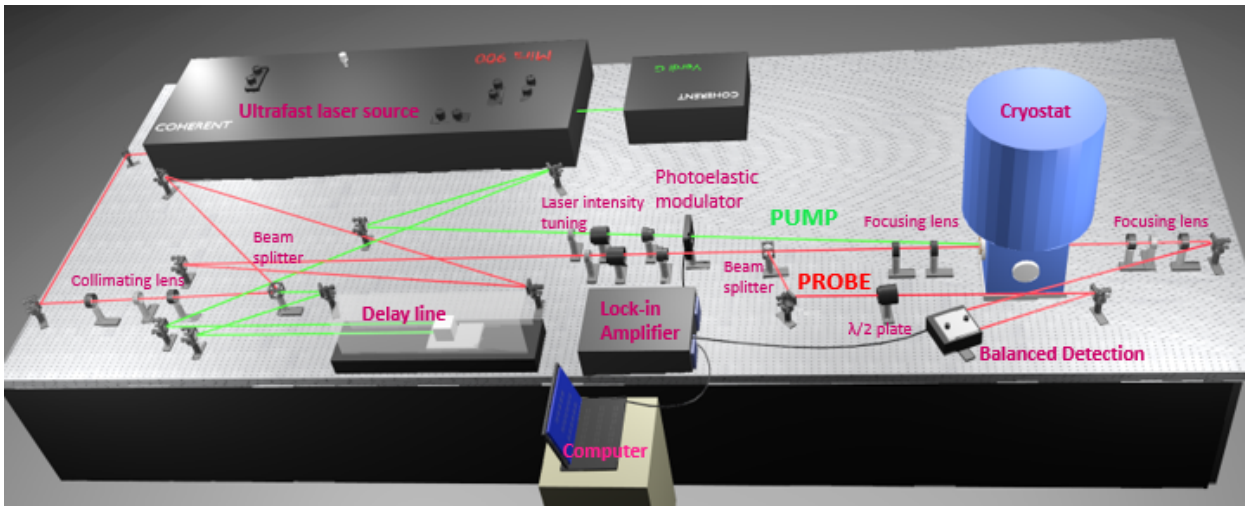

Figure 3.11: Setup for the time resolved differential transmission experiments.

3.2.4 Photoluminescence

Photoluminescence (PL) is a standard characterization technique that allows us to obtain the spectrum of the emission energies of a sample. A laser with energy higher than

the band-gap of the semiconductor sample is used to photo-excite its electrons. The excited electrons with energy above the conduction band of the material eventually fall to the lowest available non-radiative energy level after losing some energy through releasing phonons and then spontaneously recombine through various recombination paths available to the valance band emitting luminescence in the form of photons of different energies. A spectrum of the intensity of the luminescence as a function the emitted energy is obtained, the peaks in the spectrum represent a direct measure of the energy levels in the semiconductor.

For our measurements was used a Ti:Sapphire Mira 900 laser supplied by Coherent in continuous wave with wavelength of 800 nm to excite the sample inside an Oxford Cryostat at $T=$ 10 K. The sample luminescence was directed to an optical fiber and then analyzed with a Triax 550 spectrometer. Inside the spectrometer, the incoming light was separated into their frequency components by a diffraction grating and directed to a liquid nitrogen cooled charged coupled device (CCD), where the intensity of each frequency is measured by the acquisition system.

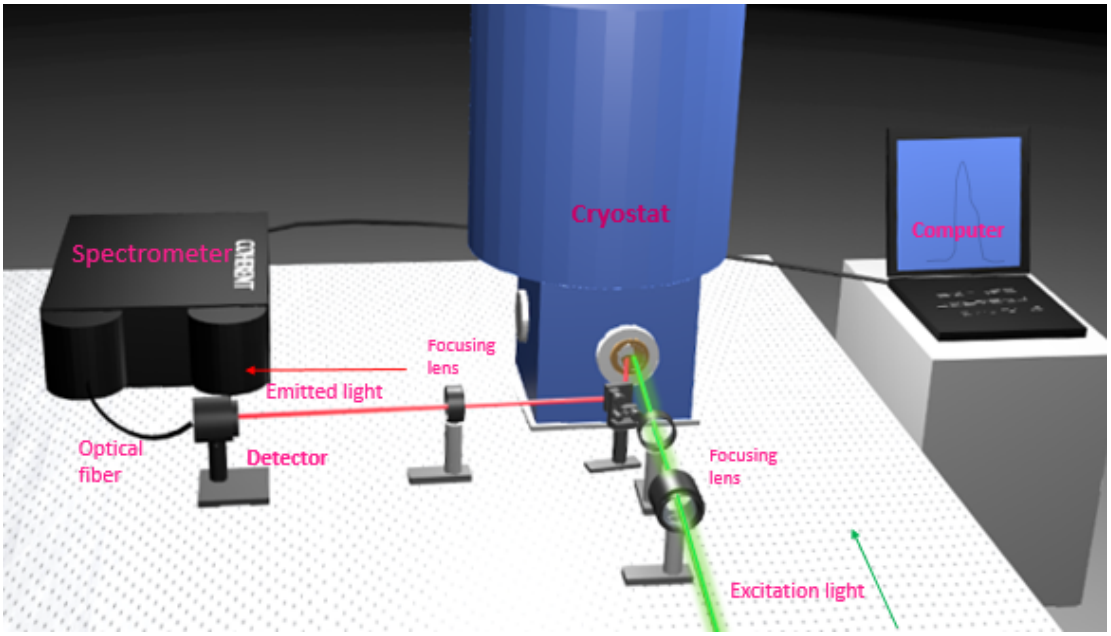

Figure 3.12: Setup for photoluminescence experiments. The excitation light was a cw light of $\lambda = 800$ nm at $T=$ 10 K.

3.2.5 Photo-induced Faraday rotation

Is a pump-probe technique used to detect the photo-induced rotation $\Delta\theta_F$ of the polarization plane of a linearly polarized probe pulse due to the Faraday effect when it crosses a sample which is photo-magnetized ΔM due the pump pulse. This Faraday rotation is analyzed as a function of an applied magnetic field and temperature.

In our experiments, the photo-induced Faraday rotation signals were measured by

using a two-color pump-probe technique. The pump light source was a frequency-doubled Nd:YAG laser (2.33 eV) supplied by Cobolt, focused on the sample with a Gaussian profile of 150 μm full width at half maximum. The Faraday rotation probe was a semiconductor laser of photon energy 1.86 eV, this photon energy is below the EuTe gap for any field and temperature used in our measurements, so the probe does not photo-excite any electron-hole pairs, and hence it does not induce any magnetic polarons. A magnetic field was applied normal to the surface of the sample, which is parallel to the [111] crystalline direction of the sample. The experiments were performed using a variable-temperature from 5 K until 110 K optical cryostat containing a superconductive coil to generate a magnetic field applied in the Faraday geometry. The pump was modulated at 2.33 kHz using a mechanical chopper. The Faraday rotation angle of the linearly polarized probe beam was measured by using a polarization bridge containing a New Focus Nirvana balanced detector coupled to a lock-in referenced to the chopper frequency.

More details of the measurement technique are explained in the Appendix section A.2.

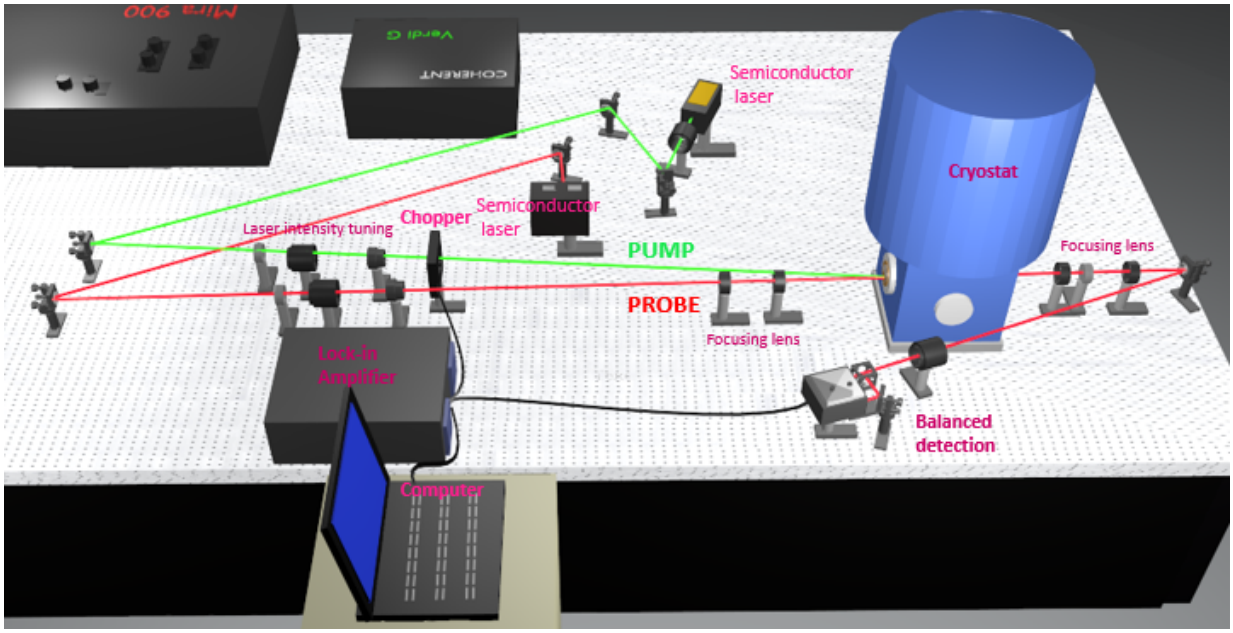

Figure 3.13: Setup for the photo-induced Faraday rotation experiments.

3.2.6 Bulk Faraday rotation

Sometimes called bulk Faraday rotation, is used to measure the absolute value θ_F of the Faraday rotation of a linearly polarized probe light which crosses a magnetized M sample due to an applied magnetic field at some temperature.

In our experiments, the bulk Faraday rotation was measured by using uniquely a probe light in the setup. The probe light source was a semiconductor laser of photon energy 1.86 eV. (same energy as in the photo-induced Faraday rotation case). A magnetic field

was applied normal to the surface of the sample, which is parallel to the [111] crystalline direction. The experiments were performed using a variable-temperature optical cryostat containing a superconductive coil to generate a magnetic field applied in the Faraday geometry. The Faraday rotation angle was measured by using a polarization bridge containing a New Focus Nirvana balanced detector. In this case without a pump-probe signal difference, the cryostat windows contribute to the Faraday rotation as an additional signal. The way to isolate just the contribution associated to the sample is by measuring the bulk FR value of the window cryostat without the sample and then subtract this value from the total bulk FR signal related to the sample and cryostat windows.

More details of the measurement technique are explained in the Appendix section A.1.

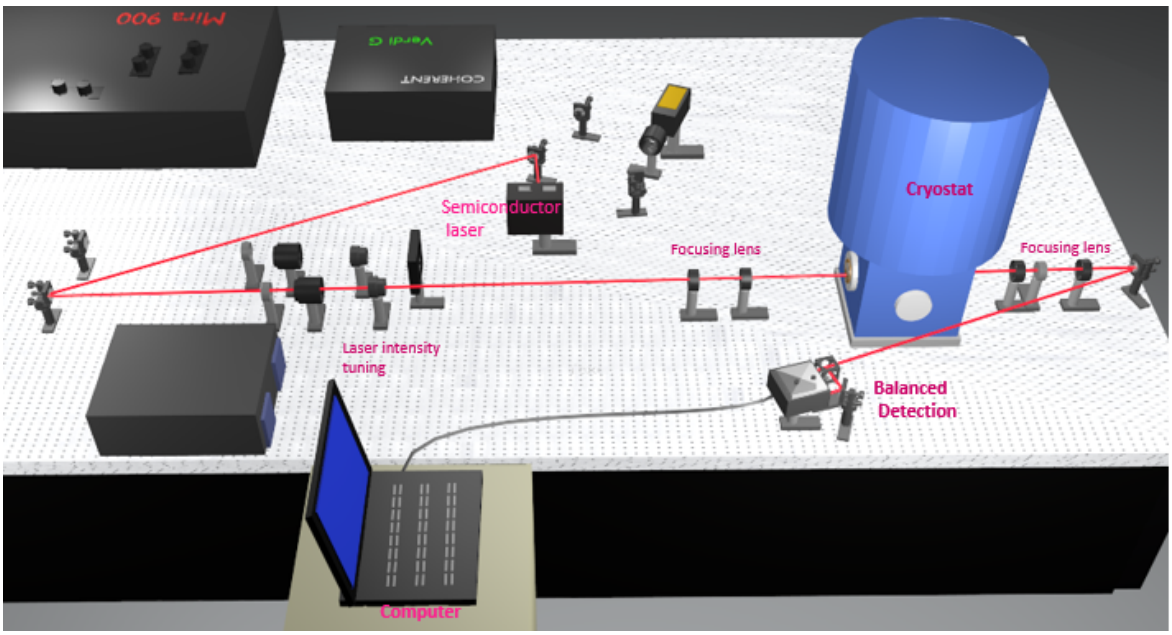

Figure 3.14: Setup for the bulk Faraday rotation experiments.

3.2.7 Superconducting Quantum Interference Device magnetometry

Sometimes called SQUID measurements, is one of the most effective and sensitive ways of measuring magnetic properties, commonly utilized in magnetometers due to their extreme sensitivity to magnetic fields weaker than 10^{-14} T. SQUID devices are based upon Josephson junctions, which consist of two superconducting materials (generally niobium alloys) connected by a weak link of non superconductor material, with the property that below the superconducting transition temperature, the superconductors have a complex wavefunction $Ae^{i\theta}$, where the amplitude and phase depends on the material and temperature, etc. When it interfaces with a non-superconducting material, the superconducting wavefunction can extend a finite distance into the non-superconducting material, thus,

the two superconductor with wavefunctions $A_1^{i\theta_1}$ and $A_2^{i\theta_2}$, have a a phase difference $(\theta_1 - \theta_2 = \Delta\theta)$ across the junction, which corresponds to a zero voltage super-current due gradient phase, $I_s = I_c \sin(\Delta\theta)$, that allows quantum tunneling between the two superconductors without bulk transport. The SQUID measurements takes this principle by connecting these two superconductors with two Josephson junctions and a hole in the middle. Now, the current that flows through the device is a function both of the phase difference between the two superconductors and the magnetic flux (ϕ) through the hole. When the sample is moved up and down it produces an alternating magnetic flux in the hole which leads to an alternating output voltage. By locking the frequency of the readout to the frequency of the movement, the magnetometer system can achieve the extremely high sensitivity for ultra small magnetic signals produced by a sample.

A clear example of the precision of SQUIDs is their ability to detect, and actually discover, that magnetic flux is quantized in units of $\phi_0 = \dfrac{h}{2e} = 2.0678 \times 10^{-15}$ [T.m^2] where h is Planck constant, and e is the electron charge. In particular, it is the only method which allows to directly determine the magnetic moment of a sample in absolute units.

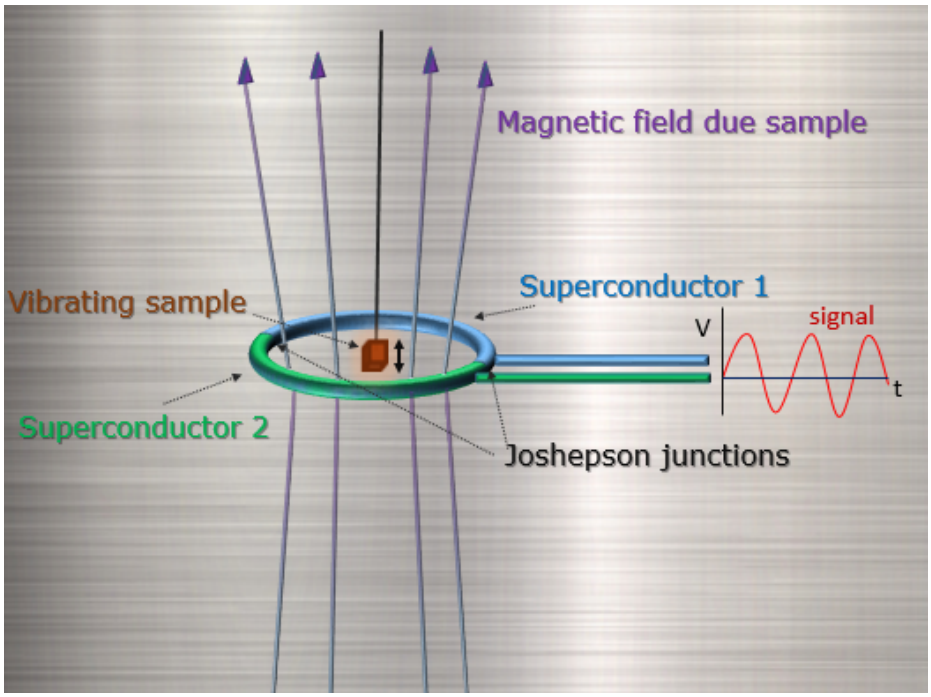

Figure 3.15: Basic operating principle of SQUID system to detect magnetic fields.

3.3 Samples

3.3.1 Sample preparation: Molecular beam epitaxy method

Is the most common method used to fabricate high quality samples because allows a high degree of control of the composition of the sample almost at the atomic scale. It takes place in a chamber at high or ultra-high vacuum (10^{-8} or 10^{-12}) mbar and high temperature. A monocrystalline substrate acts as a seed and then atoms of the same or another element (the difference in lattice parameters is refereed as lattice mismatch) is deposited at low rate to allow an ordered film growth, continuing the substrate crystallographic direction (epitaxyal growth). In particular, it enabled hetero-epitaxial growth: the possibility to grow materials of different composition monolayer by monolayer.

There are three standard growth mechanism: layer by layer (Frank-van der Merwe method), clustering (Volmer Weber) and the intermediate method **Stranski-Krastanov**.

Stranski-Krastanov method

The process start with a semiconductor material being deposited on another different semiconductor, the upper material initially assumes exactly the crystal arrangement of the material below because the upper material has a higher preferred atomic spacing, however, due a mismatch strain between the two different materials a compressive strain accumulates in the crystal. After only a few atomic layers (critical thickness), the strain is relieved spontaneously through the formation of 3D dots bulging upwards in order to reduce the mismatch strain.

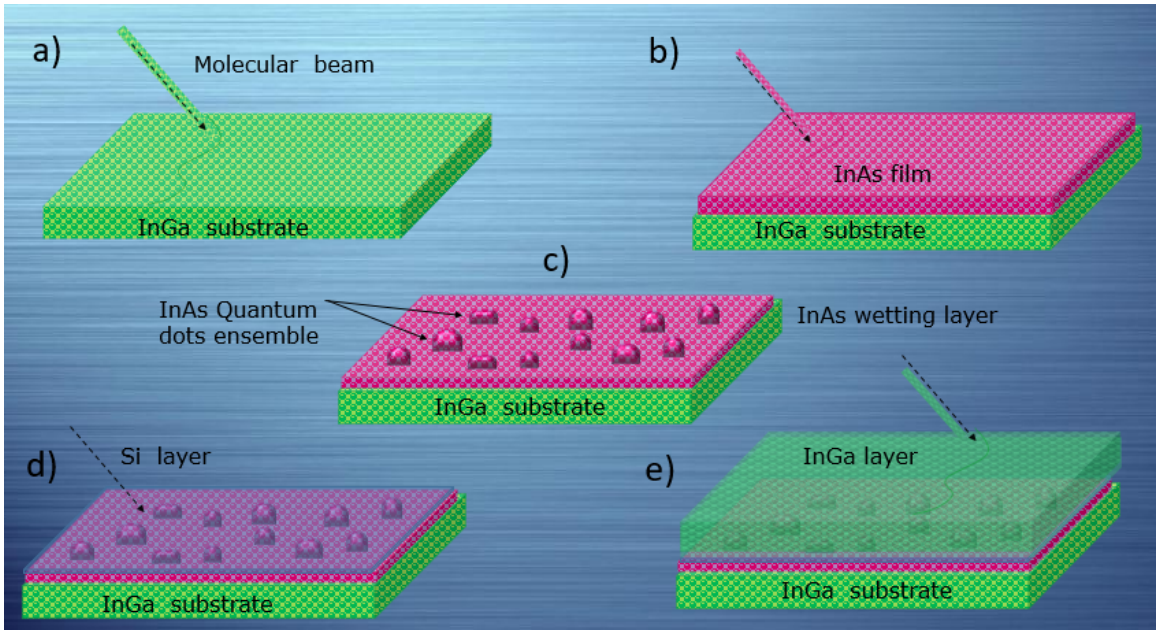

Figure 3.16: Illustration of the formation of InAs quantum dots ensembles by MBE. (a) InAs atoms are deposited over a InGa substrate. (b) Several atomic layers of InAs are formed until a critical thickness. (c) Spontaneous formation of QDs is produced in order to reduce the mismatch strain. (d) Alternativelly, QDs are doped using Si atoms. (e) Quantum dots are capped using InGa atom layers.

To avoid the deterioration of the optical properties of the QDs caused principally by surface oxidation, the QD structures composed of lower-bandgap material are embedded in a surrounding matrix of higher-bandgap semiconductor fabricated normally of the substrate material. Strong changes can occur during the subsequent capping, allowing the QD emission properties to be finely tuned, if for instance the QD emission needs to be blue-shifted or tuned to the sensitive range of silicon charge-coupled device (CCD) cameras, a capping and annealing step may be used.

Normally a flat film of the QD semiconductor atoms called *wetting layer* (WL) is still present after the growth of the quantum dots, this produce a quasi-continuum energy level close the discrete energy states of the QDs due the two-dimentional confinement of the carriers in this film.

3.4 Samples in this thesis

3.4.1 Quantum dot ensemble sample

The studied sample was grown by molecular beam epitaxy with Stranski-Krastanov method on a [100]-oriented GaAs substrate and consist of an heterostructure containing (In,Ga)As/GaAs self assembled QDs. The occupation by a single electron per dot was obtained by modulation-doping with Si-dopant density roughly equal to the dot density to obtain an average occupation of one electron per dot. The sample contained 10 layers of (In,Ga)As QDs, separated by wide GaAs barriers, and Si δ-doping sheets 15 nm above and below each QD layer. The obtained QDs are typically lens-shaped with a diameter of tens of nanometers and several nanometers in height, densities are typically in the range of 10^{10} cm^{-2}. Given the nature of the growth process, quantum dots are randomly located on the sample and are not identical, existing a dot to dot size fluctuation and they differ in their shape and chemical composition. In order to shift the emission range of the sample into the excitation wavelength range of the Ti:Sapphire lasers and detection sensitivity range of the detectors, the sample was thermally annealed for 30 s at 950° C using the rapid thermal annealing RTA technique, causing intermixing between the dots and the barrier materials due to the Ga diffusion into the InAs QDs, resulting in an increase in the QD band gap and a blue shift in the photoluminescence compared with the *as grown* sample, so its photoluminescence emission occurs around 1.42 eV (λ = 876 nm).

The (In,Ga)As/GaAs sample was growth at the department of Applied Physics in the Eindhoven University of Technology in Eindhoven, The Netherlands, by the researcher Prof. Dr. Paul Koenraad.

3.4.2 Europium telluride sample

The EuTe sample was grown by MBE on a (111)-oriented BaF_2 substrate [69]. The thickness of the EuTe epitaxial layer was 1.3 μm, and the epitaxial layer was capped with BaF_2 to ensure total protection of the EuTe surface from oxidation. The thickness of the protective layer was 200 nm. BaF_2 is completely transparent in the wavelength range used in this work, therefore the thickness of the protective layer is not critical for the present study.

The epitaxial EuTe samples were grown at the Associated Laboratory of Sensors and Materials (Laboratório Associado de Sensores e Materiais - LAS), at the National Institute of Space Research (Instituto Nacional de Pesquisas Espaciais - INPE) in São José dos Campos, SP, by the researchers Prof. Dr. Eduardo Abramof, Prof. Dr. Paulo Rappl and Dr. Beatriz Díaz. A detailed description of the growing and characterization can be found in reference [70].

Chapter 4

Results

4.1 Light induced coherent spin precession in singly-negatively charged quantum dots

The present section is assigned to the experimental estimation of the trion recombination time by using the time resolved Faraday rotation method. We want to know if this method is a viable technique compared with other existing methods.

Selection of the pump pulse energy

To estimate the trion lifetime τ through Faraday rotation measurements, we first select a suitable wavelength of the pump beam by using the photoluminescence spectra of the QD ensemble shown in figure 4.1. For quantum dot ensembles, the emission line width provides a measure of the dot uniformity. The focused pump beam had a typical diameter of 150 μm, which for a sample with dot density of 10^{10} cm^{-2}, results in the simultaneous excitation of $\sim 10^6$ quantum dots. As a consequence, the resultant spectrum is inhomogeneously broadened owing to unavoidable fluctuations in dot size, shape, and composition. We can observe in this spectra a measure of the dot uniformity, the characteristic inhomogeneous broadening of an QD ensemble with a broad full width at half maximum (FWHM) of 24.3 meV. The PL spectra is peaked at 876 nm (1.42 eV), then, in order to obtain a strong signal for TRFR measurements, we select a pump wavelength near this maximum.

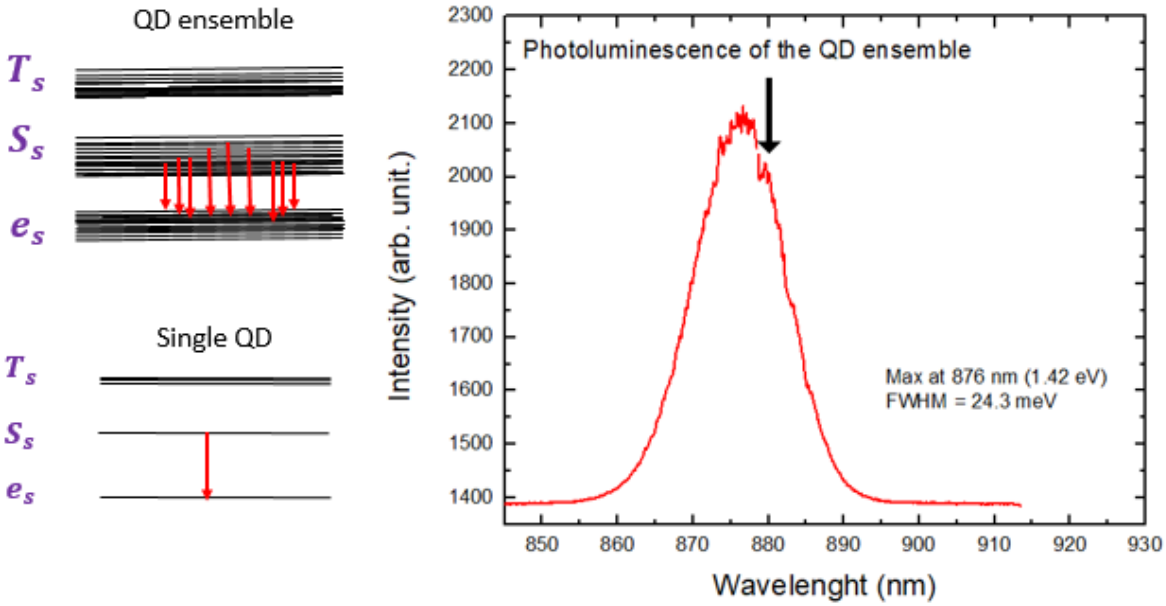

Figure 4.1: (Right) PL spectra at $T = 10$ K for the n-doped (In,Ga)As quantum dot ensemble. The black arrow indicates the selected wavelength of the pump beam for the TRFR measurements. (Left) Representation of energy levels for single and for an ensemble of inhomogeneous QDs.

Time resolved Faraday rotation measurements as a function of the delay time between the pump and the probe were performed using different applied magnetic fields, from 0.1 T up to 1.5 T. By scanning the pump wavelength across the photoluminescence peak sides, it was found that for pump wavelengths longer than 900 nm, a very low TRFR signal was obtained, revealing a too small amount of photo-excited electrons. On the other hand, pump wavelengths shorter than $\sim$ 870 nm was avoided in order to not excite higher energy states as triplets T_s, depicted in Fig. 4.1, which are not considered in the model employed in this work. The laser tuned to wavelength in the near *resonant case* with $\lambda = 880$ nm near the maximum of the photoluminescence spectra shown in Fig. 4.2 gives the best results and was the pump wavelength selected for the TRFR.

Time resolved Faraday rotation measurements

Using a pump wavelength of 800 nm, TRFR measurements were performed under different magnetic fields. The profile of the TRFR oscillations as a function of time correspond to the component of the photo-induced magnetization on the optical axis in the sample. It should be noted that for times longer than $\sim$ 0.5 ns, the photo-excited electron-hole pair has already recombined, and the detected magnetization is reduced only to the contributions arising from the remaining precessing resident electrons in the charged QDs.

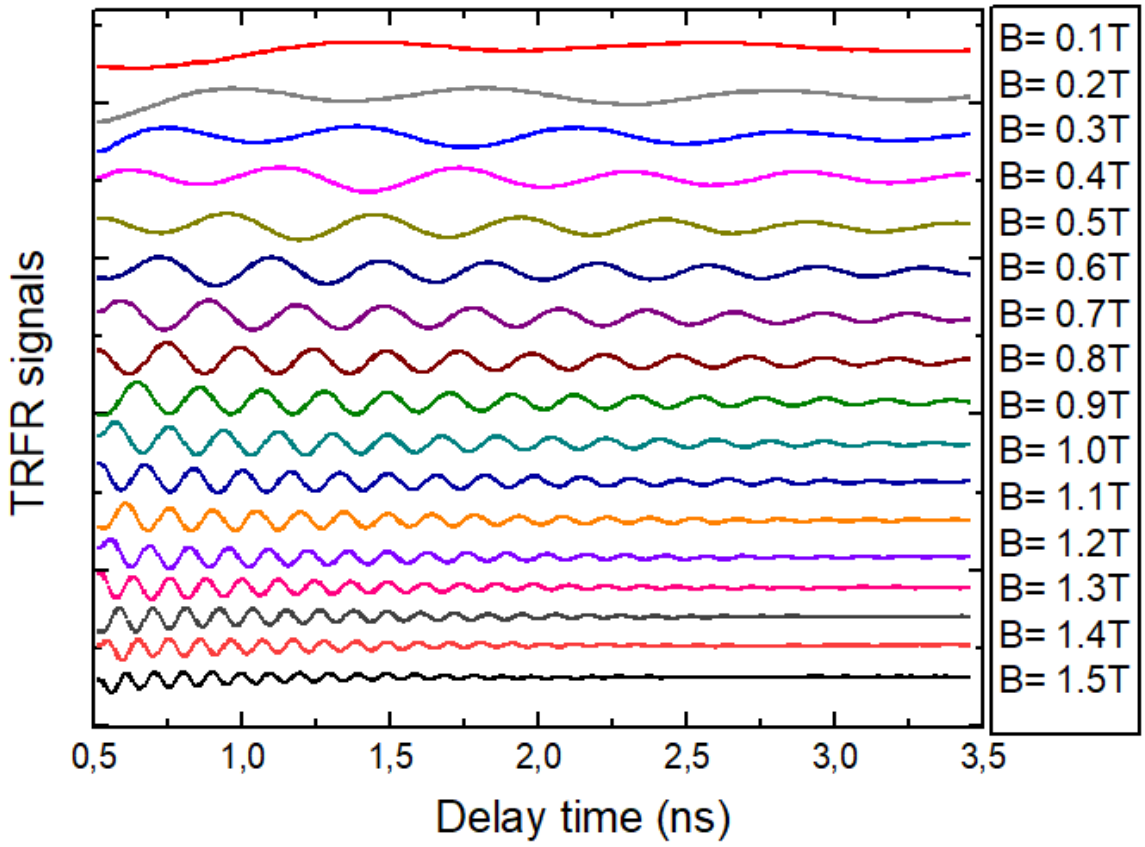

Figure 4.2: Fitted experimental data of the magnetization oscillations obtained from TRFR measurements for different magnetic fields with $\lambda_{pump} = 880$ nm for times longer than the trion recombination time.

As expected, due the linear relation between the spin frequency precession and the magnetic field, it can be observed that the Larmor precession frequency $\Omega = \frac{g_e e B}{2m_e}$ becomes higher as we increase the magnetic field. The decrease of the amplitude of the oscillations in time is due to the decreasing component of the magnetization in the optical axis due to the addition of spin precession of inhomogeneous quantum dots as observed in PL with different size and composition, leading to variations in the electron g-factor which produce variation in the precession frequencies which on turn, leads to dephasing. As expected, the Faraday rotation (magnetization) has the typical behavior of a damped oscillation, which following the model in [18] can be described as,

$$\theta_F(t) = Ae^{-\frac{t}{T_2^*}} \cos(\Omega t + \phi). \tag{4.1}$$

On the frame of the present model, the phase ϕ of the photo-induced magnetization is expressed by a function of the applied magnetic field having the trion recombination time τ, as the *only one parameter* in a fitting of the theory and the experiment, $\phi = \frac{\pi}{2} - \arctan(\Omega\tau)$, where Ω is the frequency of the oscillations which is dependent on the

magnetic field. In a similar way, the amplitude of the oscillations A, can also be described by a function of the magnetic field. This amplitude has the trion recombination time τ and the saturation amplitude A_0 as the parameters for the fitting with the experimental values, $A = \frac{A_0 \Omega \tau}{\sqrt{1+(\Omega\tau)^2}}$. The experimental values of the phase and the amplitude of the oscillations together with the plot of the theoretical expressions are depicted in Fig. 4.3. A good agreement between them is achieved. *The fitting process for* $t > 0.5$ *ns give us the value of the trion recombination time* $\tau = 0.15 \pm 0.05$ *ns* with an uncertainty related to magnetic field uncertainty.

The obtained values of the Larmor frequency Ω and the coherence time T_2^*, given by the theoretical expressions $\Omega = \frac{g_e e B}{2m_e}$, and $T_2^* = \frac{\hbar}{\mu_B \Delta g B}$ are shown in figure 4.3(c) and (d).

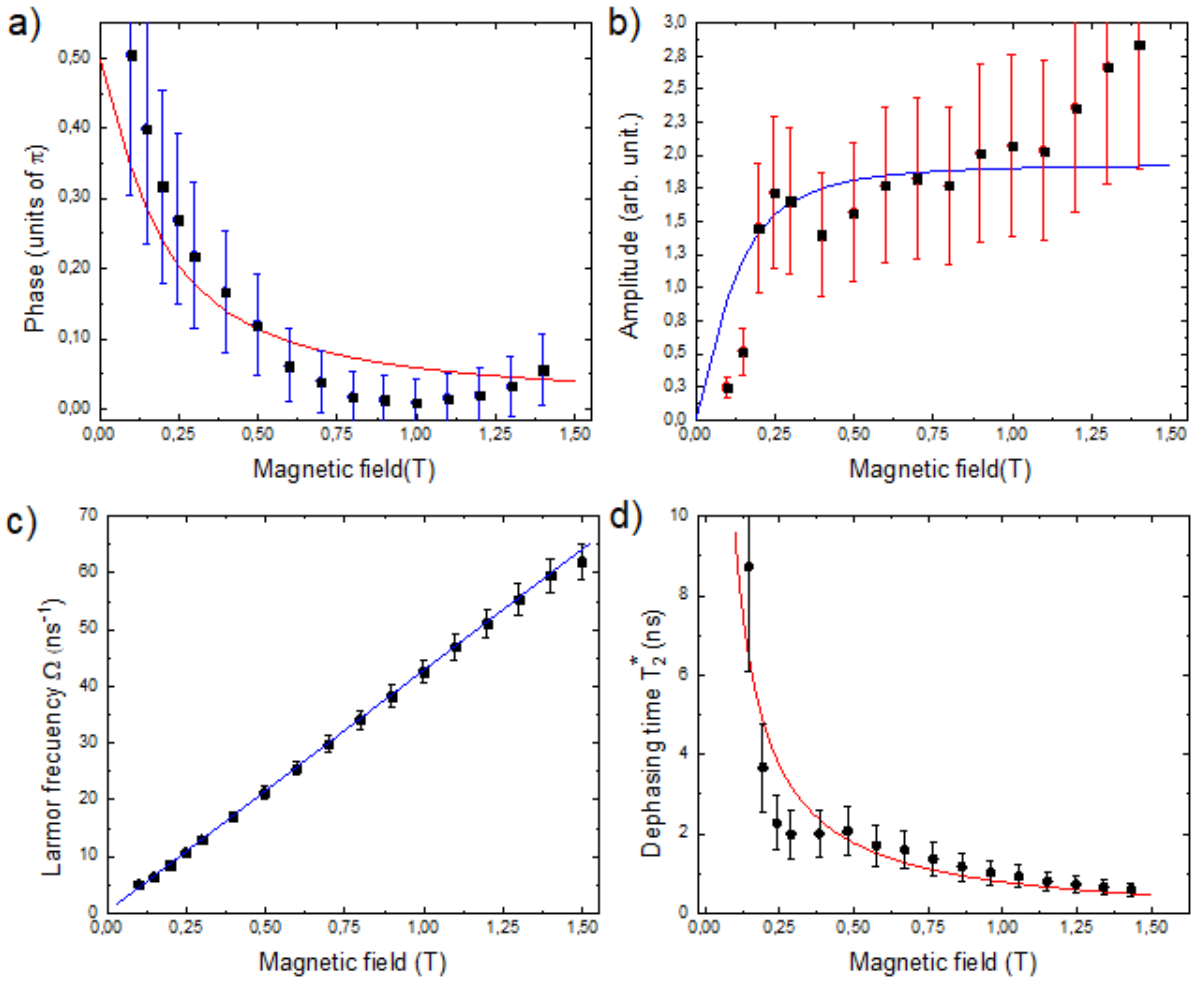

Figure 4.3: Fitted data for the phase (a) and (b) amplitude of the magnetization of the electron spin ensemble on the optical axis. Figures (c) and (d) shows the Larmor frequency and the dephasing time of the QD ensemble as a function of the magnetic field.

Time resolved differential transmission measurements

Time resolved differential transmission measurements with magnetic fields, in the same range used in the TRFR measurements (0.1 T-1.5 T) and in the resonant case $\lambda =$

800 nm were performed to compare the obtained value of the recombination time of the trion obtained by TRFR. The curves are shown in Fig. 4.4 (a) A bi-exponential decaying dynamics can be noted for different magnetic fields, which can be better seen in a logarithm scale where a linear behaviour is observed as is shown in Fig. 4.4 (b). Fitting these linear dependence with the magnetic field we obtain an almost constant recombination time value 0.33 ±0.01 ns for magnetic fields up 1.2 T. This recombination time increases from 0.34 ns to 0.38 ns for magnetic fields higher than 1.2 T, as is shown in figure 4.4(c). From the bi-exponential decaying behaviour observed, we can substract the short living component and we obtain the long living component with a recombination time value of τ_{long} = 1.8 ns for magnetic fields higher than 1 T, as can be seen in Fig. 4.4(d).

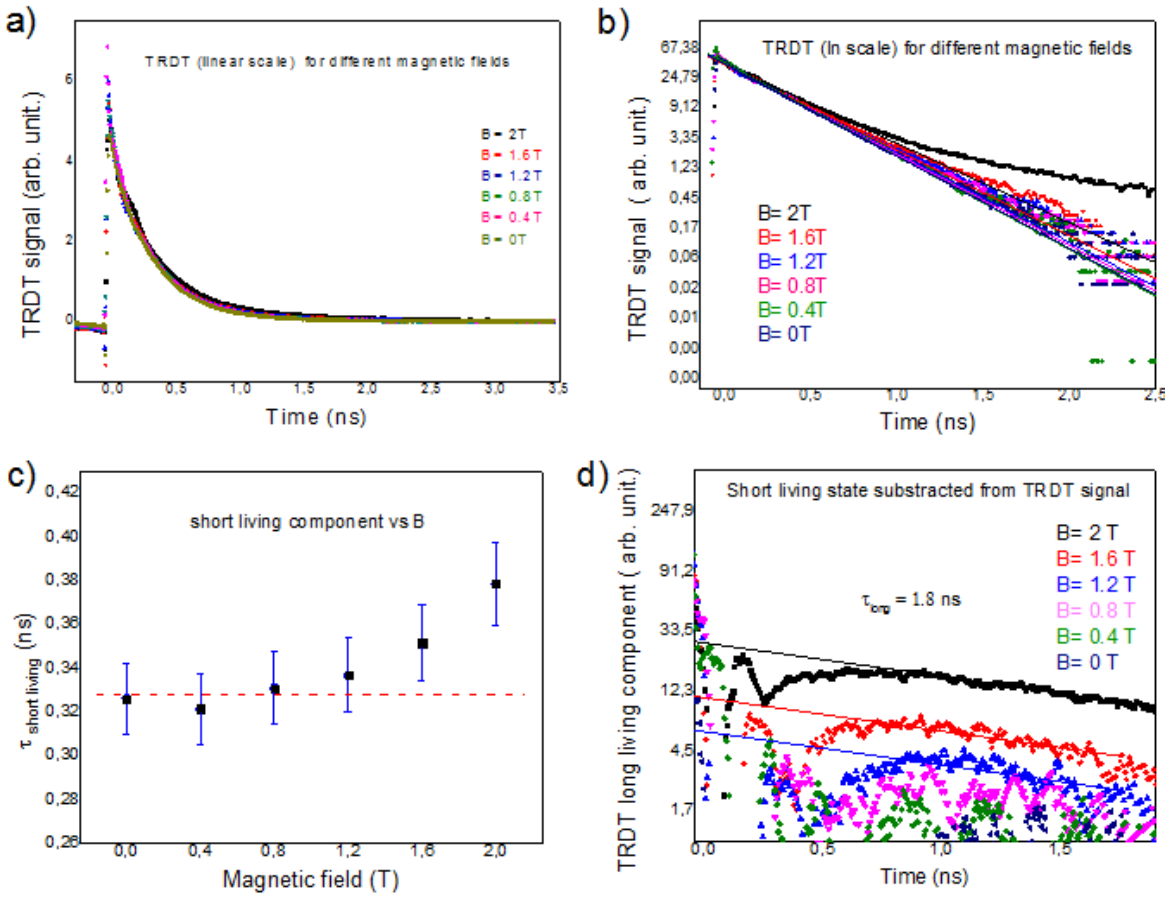

Figure 4.4: TRDT signals for magnetic fields between 0 T to 2 T in linear (a) and logarithm scales (b), respectively. Figure (c) shows the magnetic field dependence of the short living component of the recombination time and (d) shows the TRDT long living component of the recombination time.

The long living states producing the long recombination times appearing for magnetic fields higher than 1 T is probably associated with *dark excitons* that result enhanced at high magnetic fields. In that way, the interval for magnetic fields considered for the fitting

was shortened up to 1 T, then, the phase and amplitude in the TRFR measurements were again fitted with better agreement with the theory as is shown in figure 4.3, where we obtain from the fitting the trion recombination time $\tau = 0.17$ ns. However, this value is different for a factor of approximately two compared with the recombination time value ~ 0.33 ns obtained using the TRDR method. This is because, until now, we were considering the ideal situation with signals associated to pure trion carriers, but, due to the imperfect fabrication process of the quantum dot ensemble, an unavoidable concentration of undoped and multiply doped QDs are present in the sample. In this situation, particles as excitons, and bi-excitons can optically be excited by the pump light, and these states also contributes to the time resolved differential transmission measurements. The estimate of the trion recombination time with TRDT results inaccessible due to the superposition of the recombination time of the trion and the other species, specially because in general, the trion has a lifetime comparable to that of the exciton, and can even interfere in the long-term magnetization signal if their lifetime is long enough. In the present case, the obtained recombination time by TRDT is almost twice the recombination time obtained by TRFR due to the presence of excitons with probably a longer recombination time.

4.1.1 Conclusions

The use of the TRFR to obtain the trion recombination time in a singly negatively doped quantum dot ensemble, by means of a fitting process of the experimental photo-induced magnetization data with their theoretical expressions for the phase and amplitude formulated in [18], which have the trion lifetime as the only one parameter when examined as a function of the magnetic field, let us to conclude:

1. This offers a new method free of complications related to separating incident and emitted lights in the resonant case or pollution signals related to other excited states. It also offers an exclusive technique to estimate the trion lifetime in QDs samples with high dot density ($\sim 10^{10}$ cm^{-2}), considering that a measurement of the trion lifetime is normally obtained from single QDs in low density sample ($\sim 10^{8}$ cm^{-2}). The results obtained using this method yields a trion lifetime $\tau = 0.15\pm$ 0.05 ns.

2. However, this method has its own uncertainty, yielding different values of τ if it is measured repeated times. Although this is a good theoretical method it is not practical because is time consuming for good alignment in the setup.

3. TRDT measurement done under resonant conditions yields a longer recombination time $\sim$ 0.33$\pm$ 0.01 ns because of the unavoidable inclusion of signals related to excitons which are present in the very beginning of this measurement, in contrast with TRFR which extracts the information from time intervals where no longer excitons are present.

4.2 Photo-induced magnetization in EuTe

4.2.1 Calculation of the local magnetic field in EuTe thin films

To calculate the local magnetic field in the EuTe sample, we first have to obtain the value of the local photo-induced magnetization, because, as we will see later, the internal magnetic field has a linear dependence on the magnetization inside the sample.

In Ref. [72], it was established the relation between the Faraday rotation angle θ_F and the magnetization M inside the material. The Faraday rotation angle of the light that crosses an uniformly magnetized sample of thickness d_{sample} can be converted into its magnetization by using the relation:

$$\theta_F = VMd_{sample}, \tag{4.2}$$

where V is called the *Verdet constant*, which we also determine from measuring the DC Faraday rotation (bulk Faraday rotation) measurements at the probe beam wavelength, at T= 5 K, as a function of the applied magnetic field. As was explained in Chapter 3, during this measurement, there is no pump light, and to isolate the sample bulk Faraday rotation signal, the contribution coming from the cryostat windows was measured separately by taking off the sample. Figure 4.5(a) depicts the bulk FR signals related to the cryostat windows which shows a linear behaviour with slope m= -21.6 mrad/T, displaying fixed value at any temperature in the range between 4 K-150 K. The total signal related to the contribution of the window cryostat and the sample is also shown in figure 4.5(a), and the signal related just to the sample obtained subtracting the previous signals $\theta_{F(sample)} = \theta_{F(sample+windows)} - \theta_{F(windows)}$. As expected, we found that the Faraday rotation is independent of the intensity of the probe because the probe beam used is well within the EuTe transparency-wavelength range. Also, as shown in Fig. 4.5(b), the Faraday rotation depends linearly on the applied magnetic field B_{app},

$$\theta_F = m(T)B_{app}, \tag{4.3}$$

where $m(T)$ is the slope of the θ_F vs B_{app} curve at temperature T. For T= 5 K, $m(T = 5\ K)$ = 8.6 mrad/T, and because of the linear dependence with the Faraday rotation, the magnetization is also linear with respect to B_{app}, so in the saturation,

$$M = \frac{M^{SAT}}{B^{SAT}} B_{app}, \tag{4.4}$$

where $\frac{M^{SAT}}{B^{SAT}}$ is the slope of the M vs B_{app} curve at T= 5 K as described in [28], with $M^{SAT} = n_{Eu}\mu_{Eu} = 9.03 \times 10^5$ A/m as the saturation magnetization, where $n_{Eu} = 4/a^3$ is the concentration of Eu atoms in the FCC lattice with parameter a = 6.6 Å, $\mu_{Eu} = g\mu_B S$

is the magnetic moment of an Eu^{2+} atom, $g = 2$ is the gyromagnetic factor, μ_B is the Bohr magneton, and $B^{SAT} = 8.3$ T is the saturation field in the Faraday geometry [28]. Hence, the Verdet constant, for the probe wavelength λ =665 nm, can be found from the saturation at T= 5 K as

$$\theta_F^{SAT} = V M^{SAT} d_{sample} = m(T = 5K) B^{SAT}. \tag{4.5}$$

Then, we obtain,

$$V = \frac{B^{SAT} m(T = 5K)}{d_{sample} M^{SAT}} = 0.061 rad/A. \tag{4.6}$$

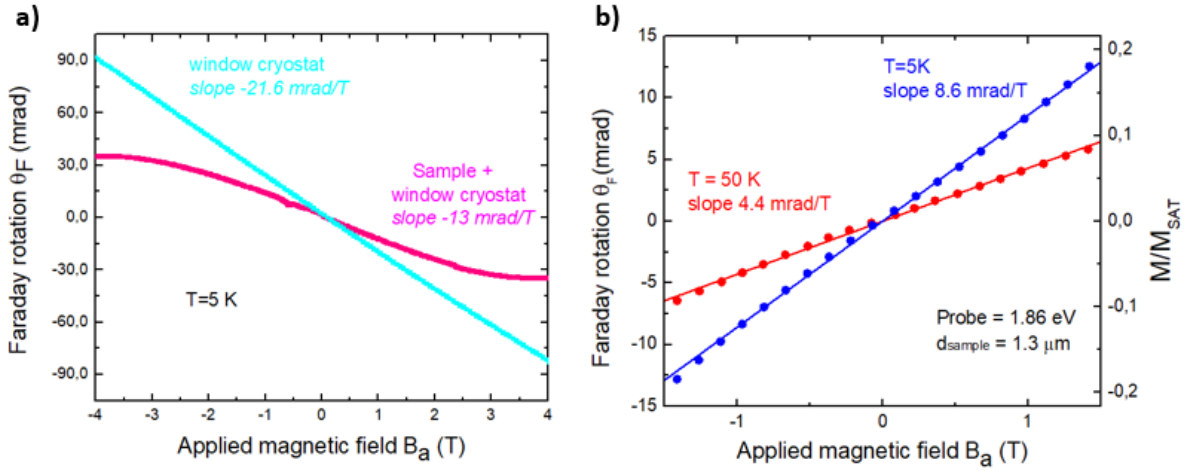

Figure 4.5: (a) Bulk Faraday rotation due to the window cryostat (lightblue) and total Faraday rotation due window cryostat and bulk EuTe sample (pink). (b) DC Faraday rotation due to the bulk EuTe sample as a function of the applied magnetic field at T = 5 K and T = 50 K.

Being determined by the electronic energy structure, the Verdet constant will remain approximately constant as a function of temperature and magnetic field, as long as the electronic energy structure and the band gap are not modified. It is well known that the EuTe band gap changes when the lattice spins are strongly polarized, but this requires magnetic fields above 3 T at liquid helium temperatures [67], and proportionally larger fields at higher temperatures. Because the magnetic fields used here are low in comparison, we can safely assume that the Verdet constant is independent of temperature and magnetic field for all the experimental results presented here.

The value of the Verdet constant allow us to convert the Faraday rotation angle into magnetization. To determine the internal magnetic field, which is smaller than the applied one due to the *demagnetization field*, we use the relation between the demagnetization field and the magnetization $B_{demag} = \mu_0 M$ in the Faraday geometry [73] used within the

epitaxial layer. Hence, the local (internal) magnetic field will be given by,

$$B_{int} = B_{app} - \mu_0 M. \tag{4.7}$$

Substituting M from Eq. 4.2, and using $\theta_F = m(T)B_{app}$, where $m(T)$ is the slope of the Faraday rotation angle as a function of B_{app} at the temperature T, we obtain,

$$B_{int} = B_{app} - \mu_0 \frac{\theta_F}{d_{sample} V} \quad = \quad B_{app} - \mu_0 \frac{m(T) B_{app}}{d_{sample} V}. \tag{4.8}$$

Then, the ratio $\dfrac{B_{int}}{B_{app}}$ will be given by,

$$\frac{B_{int}}{B_{app}} = 1 - \mu_0 \frac{m(T)}{d_{sample} V}. \tag{4.9}$$

The ratio B_{int}/B_{app}, calculated by using equation 4.9, is plotted in figure 4.6(b) as a function of the temperature. The sharp downfall of the $\dfrac{B_{int}}{B_{app}}$ ratio in the vicinity of 10 K is because EuTe is an antiferromagnet, and its temperature-dependent magnetic susceptibility shows the characteristic cusp at the Néel temperature (see, for instance, Ref. [74]). Therefore, according to Eq. 4.7, the absolute value of the internal field B_{int} is expected to show a corresponding downward cusp at the Néel temperature, as indeed observed in Fig. 4.6 (b).

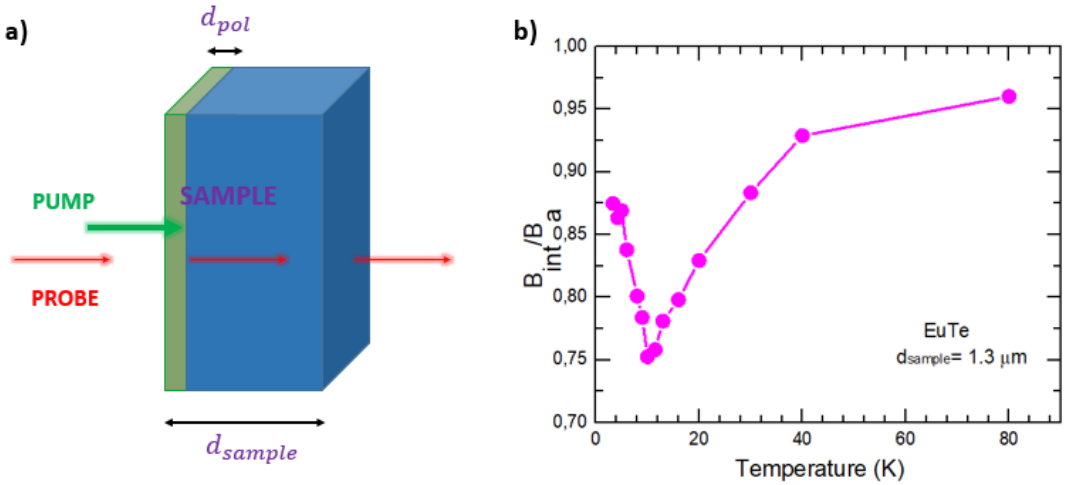

Figure 4.6: (a) Pump penetration depth d_{pol} and sample thickness d_{sample}. (b) Relation between the applied magnetic field and the internal magnetic field in Faraday geometry for a thin film EuTe sample.

By using the results of the preceding preliminary analysis, we can convert the measured **photo-induced** Faraday rotation, as a function of applied magnetic field B_{app} into photo-

induced magnetization as a function of the internal magnetic field B_{int}. Figure 4.7 shows the photo-induced Faraday rotation signal (PFR) at T= 5 K as a function of the internal field for a pump intensity of 10 mW/cm^2. The photo-induced Faraday rotation angle was converted into magnetization by using the Verdet constant determined before and assuming that the thickness d_{pol} of the layer where magnetic polarons are photo-generated is equal to the pump-light penetration depth i.e., $d_{pol} = \frac{1}{\alpha}$, where $\alpha = 10\ \mu m^{-1}$ is the absorption coefficient at the pump wavelength [67]. The photo-induced magnetization scale obtained in this way is shown on the right-hand side of Fig. 4.7.

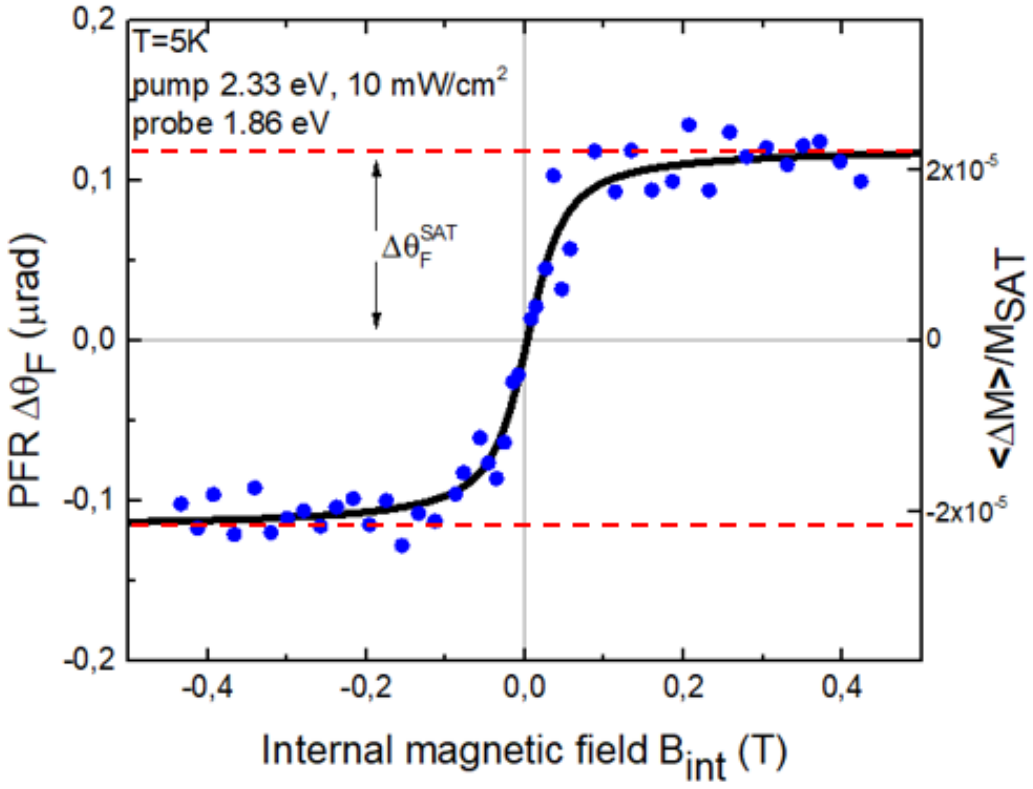

Figure 4.7: Photo-induced Faraday rotation (PFR) signal as a function of the internal magnetic field at $T = 5\ K$.

The photo-induced Faraday rotation signal shown in Fig. 4.7 has all the characteristics expected for an ensemble of photo-excited polarons. First, the signal shows a resonance when the energy of the pump photons meets the EuTe band gap [67]. Second, the signal is zero at $B = 0$ T, because at $B = 0$ T there is no preferential direction in space, therefore photo-excited magnetic polarons will point randomly, and the net magnetic moment of the sample will remain zero. Third, the photo-induced signal tends to saturate rapidly when a magnetic field is applied, exactly as expected for magnetic polarons with large magnetic moment of several hundreds of Bohr magnetons.

4.2.2 Calculation of the quantum efficiency of the polaron generation

Assuming that the photo-excited polarons do not diffuse, the saturation value of the photo-induced Faraday rotation seen in Fig. 4.7, $\Delta\theta_F^{SAT} = 0.12$ μ rad, can be converted to the *average* photo-induced saturation magnetization (due all the magnetic moments of the polaron) as

$$\langle \Delta M \rangle^{SAT} = \frac{\Delta\theta_F^{SAT}}{d_{pol} V} = 2.2 \times 10^{-5} M^{SAT}, \tag{4.10}$$

where $d_{pol} = 1/\alpha$, with $\alpha = 10$ μm^{-1}. This value can be compared with the theoretical value expected for photo-induced polarons in saturation,

$$\langle \Delta M \rangle^{SAT} = n_{pol} \ \ \mu_{pol}, \tag{4.11}$$

where $\mu_{pol} \sim 610$ μ_B is the magnetic moment of a polaron at T= 5 K [39], and n_{pol} is the steady-state population of magnetic polarons when the sample is illuminated with pump intensity p. The inertial effective mass of a magnetic polaron has been predicted to increase exponentially with the ratio of the polaron radius and the lattice parameter, R_{pol}/a [71]. Because in our case this ratio is quite large, $R_{pol}/a \sim 4$ [41], we expect the photo-induced magnetic polarons to be quite heavy and immobile, and they, therefore, remain in the layer penetrated by the pump light (d_{pol}). In this case, the steady-state polaron population will be given by kinetics equation for the polaron generation,

$$\frac{dn_p}{dt} = G - \frac{n_p}{\tau_0}, \tag{4.12}$$

where G is the polaron average generation rate per unit volume within the light penetration depth $1/\alpha$, n_p is the is the polaron density at time t and τ_0 is the polaron lifetime.

Then, in the stationary case, we have

$$\frac{dn_p}{dt} = 0 \quad \Rightarrow \quad n_p = n_{pol} = G\tau_0. \tag{4.13}$$

In this condition, when the material is illuminated until saturation, we can calculate G taking into account the quantum efficiency, χ, of polaron generation which is defined as

$$\chi = \frac{\text{Number of created polarons}}{\text{Number of incident photons}}. \tag{4.14}$$

We consider the absorbed incident energy per unit of time and volume,

$$E = \frac{pA}{Ad_{pol}}, \tag{4.15}$$

where p is the intensity of the pump beam incident on the surface of the sample and A is the cross-section area of the sample. Thus, the rate of polaron generation per unit of time and per unit of the volume is given by

$$G = \chi \frac{\text{Energy per unit of time and volume}}{\text{Energy of one photon}} \quad [m^{-3}]. \tag{4.16}$$

Replacing the values for the energy per unit of time and volume and the energy of one photon $h\nu$, we have

$$G = \chi \frac{\frac{\alpha p A}{A}}{h\nu} \quad \Rightarrow \quad G = \chi \frac{p\alpha}{h\nu}. \tag{4.17}$$

Here, $\tau_0 = 15\ \mu s$ is the polaron lifetime at $T = 5$ K which was obtained in Ref. [46]. All parameters determining $\langle \Delta M \rangle^{SAT}(p,T) = n_{pol}(p,T)\mu_{pol}(T) = G(p)\tau_0(T)\mu_{pol}(T)$ are known, except for the quantum efficiency, so comparing Eqs. 4.10 and 4.11, we obtain the relation:

$$\langle \Delta M \rangle^{SAT} = 2.2\ 10^{-5} M^{SAT} \quad = \quad n_{pol}(p)\ \mu_{pol}(T) = G(p)\ \tau_0(T)\ \mu_{pol}(T). \tag{4.18}$$

From this equality, we can obtain the quantum efficiency at $T = 5$ K, yielding $\chi \sim 0.09$. This result is very reasonable and can be taken as further evidence that photo-induced magnetic polarons are the source of the photo-induced Faraday rotation signal observed.

Again by using equation 4.17 and relying on the deduced quantum efficiency, the steady-state polaron population for $p = 10$ mW/cm^2 is found to be $n_{pol} = 3.6 \times 10^{15}$ cm^{-3}. Therefore, the average distance between polarons is estimated to be $d = 2(\frac{3}{4\pi n_{pol}})^{1/3} \sim 120\ a_{EuTe}$ where, a_{EuTe}, is the EuTe lattice parameter. Taking into account that the radius of a polaron is $R_{pol} \sim 4\ a_{EuTe}$, then the distance between polarons is two orders of magnitude greater than the polaron radius, hence it can be assumed that *polarons are non-interacting.*

4.2.3 Photo-induced magnetic polarons as a function of the pump intensity

With the established photo-induced Faraday rotation signal due to optically generated and non interacting magnetic polarons with magnetic moment equals several hundreds of Bohr magnetons, we can conjecture that the magnetization of a magnetic polaron ensemble will *obey a Langevin function*, which describes a paramagnetic system in the classical limit. In this hypothesis, the magnetization associated with a photo-induced magnetic polaron ensemble will be given by

$$\langle \Delta M(B,T) \rangle = n_{pol}\ \mu_{pol}\ L(x), \tag{4.19}$$

where the Langevin function is given by

$$L(x) = coth(x) - \frac{1}{x} \quad with \quad x = \frac{\mu_{pol} B}{k_B T}, \tag{4.20}$$

where k_B is the Boltzmann constant. Notice that, below the Néel temperature, the magnetic moment of the polaron is known from photoluminescence studies to be 610 μ_B [39][41], hence in that temperature range there are no free parameters in Eq. 4.19. Nevertheless, to test the validity of our Langevin conjecture, we have fitted the photo-induced magnetization data taken at $T = 5$ K with Eq. 4.19, whereby the polaron magnetic moment is the *sole* adjustable parameter. The fitted curve is depicted by the solid line in Fig. 4.7, yielding $\mu_{pol} \sim 600\ \mu_B$. This coincides almost exactly with the known value, which demonstrates that the magnetization of the photo-induced magnetic polaron ensemble indeed follows a Langevin function.

Next, we investigate the possibility of generating a higher population of photo-induced polarons by increasing the pump intensity. Figure 4.8 (a) shows the dependence of the PFR as a function of pump intensity for $T = 5$ K. As the pump intensity is increased, a linear background appears, whose slope is proportional to the pump intensity, suggesting a *heating effect*.

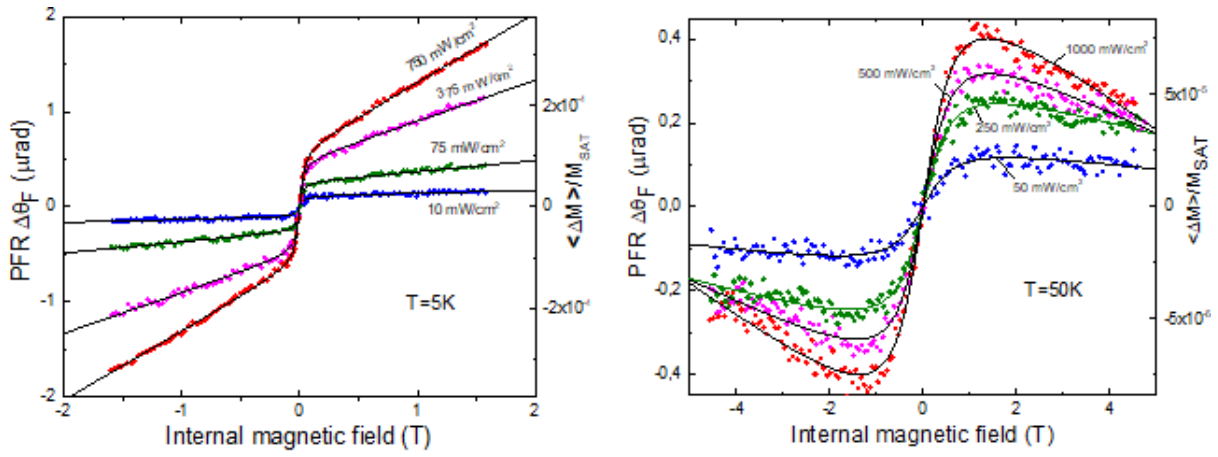

Figure 4.8: Photo-induced Faraday rotation vs the internal magnetic field for different pump intensities at $T = 5$ K (a) and at $T = 50$ K (b).

In order to take into account the heating effect in the Faraday rotation, we analyze the effect of a variation of the bulk temperature on the magnetization *M(T,B)*.

A temperature increase of the bulk by ΔT^{Bulk} *will cause a change in its magnetization* given by

$$\Delta M(B,T) = \left.\frac{\partial M}{\partial T}\right|_B \Delta T^{Bulk}. \tag{4.21}$$

Here $\Delta M(B,T) = \Delta M$ represents the change in magnetization due to sample heating

produced by the pump-beam within the penetration depth $d_{pol} = 1/\alpha$. From PFR, this change in magnetization can be written following from Eq. 4.2 as

$$\Delta M(B,T) = \frac{\Delta\theta_F}{V d_{pol}}, \tag{4.22}$$

where the experimental $\Delta\theta_F$ includes the contribution of the polaron and thermal effect. At sufficiently large magnetic fields, when the polaron magnetization is saturated, only a thermal effect can contribute to the slope of ΔM.

Similarly, $\left.\frac{\partial M}{\partial T}\right|_B$ is also related to the bulk Faraday rotation,

$$\left.\frac{\partial M}{\partial T}\right|_B = \frac{1}{V d_{sample}} \left.\frac{\partial\theta_F}{\partial T}\right|_B. \tag{4.23}$$

Therefore, substituting Eqs. 4.23 and 4.22 in Eq. 4.21, and resolving for ΔT^{Bulk}, we get

$$\frac{\Delta\theta_F}{V d_{pol}} = \frac{1}{V d_{sample}} \left.\frac{\partial\theta_F}{\partial T}\right|_B \Delta T^{Bulk} \quad \Rightarrow \quad \Delta T^{Bulk} = \frac{d_{sample}}{d_{pol}} \frac{\Delta\theta_F}{\left.\frac{\partial\theta_F}{\partial T}\right|_B}, \tag{4.24}$$

with the linear dependence

$$\Delta\theta_F = m(p)B \qquad and \qquad \left.\frac{\partial\theta_F}{\partial T}\right|_B = n(T)B, \tag{4.25}$$

where *m(p)* and *n(T)* are the slopes of the curves $\Delta\theta_F$ vs B and $\left.\frac{\partial\theta_F}{\partial T}\right|_B$ vs B, respectively. Then, we can finally write the equation for ΔT^{Bulk} as,

$$\Delta T^{Bulk} = \frac{d_{sample}}{d_{pol}} \frac{m(p)}{n(T)} \tag{4.26}$$

The slope of $\frac{\partial\theta_F}{\partial T}$ was taken from Fig. 4.9 (a), and the slope of θ_F was taken from the high-field limit in Figs. 4.8 (a) and 4.8 (b). Then, the temperature increase ΔT^{Bulk} calculated from Eq. 4.26 is shown as a function of the pump intensity in Fig. 4.9(c).

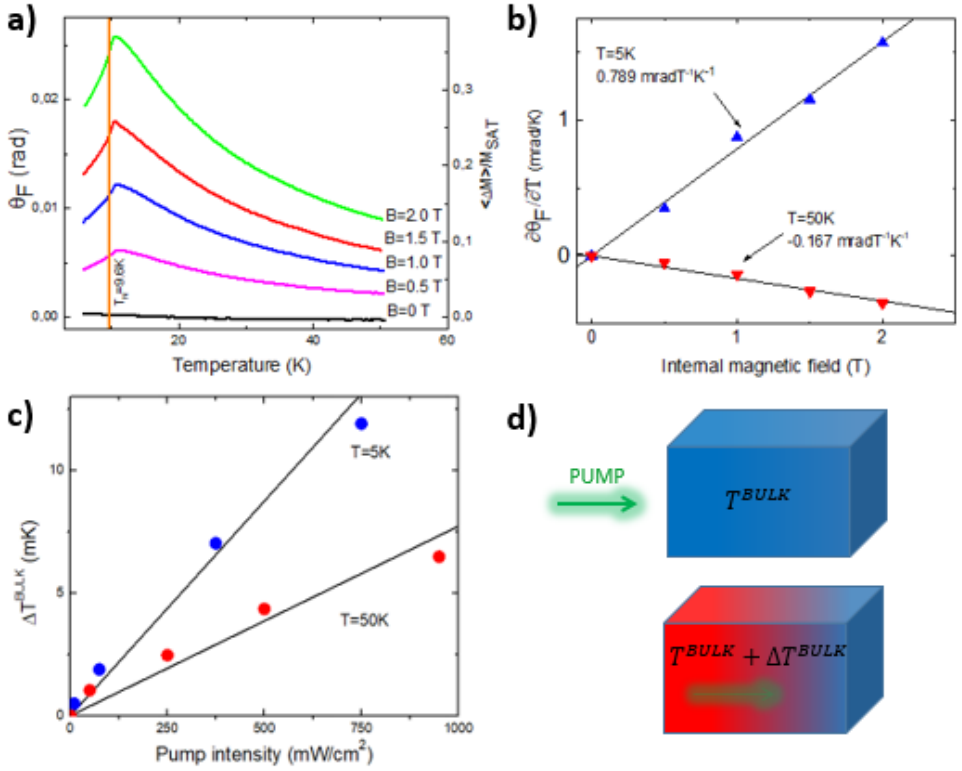

Figure 4.9: (a) Faraday rotation due the bulk EuTe sample as a function of temperature for various magnetic fields. (Notice that for our sample the observed Néel temperature is slightly larger than the accepted value of 9.6 K for EuTe, in agreement with direct measurements reported in Ref. [69]). (b) The dependence of $\dfrac{\partial\theta_F}{\partial T}$ on B shows a linear behaviour. (c) The deduced temperature modulation of the illuminated region is shown as a function of the pump intensity for $T = 5$ K and $T = 50$ K.

The interpretation in terms of a heating effect is confirmed by the photo-induced Faraday rotation curves as a function of intensity, done at T= 50 K [Fig. 4.8(b)]. Because for EuTe, the Faraday rotation dependence has the typical behavior of an antiferromagnet, with a maximum at the Néel temperature [see Fig. 4.9 (a)], the slope of the thermal background seen in the PFR signal should change from positive to negative when we cross the Néel temperature. This is exactly what we observe, as can be seen from Fig. 4.8(a) for $T = 5$ K, where the thermal background has a positive slope, and Fig. 4.8(c) for $T = 50$ K, where the slope of the background signal is negative. The temperature modulation at $T = 50$ K was found by using Eq. 4.26, and it is also shown in Fig. 4.9(b). At $T = 50$ K the heating effect is smaller than at $T = 5$ K due to a larger heat capacity of the EuTe crystal [75].

Another aspect worthy of comment is that, upon closer inspection of Fig. 4.9(c), the temperature modulation ΔT presents a slightly sub-linear dependence on pump intensity. This can be attributed to the fact that, for a larger excitation power, the effective volume excited by light increases, because the threshold excitation light penetrates deeper into

the sample. In this case, the temperature increase for doubled excitation power will obviously be less than doubled, which explains the sub-linear behavior of ΔT on the excitation power.

Having subtracted the linear thermal background from the $\Delta\theta_F$ vs B curves, as deduced above, the saturation polaron magnetization $\Delta\theta_F^{SAT}$ for every pump intensity was extracted and it is plotted in Fig. 4.11. $\Delta\theta_F^{SAT}$ increases sub-linearly with pump intensity, indicating that polarons are less and less efficiently generated when the pump intensity is increased.

Taking into account that optical absorption leads to an exponentially decreasing of the incident pump intensity p_0 below the surface of the sample, then, the pump intensity at the depth x can be written as:

$$p(x) = p_0 e^{-\alpha x}. \tag{4.27}$$

Then, the intensity retained in a layer of width dx of the sample is given by

$$dp(x) = \alpha p_0 e^{-\alpha x} dx. \tag{4.28}$$

Therefore, the number of polarons created in a volume of cross section A and depth x is given by

$$\overline{G}(x) = \frac{\text{Number of polarons created in } Adx}{Adx} = \frac{\chi \dfrac{Adp(x)}{h\nu}}{Adx}, \tag{4.29}$$

which can be written as

$$\overline{G}(x) = \frac{\chi \alpha p_0 e^{-\alpha x}}{h\nu}. \tag{4.30}$$

However, this value is limited to a *maximum value of photo-generated polarons* that we represent by n_D. Then, in the stationary case when the number of photo-generated polarons n_p is below the saturation case, we have

$$\frac{dn_p(x)}{dt} = \overline{G}(x) - \frac{n_p(x)}{\tau_0} = 0 \quad \Rightarrow \quad n_{pol} = \overline{G}(x)\tau_0. \tag{4.31}$$

In this situation, the concentration of photo-generated polarons at a depth x below the surface will be given by,

$$n_{pol}(x) = \chi \frac{\alpha p_0 e^{-\alpha x}}{h\nu} \tau_0. \tag{4.32}$$

Here we can observe that in the saturation case, which we define happening at depth x_0 when $n_{pol} = n_D$. Then, if we use Eq. 4.32, we can write

$$n_D = \chi \frac{\alpha p_0 e^{-\alpha x_0}}{h\nu} \tau_0 \quad \Rightarrow \quad x_0 = \frac{1}{\alpha} \ln\left(\frac{\chi \alpha p_0 \tau_0}{n_D h\nu}\right). \tag{4.33}$$

If we define $\frac{n_D h\nu}{\chi\alpha\tau_0} = p_D$, we note that this is the minimum intensity necessary to produce a polaron generation saturation in the sample. Hence, we can use this to identify the saturation depth x_0 as

$$x_0 = \frac{1}{\alpha}\ln(\frac{p_0}{p_D}) \begin{cases} x_0 < 0, & if \quad p_0 < p_D \quad \text{Saturation does not exist at any point} \\ x_0 > 0, & if \quad p_0 > p_D \quad \text{Sample presents saturation until } x = x_0 \end{cases} . \tag{4.34}$$

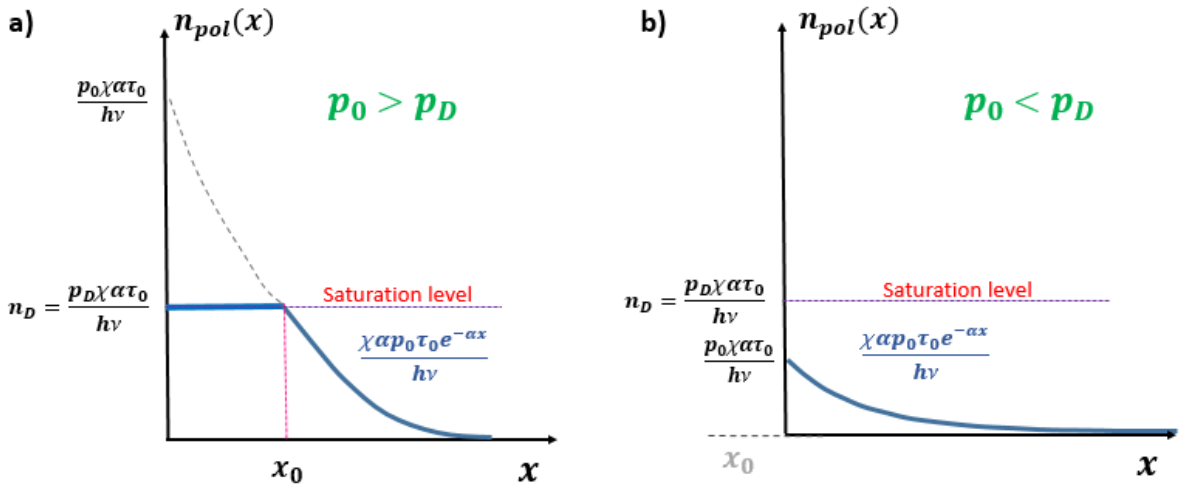

Figure 4.10: (a) Saturation level is obtained until depth x_0 when the pump p_0 is higher than the critical value p_D. (b) For pump intensity lower than the critical intensity, then no saturation is obtained at any depth in the sample.

Then, we can calculate the total number of photo-generated polarons in the sample

$$N_{pol} = \int_0^\infty n_p(x) A dx. \tag{4.35}$$

To obtain N_{pol} we again separate the two different cases, when the intensity of the pump light is higher or lower than the critical intensity p_D,

$$N_{pol} = \int_0^\infty n_{pol}(x) A dx = \begin{cases} \int_0^\infty \chi \frac{\alpha p_0 e^{-\alpha x_0}}{h\nu} \tau_0 A dx, & if \quad p < p_D \\ \int_0^{x_0} n_D A dx + \int_{x_0}^\infty \chi \frac{\alpha p_0 e^{-\alpha x_0}}{h\nu} \tau_0 A dx, & if \quad p > p_D \end{cases} . \tag{4.36}$$

The results of these integrals are summarized in the next equation, where we also take into account that the photo-induced Faraday rotation is proportional to the number of

photo-excited polarons in the sample, and then we can write,

$$\Delta\theta_F^{SAT} \sim \int_0^\infty n_{pol}(x)Adx = \begin{cases} \frac{n_D}{\alpha}\frac{p}{p_D}, & if \quad p_0 < p_D \\ \frac{n_D}{\alpha}(1+ln\frac{p}{p_D}), & if \quad p_0 > p_D \end{cases}, \tag{4.37}$$

where $p_D = \frac{n_D h\nu}{\chi\alpha\tau_0}$. Equation 4.37 gives a photo-induced Faraday rotation angle that increases linearly with pump intensity for $p < p_D$ and logarithmically for $p > p_D$. Figure 4.11 shows that Eq. 4.37 provides a very good fit of our data, whereby n_D is the single adjustable parameter, yielding $n_D = 4.5 \times 10^{15}$ cm^{-3}. This is again far less than the concentration of polarons that would completely fill the excited layer, $(\frac{4}{3}\pi R_{pol}^3)^{-1} = 1.3 \times 10^{19}$ cm^{-3}. We attribute the limited concentration of polarons that can be photo-generated to their binding by residual defects of concentration n_D.

For T= 5 K, we can calculate the critical intensity p_D and the saturation depth x_0 for p_0= 10 mW/cm^2,

$$\begin{aligned} p_D &= \frac{n_D h\nu}{\chi\alpha\tau_0} = \frac{4.5\times10^{15}[cm^{-3}]\ \ 3.73\times10^{-19}[J]}{0.09\times10^{7}[m^{-1}]\ \ 15\times10^{-6}[s^{-1}]} = 12.5\ \ \text{mW/cm}^2 \\ \Rightarrow \quad x_0 &= d_{pol}\ln(\frac{p_0}{p_D}) = 10^{-7}[m]\ln\left(\frac{10[mW/cm^2]}{12.5[mW/cm^2]}\right) = -0.02\ \ \mu\text{m}. \end{aligned} \tag{4.38}$$

This is a negative value because it does not exist a depth for saturation for this intensity which is below the saturation intensity.

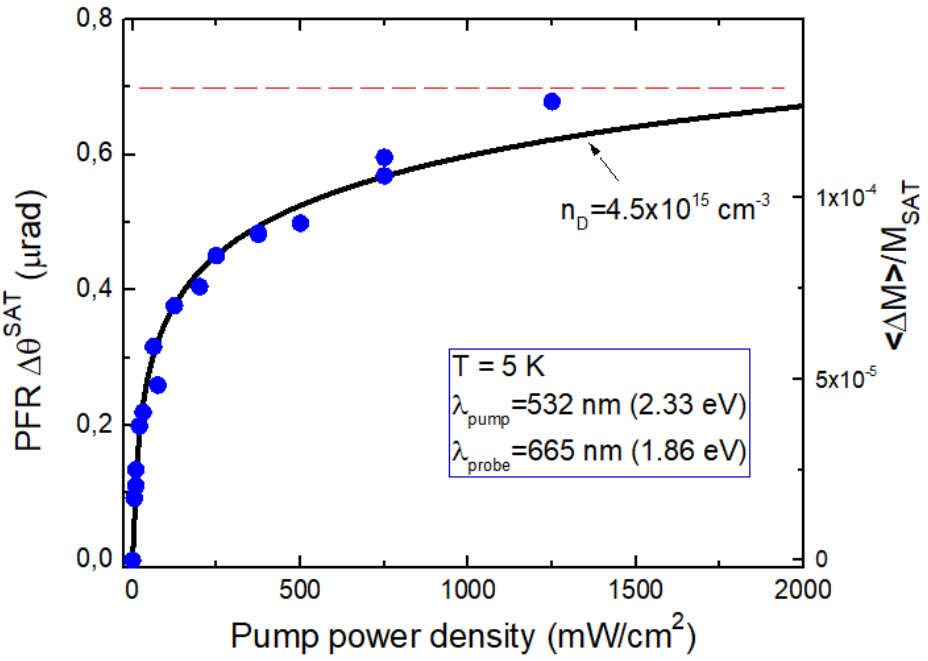

Figure 4.11: Dots show the photo-induced Faraday rotation angle at saturation as a function of the pump intensity. The full line shows a fit of the dots with Eq. 4.37, which yields the maximum polaron concentration to be $n_D = 4.5 \times 10^{15}$ cm^{-3}.

At $T = 5$ K, these bound polarons are long-lived with lifetime is 15 μs [46] and therefore have a supremacy over magnetic polarons seen in the photoluminescence, which have a much shorter lifetime, of the order of a nanosecond [57]. The shorter lifetime implies a stationary concentration of magnetic polarons that is four orders of magnitude smaller, and effectively only the long-lived magnetic polarons will be observed in the photo-induced Faraday rotation. A plausible source of defects at a low concentration of the order of 10^{15} cm^{-3} is the unbalanced stoichiometry of the Eu and Te atomic fluxes during the MBE growth. It should be observed that the binding of polarons to defects provides further support for our previous assumption that photo-excited polarons remain localized in the penetration layer of the pump light and do not diffuse into the interior of the EuTe crystal.

4.2.4 Photo-induced magnetic polarons as a function of the temperature

In this part, we studied how the magnetic polarons are affected by temperature.

From equation 4.19, the equation for the PFR can be rewritten as,

$$\Delta\theta_F(B,T) = \Delta\theta_F^{SAT}(T)\ \ L(\frac{\mu_{pol}B}{k_BT}), \tag{4.39}$$

where $\Delta\theta_F(B,T)$ is the photo-induced Faraday rotation at a magnetic field B and at temperature T, and $\Delta\theta_F^{SAT}(T)$ is the corresponding saturation value, depicted in Fig. 4.7. Then, the PFR as a function of the magnetic field was measured for various temperatures and it was fitted using Eq. 4.39, yielding two parameters for each temperature: the magnetic moment of the photo-induced magnetic polaron, $\mu_{pol}(T)$, and the Faraday rotation saturation $\Delta\theta_F^{SAT}(T)$ (see Fig. 4.7). It is worth pointing out that the polaron magnetic moment is the only parameter defining the smoothness of the step, so the value for μ_{pol} obtained from the fit is independent of any other parameter entering Eq. 4.39, such as the polaron lifetime and steady-state population, which depend on temperature.

We can consider the polaron magnetic moment dependence with temperature by relaying on another formalism. The polaron magnetic moment can be given by the average magnetization inside the polaron multiplied by the polaron volume as is shown in Fig 4.12

$$\mu_{pol} = \frac{4}{3}\pi R_{pol}^3 \langle M \rangle, \tag{4.40}$$

where $\langle M \rangle$ is the average EuTe magnetization within the magnetic polaron sphere under the action of the exchange field of the photo-excited electron, $B_{xf} \sim 1$ T [33][41], which we can approximate as

$$\langle M \rangle = n_{Eu}\ \mu_{Eu}\ \beta_S(B_{xf}, T), \tag{4.41}$$

where β_S is the Brillouin function. The magnetization outside the polaron is zero.

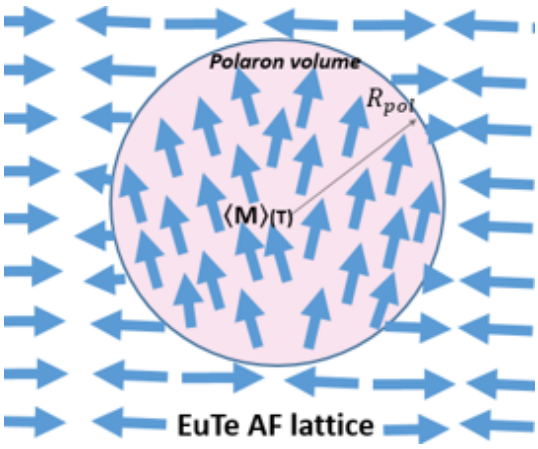

Figure 4.12: Antiferromagnetic spins inside and outside the magnetic polaron in EuTe.

In the high temperature condition $\beta_S(x) \sim \frac{S+1}{3S}x$. We also consider the antiferromagnetic system for $T > T_N$, in this situation we have the separate magnetization for each sublattice

$$\langle M_A \rangle = n_{Eu}\ \mu_{Eu} \frac{S+1}{S} \frac{g\mu_B S}{k_B T}(B_{xf} - \lambda\langle M_B \rangle). \tag{4.42}$$

and

$$\langle M_B \rangle = n_{Eu}\ \mu_{Eu} \frac{S+1}{S} \frac{g\mu_B S}{k_B T}(B_{xf} - \lambda \langle M_A \rangle). \tag{4.43}$$

We know the total magnetization is $\langle M_A \rangle + \langle M_B \rangle = \langle M \rangle$. Thus, a Curie-Weiss approximation [73] can be obtained

$$\langle M \rangle = n_{Eu}\ \mu_{Eu} \frac{g\mu_B(S+1)}{3k_B} \frac{B_{xf}}{T+T_N}. \tag{4.44}$$

Figure 4.13 shows the polaron magnetic moment as a function of temperature so obtained.

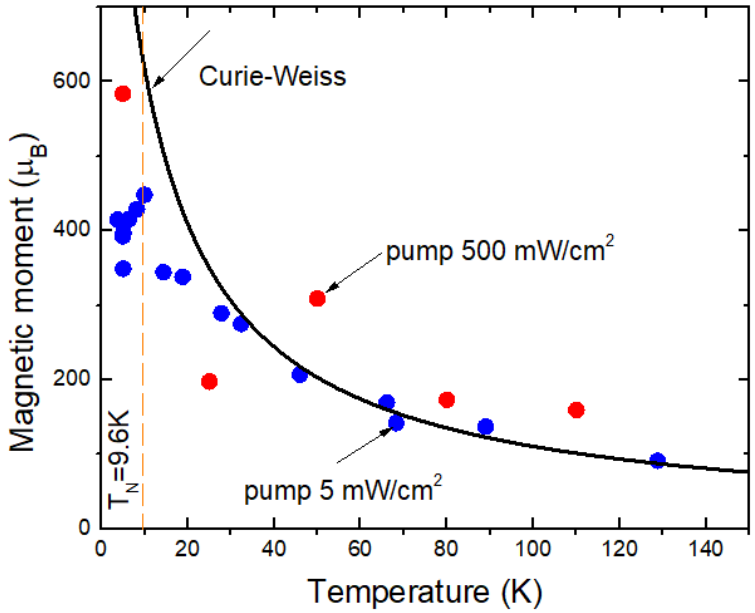

Figure 4.13: Temperature dependence of the magnetic moment of a polaron. For comparison, the dashed line is given by the magnetic moment associated with the polaron sphere obtained by using Eq. 4.40.

It can be seen that the Curie-Weiss law describes the data quite well, without any adjustable parameter.

Finally, Fig. 4.14 shows a plot of the photo-induced Faraday rotation saturation, $\Delta\theta_F^{SAT}(T)$ as a function of temperature, obtained from the fit of the experimental PFR and the theoretical values estimated by considering the proportionality between the Faraday rotation in saturation and the polaron population in steady-state given by

$$\frac{dn_p}{dt} = G - \frac{n_p}{\tau_0} - \frac{n_p}{\tau'} = 0, \tag{4.45}$$

where is considered now the recombination due to thermal effects with recombination time τ' and we consider $\tau' = \tau_0 e^{-E_A/k_B T}$ which gives

$$\Delta\theta_F^{SAT}(T) \sim const \times e^{E_A/k_B T} \tag{4.46}$$

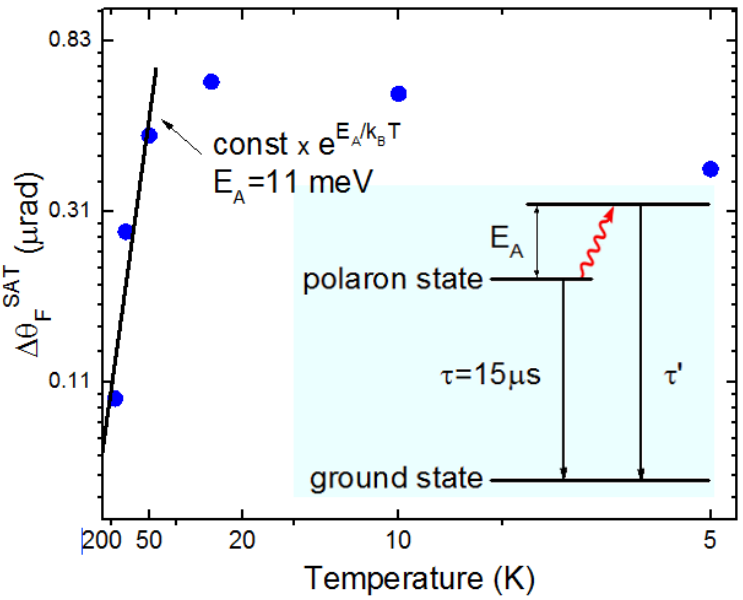

Figure 4.14: Temperature dependence of the photo-induced Faraday rotation angle at saturation. Above $T \sim 100$ K, $\Delta\theta_F^{SAT}$ decreases exponentially with a characteristic activation energy of $E_A = 11$ meV. The inset shows schematically the magnetic polaron energy level, the ground state (when the photo-excited electron is absent), and the thermally activated state, which drains the polaron population when the temperature of the sample is increased.

Above $T = 100$ K, the photo-induced Faraday rotation decreases exponentially with an activation energy of about 11 meV. The rapid decrease of the photo-induced Faraday rotation signal is interpreted in terms of the thermal activation of a fast recombination channel, which causes a reduction of the polaron lifetime and hence of the steady-state polaron population. The thermally activated magnetic polaron quenching process is illustrated by the energy-level scheme shown in the inset of Fig. 4.14.

4.2.5 Conclusions

1. In conclusion, we have shown that EuTe can be magnetized by light through optical generation of magnetic polarons, with a quantum efficiency of $\chi \sim 0.09$ and a maximum concentration, which is about 4.5×10^{15} cm^{-3} in the case of the sample studied in this work. Such a low concentration is evidence that the magnetic polarons are bound to defects, plausibly generated during the growth process due to a deviation from stoichiometry. We believe that photo-generated polarons remain in the light-penetration depth layer, and do not diffuse into the interior of the crystal. A path to clarify this point would be to investigate samples with an intentional deviation from stoichiometry and check if the deviation correlates with the maximum polaron concentration. At low temperatures, the polarons are immobile and do not diffuse out of the illuminated volume. The polaron population can be thermally quenched, with an activation energy of 11 meV, which could be due to thermally activated recombination, or to polaron diffusion out of the path of the probe beam. Thus, we demonstrated a novel approach for the optical manipulation of magnetic states in EuTe, which in principle should be valid for any intrinsic magnetic semiconductor, as well as for diluted semiconductors and for hybrid ferromagnetic-semiconductor structures.

2. The results shown here for EuTe should remain valid for all europium chalcogenides as EuSe and as well as for other magnetic semiconductors with a large band-lattice exchange interaction. The magnetic polaron ensemble forms a paramagnet that is fully controlled by light within a host that has ideal optical quality.

4.3 Conversion of Faraday rotation into magnetization in europium chalcogenides

4.3.1 Faraday rotation basics

A linearly polarized wave along the X-axis can be described by:

$$\boldsymbol{E} = E_0 \cos(kz - \omega t)\hat{\boldsymbol{x}}. \tag{4.47}$$

This linearly polarized light beam can be expressed as the superposition of two rays of equal intensity, one of which is circularly polarized according to the right-hand rule (RCP), and the other according to left-hand one (LCP):

$$\boldsymbol{E} = \frac{1}{2}\boldsymbol{E_{RCP}} + \frac{1}{2}\boldsymbol{E_{LCP}}, \tag{4.48}$$

where

$$\boldsymbol{E_{RCP}} = E_0 \cos(kz - \omega t)\hat{\boldsymbol{x}} - E_0 \sin(kz - \omega t)\hat{\boldsymbol{y}} \tag{4.49}$$

and

$$\boldsymbol{E_{LCP}} = E_0 \cos(kz - \omega t)\hat{\boldsymbol{x}} + E_0 \sin(kz - \omega t)\hat{\boldsymbol{y}}. \tag{4.50}$$

In general, the refractive index will be different for the RHC and the LCP in a birefringent material, then we have $k \to k_\pm = \dfrac{\omega n_\pm}{c}$, where $n_\pm$ is the refractive index, and the plus or minus sign applies to RCP or LCP, respectively, and we can write

$$\boldsymbol{E_{RCP}} = E_0 \cos(\frac{\omega n_+}{c}z - \omega t)\hat{\boldsymbol{x}} - E_0 \sin(\frac{\omega n_+}{c}z - \omega t)\hat{\mathbf{y}} \tag{4.51}$$

and

$$\boldsymbol{E_{LCP}} = E_0 \cos(\frac{\omega n_-}{c}z - \omega t)\hat{\mathbf{x}} + E_0 \sin(\frac{\omega n_-}{c}z - \omega t)\hat{\mathbf{y}}. \tag{4.52}$$

Thus, after traversing a distance z in the optical medium, and using the relation for the wave in the vacuum $\omega = kc = \dfrac{2\pi c}{\lambda}$, the travelling wave become

$$\boldsymbol{E} = E_0 \cos\left(\frac{(n_- + n_+)\pi}{2\lambda}z - \omega t\right)\left(\cos(\frac{(n_- - n_+)\pi}{\lambda}z)\hat{\boldsymbol{x}} + \sin(\frac{(n_- - n_+)\pi}{\lambda}z)\hat{\mathbf{y}}\right). \tag{4.53}$$

This beam is still linearly polarized, but the plane of polarization has been twisted by an angle θ_F, the FR angle, which per unit length and at the wavelength λ is given by

$$\theta_F = \frac{(n_- - n_+)\pi}{\lambda}. \tag{4.54}$$

This formula shows that circular birefringence, i.e. the inequality between n_+ and n_-, is the source of FR and is the origin for the classical model for the Faraday rotation which is shown in the Appendix B.1

In general, semiconductor materials will contain several valence bands contributing to the birefringence. Photons of energy within the band gap of the semiconductor are closest to resonance with the top valence band, hence the polarization effects of lower lying bands can be discarded in a first examination.

The amplitude of the circular polarization induced in the crystal by the rotating electric field of the incoming light in the X-Y plane, is given by,

$$P_0^{\pm} = N\alpha^{\pm}(\omega)E_0 \tag{4.55}$$

where $\alpha^{\pm}$ is the electronic polarizability of the atoms forming the valence band and is a measure of how easy it is to induce a moment in a material with an electric field. N is the number density of atoms in the solid, and E_0 is the electric field amplitude of the RCP or LCP incident wave. It should be emphasized that α is the polarizability of an atom embedded in the solid, it is not the polarizability of an isolated atom. These polarizabilities are different from one another because the polarization of atoms, by light within the bandgap, is a perturbation and resonance effect. The electron-photon interaction resonance depends on the spacing between electronic energy levels, which in the solid differ from that of the isolated atom, due to energy band formation, hence the polarizability of an embedded atom differs from that of an isolated one.

On the other hand, taking the photo-induced polarization to be the number density times the atomic polarizability, modified due to the atoms being embedded in the solid, as by (4.55), is known to provide a very good description of the linear optical properties of nonmetallic solids (see, for instance, Ref. [82], section 1.4, formula (1.4.16), which justifies the application of Eq. (4.55) to describe the Faraday effect in europium chalcogenides.

Using the relation connecting the refractive index to the electronic polarizability [80] and demonstrated in the Appendix section B.2,

$$n_{\pm}^2 = 1 + \frac{N}{\epsilon_0}\alpha^{\pm}(\omega), \tag{4.56}$$

we arrive at

$$n_- - n_+ = \frac{n_-^2 - n_+^2}{2n_0} = \frac{N}{\epsilon_0}\frac{(\alpha^-(\omega) - \alpha^+(\omega))}{2n_0}, \tag{4.57}$$

where $n_0 = \dfrac{(n_- + n_+)}{2}$ is the refractive index that the material would have, if no other valence band was present except the one under scrutiny, and $\epsilon_0 = 8.85 \times 10^{-12}$ F/m is the vacuum permittivity.

Equation 4.57 shows that for FR to be present, the induced polarization current in

the valence orbitals must be different for LCP and RCP. This is explored in the models below.

4.3.2 A semiclassical model connecting FR to the magnetization in europium chalcogenides

In EuX, the highest valence band states are formed by $4f$ orbitals of the Eu atom [78], which are buried deep within the ion, beneath the filled $5p$ shell, hence the characteristics of the isolated orbital are well preserved [83], therefore the spin of the Eu atom, S=7/2, is maintained in the crystal.

In the semiclassical approach, the magnetic moment, or spin, of an atom, is associated with a circulating electrical current, whose direction and magnitude are described by a vector $\boldsymbol{S}$. Let us inspect the interaction of the incident linearly polarized light with an *average* Eu atom in the solid, whose spin $\boldsymbol{S}$ makes an angle θ with the direction of light propagation, as is shown in figure 4.15.

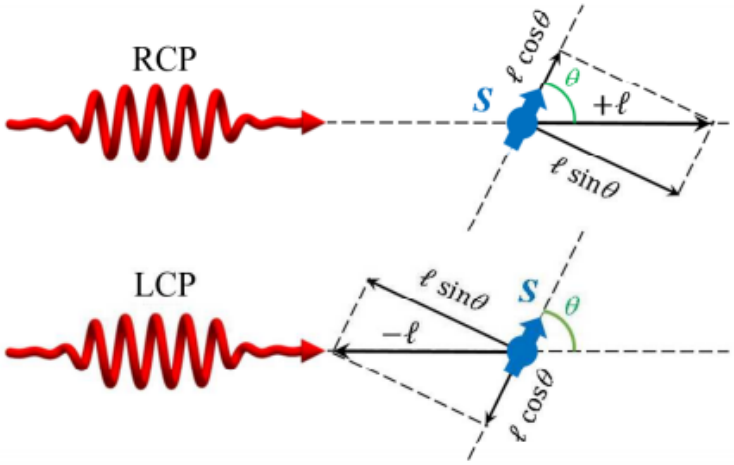

Figure 4.15: The electric field E of the linearly polarized light is equivalent to the superposition of RCP (top) and LCP light of equal amplitude (bottom), carrying an angular momentum of $+\ell$ and $-\ell$, respectively.

We express the incident light as a superposition of RCP and LCP, which carry an angular momentum $+\ell$ and -ℓ, respectively, along the direction of light path. The angular momentum vector of the incoming RCP or LCP light can be divided into two components, parallel and perpendicular to the vector $\boldsymbol{S}$, as shown in figure 4.15. By symmetry, in a direction perpendicular to $\boldsymbol{S}$, RCP and LCP will induce identical polarizations in magnitude, but in opposite directions, totaling zero. Therefore, birefringence must be associated with the circular polarization light induces parallel to $\boldsymbol{S}$, which is proportional to the projection of the light angular momenta onto $\boldsymbol{S}$. Hence, when the angle between

$\boldsymbol{S}$ and the direction of light travel is increased from zero to θ, the induced polarization is reduced by a factor of $\cos\theta$, i.e,

$$P^{\pm} = N\alpha_{\parallel}^{\pm} E_0 \cos\theta, \tag{4.58}$$

where $\alpha_{\parallel}^{\pm}$ is the circular electronic polarizability of the solid, when its spins are fully aligned with the direction of light travel ($\theta = 0$ in figure 4.15).

On the other hand, the magnetization projection in the direction of light propagation, M, is given by

$$M = N\mu^* \cos\theta \tag{4.59}$$

hence a comparison between equations 4.58 and 4.59 leads to

$$P^{\pm} = \frac{M}{\mu^*}\alpha_{\parallel}^{\pm} E_0. \tag{4.60}$$

Equating 4.60 and B.8 gives

$$\alpha^{\pm} = \frac{M}{M^{SAT}}\alpha_{\parallel}^{\pm} \tag{4.61}$$

where $M^{SAT} = N\mu^*$ is the saturation magnetization. Substituting 4.61 in 4.57, and using 4.54, we get,

$$\theta_F^{mag} = \frac{\pi N M}{\lambda\epsilon_0 M^{SAT}} \frac{\alpha_{\parallel}^{-} - \alpha_{\parallel}^{+}}{2n_0}. \tag{4.62}$$

Equation 4.62 shows that the contribution from Eu atoms to the FR is proportional to their magnetization, the proportionality coefficient being determined by the polarizability. Because the polarizability is determined by the electronic energy structure, the ratio θ_F/M will remain unchanged as long as the relative position of the electronic energy levels, as well as their occupation, is invariant. In a semiconductor, the essential parameter is the energy gap, E_g, between the valence and the conduction bands. If $k_BT \ll E_g$, the occupation of the electronic energy levels will be unchanged, which gives a measure of the range of temperatures in which θ_F/M is expected to be constant in EuX, except for deviations due to band gap variations. Thus θ_F/M behaves in the same fashion as the refractive index of dielectrics, which is also tied to variations of the band gap [84, 85]. As long as the photon energy is within the band gap, which is the situation considered in this work, contributions from other valence bands will generally be much smaller, due to their excitations being off-resonance with the incident photons, and the central result given by Eq. 4.62 will remain valid.

The significance and the value of the semiclassical model, with which the proportionality between FR and magnetization was demonstrated as expressed by Eq. 4.62, based on a simple argument of forced oscillations and symmetry, can be well appreciated if we compare our model to the full quantum mechanical calculation, described in detail in Ref. [79], which requires the use of perturbation theory, Wigner rotations of spins, and

statistical averaging. The end result is the same, but the semiclassical model is much simpler and transparent.

4.3.3 Test of the semiclassical model in the magnetic semiconductor EuSe

In the previous section it was argued that in EuX FR is proportional to the magnetization. In this section this hypothesis is thoroughly tested using the magnetic semiconductor EuSe. This material was chosen for the test because of its very rich magnetic phase diagram, therefore by applying a magnetic field and adjusting the temperature, the proportionality between FR and magnetization can be tested in all possible magnetic scenarios.

The EuSe crystalline samples were grown by molecular beam epitaxy (MBE) onto (111) BaF_2 substrate. Because of the almost perfect lattice constant matching (a = 6.1 Å and a = 6.6 Å for EuSe and BaF_2, respectively), the EuSe layer was bulklike and nearly unstrained [89]. The EuSe epilayer sample was a thickness of 2.5 μm. The magnetization was measured using a SQUID magnetometer, which had a magnetic moment resolution better than 10^{-11} Am^2 . The FR was measured using a linearly polarized beam from a semiconductor laser as the monochromatic light source, and a polarization bridge containing balanced photodetectors.

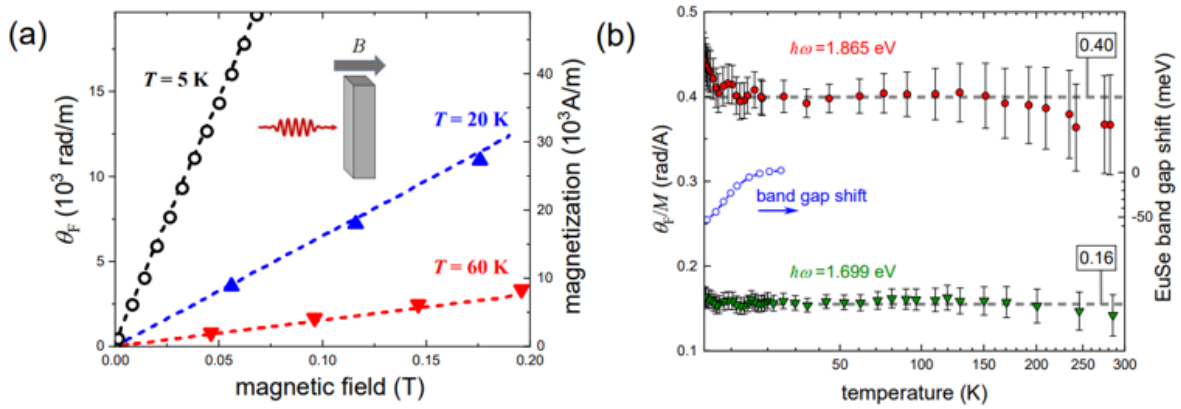

Figure 4.16: (a) Lines depict FR, for photons of energy 1.865 eV, while dots represent magnetization, as a function of applied magnetic field, for T = 5, 20 and 60 K. The magnetic field was applied perpendicular to the EuSe epitaxial layer. (b) Ratio θ_F/M as a function of temperature for photons with energy 1.865 eV (full circles) and 1.699 eV (triangles). The error bars were estimated at 15 percent at low temperatures but increase towards room temperature, when the contribution to the epilayer becomes comparable to that of the substrate. Below T = 20 K, θ_F/M increases slightly for 1.865 eV, which is explained by the concomitant narrowing of the band gap, shown by the empty circles, taken from Ref. [86].

The contribution coming from the substrate to the FR was measured separately, using a substrate piece without the epilayer, and subtracted from the FR produced by the EuSe epilayer.

In fields up to 0.2 T at all temperatures, both the magnetization and the FR angle displayed a linear dependence on B: typical results are shown in figure 4.16(a). It can be seen that the slopes of θ_F and M vary several orders of magnitude with temperature, however, the ratio θ_F/M, obtained from the slopes for $B < 0.2$ T,

$$\frac{\theta_F}{M} = \frac{d\theta_F/dB}{dM/dB} \tag{4.63}$$

and shown in figure 4.16(b) for the 4.8-300 K interval, remains constant. The vertical bars represent the estimated experimental error, which increases towards room temperature, when the response from the substrate becomes comparable to that of the epilayer, both in θ_F as well as in M measurements.

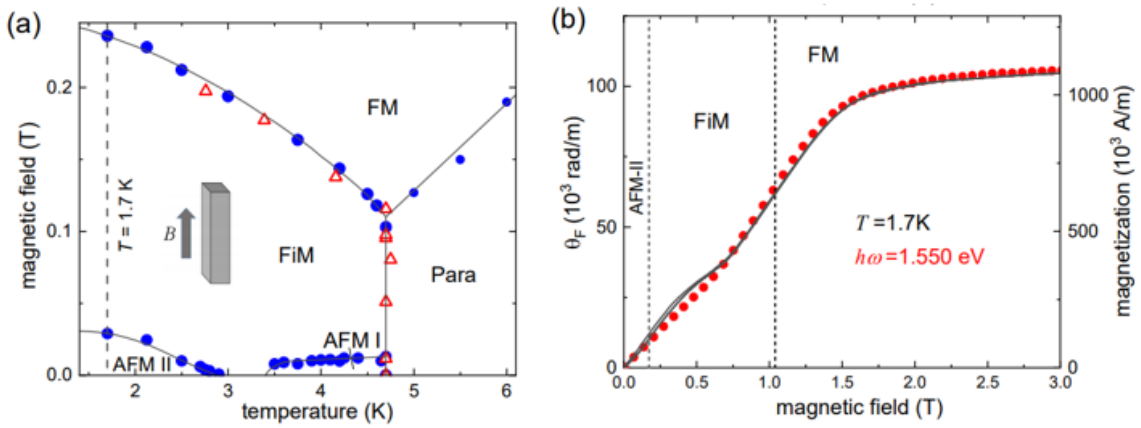

Figure 4.17: (a) Magnetic phase diagram of the studied EuSe layer. The full and open dots represent data obtained from M vs B (T = const) and M vs T (B = const) traces, respectively. The magnetic field was applied parallel to the surface of the epitaxial sample. The solid lines are guides to the eye. The dotted line shows that at $T = 1.7$ K a magnetic field drives EuSe through an antiferromagnetic (AFMII), a ferrimagnetic (FiM), and a ferromagnetic (FM) phase. (b) Magnetization (solid line) and FR at $\hbar\omega = 1.55$ eV (dots), as a function of magnetic field, at $T = 1.7$ K. The magnetic field was applied perpendicular to the surface of the epitaxial sample. When B is applied perpendicular to the layer, the AFMII-FiM and FiM-FM phase boundaries are shifted to $B = 0.17$ T and $B = 1.04$ T, respectively, due to the demagnetization effect [87]. Vertical lines show the boundaries between the magnetic phases indicated.

For the photon energy of 1.865 eV, which is in near resonance with the band gap, θ_F/M increases slightly when the sample is cooled below 20 K. This is explained by the concomitant narrowing of the gap (depicted by the empty circles), which makes the light even closer to resonance with the band gap, which enhances the FR angle, as explained

at the end of this section.

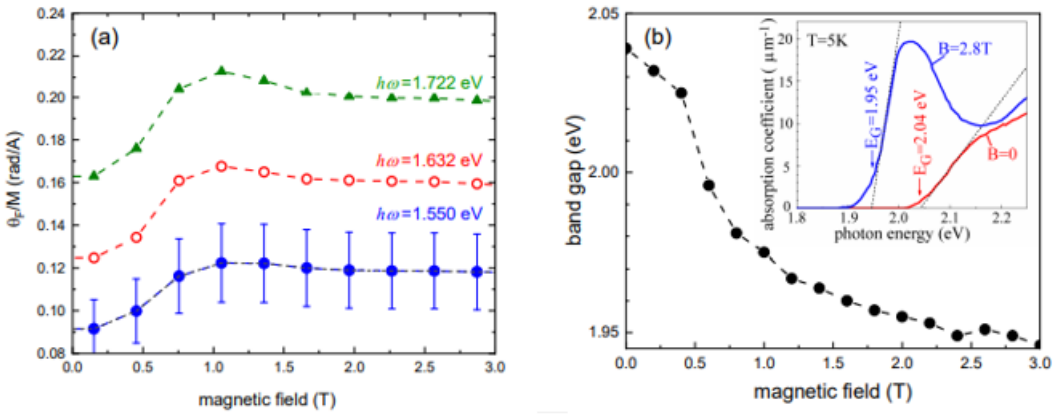

Figure 4.18: (a) Ratio of the FR, at the indicated photon energies, to the magnetization, as a function of magnetic field, for $T = 1.7$ K. At low fields, the ratio increases beyond the estimated uncertainty of 15 percent; (b) EuSe band gap as a function of B, obtained from optical absorption measurements as shown in the inset. The absorption experiments are detailed in Ref. [88]

In the temperature interval 4.8-300 K examined so far, EuSe is in the paramagnetic phase, because its Néel temperature is $T_N = 4.75$ K [77]; the magnetic phase diagram of our sample was measured, and it is shown in figure 4.17(a). To investigate θ_F/M in the phases other than the paramagnetic one, the magnetization and FR, at various photon energies, were measured at $T = 1.7$ K as a function of field. At this temperature the magnetic field drives the EuSe sample through an antiferromagnetic, a ferrimagnetic, and a ferromagnetic phase, as figure 4.17(a) shows (see also [90]). A comparison of the magnetization and FR curves can be seen in figure 4.17(b), both exhibit an almost identical dependence on B, minor differences in the B-dependencies are within the range of the experimental uncertainties. The dependence of θ_F/M on B is shown in fig. 4.18(a), for various photon energies. At low fields, θ_F/M remains at the same value measured in the paramagnetic phase up to 300 K.

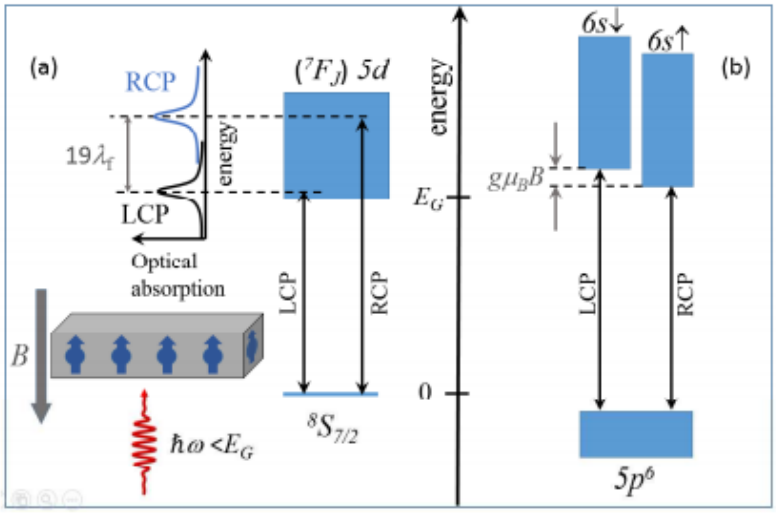

Figure 4.19: Electronic levels in EuTe. (a) Under a strong magnetic field, the Eu spins are aligned ferromagnetically, and the absorption spectrum shows a strong magnetic circular dichroism, whereby the RCP and LCP absorption peaks, corresponding to transitions from the Eu atoms in the $S_{7/2}$ state to the $5d_{t2g}$ conduction band, are split by $\sim 19\lambda_f$, where λ_f is the spin-orbit coupling constant for the Eu^{3+} ion [91] (b) RCP and LCP optical transitions between the valence band formed by *5p* orbitals of the Te atoms and a conduction band formed by *6s* Eu states [78, 86].

Increasing the field, θ_F/M increases and tends to a saturation. This process can be understood within the frame of the semiclassical model. When B is increased at $T = 5$ K, the EuSe band-gap narrows, as shown in figure 4.18(b), because the applied field imposes ferromagnetic order over a paramagnetic lattice, which lowers the energy of the conduction electrons due to the band-lattice exchange interaction. The dichroic spectrum showing the LCP/RCP splitting was investigated in Ref. [91]. A similarly large band-gap red-shift of about 100 meV by applying a magnetic field is also observed in YIG [92], and it is also associated with the conduction band-lattice exchange interaction. As figure 4.18 shows, the band-gap red-shift saturates around 2.5 T. The increase of the FR angle with increasing applied magnetic field is because the photon energy of the incident light becomes closer to resonance with the bandgap, which implies that the electronic polarizability increases, as the classical Lorentz model of forced atomic oscillators predicts.

4.3.4 Proportionality constant between magnetization and FR in europium chalcogenides

We already showed that in EuX FR is proportional to the magnetization. Here we go a step forward and determine the proportionality coefficient in EuX, using their well-known specific electronic energy structure, sketched in figure 4.19 [78]. First we shall estimate the

weight of the various valence bands to the FR. Using quantum mechanical time-dependent perturbation theory B.3 [82] applied to EuTe it can be shown that (See Appendix B.4)

$$\alpha^{\pm} = \frac{1}{2}\sum_{n}\frac{\mid \mu_{gn}^{\pm} \mid^2}{E_{ng} - \hbar\omega}, \tag{4.64}$$

where $\mid g\rangle$ represents the ground state of energy E_g, described by an electron in the valence band, $\mid n\rangle$ represents the excited states of energy E_n, corresponding to an electron in the conduction band, $E_{ng} = E_n - E_g$, and $\mu_{gn}^{\pm}$ is the electric dipole matrix element

$$\mu_{gn}^{\pm} = -e < n \mid x + iy \mid g\rangle \tag{4.65}$$

Equation (4.64) shows that the coupling through light between the ground and excited electronic states determines the induced polarization current.

In EuTe, when the spins are aligned with the direction of light by the application of a large magnetic field, the band-edge optical absorption becomes strongly dichroic [88, 91, 93, 94] and shows two narrow peaks, one for LCP and another for RCP, split by $\sim 19\lambda_f$ [91], where λ_f is the spin-orbit coupling constant for the Eu^{3+} atom, as sketched on figure 4.19(a). The circular dichroism is associated with optical transitions between the valence level, ${}^8S_{7/2}$, formed by the magnetic Eu atoms, into the $5d_{t2g}$ conduction band. The equal height of the two lines implies that $\mid \mu_{gn}^{+} \mid^2 \sim \mid \mu_{gn}^{-} \mid^2 \sim \mu_{gn}^2$. Taking the approximated absorption spectrum into account, the equation 4.64 leads to

$$\alpha_{||}^{-} = \frac{1}{2}\frac{\mu_{df}^2}{E_g - \hbar\omega}, \qquad \alpha_{||}^{+} = \frac{1}{2}\frac{\mu_{df}^2}{E_g + 19\lambda_f - \hbar\omega}. \tag{4.66}$$

Substituting (4.66) in (4.62), and using (4.56), we get

$$\theta_F^{mag} \approx \frac{\pi}{\lambda}\frac{M}{M^{SAT}}\frac{n_0^2 - 1}{2n_0}\frac{19\lambda_F}{E_g - \hbar\omega}. \tag{4.67}$$

In obtaining (4.67), the condition $19\lambda_f \ll E_g - \hbar\omega$ was assumed, which requires the incoming photons to be sufficiently away from resonance with the band gap.

It must be emphasized, however, that to arrive at (4.67), we did not make any approximation concerning the EuX band edge electronic energy structure and we did not substitute the energy bands of EuTe by zero width atomic energy levels. We worked within the frame of the full (${}^8S_{7/2}$-valence band, $5d_{t2g}$-conduction band) model, which is specific for EuX, that model has successfully described such effects as the continuous evolution of a 500 meV broad featureless absorption band at zero field to a doublet of sharp dichroic lines in high fields [88, 91, 93, 94], as well as second harmonic generation [95, 96], linear dichroism [97], and Faraday rotation [79, 98] in EuTe and EuSe. We simply exploited the well-known experimental fact that at high fields, when all Eu spins align

ferromagnetically, two birrefringent narrow lines emerge in the optical absorption threshold of EuX, their width being much less than the band gap [91, 93, 94], which has nothing to do with a substitution of bands by energy levels.

Now we shall inspect the contribution to the FR coming from valence bands generated by completely filled atomic states, whose magnetic moment is zero. In EuTe, just below the ${}^8S_{7/2}$ valence state, there is a valence band built from $5p^6$ shells of the Te atoms [78], which can be polarized by the incoming light through the dipole allowed admixture of empty *6s* states, as indicated on the right-hand side in figure 4.19. In the absence of a magnetic field, the *5p*-band will give no birefringence, because optical absorption associated with $5p \rightarrow 6s$ transitions will be identical in position and strength for RCP and LCP. But when a magnetic field is applied, the RCP and LCP absorption bands are split by the Zeeman energy, $g\mu_B B$. Then, proceeding exactly in the same way as when obtaining (4.67), the diamagnetic contribution to the FR is found to be

$$\theta_F^{diamagnetic} \sim -\frac{\pi}{\lambda}\frac{n_1^2-1}{4n_1}\frac{g\mu_B B}{E_g-\hbar\omega}, \tag{4.68}$$

where n_1 is the refractive index associated with the diamagnetic valence band. Equation 4.68 shows that the diamagnetic FR is proportional to the magnetic field, in stark contrast to the contribution from the magnetic valence band, given by Eq. (4.67), which is proportional to the magnetization.

Dividing (4.67) by (4.68), the relative weight of the diamagnetic FR is found

$$\left|\frac{\theta_F^{diamagnetic}}{\theta_F^{magnetic}}\right| \sim \frac{M^{SAT}}{M}\frac{g\mu_B B}{19\lambda_F}, \tag{4.69}$$

where $n_0 \sim n_1$ was used. Given that $g\mu_B B = 0.116$ meV/T, and that $19\lambda_f = 180$ meV [91], then the diamagnetic FR will generally be much smaller than the magnetic one.

We shall take a step further to investigate in more detail the proportionality coefficient between magnetization and FR. We rewrite equation (4.67) as

$$\frac{\theta_F}{M} = \frac{E_g-\hbar\omega}{\hbar\omega} \sim \text{constant}, \tag{4.70}$$

where the constant is determined by the materials refractive index, spin-orbit coupling constant, and saturation magnetization. Equation (4.70) was tested by plotting θ_F/M as a function of photon energy, using data taken in a wide temperature and magnetic field range, covering all EuSe magnetic phases, and figure 4.20 shows the result. It can be seen that the data points deviate from the average of 0.03 rad/A by at most 15 percent, which is the estimated error bar in our experiment, also shown in figure 4.20. The deviation at lower energies is larger, because the FR angle is smaller, hence the experimental error is larger. This is quite remarkable, because the data shown in figure 4.20 covers a 300 K temperature

and a 0-7 T magnetic field interval, respectively, where all possible magnetic phases occur, and where the ratio θ_F/M changes by an order of magnitude, and where M and θ_F vary several orders of magnitude, nevertheless (4.70) remains constant within experimental error. This not only validates our semiclassical model, but it makes equation (4.70) a practical formula to describe θ_F/M in all circumstances, substituting a full complex quantum-mechanical calculation in EuX.

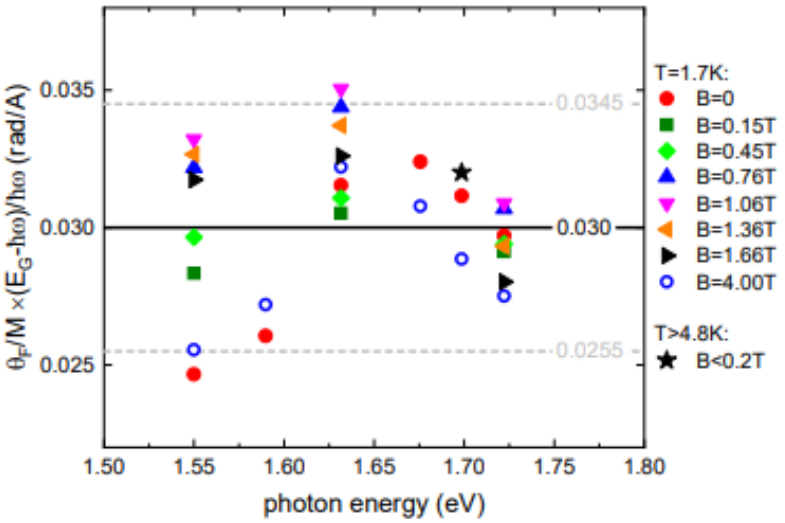

Figure 4.20: Measured ratio θ_F/M multiplied by $\dfrac{Eg-\hbar\omega}{\hbar\omega}$, as a function of photon energy, for various magnetic fields at $T = 1.7$ K, and in 1.7-300 K interval, for fields $B \leq 0.2$ T. The thickness of the EuSe epilayer was 2.5 μm. The average is shown by the full line, and a 15 percent deviation is shown by the dashed lines.

Equation (4.70) should remain valid for other intrinsic magnetic semiconductors, in which a valence level is formed by strongly localized atomic orbitals with nonzero magnetic moment. For the case of magnetic semiconductors where the top valence band is diamagnetic, FR will be a superposition of one component proportional to the magnetization and another proportional to B. As an example, GdN has a top valence band built from nitrogen $2p$ states [99], situated above the localized ${}^8S_{7/2}$ valence state of the Gd rare earth atoms (i.e., the position of the p valence band and of the localized ${}^8S_{7/2}$ valence level, shown in figure 4.19 for EuTe and EuSe, are inverted in order). The magnetic circular dichroism observed in GdN [100] is an indication that FR will also be connected to the magnetization in this system. However, because in GdN the p valence band forms the band-gap, for below-the-gap FR the diamagnetic contribution may be of the same magnitude as the ferromagnetic one, making a more complicated scenario. An analysis of the relationship between FR and magnetization in GdN and its dependence on the photon energy will require a separate investigation.

4.3.5 Conclusions

We developed a semiclassical model to show that in europium chalcogenides the FR is proportional to the magnetization. The model is based on classical physics concepts only. Our model for FR in the magnetic semiconductors EuX adds to the well known classical model of FR in a diamagnetic semiconductor, forming a didactic picture of the diversity of the FR in different solids. The model is validated by data taken on EuSe in a large temperature and magnetic field range, covering all possible magnetic phases. Moreover, we provided a formula connecting the Faraday rotation angle, the magnetization, the photon energy and the semiconductor band gap, which is a valuable practical solution for the conversion of FR into magnetization, at any temperature and magnetic phase in any member of the EuX family.

Appendices

Appendix A

Magneto-optical measurements details

A.1 Measurement of bulk Faraday rotation using an autobalanced photodetector system

When a linearly polarized probe light hits the sample under an externally applied magnetic field in the direction of the light beam, it produces a Faraday rotation angle θ_F. The objective of the experiment is to measure the absolute value of this rotation θ_F. The setup used in the experiment is presented in Fig. A.1.

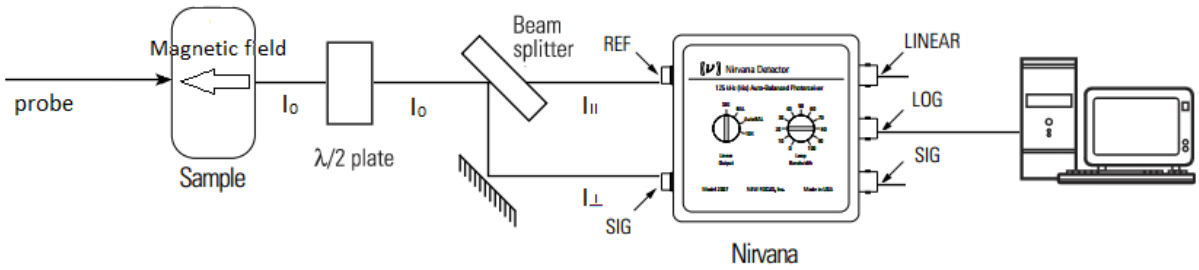

Figure A.1: Setup for measuring bulk Faraday rotation

The probe light, which carries the information of the rotated angle after passing through the sample, in its way to the detector, pass first through a $\lambda/2$ plate and later is splitted into its orthogonal components by a beam splitter, these orthogonal component signals are sent to the detector. The value of the intensity of the orthogonal components of the probe light are obtained from the Malus law:

$$I_{||} = I_0 \cos^2\theta \qquad \text{and} \qquad I_{\perp} = I_0 \sin^2\theta. \tag{A.1}$$

To eliminate any possible noise in the laser, the *autobalanced mode* of the detector is used, in which, for an accurate operation condition, we adjust the probe intensity using the $\lambda/2$

plate such as $I^{REF}/I^{SIG} \sim 2$, where I^{REF} is the intensity of the signal that arrives to the REF channel of the detector and I^{SIG} is the intensity of the signal that arrives to the SIG channel of the detector. The value of these intensities are expressed in terms of a constant α_X, which characterize the optical coupling and depend of the detector.

$$I^{SIG} = \alpha_{SIG} I_{||} \Longrightarrow I^{SIG} = \alpha_{SIG} I_0 \cos^2\theta_F, \tag{A.2}$$

$$I^{REF} = \alpha_{REF} I_{\perp} \Longrightarrow I^{REF} = \alpha_{REF} I_0 \sin^2\theta_F. \tag{A.3}$$

In these conditions, in the auto-balanced mode of the detector, we have the values of the outputs of the detector:

$$V_{SIG}^{auto} = -10 \times R \times I^{SIG}, \tag{A.4}$$

$$V_{LIN}^{auto} = 100 \times R \times [I^{SIG}(f) - gI^{REF}(f)], \tag{A.5}$$

$$V_{LOG}^{auto} = -ln(1/g - 1), \tag{A.6}$$

where R is the responsivity of the detector, $g = \dfrac{I^{SIG}}{I^{REF}}$ is a value obtained automatically for the internal detector circuitry, and $I^X(f)$ is the variation of the intensity in the X channel detected at the modulated frequency f. Now we use the automatically obtained g value in the detector in autobalanced mode:

$$g = \frac{I_{SIG}}{I_{REF}} = \frac{\alpha_{SIG} I_0 \cos^2\theta_F}{\alpha_{REF} I_0 \sin^2\theta_F} = \frac{\alpha_{SIG}}{\alpha_{REF}} \frac{1}{\tan^2\theta_F}, \tag{A.7}$$

And from Eq. A.6

$$\frac{1}{g} = e^{-V_{LOG}^{auto}} + 1 = \frac{\alpha_{REF}}{\alpha_{SIG}} \tan^2\theta_F. \tag{A.8}$$

Then

$$\theta_F = \arctan \sqrt{\frac{\alpha_{SIG}}{\alpha_{REF}}(1 + e^{-V_{LOG}^{auto}})}. \tag{A.9}$$

Thus, finally on the computer, we calculate the absolute value of θ_F from measuring the output the autobalanced detector V_{LOG}^{auto}. The value of $\dfrac{\alpha_{SIG}}{\alpha_{REF}} \sim 1$, was previoslly determined experimentally.

$$\theta_F = \arctan \sqrt{(1 + e^{-V_{LOG}^{auto}})}. \tag{A.10}$$

We can set θ_F =0 for B= 0 put an magnetic field dependence.

A.2 Measurement of the photo-induced Faraday rotation using an autobalanced photodetector system

When a pump light mechanically modulated at frequency f hits the sample, it produces a small variation $\Delta\theta_F$, in the Faraday rotation angle θ_F of the linearly polarized probe light. The objective of the experiment is to measure the absolute value of $\Delta\theta_F$. The used setup in the experiment is presented in Fig. A.2.

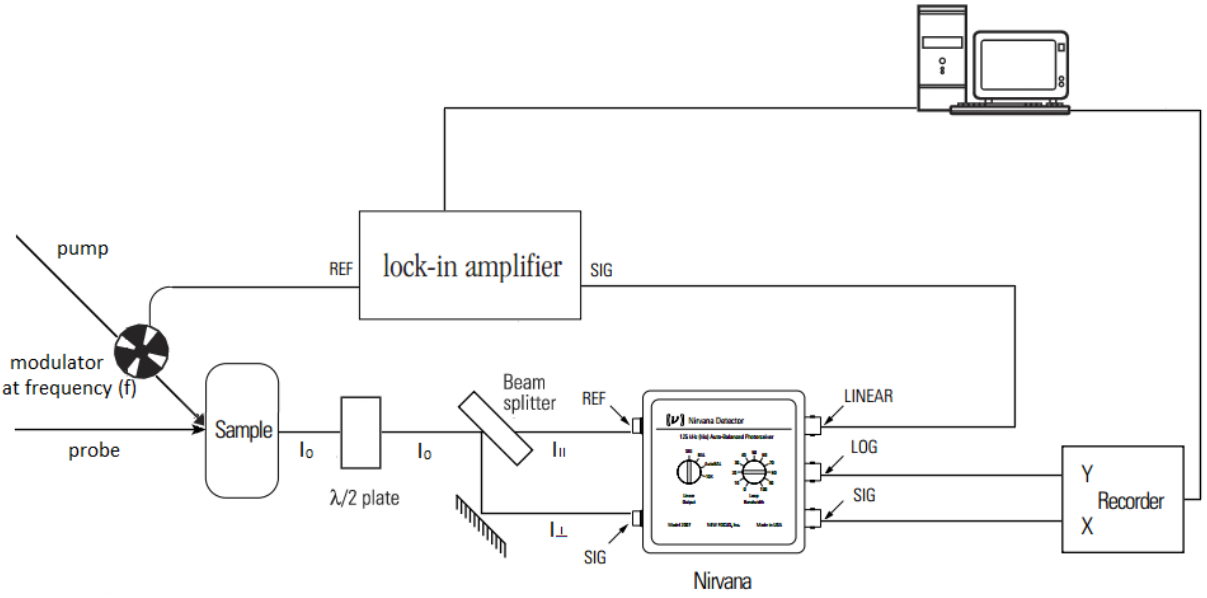

Figure A.2: Setup for measuring photo-induced Faraday rotation

The probe light, which carries the information of the rotated angle after passing through the sample, in its way to the detector, pass first through a $\lambda/2$ plate and later is splitted into its orthogonal components by a beam splitter, these orthogonal component signals are sent to the detector. The value of the intensity of the orthogonal components of the probe light are obtained from the Malus law:

$$I_{||} = I_0 \cos^2 \theta_F, \tag{A.11}$$

$$I_{\perp} = I_0 \sin^2 \theta_F. \tag{A.12}$$

To eliminate any possible noise in the laser, the *auto-balanced mode* of the detector is used, in which, for an accurate operation condition, we adjust the probe intensity using the $\lambda/2$ plate such as $I^{REF}/I^{SIG} \sim 2$, where I^{REF} is the intensity of the signal that arrives to the REF channel of the detector and I^{SIG} is the intensity of the signal that arrives to the SIG channel of the detector. The value of these intensities are expressed

in terms of a constant α_X, which characterize the optical coupling and depend of the detector.

$$I^{SIG} = \alpha_{SIG} I_{||} \Longrightarrow I^{SIG} = \alpha_{SIG} I_0 \cos^2\theta_F, \tag{A.13}$$

$$I^{REF} = \alpha_{REF} I_{\perp} \Longrightarrow I^{REF} = \alpha_{REF} I_0 \sin^2\theta_F. \tag{A.14}$$

In these conditions, in the auto-balanced mode of the detector, we have the values of the outputs of the detector:

$$V^{auto}_{SIG} = -10 \times R \times I^{SIG}, \tag{A.15}$$

$$V^{auto}_{LIN} = 100 \times R \times [I^{SIG}(f) - gI^{REF}(f)], \tag{A.16}$$

$$V^{auto}_{LOG} = -ln(1/g - 1). \tag{A.17}$$

where R is the responsivity of the detector, $g = \dfrac{I^{SIG}}{I^{REF}}$ is a value obtained automatically for the internal detector circuitry, and $I^X(f)$ is the variation of the intensity in the X channel detected at the modulated frequency f. From Eq. A.11 and Eq. A.12

$$I^{SIG}(f) = \Delta I^{SIG} = -\alpha_{SIG} I_0 2 \cos\theta_F \sin\theta_F \Delta\theta_F = -\alpha_{SIG} I_0 2 \sin 2\theta_F \Delta\theta_F. \tag{A.18}$$

$$I^{REF}(f) = \Delta I^{REF} = -\alpha_{REF} I_0 2 \cos\theta_F \sin\theta_F \Delta\theta_F = -\alpha_{REF} I_0 2 \sin 2\theta_F \Delta\theta_F. \tag{A.19}$$

Replacing the R value from Eq. A.15 in A.16 we obtain

$$V^{auto}_{LIN} = -10 \times R \times V^{auto}_{SIG} \Big\{ \frac{I_{SIG}(f)}{I_{SIG}} - \frac{I_{REF}(f)}{I_{REF}} \Big\}. \tag{A.20}$$

Replacing the obtained values for $I_{SIG}(f)$ and $I_{REF}(f)$ we obtain:

$$V^{auto}_{LIN} = \frac{40 V^{auto}_{SIG} \Delta\theta_F}{\sin 2\theta_F}. \tag{A.21}$$

Here we are interested in the $\Delta\theta_F$ value and not in θ_F, then, to eliminate the θ_F value we recall the automatically obtained g value:

$$g = \frac{I_{SIG}}{I_{REF}} = \frac{\alpha_{SIG} I_0 \cos^2\theta_F}{\alpha_{REF} I_0 \sin^2\theta_F} = \frac{\alpha_{SIG}}{\alpha_{REF}} \frac{1}{\tan^2\theta_F}. \tag{A.22}$$

Also from Eq. A.17

$$\frac{1}{g} = e^{-V^{auto}_{LOG}} + 1 = \frac{\alpha_{REF}}{\alpha_{SIG}} \tan^2\theta_F. \tag{A.23}$$

Then

$$\theta_F = \arctan\sqrt{\frac{\alpha_{SIG}}{\alpha_{REF}}(1+e^{-V_{LOG}^{auto}})}. \tag{A.24}$$

And from Eq. A.24 and Eq. A.21 we have:

$$V_{LIN}^{auto} = \frac{40V_{SIG}^{auto}\Delta\theta_F}{\sin 2\{\arctan\sqrt{\frac{\alpha_{SIG}}{\alpha_{REF}}(1+e^{-V_{LOG}^{auto}})}\}}. \tag{A.25}$$

This is the output of the auto-balanced detector which goes to the lock-in amplifier. And the value of $\Delta\theta_F$ is:

$$\Delta\theta_F = \frac{\sin 2\{\arctan\sqrt{\frac{\alpha_{SIG}}{\alpha_{REF}}(1+e^{-V_{LOG}^{auto}}\}}V_{LIN}^{auto}}{40V_{SIG}^{auto}}. \tag{A.26}$$

The lock-in amplifies this signal and operates just with the signal at the frequency f of the modulator. The output of the lock-in will be:

$$V^{lock-in} = \sqrt{2}\{\text{first harmonic amplitude of the entering signal}\} = \sqrt{2}V_{LIN}^{auto}. \tag{A.27}$$

case 1: Modulation from a chopper

Now, in the particular case of a square modulation by a chopper:

$$V^{lock-in} = \sqrt{2}(\frac{2}{\pi}V_0) = \sqrt{2}(\frac{2}{\pi}|V_{LIN}^{auto}|). \tag{A.28}$$

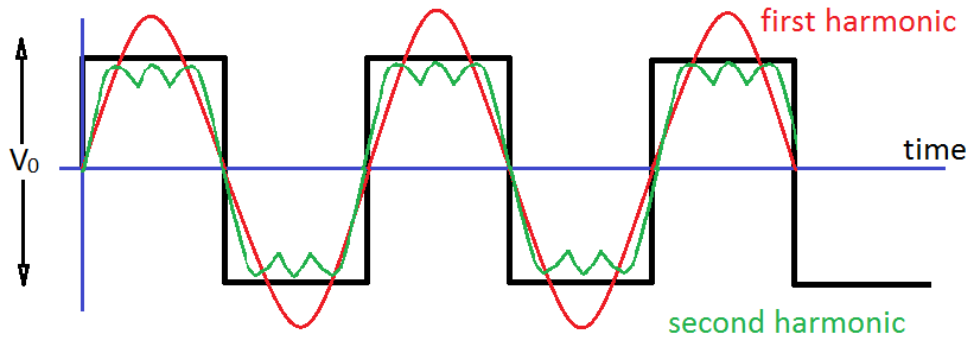

Figure A.3: Square modulated signal with frequency f generated for the chopper.

Thus, finally, on the computer, we calculate the absolute value of $\Delta\theta_F$ from measuring the output of the lock-in $V^{lock-in}$ and the outputs of the autobalanced detector V_{LOG}^{auto}, V_{LIN}^{auto}

and V_{SIG}^{auto}.

$$\Delta\theta_F = \frac{\pi V^{lock-in}}{80\sqrt{2}V_{SIG}^{auto}} \sin 2\{ \arctan \sqrt{\frac{\alpha_{SIG}}{\alpha_{REF}}(1+e^{-V_{LOG}^{auto}})}\} V_{LIN}^{auto}. \tag{A.29}$$

case 2: Modulation from a photo-elastic modulator

In the particular case of a sinusoidal modulation by a photo-elastic modulator:

$$V^{lock-in} = \sqrt{2}(V_0) = \sqrt{2}(|V_{LIN}^{auto}|). \tag{A.30}$$

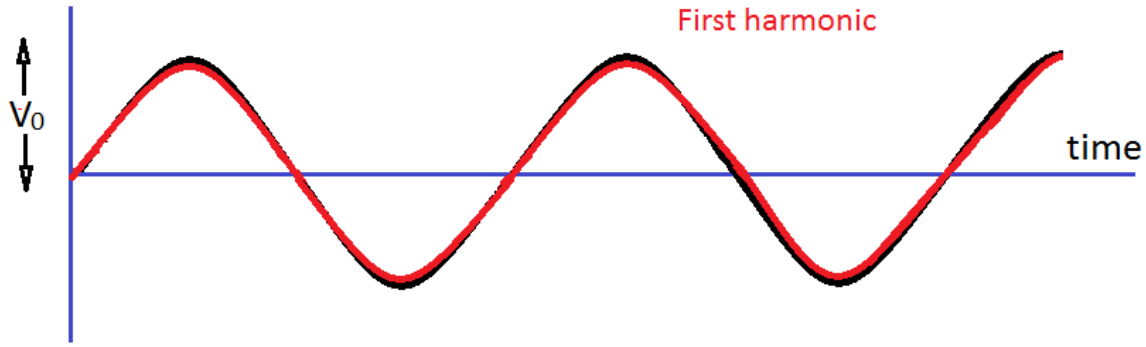

Figure A.4: Sinusoidal modulated signal with frequency f generated for the chopper.

Thus, finally, on the computer, we calculate the absolute value of $\Delta\theta_F$ from measuring the output of the lock-in $V^{lock-in}$ and the outputs of the autobalanced detector V_{LOG}^{auto}, V_{LIN}^{auto} and V_{SIG}^{auto}

$$\Delta\theta_F = \frac{V^{lock-in}}{40\sqrt{2}V_{SIG}^{auto}} \sin 2\{ \arctan \sqrt{\frac{\alpha_{SIG}}{\alpha_{REF}}(1+e^{-V_{LOG}^{auto}})}\} V_{LIN}^{auto}. \tag{A.31}$$

The value of $\frac{\alpha_{SIG}}{\alpha_{REF}} \sim 1$, which was previouslly determined.

A.3 Measurement of the time resolved differential transmission using an auto-balanced photo-detector system

When a pump light mechanically modulated by a chopper at frequency f hits the sample, it produces a small variation ΔI, in the intensity I_0 of the probe light. The objective of the experiment is to measure the differential variation $\Delta I/I$ of the probe light that pass through the sample, which is proportional to the differential transmission $\Delta T/T$, which is defined as $\dfrac{T^{pump} - T}{T}$, with $T = \dfrac{I}{I_0}$. The used setup in the experiment is presented in Fig. A.5.

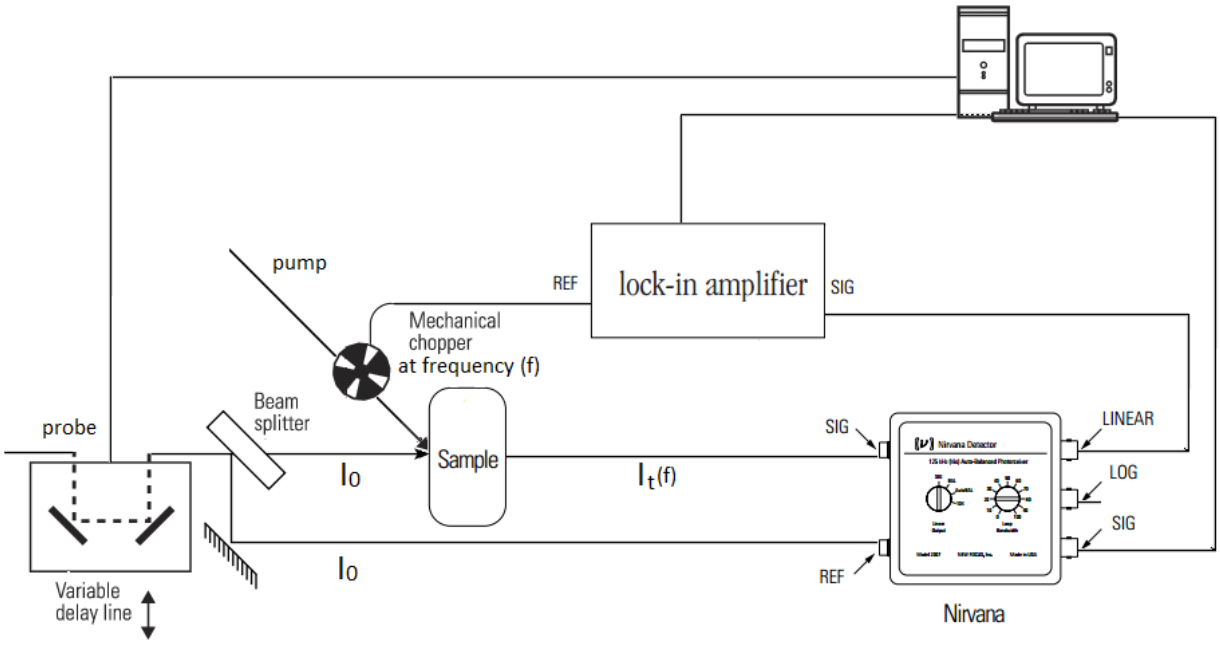

Figure A.5: Setup for measuring time-resolved differential transmission

The time delayed probe light, before passing through the sample is splitted in two equally intense beams, the first one goes directly to the REF channel of the detector and the second one crosses the sample with intensity I arriving to the SIG channel of the detector. The value of the intensity of the these signal can be written as:

$$I_{SIG} = I + I(f) = I + \Delta I \qquad and \qquad I_{REF} = I_0. \tag{A.32}$$

In these conditions, in the auto-balanced mode of the detector, we have the values of the outputs of the detector:

$$V_{SIG}^{auto} = -10 \times R \times I^{SIG}, \tag{A.33}$$

$$V_{LIN}^{auto} = 100 \times R \times [I^{SIG}(f) - gI^{REF}(f)], \tag{A.34}$$

$$V_{LOG}^{auto} = -ln(1/g - 1). \tag{A.35}$$

where R is the responsivity of the detector, $g = \dfrac{I^{SIG}}{I^{REF}}$ is a value obtained automatically for the internal detector's circuitry, and $I^X(f)$ is the variation of the intensity in the X channel detected at the modulated frequency f.

From Eq. A.33 we have:

$$R = \frac{-V_{LIN}^{auto}}{10 I_{SIG}}. \tag{A.36}$$

Replacing this value in Eq. A.34 and taking into account that $I_{REF}(f) = 0$ because this value does not depend of the periodic pump pulse, we have:

$$V_{LIN}^{auto} = -10 V_{SIG}^{auto} \frac{I_{SIG}(f)}{I_{SIG}}. \tag{A.37}$$

This is the output of the auto-balanced detector which goes to the lock-in amplifier.

The lock-in amplifies this signal and operates just with the signal at the frequency f of the modulator. The output of the lock-in will be:

$$V^{lock-in} = \sqrt{2}\{\text{first harmonic amplitude of the entering signal}\} = \sqrt{2} V_{LIN}^{auto}. \tag{A.38}$$

In the particular case of a square modulation by a chopper:

$$V^{lock-in} = \sqrt{2}(\frac{2}{\pi} V_0) = \sqrt{2}(\frac{2}{\pi} |V_{LIN}^{auto}|). \Longrightarrow V_{LIN}^{auto} = \frac{\pi}{2\sqrt{2}} V^{lock-in}. \tag{A.39}$$

Then

$$-10 V_{SIG}^{auto} (\frac{\Delta I}{I}) = \frac{\pi}{2\sqrt{2}} V^{lock-in}. \tag{A.40}$$

Thus, finally, on the computer, we calculate the absolute value of $\dfrac{\Delta I}{I}$ from measuring the output of the lock-in $V^{lock-in}$

$$\frac{\Delta I}{I} = -\frac{\pi}{20\sqrt{2}} \frac{V^{lock-in}}{V_{SIG}^{auto}}. \tag{A.41}$$

As we said before, $\Delta I/I$ is proportional to the differential transmission $\Delta T/T$, and we are interest just in its relative temporal evolution and not in its exact absolute value, then, we can write:

$$\frac{\Delta T}{T} = \alpha V^{lock-in}, \tag{A.42}$$

where $\alpha = -\dfrac{\pi}{20\sqrt{2}10RI_{SIG}}$ is a constant.

Appendix B

Mathematical Proofs of equations

B.1 Classical model of FR in diamagnetic materials

To build a contrast between FR in a magnetic semiconductor, i. e. one that contains atoms with unpaired electrons, to FR in a diamagnetic semiconductor, whose electrons are all paired, let us review very briefly the well-known classical model for FR in the diamagnetic semiconductor. This simple classical model is based on the Lorentz oscillator model of atoms and it is described in detail in Ref. [76].

Linear polarization is a superposition of RCP and LCP of equal amplitudes. For a non-magnetic atom, its angular momentum (orbital and spin) is zero, therefore there is no spatial orientation of the atom. Hence, by symmetry, both RCP and LCP will induce equal and opposite polarization currents, therefore there will be no FR. However, if a magnetic field is applied in the direction of light travel (i. e., in the Faraday geometry), then the Lorentz force will have opposite effects on the LCP and RCP induced polarization currents, which become different from one another, and FR emerges. In the linear regime, the FR in this case is proportional to the intensity of the applied magnetic field.

The following derivation assumes that the electrons having mass m and charge e in the medium behave according to classical mechanics under the combined effect of an external electromagnetic wave $\boldsymbol{E}$ and a constant applied magnetic field $\boldsymbol{B}$ in the propagation direction (Z axis) as is shown in Fig. B.1. The interaction of an electromagnetic field with a material occurs via perturbations to the electrons in atomic or molecular orbitals forming the bands. The differential equation governing the electron movement is given by

$$m\ddot{\boldsymbol{r}} = -m\omega_0^2\boldsymbol{r} + e(\boldsymbol{E} + \dot{\boldsymbol{r}} \times \boldsymbol{B}), \tag{B.1}$$

where ω_0 is the absorption frequency of the material. Separating, for simplicity, this equation in the X and Y components we obtain,

$$m\ddot{x} = -m\omega_0^2 x + eE_0 \cos\omega t + eB\dot{y} \tag{B.2}$$

and

$$m\ddot{y} = -m\omega_0^2 y + eE_0 \cos\omega t + eB\dot{x}. \tag{B.3}$$

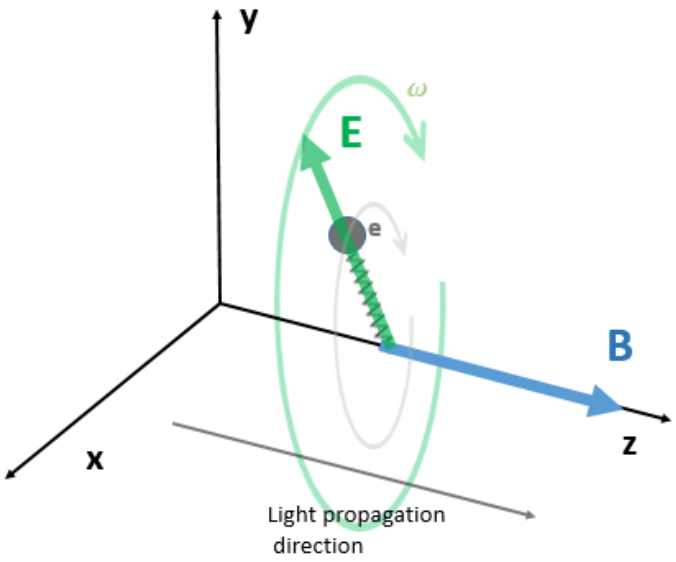

Figure B.1: Classical model for the FR. The electrons in the material become polarized following the combined effect of the rotating electric field E of a circular polarized light and a magnetic field B in the propagation direction of the light. This effect is different for RCP and LCP light.

Solving these equations, we obtain the transverse motion of an electron in the X-Y plane,

$$\begin{aligned} \boldsymbol{r_{RCP}} = \boldsymbol{r}^+ &= \frac{eE_0}{m(\omega_0^2 - \omega^2) + eB\omega} \ (\cos(kz - \omega t)\hat{\mathbf{x}} + \sin(kz - \omega t)\hat{\mathbf{y}}) \\ = \quad E^+(\cos(kz - \omega t)\hat{\mathbf{x}} + \sin(kz - \omega t)\hat{\mathbf{y}}) &\quad where \quad E^+ = \frac{eE_0}{m(\omega_0^2 - \omega^2) + eB\omega} \end{aligned} \tag{B.4}$$

and

$$\begin{aligned} \boldsymbol{r_{LCP}} = \boldsymbol{r}^- &= \frac{eE_0}{m(\omega_0^2 - \omega^2) - eB\omega} \ (\cos(kz - \omega t)\hat{\mathbf{x}} - \sin(kz - \omega t)\hat{\mathbf{y}}) \\ = \quad E^-(\cos(kz - \omega t)\hat{\mathbf{x}} + \sin(kz - \omega t)\hat{\mathbf{y}}) &\quad where \quad E^- = \frac{eE_0}{m(\omega_0^2 - \omega^2) - eB\omega}. \end{aligned} \tag{B.5}$$

The induced dipole moment $\boldsymbol{p}$ of a single atom in the material is given by

$$\boldsymbol{p}^{\pm} = e \ \boldsymbol{r}^{\pm} = \frac{e^2}{m(\omega_0^2 - \omega^2) \pm eB\omega} \ \boldsymbol{E_0}^{\pm}, \tag{B.6}$$

where $\boldsymbol{E_0}^{\pm}$ indicates the RCP (LHC) case for the plus (minus) sign. In general, the dipole

moment $\boldsymbol{p}$ is indeed proportional to the electric field and the amplitude of the circular polarization induced in the crystal by the rotating electric field of the incoming light in the X-Y plane, is given by [80, 81],

$$p^{\pm} = \alpha^{\pm}(\omega)E_0, \tag{B.7}$$

where, for our case, $\alpha^{\pm}(\omega) = \dfrac{e^2}{m(\omega_0^2 - \omega^2) \pm eB\omega}$. If there are N atoms in a unit volume, the polarization $\boldsymbol{P}$, the dipole moment per unit volume is given by

$$\boldsymbol{P}^{\pm} = N\boldsymbol{p}^{\pm} = N\alpha^{\pm}(\omega)\boldsymbol{E_0}^{\pm}. \tag{B.8}$$

The amplitude of the polarization we can write as

$$P^{\pm} = Np^{\pm} = N\alpha^{\pm}(\omega)E_0, \tag{B.9}$$

Since

$$\epsilon\boldsymbol{E_0}^{\pm} = \epsilon_0\boldsymbol{E_0}^{\pm} + \boldsymbol{P}^{\pm}. \tag{B.10}$$

Also using the definition

$$\omega = \frac{kc}{n} = kv \qquad c^2 = \frac{1}{\epsilon_0\mu_0} \qquad and \qquad v^2 = \frac{1}{\epsilon\mu}. \tag{B.11}$$

We can get

$$n^2 = \frac{\epsilon\mu}{\epsilon_0\mu_0}, \tag{B.12}$$

where we assume $\mu \approx \mu_0$. Then, replacing the electric field dependence of the polarization in equation B.10 we obtain

$$\epsilon^{\pm} = \epsilon_0 + N\alpha^{\pm}(\omega). \tag{B.13}$$

Then

$$n_{\pm}^2 = 1 + \frac{N}{\epsilon_0}\alpha^{\pm}(\omega) \quad = \quad 1 + \frac{N}{\epsilon_0}\frac{e^2}{m(\omega_0^2 - \omega^2) \pm eB\omega}. \tag{B.14}$$

We can even calculate the approximation

$$n_-^2 - n_+^2 \approx \frac{Ne^2}{\epsilon_0}\frac{2e\omega B}{m^2(\omega_0^2 - \omega^2)^2}. \tag{B.15}$$

And finally we get the well-know equation

$$\theta_F = \frac{\pi}{\lambda}(n_- - n_+) = \frac{\pi Ne^2}{\lambda\epsilon_0 n_0}\frac{e\omega}{m^2(\omega_0 - \omega^2)^2}B, \tag{B.16}$$

where $n_0 = \dfrac{n_- + n_+}{2}$

B.2 Connecting refractive index to the electronic polarizability

We want to find first what kind of electromagnetic waves can exist in a dielectric material in which there are no extra charges other than those bound in atoms. So we have

$$\rho = -\nabla \cdot \boldsymbol{P} \qquad and \qquad \boldsymbol{J} = \frac{\partial \boldsymbol{P}}{\partial t}. \tag{B.17}$$

In this situation, the Maxwell equations then become:

$$\nabla \cdot \boldsymbol{E}(r,t) = -\frac{\nabla \cdot \boldsymbol{P}}{\epsilon_0}, \tag{B.18}$$

$$\nabla \times \boldsymbol{B}(r,t) = \mu_0 \varepsilon_0 \frac{\partial \boldsymbol{E}(r,t)}{\partial t} + \mu_0 \frac{\partial \boldsymbol{P}}{\partial t}, \tag{B.19}$$

$$\nabla \times \boldsymbol{E}(r,t) = -\frac{\partial \boldsymbol{B}(r,t)}{\partial t}, \tag{B.20}$$

$$\nabla \cdot \boldsymbol{B}(r,t) = 0, \tag{B.21}$$

where $\boldsymbol{E}(r,t)$, $\boldsymbol{B}(r,t)$, ε_0, and μ_0 represents the electric field, the magnetic field, the permittivity and the permeability, respectively.

These equations describe the propagation of the electromagnetic fields within and at the boundary of the material.

In order to obtain analytical expressions for $\boldsymbol{E}(r,t)$ and $\boldsymbol{B}(r,t)$, we are going to find differential equations for these fields from the Maxwell equations and the following vectorial identity:

$$\nabla \times (\nabla \times \boldsymbol{A}) = \nabla(\nabla \cdot \boldsymbol{A}) - \nabla^2 \boldsymbol{A}, \tag{B.22}$$

where $\boldsymbol{A}$ is a vector field. Then, taking the curl of equation B.20 we have:

$$\nabla \times (\nabla \times \boldsymbol{E}(r,t)) = -\frac{\partial(\nabla \times \boldsymbol{B}(r,t))}{\partial t}. \tag{B.23}$$

Replacing equations B.19, B.20 and B.23 in equation B.22 where we change $\boldsymbol{A}$ by $\boldsymbol{E(r,t)}$ we obtain

$$\nabla^2 \boldsymbol{E}(r,t) - \mu_0 \varepsilon_0 \frac{\partial^2 \boldsymbol{E}(r,t)}{\partial t^2} = -\frac{1}{\varepsilon_0} \nabla(\nabla \cdot \boldsymbol{P}) + \mu_0 \frac{\partial^2 \boldsymbol{P}}{\partial^2 t}. \tag{B.24}$$

So instead of the wave equation, we now get that the D'Alembertian of $\boldsymbol{E}$ is equal to two terms involving the polarization $\boldsymbol{P}$. Since $\boldsymbol{P}$ depends on $\boldsymbol{E}$, we can have a solution for this master equation.

We consider the case for the electric field

$$E_{\pm} = \frac{(\hat{x} \pm i\hat{y})}{2} E_0 e^{i(kz - w_p t)}. \tag{B.25}$$

We know that any function of $(z - vt)$ represents a wave that travels with speed v. The exponent of equation B.25 can be writen as

$$ik(z - \frac{\omega_p}{k}t). \tag{B.26}$$

So equation B.25 represents a wave with the phase velocity

$$v_{ph} = \frac{\omega_p}{k}. \tag{B.27}$$

The index of refraction n is defined by letting

$$v_{ph} = \frac{c}{n}. \tag{B.28}$$

Thus, equation B.25 becomes

$$\boldsymbol{E}_{\pm} = \frac{(\hat{x} \pm i\hat{y})}{2} E_0 e^{i(\omega_p n z/c - w_p t)}. \tag{B.29}$$

So we can find n by finding what value of k is required if equation B.25 is to satisfy the master equation, and then using

$$n = \frac{kc}{\omega_p}. \tag{B.30}$$

In an isotropic material, the polarization has no variation with the coordinates, so $\nabla \cdot \boldsymbol{P} = 0$, and we get rid of the first term on the right hand of the master equation. Also, since we are assuming a linear dielectric, $\boldsymbol{P}$ will also vary as $e^{i\omega_p t}$, and $\frac{\partial^2 \boldsymbol{P}}{\partial^2 t} = -\omega_p \boldsymbol{P}$. the Laplacian in the master equation becomes simply $\frac{\partial^2 \boldsymbol{E}}{\partial^2 t} = -k^2 \boldsymbol{E}$, so we have

$$-k^2 \frac{(\hat{x} \pm i\hat{y})}{2} E_0 + \frac{\omega_p^2}{c^2} \frac{(\hat{x} \pm i\hat{y})}{2} E_0 = \frac{-\omega_p^2}{\varepsilon_0 c^2} \boldsymbol{P}. \tag{B.31}$$

Now we let assume for the moment that since $\boldsymbol{E}$ is varying sinusoidally. We can set $\boldsymbol{P}$ proportional to $\boldsymbol{E}$, and we write

$$\boldsymbol{P} = N\alpha \boldsymbol{E}. \tag{B.32}$$

If we consider the circular polarization case we can write

$$\boldsymbol{P}^{\pm} = N\alpha^{\pm} \boldsymbol{E} \quad = \quad N\alpha^{\pm} \frac{(\hat{x} \pm i\hat{y})}{2} E_0 e^{i(kz - w_p t)}. \tag{B.33}$$

Then E_0 drops out of B.29 and we find

$$k^2 = \frac{\omega_p^2}{c^2}(1 + \frac{N}{\varepsilon_0}\alpha). \tag{B.34}$$

We have found the a wave like B.25, with a number k given by B.30, will satisfy the master equation. Using B.31 the refractive index is given by

$$(\frac{ck}{\omega_p})^2 = n^2 = 1 + \frac{N}{\varepsilon_0}\alpha. \tag{B.35}$$

We can put the specific case for the RHP and the LCP light as

$$n_\pm^2 = 1 + \frac{N}{\varepsilon_0}\alpha^\pm. \tag{B.36}$$

B.3 First order time-dependent perturbation theory

Time-dependent perturbation theory, developed by Paul Dirac and explained in Sakurai [101], studies the effect of a time-dependent perturbation *W(t)* applied to a time-independent Hamiltonian H_0. Since the perturbed Hamiltonian $H(t) = H_0 + W(t)$ is time-dependent, so are its energy levels and eigenstates.

We will briefly examine the method behind Dirac's formulation of time-dependent perturbation theory. Choose an energy basis $|\psi_n\rangle$ for the unperturbed system.

Let $c_n(t)$ be the components of the unperturbed wavefunction $\mid \Psi(t)\rangle$ in the $\mid \psi_n\rangle$ basis

$$\mid \Psi(t)\rangle = \sum_n c_n(t) \mid \psi_n\rangle \qquad \text{with} \qquad c_n(t) = \langle \psi_n \mid \Psi(t)\rangle. \tag{B.37}$$

We define $W_{nm} = \langle \psi_n \mid W(t) \mid \psi_m\rangle$. The Schrodinger equation is

$$i\hbar \frac{d}{dt} \mid \Psi(t)\rangle = (H_0 + W(t)) \mid \Psi(t)\rangle. \tag{B.38}$$

Multiplying this equation by $\langle \psi_n \mid$ and using B.37 we obtain

$$i\hbar \frac{d}{dt} c_n(t) = E_n c_n(t) + \sum_k W_{nk} c_k(t) \qquad \text{where} \qquad \omega_{nk} = \frac{E_n - E_k}{\hbar}. \tag{B.39}$$

The substitution $c_n(t) = a_n(t) e^{-iE_n t/\hbar}$ in B.39 gives

$$i\hbar \frac{d}{dt} a_n(t) = \sum_k W_{nk} a_k(t) e^{i\omega_{nk} t}. \tag{B.40}$$

We can write

$$a_n(t) = a_n^0(t) + \lambda a_n^1(t) + \lambda^2 a_n^2(t) + ... \tag{B.41}$$

We seek solution for the first order approximation in λ. For $t < 0$ we assume the system to be in the state $\mid \psi_i\rangle$, so according to B.37 and the relation between $a_n(t)$ and $c_n(t)$, we have

$$a_n(t = 0) = \delta_{ni}. \tag{B.42}$$

If we substitute B.41 in B.40 and equate the coefficients of λ on both sides of the equation, we obtain (by using B.42)

$$i\hbar \frac{d}{dt} a_n^1(t) = \sum_k W_{nk}(t) e^{i\omega_{nk} t} a_k^0(t) = \sum_k W_{nk}(t) e^{i\omega_{nk} t} \delta_{ki} = W_{ni}(t) e^{i\omega_{ni} t}, \tag{B.43}$$

which we can integrate to finally obtain

$$a_n^1(t) = \frac{1}{i\hbar} \int W_{nk}(t) e^{i\omega_{nk} t} dt. \tag{B.44}$$

B.4 First order time-dependent electronic polarization

We now study the specific case of the perturbation given by the incidence of a circularly polarized monochromatic electromagnetic wave traveling along the Z direction carrying an electric field

$$\boldsymbol{E}_{\pm} = \frac{(\hat{\boldsymbol{x}} \pm i\hat{\boldsymbol{y}})}{2} E_0 e^{i(kz - w_p t)} = \boldsymbol{E_{0\pm}} e^{i(kz-\omega t)}, \tag{B.45}$$

where $\boldsymbol{E_{0\pm}} = \frac{(\hat{\boldsymbol{x}} \pm i\hat{\boldsymbol{y}})}{2} E_0$ and the plus sign is associated with a righ-hand circularly polarized wave (RHP) and the minus sign with a left-hand circularly polarized one (LHC). The circulating electric field of the incident wave will induce a circulating polarization vector in the material. The interaction between an electron and the electromagnetic wave can be described by the perturbation,

$$W(t) = -\boldsymbol{\mu} \cdot \boldsymbol{E}_{\pm} \qquad \text{with} \qquad \boldsymbol{\mu} = -e \sum_i \boldsymbol{r_i}, \tag{B.46}$$

where $\boldsymbol{\mu}$ is the electric dipole momentum operator for the electrons involved in the excitation and -e is the charge of the electron.

Making the inner product, we have

$$W(t) = \frac{e}{2}(x\hat{\boldsymbol{x}} + y\hat{\boldsymbol{y}} + z\hat{\boldsymbol{z}}) \cdot (\hat{\boldsymbol{x}} \pm i\hat{\boldsymbol{y}}) E_0 e^{i(kz - w_p t)}. \tag{B.47}$$

Then

$$W(t) = \frac{e}{2}(x \pm iy) E_0 e^{i(kz - w_p t)}. \tag{B.48}$$

The induced circular polarization in a medium, when electrons are in a state $\mid \Psi(t)\rangle$ is given by the expectation value,

$$\langle \boldsymbol{P} \rangle = N \langle \Psi(t) \mid \boldsymbol{\mu} \mid \Psi(t) \rangle \tag{B.49}$$

where N is the density of electrons. Then, the lowest dipole order contribution to the polarization linear in the electric field amplitude of the incident wave can be obtained from,

$$\langle \boldsymbol{P} \rangle = N \langle \Psi_n^0 + \Psi_n^1(t) \mid \boldsymbol{\mu} \mid \Psi_n^0 + \Psi_n^1(t) \rangle, \tag{B.50}$$

where the linear contribution is given by

$$\langle \boldsymbol{P^1} \rangle = N(\langle \Psi_n^0 \mid \boldsymbol{\mu} \mid \Psi_n^1(t) \rangle + \langle \Psi_n^1(t) \mid \boldsymbol{\mu} \mid \Psi_n^0 \rangle). \tag{B.51}$$

The right term, the "antiresonant" term, can be discarded. Then

$$\langle \boldsymbol{P^1} \rangle = N \langle \Psi_n^0 \mid \boldsymbol{\mu} \mid \Psi_n^1(t) \rangle. \tag{B.52}$$

In order to obtain this expectation value, we need the first order approximation wave function $\Psi_n^1(t)$ when is perturbed by a time-dependent function $W(t) = -\boldsymbol{\mu} \cdot \boldsymbol{E}_{\pm}$.

By using general relation obtained in the section above, the equation B.44

$$a_n^1(t) = \frac{1}{i\hbar} \int \langle \psi_n \mid W_{nk}(t) \mid \psi_k \rangle e^{i\omega_{nk}t} dt. \tag{B.53}$$

For this particular case we have $W(t) = -\boldsymbol{\mu} \cdot \boldsymbol{E}_{\pm}$, then we get

$$a_n^1(t) = \frac{1}{i\hbar} \int \langle \psi_n \mid -\boldsymbol{\mu} \cdot \boldsymbol{E}_{\pm} \mid \psi_k \rangle e^{i\omega_{nk}t} dt \tag{B.54}$$

$$= \frac{e}{2i\hbar} \int \langle \psi_n \mid x \pm iy \mid \psi_k \rangle E_0 e^{i(kz - w_p t)} e^{i\omega_{nk}t} dt \tag{B.55}$$

$$= \frac{e}{2i\hbar} \langle \psi_n \mid x \pm iy \mid \psi_k \rangle E_0 e^{ikz} \int e^{i\omega_{nk}t} e^{-iw_p t} dt. \tag{B.56}$$

Solving the integral we obtain

$$= -\frac{e}{2\hbar} \langle \psi_n \mid x \pm iy \mid \psi_k \rangle E_0 e^{ikz} \frac{e^{i(\omega_{nk} - \omega_p)t}}{\omega_{nk} - \omega_p}. \tag{B.57}$$

Finally, we get

$$a_n^1(t) = \frac{1}{2} \frac{V_{nk} e^{i\omega_{nk}t}}{E_{nk} - E_p} e^{i(kz - \omega_p t)}, \tag{B.58}$$

where $E_{nk} = \hbar\omega_n - \hbar\omega_k$, $E_p = \hbar\omega_p$ and $V_{nk} = -e\langle \psi_n \mid x \pm iy \mid \psi_k \rangle = -2\langle \psi_n \mid \boldsymbol{\mu} \mid \psi_k \rangle \cdot \boldsymbol{E}_{\mathbf{0}\pm}$. From this, we can obtain the first order state of the perturbed wavefunction

$$|\Psi^1(t)\rangle = \sum_n c_n^1(t) |\psi_n\rangle, \tag{B.59}$$

which we can write as

$$|\Psi^1(t)\rangle = \sum_n a_n^1(t) e^{-i\omega_n t} |\psi_n\rangle. \tag{B.60}$$

Or

$$|\Psi^1(t)\rangle = \sum_n \frac{1}{2} \frac{V_{nk} e^{i\omega_{nk}t}}{E_{nk} - \hbar\omega_p} e^{i(kz - \omega_p t)} e^{-i\omega_n t} |\psi_n\rangle. \tag{B.61}$$

Finally

$$|\Psi^1(t)\rangle = \frac{1}{2} \sum_n \frac{V_{nk} e^{-i\omega_k t}}{E_{nk} - \hbar\omega_p} e^{i(kz - \omega_p t)} |\psi_n\rangle. \tag{B.62}$$

Also, $\mid \Psi^0 \rangle$ is the solution of the unperturbed Schrodinger equation

$$\mid \Psi^0 \rangle = e^{-i\omega_k t} \mid \psi_k \rangle. \tag{B.63}$$

Then, the linear contribution of the induced polarization (B.52) can be writen as,

$$\langle \boldsymbol{P^1} \rangle = N \langle \psi_g e^{+i\omega_g t} \mid \boldsymbol{\mu} \mid \frac{1}{2} \sum_n \frac{V_{nk} e^{-i\omega_g t}}{E_{ng} - \hbar\omega_p} e^{i(kz-\omega_p t)} | \psi_n \rangle. \tag{B.64}$$

This can be simplified to,

$$\langle \boldsymbol{P^1_\pm} \rangle = \frac{N}{2} \sum_m \frac{\langle \psi_g \mid \boldsymbol{\mu} \mid \psi_m \rangle V_{mk}}{E_{mg} - \hbar\omega_p} e^{i(kz-\omega_p)t}. \tag{B.65}$$

Remembering that $V_{mg} = 2\langle \psi_m \mid \boldsymbol{\mu} \mid \psi_g \rangle \boldsymbol{E_{0\pm}}$, we can write this equation as

$$\langle \boldsymbol{P^1_\pm} \rangle = N \sum_m \frac{\langle \psi_g \mid \boldsymbol{\mu} \mid \psi_m \rangle \langle \psi_m \mid \boldsymbol{\mu} \mid \psi_g \rangle \boldsymbol{E_{0\pm}}}{E_{mg} - \hbar\omega_p} e^{i(kz-\omega_p)t}. \tag{B.66}$$

Or

$$\langle \boldsymbol{P^1_\pm} \rangle = N \sum_m \frac{\boldsymbol{\mu_{gm}} \left[\boldsymbol{\mu_{mg}} \cdot \boldsymbol{E_{0\pm}} \right]}{E_{mg} - \hbar\omega} e^{i(kz-\omega_p t)} \qquad \text{where} \qquad \boldsymbol{E_{0\pm}} = \frac{\hat{x} \pm i\hat{y}}{2} E_0, \tag{B.67}$$

where $\boldsymbol{\mu_{gm}} = \langle \psi_g \mid \boldsymbol{\mu} \mid \psi_m \rangle$, $\boldsymbol{\mu_{mg}} = \langle \psi_m \mid \boldsymbol{\mu} \mid \psi_g \rangle$ and $\boldsymbol{\mu} = -e \sum \boldsymbol{r_i}$. On the other hand, remembering the definition of the polarization $\boldsymbol{P}$

$$\boldsymbol{P_\pm} = N \alpha_\pm \boldsymbol{E_{0\pm}} e^{i(kz-\omega_p t)}. \tag{B.68}$$

We can equate this equation with equation B.67 and we obtain

$$N \sum_m \frac{\boldsymbol{\mu_{gm}} \left[\boldsymbol{\mu_{mg}} \cdot \boldsymbol{E_{0\pm}} \right]}{E_{mg} - \hbar\omega} e^{i(kz-\omega_p t)} = N \alpha_\pm \boldsymbol{E_{0\pm}} e^{i(kz-\omega_p t)}. \tag{B.69}$$

Then

$$\alpha_\pm = \sum_m \frac{\boldsymbol{\mu_{gm}} \boldsymbol{\mu_{mg}}}{E_{mg} - \hbar\omega_p}. \tag{B.70}$$

Finally we can write, for the particular case of the circularly polarized light we calculated

$$\alpha_\pm = \frac{1}{2} \sum_m \frac{\mid \mu^\pm_{gm} \mid^2}{E_{mg} - \hbar\omega_p}, \tag{B.71}$$

where $\mu^\pm_{gm} = -e\langle \psi_g \mid x \pm iy \mid \psi_m \rangle$

Appendix C

Publications

PHYSICAL REVIEW B **95**, 045205 (2017)

Photoinduced giant magnetic polarons in EuTe

A. B. Henriques,[1] A. R. Naupa,[1] P. A. Usachev,[2] V. V. Pavlov,[2] P. H. O. Rappl,[3] and E. Abramof[3]
[1]*Instituto de Fisica, Universidade de Sao Paulo, 05315-970 Sao Paulo, Brazil*
[2]*Ioffe Institute, 194021 St. Petersburg, Russia*
[3]*LAS-INPE, 12227-010 Sao Jose dos Campos, Brazil*
(Received 8 October 2016; published 13 January 2017)

Photoinduced magnetic polarons in EuTe, with a magnetic moment of several hundred Bohr magnetons, were investigated as a function of pump intensity and temperature by pump-probe Faraday rotation. The quantum efficiency for optical generation of magnetic polarons is found to be 0.09. The pump-intensity dependence of the photoinduced Faraday rotation shows a sublinear increase, from which we deduce that the population of photoexcited polarons is limited by a maximum value of 4.5×10^{15} cm^{-3}. This is four orders of magnitude less than the concentration of polarons that would completely fill the crystal, which suggests that the photoexcited polarons are anchored by defects. In addition to the generation of polarons, at high pump densities the modulated pump light also causes a small alternating heating of the illuminated region. The temperature dependence of the polaron magnetic moment is well described by the Curie–Weiss law. Above 100 K, polarons are thermally quenched with an activation energy of 11 meV.

DOI: 10.1103/PhysRevB.95.045205

Optical manipulation of the magnetic state of matter is a topic of current interest both from the fundamental point of view as well as due to its high relevance in respect to technological applications [1]. Magnetic semiconductors represent a family of materials with a huge potential for fast optomagnetism [2–4], yet they remain largely unexplored in respect to optical manipulation of their magnetic state. Europium telluride is an intrinsic magnetic semiconductor of the face-centered cubic structure, where an europium spin $S = 7/2$ is associated with every lattice site. EuTe is an antiferromagnet with a Néel temperature of $T_N = 9.6$ K, hence its equilibrium magnetization is zero. Recently it was demonstrated that in EuTe light in resonance with the band gap can generate magnetic polarons with a magnetic moment of several hundred Bohr magnetons at temperatures as high as 100–150 K [5–7]. A magnetic polaron consists of a conduction-band electron localized in space by a photoexcited hole and the attractive exchange field generated by the spins of the europium atoms within the range of the electronic wave function. Magnetic polarons have been widely studied in diluted magnetic semiconductors (see, for instance, Refs. [8,9]). In intrinsic magnetic semiconductors, the theory of magnetic polarons was first studied by Kasuya and Nagaev [10,11]. A variational approximation to describe magnetic polarons is described in Ref. [12]. In Ref. [6], the more sophisticated self-consistent field approximation was used, and the theory was used to extract magnetic polaron parameters from the EuTe low temperature photoluminescence, which was measured as a function of applied magnetic field. It was found that, for EuTe, the magnetic polaron is described by a sphere of radius $R_{Pol} \approx 4$ (in units of the EuTe lattice parameter), which is nearly independent of temperature and field, and the magnetic moment of the polaron is $\sim 610\mu_B$ below the Néel temperature [5,6]. Because of the giant magnetic moment of a polaron, a modest magnetic field of a few tens of mT leads to a full alignment of polarons, which opens the prospect of using light to magnetize EuTe. To determine how efficiently this light magnetization mechanism can be exploited, here we investigate photoinduced magnetic polarons in EuTe as a function of pump intensity and temperature by using pump-probe Faraday rotation.

The EuTe sample was grown by molecular beam epitaxy (MBE) on a (111)-oriented BaF_2 substrate [13]. The thickness of the EuTe epitaxial layer was $d_{Sample} = 1.3$ μm, and the epitaxial layer was capped with BaF_2 to ensure total protection of the EuTe surface from oxidation. The thickness of the protective layer was 200 nm. BaF_2 is completely transparent in the wavelength range used in this paper, therefore the thickness of the protective layer is not critical for the present study. The photoinduced Faraday rotation (PFR) was measured by using a two-color pump-probe technique. The pump light source was a frequency-doubled Nd:YAG laser (2.33 eV), focused on the sample with a Gaussian profile of 150 μm full width at half maximum. The Faraday rotation probe was a semiconductor laser of photon energy 1.86 eV. This photon energy is well within the EuTe gap for any field and temperature used in our measurements, so the probe is not absorbed. Therefore it does not photoexcite any electron-hole pairs, and hence it does not induce any magnetic polarons (the photoinduced magnetic polaron excitation spectrum is given in Ref. [7]). A magnetic field was applied normal to the surface of the sample, which is parallel to the [111] crystalline direction. The experiments were performed using a variable-temperature optical cryostat containing a superconductive coil to generate a magnetic field applied in the Faraday geometry. The pump was modulated at 2.33 kHz using a chopper. The Faraday rotation angle of the linearly polarized probe beam was measured by using a polarization bridge containing a New Focus Nirvana balanced detector coupled to a lock-in referenced to the chopper frequency [14].

The Faraday rotation angle θ_F of the light that crosses a uniformly magnetized sample of thickness d_{Sample} can be converted into its magnetization M by using [15]

$$\theta_F = V M d_{Sample}, \tag{1}$$

where V is the Verdet constant. The Verdet constant at the probe wavelength was determined from a measurement of the Faraday rotation of the probe light, at 5 K, as a function

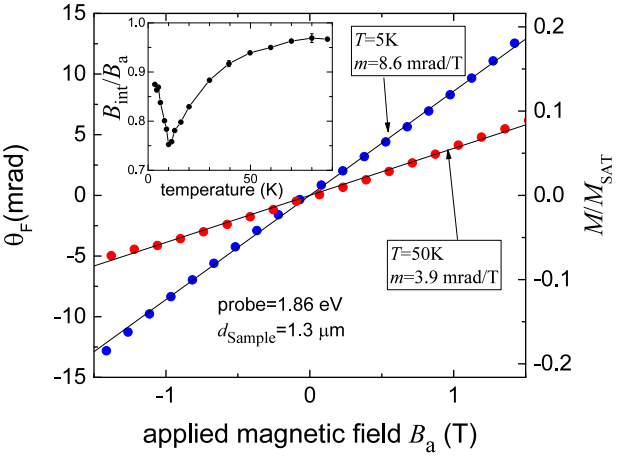

FIG. 1. Faraday rotation by the bulk EuTe sample as a function of the applied magnetic field at $T = 5$ K and $T = 50$ K. The inset shows the ratio of the internal magnetic field to the applied magnetic field.

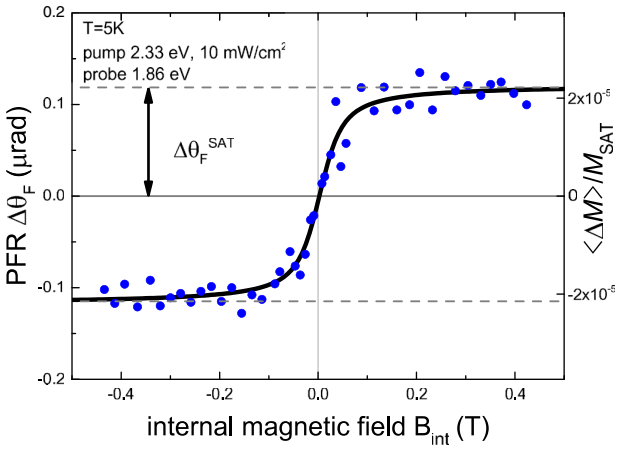

FIG. 2. Photoinduced Faraday rotation (PFR) signal as a function of the internal magnetic field at $T = 5$ K.

of the applied magnetic field. During this measurement the pump light was switched off. To isolate the EuTe Faraday rotation signal, the contribution coming from the cryostat windows was subtracted. As expected, we found that the photoinduced Faraday rotation is independent of the intensity of the probe because the probe used is well within the EuTe transparency-wavelength range. As shown in Fig. 1, the Faraday rotation depends linearly on applied field B_a with a slope of $m(T = 5\ \text{K}) = 8.6$ mrad/T. At $T = 5$ K the magnetization is also linear in B_a, with a slope of $M_{\text{SAT}}/B_{\text{SAT}}$ [16], where $M_{\text{SAT}} = n_{\text{Eu}}\mu_{\text{Eu}} = 9.03\times10^5$ A/m is the saturation magnetization, where $n_{\text{Eu}} = 4/a^3$ is the concentration of Eu atoms in the fcc lattice of parameter $a = 6.6$ Å, $\mu_{\text{Eu}} = g\mu_B S$ is the magnetic moment of an Eu atom, $g = 2$ is the Eu^{2+} gyromagnetic factor, μ_B is the Bohr magneton, and $B_{\text{SAT}} = 8.3$ T is the saturation field in the Faraday geometry [16]. Hence the Verdet constant, for the probe wavelength $\lambda = 665$ nm, is found to be

$$V = \frac{B_{\text{SAT}} m(T = 5\,\text{K})}{d_{\text{Sample}} M_{\text{SAT}}} = 0.061\ \text{rad/A}. \tag{2}$$

Being determined by the electronic energy structure, the Verdet constant will remain approximately constant as a function of temperature and magnetic field, as long as the electronic energy structure and the band gap are not modified. It is well known that the EuTe band gap changes when the lattice spins are strongly polarized, but this requires magnetic fields above 3 T at helium temperatures (see, for instance, Figs. 4 and 5 in Ref. [17]), and proportionally larger fields at higher temperatures. Because the magnetic fields used here are modest in comparison, we can safely assume, to a good approximation, that the Verdet constant is independent of temperature and magnetic field for all the experimental results presented here.

In addition to converting a Faraday rotation angle to magnetization, the Verdet constant also allows us to determine the internal magnetic field, which is smaller than the applied one due to the demagnetization field. In the Faraday geometry used, the demagnetization field within the epitaxial layer is given by $\mu_0 M$ [18], hence the internal magnetic field will be given by

$$B_{\text{int}} = B_{\text{a}} - \mu_0 M. \tag{3}$$

Substituting M from Eq. (1), and using $\theta_F = m(T)B_{\text{a}}$, where $m(T)$ is the slope of the Faraday rotation angle as a function of B_{a} at a temperature T (see Fig. 1), then the ratio $B_{\text{int}}/B_{\text{a}}$ will be given by

$$\frac{B_{\text{int}}}{B_{\text{a}}} = 1 - \mu_0 \frac{m(T)}{d_{\text{Sample}} V}. \tag{4}$$

The ratio $B_{\text{int}}/B_{\text{a}}$, calculated by using Eq. (4), is plotted in the inset of Fig. 1 as a function of temperature. The sharp downfall of the $B_{\text{int}}/B_{\text{a}}$ ratio in the vicinity of 10 K is because EuTe is an antiferromagnet, therefore its temperature-dependent magnetic susceptibility shows the characteristic cusp at the Néel temperature (see, for instance, Ref. [19]). Therefore, according to Eq. (3), the absolute value of the internal field B_{int} is expected to show a corresponding downward cusp at the Néel temperature, as indeed observed in the inset of Fig. 1.

By using the results of the preceding preliminary analysis, we can convert the measured photoinduced Faraday rotation, as a function of *applied* magnetic field B_{a} into photoinduced magnetization as a function of the *internal* magnetic field B_{int}. Figure 2 shows the photoinduced Faraday rotation signal (PFR) at 5 K as a function of the internal field for a pump intensity of 10 mW/cm^2. The photoinduced Faraday rotation angle was converted into magnetization by using the Verdet constant determined above and assuming that the thickness d_{Pol} of the layer where magnetic polarons are photogenerated is equal to the pump-light penetration depth $1/\alpha$, i.e., $d_{\text{Pol}} = \frac{1}{\alpha}$, where $\alpha = 10\ \mu\text{m}^{-1}$ is the absorption coefficient at the pump wavelength [17]. The photoinduced magnetization scale obtained in this way is shown on the right-hand side of Fig. 2.

The photoinduced Faraday rotation signal shown in Fig. 2 has all the characteristics expected for an ensemble of photoexcited polarons. First, the signal shows a resonance

when the energy of the pump photons meets the EuTe band gap [7]. Second, the signal is zero at $B = 0$, because at $B = 0$ there is no preferential direction in space, therefore photoexcited magnetic polarons will point randomly, and the net magnetic moment of the sample will remain zero. Third, the photoinduced signal tends to saturate rapidly when a magnetic field is applied, exactly as expected for magnetic polarons of a large magnetic moment—several hundreds of Bohr magnetons.

Assuming that the photoexcited polarons do not diffuse, the saturation value of the photoinduced Faraday rotation seen in Fig. 2, $\Delta\theta_F^{\mathrm{SAT}} = 0.12$ μrad, can be converted to an average photoinduced magnetization

$$\langle \Delta M \rangle^{\mathrm{SAT}} = \frac{\alpha \Delta\theta_F^{\mathrm{SAT}}}{V} = 2.2\times10^{-5} M_{\mathrm{SAT}}. \tag{5}$$

This value can be compared with the value expected for photoinduced polarons

$$\langle \Delta M \rangle^{\mathrm{SAT}} = n_{\mathrm{Pol}} \mu_{\mathrm{Pol}}, \tag{6}$$

where $\mu_{\mathrm{Pol}} \sim 610\mu_B$ is the magnetic moment of a polaron at 5 K [5,6], and n_{Pol} is the steady-state population of magnetic polarons when the sample is illuminated with the pump light. The inertial effective mass of a magnetic polaron has been predicted to increase exponentially with the ratio of the polaron radius and the lattice parameter, R_{Pol}/a [20]. Because in our case this ratio is quite large, $R_{\mathrm{Pol}}/a \sim 4$ [6], we expect the photoinduced magnetic polarons to be quite heavy and immobile, and they therefore remain in the layer penetrated by the pump light. In this case the steady-state polaron population will be given by $n_{\mathrm{Pol}} = G\tau_0$, where G is the polaron average generation rate per unit volume within the light penetration depth $1/\alpha$, $G = \chi \frac{p\alpha}{h\nu}$, p is the intensity of the pump beam incident on the surface of the sample, χ is the quantum efficiency of polaron generation, $h\nu$ is the pump photon energy, and $\tau_0 = 15$ μs is the polaron lifetime at $T = 5$ K [7]. All parameters determining $\langle \Delta M \rangle^{\mathrm{SAT}}$ are known, except for the quantum efficiency, so a comparison of Eqs. (5) and (6) yields the quantum efficiency $\chi \approx 0.09$. This result is very reasonable and can be taken as further evidence that photoinduced magnetic polarons are the source of the photoinduced Faraday rotation signal observed.

By using the deduced quantum efficiency, the steady-state polaron population is found to be $n_{\mathrm{Pol}} = 3.6\times10^{15}$ cm^{-3}. Therefore the average distance between polarons is estimated to be $d = 2(\frac{3}{4\pi n_{\mathrm{Pol}}})^{1/3} \sim 120a$, where a is the EuTe lattice parameter. Taking into account that the radius of a polaron is $R_{\mathrm{Pol}} \sim 4a$ [6], then the distance between polarons is two orders of magnitude greater than the polaron radius, hence it can be assumed that polarons are noninteracting.

Having firmly established that the photoinduced Faraday rotation signal is due to optically generated magnetic polarons, that these polarons are very distant from one another, and knowing that the magnetic moment of a polaron equals several hundreds of Bohr magnetons [5,6], we can conjecture that the magnetization of a magnetic polaron ensemble will obey a Langevin function, which describes a paramagnetic system in the classical limit. In this hypothesis the magnetization associated with a photoinduced magnetic polaron ensemble will be given by

$$\langle \Delta M(B,T) \rangle = n_{\mathrm{Pol}} \mu_{\mathrm{Pol}} L(x), \tag{7}$$

where the Langevin function is given by

$$L(x) = \coth(x) - \frac{1}{x}, \tag{8}$$

where $x = \frac{\mu_{\mathrm{Pol}} B}{k_B T}$. Notice that, below the Néel temperature, the magnetic moment of the polaron is known from photoluminescence studies to be $610\mu_B$ [5,6], hence in that temperature range there are no free parameters in Eq. (7). Nevertheless, to test the validity of our Langevin conjecture, we have fitted the photoinduced magnetization data taken at $T = 5$ K with Eq. (7), whereby the polaron magnetic moment is the sole adjustable parameter. The fitted curve is depicted by the solid line in Fig. 2, yielding $\mu_{\mathrm{Pol}} \sim 600\mu_B$. This coincides almost exactly with the known value, which demonstrates that the magnetization of the photoinduced magnetic polaron ensemble indeed follows a Langevin function.

Next we investigate the possibility of generating a higher population of photoinduced polarons by increasing the pump intensity. Figure 3(a) shows the dependence of the PFR as a function of pump intensity for $T = 5$ K. As the pump intensity is increased, a linear background appears, whose slope is proportional to the pump intensity, suggesting a heating effect. A temperature increase of the bulk by ΔT will cause a change in its magnetization by

$$\Delta M = \frac{\partial M}{\partial T} \Delta T. \tag{9}$$

Here ΔM represents the change in magnetization due to sample heating within the pump-light penetration depth $d_{\mathrm{Pol}} = \frac{1}{\alpha}$, which from Eq. (1) is given by

$$\Delta M = \frac{\Delta\theta_F}{V d_{\mathrm{Pol}}}. \tag{10}$$

Similarly, $\frac{\partial M}{\partial T}$ is also related to the bulk Faraday rotation,

$$\frac{\partial M}{\partial T} = \frac{1}{V d_{\mathrm{Sample}}} \frac{\partial \theta_F}{\partial T}. \tag{11}$$

At fields sufficiently large, when the polaron magnetization is saturated, only a thermal effect can contribute to the slope of ΔM. Therefore, substituting Eqs. (10) and (11) in Eq. (9), and resolving for ΔT, we get

$$\Delta T = \frac{d_{\mathrm{Sample}}}{d_{\mathrm{Pol}}} \frac{\text{slope of } \Delta\theta_F \text{ at high fields}}{\text{slope of } \frac{\partial \theta_F}{\partial T}}, \tag{12}$$

where the slope of $\frac{\partial \theta_F}{\partial T}$ was taken from the inset of Fig. 3(c), and the slope of $\Delta\theta_F$ was taken from the high-field limit in Figs. 3(a) and 3(b).

The temperature increase ΔT calculated from Eq. (12) is shown as a function of the pump intensity in Fig. 3(d). Our interpretation in terms of a heating effect is confirmed by the photoinduced Faraday rotation curves as a function of intensity, done at a temperature of 50 K [Fig. 3(b)]. Because for EuTe the Faraday rotation dependence has the typical behavior of an antiferromagnet, with a maximum at the Néel temperature [see Fig. 3(c)], the slope of the thermal background seen in the PFR signal should change from positive

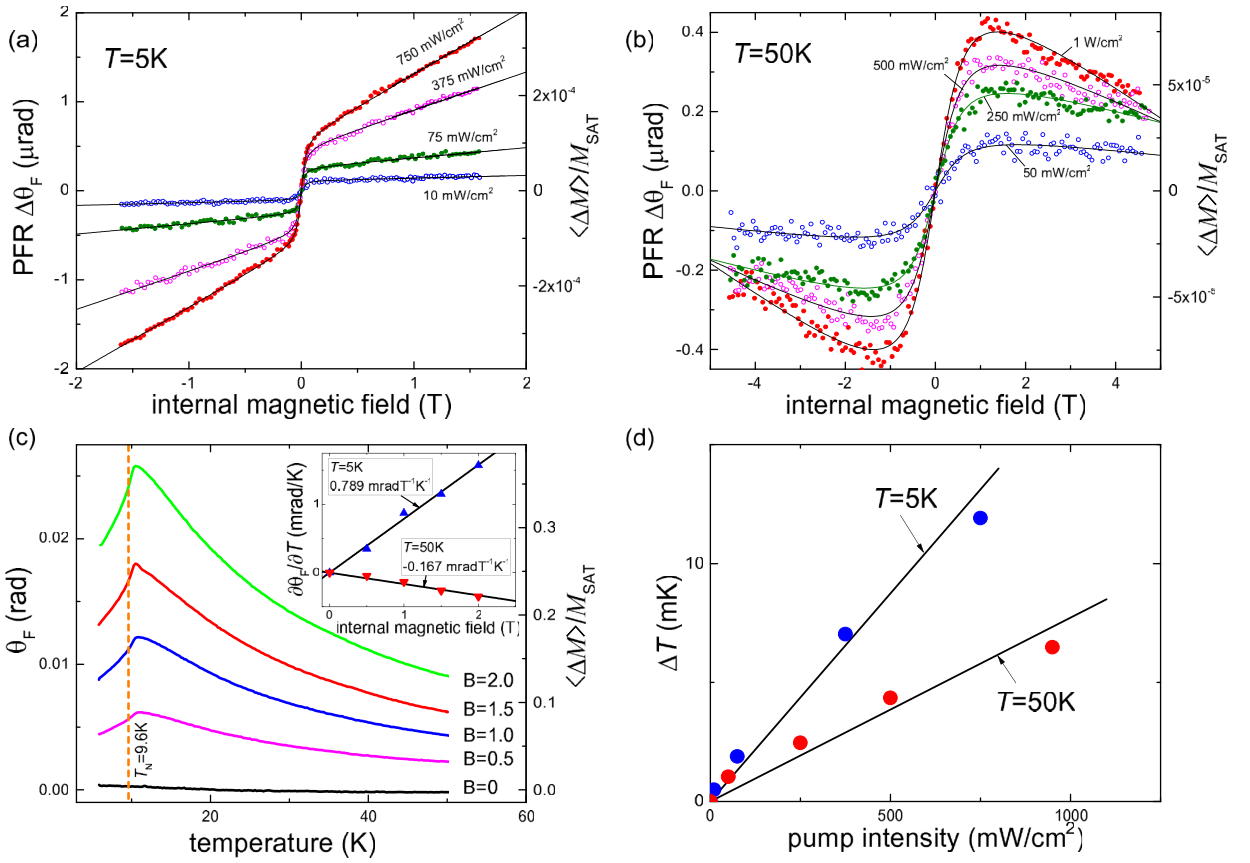

FIG. 3. (a) Photoinduced Faraday rotation at 5 K and (b) at 50 K. (c) Faraday rotation by the bulk EuTe sample as a function of temperature for various magnetic fields. (Notice that for our sample the observed Néel temperature is slightly larger than the accepted value of 9.6 K for EuTe, in agreement with direct measurements reported in Ref. [13]). The slope of the dependance of $\partial\theta_F/\partial T$ on B is shown in the inset. (d) The deduced temperature modulation of the illuminated region is shown as a function of the pump intensity for $T = 5$ K and $T = 50$ K.

to negative when we cross the Néel temperature. This is exactly what we observe, as can be seen from Fig. 3(a) for $T = 5$ K, where the thermal background has a positive slope, and Fig. 3(b) for $T = 50$ K, where the slope of the background signal is negative. The temperature modulation at $T = 50$ K was found by using Eq. (12), and it is also shown in Fig. 3(d). At 50 K the heating effect is smaller than at 5 K due to a larger heat capacity of the EuTe crystal [21]. Another aspect worthy of comment is that, upon closer inspection of Fig. 3(d), the temperature modulation ΔT presents a slightly sublinear dependence on pump intensity. This can be attributed to the fact that, for a larger excitation power, the effective volume excited by light increases, because the threshold excitation light penetrates deeper into the sample. In this case, the temperature increase for doubled excitation power will obviously be less than doubled, which explains the sublinear behavior of ΔT on the excitation power.

Having subtracted the linear thermal background from the $\Delta\theta_F$ vs B curves, as deduced above, the saturation polaron magnetization $\Delta\theta_F^{\mathrm{SAT}}$ for every pump intensity was extracted and it is plotted in Fig. 4. $\Delta\theta_F^{\mathrm{SAT}}$ increases sublinearly with pump intensity, indicating that polarons are less and less efficiently generated when the pump intensity is increased. Taking into account that optical absorption leads to an exponentially decreasing pump intensity below the surface of

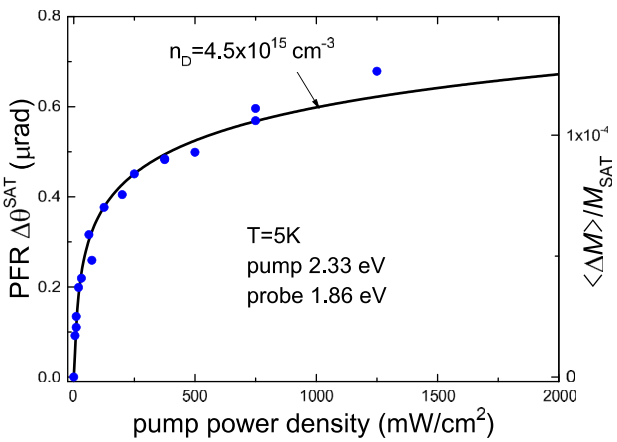

FIG. 4. Dots show the photoinduced Faraday rotation angle at saturation as a function of the pump intensity. The full line shows a fit of the dots with Eq. (14), which yields the maximum polaron concentration to be $n_{\mathrm{D}} = 4.5\times10^{15}$ cm^{-3}.

the sample, then the concentration of photogenerated polarons at a depth x below the surface will be

$$n_{\mathrm{Pol}}(x) = \chi \frac{p e^{-\alpha x} \alpha}{h\nu} \tau_0. \tag{13}$$

We shall assume, however, that the concentration of polarons that can be generated is limited by a maximum value, represented by n_{D}. Then the photoinduced Faraday rotation in the saturated fields will be given by

$$\Delta\theta_F^{\mathrm{SAT}} \sim \int_0^\infty n_{\mathrm{Pol}}(x)dx = \frac{n_{\mathrm{D}}}{\alpha} \begin{cases} \frac{p}{p_{\mathrm{D}}} & \text{if } p < p_{\mathrm{D}} \\ \left(1 + \ln \frac{p}{p_{\mathrm{D}}}\right) & \text{if } p > p_{\mathrm{D}}, \end{cases} \tag{14}$$

where $p_{\mathrm{D}} = \frac{n_{\mathrm{D}} h\nu}{\chi \alpha \tau_0}$. Equation (14) gives a photoinduced Faraday rotation angle that increases linearly with pump intensity for $p < p_{\mathrm{D}}$ and logarithmically for $p > p_{\mathrm{D}}$. Figure 4 shows that Eq. (14) provides a very good fit of our data, whereby n_{D} is the single adjustable parameter, yielding $n_{\mathrm{D}} = 4.5\times10^{15}$ cm^{-3}. This is again far less than the concentration of polarons that would completely fill the excited layer, $(\frac{4}{3}\pi R_{\mathrm{Pol}}^3)^{-1} = 1.3\times10^{19}$ cm^{-3}. We attribute the limited concentration of polarons that can be photogenerated to their binding by residual defects of concentration n_{D}. At $T = 5$ K, these bound polarons are long-lived—their lifetime is 15 μs [7]—and therefore have a supremacy over magnetic polarons seen in the photoluminescence, which have a much shorter lifetime, of the order of a nanosecond [22]. The shorter lifetime implies a stationary concentration of magnetic polarons that is four orders of magnitude smaller, and effectively only the long-lived magnetic polarons will be observed in the photoinduced Faraday rotation. A plausible source of defects at a low concentration of the order of 10^{15} cm^{-3} is the unbalanced stoichiometry of the Eu and Te atomic fluxes during the MBE growth. It should be observed that the binding of polarons to defects provides further support for our previous assumption that photoexcited polarons remain localized in the penetration layer of the pump light and do not diffuse into the interior of the EuTe crystal.

Equation (7) can be rewritten as

$$\Delta\theta_F(B,T) = \Delta\theta_F^{\mathrm{SAT}}(T) L\left(\frac{\mu_{\mathrm{Pol}} B}{k_B T}\right), \tag{15}$$

where $\Delta\theta_F(B,T)$ is the photoinduced Faraday rotation at a field B and a temperature T, and $\Delta\theta_F^{\mathrm{SAT}}(T)$ is the corresponding saturation value, depicted in Fig. 2. The measured data for various temperatures was fitted with Eq. (15), yielding two parameters for each temperature: the magnetic moment of the photoinduced magnetic polaron, $\mu_{\mathrm{Pol}}(T)$, and the Faraday rotation step height when B is varied, $\Delta\theta_F^{\mathrm{SAT}}(T)$ (see Fig. 2). It is worth pointing out that the polaron magnetic moment is the only parameter defining the smoothness of the step, so the value for μ_{Pol} obtained from the fit is independent of any other parameter entering Eq. (15), such as the polaron lifetime and steady-state population, which depend on temperature. Figure 5(a) shows the polaron magnetic moment as a function of temperature so obtained. For comparison, the dashed line in Fig. 5(a) is given by the magnetic moment associated with

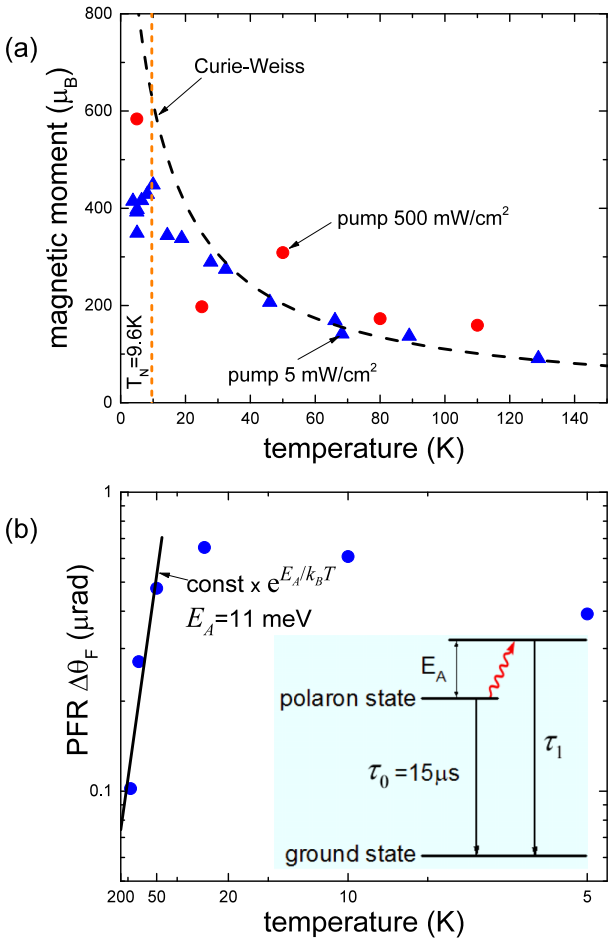

FIG. 5. (a) Temperature dependence of the magnetic moment of a polaron. (b) Temperature dependence of the photoinduced Faraday rotation angle at saturation. Above T ~ 50 K, $\Delta\theta_F^{\mathrm{SAT}}$ decreases exponentially with a characteristic activation energy of $E_A = 11$ meV. The inset shows schematically the magnetic polaron energy level, the ground state (when the photoexcited electron is absent), and the thermally activated state, which drains the polaron population when the temperature of the sample is increased.

the polaron sphere

$$\mu_{\mathrm{Pol}} = \tfrac{4}{3}\pi R_{\mathrm{Pol}}^3 \langle M \rangle, \tag{16}$$

where $\langle M \rangle$ is the average EuTe magnetization within the magnetic polaron sphere under the action of the exchange field of the photoexcited electron, $B_{\mathrm{Xf}} \approx 1$ T [5,6], taken in the Curie–Weiss approximation [18]

$$\langle M \rangle = n_{\mathrm{Eu}} \mu_{\mathrm{Eu}} \frac{g\mu_B(S+1)}{3k_{\mathrm{B}}} \frac{B_{\mathrm{Xf}}}{T + T_{\mathrm{N}}}.$$

It can be seen that the Curie–Weiss law describes the data quite well, without any adjustable parameter.

Finally, Fig. 5(b) shows a plot of the second parameter obtained from the fit, i.e., the photoinduced Faraday rotation at the saturation level, $\Delta\theta_F^{\mathrm{SAT}}(T)$, as a function of temperature. Above 100 K, the photoinduced Faraday rotation decreases exponentially with an activation energy

of about 11 meV. The rapid decrease of the photoinduced Faraday rotation signal is interpreted in terms of the thermal activation of a fast recombination channel, which causes a reduction of the polaron lifetime and hence of the steady-state polaron population. The thermally activated magnetic polaron quenching process is illustrated by the energy-level scheme shown in the inset of Fig. 5(b).

In conclusion, we have shown that EuTe can be magnetized by light through optical generation of magnetic polarons, with a quantum efficiency of $\chi \sim 0.09$ and a maximum concentration, which is about 4.5×10^{15} cm^{-3} in the case of the sample studied in this work. Such a low concentration is evidence that the magnetic polarons are bound to defects, plausibly generated during the growth process due to a deviation from stoichiometry. A path to clarify this point would be to investigate samples with an intentional deviation from stoichiometry and check if the deviation correlates with the maximum polaron concentration. At low temperatures, the polarons are immobile and do not diffuse out of the illuminated volume. The polaron population can be thermally quenched, with an activation energy of 11 meV, which could be due to thermally activated recombination, or to polaron diffusion out of the path of the probe beam. Thus, we demonstrated a novel approach for the optical manipulation of magnetic states in EuTe, which in principle should be valid for any intrinsic magnetic semiconductor, as well as for diluted semiconductors and for hybrid ferromagnetic-semiconductor structures.

This work was supported by the Brazilian agency CNPq (Projects 401694/2012-7, 307400/2014-0, and 456188/ 2014-2) and by the Ministry of Education and Science of the Russian Federation (Project ID RFMEF161315X0048/ 14.613.21.0048). A.R.N. was supported by a fellowship from CAPES-Brazil.

[1] A. Kirilyuk, A. V. Kimel, and T. Rasing, Rev. Mod. Phys. **82**, 2731 (2010).
[2] T. Makino, F. Liu, T. Yamasaki, Y. Kozuka, K. Ueno, A. Tsukazaki, T. Fukumura, Y. Kong, and M. Kawasaki, Phys. Rev. B **86**, 064403 (2012).
[3] M. Matsubara, A. Schroer, A. Schmehl, A. Melville, C. Becher, M. Trujillo-Martinez, D. G. Schlom, J. Mannhart, J. Kroha, *et al.*, Nat. Commun. **6**, 6724 (2015).
[4] R. R. Subkhangulov, A. B. Henriques, P. H. O. Rappl, E. Abramof, T. Rasing, and A. V. Kimel, Sci. Rep. **4**, 4368 (2013).
[5] A. B. Henriques, G. D. Galgano, E. Abramof, B. Diaz, and P. H. O. Rappl, Appl. Phys. Lett. **99**, 091906 (2011).
[6] A. B. Henriques, F. C. D. Moraes, G. D. Galgano, A. J. Meaney, P. C. M. Christianen, J. C. Maan, E. Abramof, and P. H. O. Rappl, Phys. Rev. B **90**, 165202 (2014).
[7] A. B. Henriques, G. D. Galgano, P. H. O. Rappl, and E. Abramof, Phys. Rev. B **93**, 201201(R) (2016).
[8] T. Dietl, Acta Phys. Pol. **94**, 111 (1998).
[9] *Introduction to the Physics of Diluted Magnetic Semiconductors*, edited by J. Kossut and J. A. Gaj, Springer Series in Materials Science (Springer, Berlin, Heidelberg, 2010).
[10] T. Kasuya, A. Yanase, and T. Takeda, Solid State Commun. **8**, 1543 (1970).
[11] E. L. Nagaev, Phys. Status Solidi B **145**, 11 (1988).
[12] A. Mauger and D. L. Mills, Phys. Rev. B **31**, 8024 (1985).
[13] B. Díaz, E. Granado, E. Abramof, P. H. O. Rappl, V. A. Chitta, and A. B. Henriques, Phys. Rev. B **78**, 134423 (2008).
[14] C.-Y. Chang, L. Wang, J.-T. Shy, C.-E. Lin, and C. Chou, Rev. Sci. Instrum. **82**, 063112 (2011).
[15] A. Mauger and C. Godart, Phys. Rep. **141**, 51 (1986).
[16] L. K. Hanamoto, A. B. Henriques, N. F. Oliveira, P. Rappl, E. Abramof, and Y. Ueta, J. Phys.: Condens. Matter **16**, 5597 (2004).
[17] A. B. Henriques, A. Wierts, M. A. Manfrini, G. Springholz, P. H. O. Rappl, E. Abramof, and A. Y. Ueta, Phys. Rev. B **72**, 155337 (2005).
[18] S. Blundell, *Magnetism in Condensed Matter* (Oxford University Press, Oxford, UK, 2001).
[19] R. T. Lechner, G. Springholz, T. U. Schülli, J. Stangl, T. Schwarzl, and G. Bauer, Phys. Rev. Lett. **94**, 157201 (2005).
[20] N. F. Mott, in *Metal-Insulator Transitions*, 2nd ed., Springer Series in Materials Science (Taylor & Francis, London, 1990), p. 93.
[21] I. A. Smirnov, Phys. Status Solidi A **14**, 363 (1972).
[22] W. Heiss, R. Kirchschlager, G. Springholz, Z. Chen, M. Debnath, and Y. Oka, Phys. Rev. B **70**, 035209 (2004).

Journal of Applied Physics ARTICLE scitation.org/journal/jap

Converting Faraday rotation into magnetization in europium chalcogenides

Cite as: J. Appl. Phys. **126**, 095701 (2019); doi: 10.1063/1.5116150
Submitted: 21 June 2019 · Accepted: 11 August 2019 ·
Published Online: 3 September 2019

S. C. P. van Kooten,[1,a)] P. A. Usachev,[1,b)] X. Gratens,[1] A. R. Naupa,[1] V. A. Chitta,[1] G. Springholz,[2] and A. B. Henriques[1,c)]

AFFILIATIONS

[1]Instituto de Fisica, Universidade de Sao Paulo, 05315-970 Sao Paulo, Brazil
[2]Institut für Halbleiter und Festkörperphysik, Johannes Kepler Universität Linz, 4040 Linz, Austria

[a)]**On leave from:** Department of Applied Physics, Eindhoven University of Technology, Eindhoven 5612 AZ, The Netherlands.
[b)]**Permanent address:** Ioffe Institute, 194021 St. Petersburg, Russia.
[c)]andreh@if.usp.br.

ABSTRACT

We present a simple semiclassical model to sustain that in europium chalcogenides (EuX), Faraday rotation (FR) in the transparency gap is proportional to the magnetization of the sample, irrespective of the material's magnetic phase, temperature, or applied magnetic field. The model is validated by FR and magnetization measurements in EuSe in the temperature interval 1.7–300 K, covering all EuSe magnetic phases (paramagnetic, antiferromagnetic type I or type II, ferrimagnetic, and ferromagnetic). Furthermore, by combining the semiclassical model with the explicit electronic energy structure of EuX, the proportionality coefficient between magnetization and FR is shown to be dependent only on the wavelength and the bandgap. Due to its simplicity, the model has didactic value; moreover, it provides a working tool for converting FR into magnetization in EuX. The possible extension of the model to other intrinsic magnetic semiconductors is discussed.

I. INTRODUCTION

Faraday and Kerr rotations are powerful investigation tools of spin phenomena, the use of which have led, for example, to the demonstration of the spin Hall effect.[1,2] Modern technology allows the measurement of extremely small Faraday rotation (FR) angles, in the nanoradian range,[3] so much that even the contribution of a single electron to the FR has been reported.[4] Time-resolved FR gives access to fundamental parameters of spin coherence, such as its formation and extinction times.[5–9] However, in most reports, FR is used only as an indicative measure of spin coherence, and it is not converted numerically into the associated magnetization. A quantitative connection between FR and magnetization is the subject of the present report.

In basic books on solid state physics,[10] and in the literature specialized on magneto-optics,[11–13] FR per unit length of material is often described for diamagnetic materials, where FR is proportional to the magnetic field, B. In a separate class of materials, the diluted magnetic semiconductors (DMS), FR was studied extensively, and various mechanisms of FR have been identified.[14] However, the topic of the present investigation are concentrated, or intrinsic, magnetic semiconductors, whereby the magnetic atoms give origin to the top valence band, whose presence is essential for the FR, and, therefore, the mechanisms seen in DMS, or in diamagnetic semiconductors, do not apply.

For the diamagnetic case, a proportionality between FR and B can be justified by a simple classical model.[15,16] In contrast, in intrinsic magnetic semiconductors, the assumption of a constant FR/B ratio fails squarely, as shown in Ref. 17. In many magnetic semiconductors, FR is proportional to the magnetization, as demonstrated in Ref. 18, using Maxwell equations and the polarizability tensor for a cubic crystal. The proportionality between FR and magnetization has also been demonstrated for EuTe[19] and other concentrated[20,21] and diluted magnetic semiconductors,[22] using quantum mechanics, but these calculations are very involved and require a detailed knowledge of the electronic structure of the investigated material. A simple conceptual model, based on elementary classical ideas, justifying that FR can be proportional to the magnetization in an intrinsic magnetic semiconductor, is lacking, and this work fills this gap.

In this paper, we develop a simple semiclassical model, showing that in europium chalcogenides, where the magnetic atoms are the source of the highest energy valence band, for photon energies below the bandgap, FR is proportional to the magnetization, independently of the magnetic phase (paramagnetic, antiferromagnetic, ferrimagnetic, or ferromagnetic), temperature, or magnetic field. The model is validated by measurements of FR and magnetization in the 1.7–300 K temperature range and in 0–7 T magnetic fields. The material chosen for the validation was the intrinsic magnetic semiconductor EuSe, whereby adjusting the external parameters, all possible magnetic phases were covered. Our semiclassical model has the advantage over existing quantum-mechanical theories due to its simplicity. Moreover, we show that for EuX, the proportionality constant between FR and magnetization is dependent only on the photon energy and the bandgap of the semiconductor.

The paper is organized as follows. In Sec. II, FR is introduced; in Sec. III, the classical model for FR in a diamagnetic semiconductor is briefly reviewed; in Sec. IV, we introduce our semiclassical model for FR in EuX; in Sec. V, the proportionality between FR and magnetization for EuSe in any scenario is thoroughly demonstrated experimentally; and in Sec. VI, the semiclassical model is combined with the specific electronic energy structure of EuX to obtain a working expression for the proportionality constant between magnetization and FR.

II. FARADAY ROTATION BASICS

A linearly polarized light ray can be expressed as the superposition of two rays of equal intensity, one of which is circularly polarized according to the right-hand rule (RCP) and the other according to the left-hand one (LCP). The superposition on these rays on exiting the sample gives the FR angle, per unit length, at the wavelength λ,[11,15,23]

$$\theta_F = \pi \frac{n_- - n_+}{\lambda}, \tag{1}$$

where $n_\pm$ is the refractive index and the plus or minus sign applies to RCP or LCP, respectively. This formula shows that circular birefringence, i.e., the inequality between n_+ and n_-, is the source of FR.

In general, semiconductor materials will contain several valence bands contributing to the birefringence. Photons of energy within the bandgap of the semiconductor are closest to resonance with the top valence band; hence, the polarization effects of lower lying bands can be discarded in a first examination. The amplitude of the circular polarization induced in the crystal by the rotating electric field of the incoming light is given by[24,25]

$$P_0^\pm = N\alpha^\pm E_0, \tag{2}$$

where $\alpha^\pm$ is the electronic polarizability of the atoms forming the valence band, N is the number density of atoms in the solid, and E_0 is the electric field amplitude of the RCP or LCP incident wave. It should be emphasized that α in (2) is the polarizability of an atom "embedded in the solid," it is "not" the polarizability of an isolated atom. These polarizabilities are different from one another because the polarization of atoms, by light within the bandgap, is a perturbation and resonance effect. The electron-photon interaction resonance depends on the spacing between electronic energy levels, which in the solid differ from that of the isolated atom, due to energy band formation; hence, the polarizability of an embedded atom differs from that of an isolated one.

On the other hand, taking the photoinduced polarization to be the number density times the atomic polarizability, modified due to the atoms being embedded in the solid, as by (2), is known to provide a very good description of the linear optical properties of nonmetallic solids [see, for instance, Ref. 26, Sec. 1.4, formula (1.4.16)], which justifies the application of Eq. (2) to describe the Faraday effect in semiconductors.

Using the relation connecting the refractive index to the electronic polarizability,[25]

$$n_\pm^2 = 1 + \frac{N}{\varepsilon_0}\alpha^\pm, \tag{3}$$

we arrive at

$$n_- - n_+ = \frac{n_-^2 - n_+^2}{2n_0} = \frac{N}{\varepsilon_0}\frac{\alpha^- - \alpha^+}{2n_0}, \tag{4}$$

where $n_0 = (n_+ + n_-)/2$ is the refractive index that the material would have, if no other valence band was present except the one under scrutiny, and $\varepsilon_0 = 8.85 \times 10^{-12}$ F/m is the vacuum permittivity.

Equation (4) shows that for FR to be present, the induced polarization current in the valence orbitals must be different for LCP and RCP. This is explored in the models below.

III. CLASSICAL MODEL OF FR IN A DIAMAGNETIC SEMICONDUCTOR

To build a clear contrast between FR in a magnetic semiconductor, i.e., one that contains atoms with unpaired electrons, to FR in a diamagnetic semiconductor, whose electrons are all paired, let us review very briefly the well-known classical model for FR in the diamagnetic semiconductor. This simple classical model is based on the Lorentz oscillator model of atoms, and it is described in detail in Refs. 15 and 16.

For a nonmagnetic atom, its angular momentum (orbital and spin) is zero; therefore, there is no spatial orientation of the atom. Hence, by symmetry, both RCP and LCP will induce equal and opposite polarization currents; therefore, there will be no FR. However, if a magnetic field is applied in the direction of light travel (i.e., in the Faraday geometry), then the Lorentz force will have opposite effects on the LCP and RCP induced polarization currents, which become different from one another, and FR emerges. In the linear regime, the FR in this case is proportional to the intensity of the applied magnetic field.

IV. A SEMICLASSICAL MODEL CONNECTING FR TO THE MAGNETIZATION IN EUROPIUM CHALCOGENIDES

In EuX, the highest valence band states are formed by half-filled $4f$ orbitals of the Eu atom,[18] which are buried deep

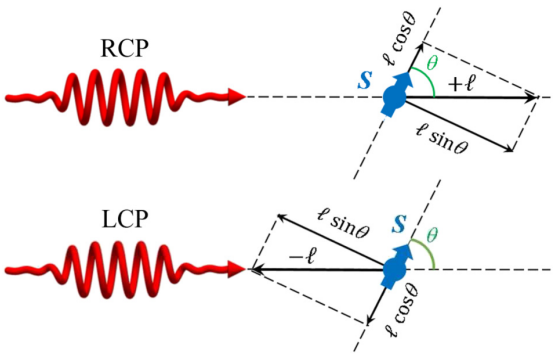

FIG. 1. The electric field E of the linearly polarized light is equivalent to the superposition of RCP (top) and LCP light of equal amplitude (bottom), carrying an angular momentum of $+\ell$ and $-\ell$, respectively.

within the ion, beneath the filled 5p shell; hence, the characteristics of the isolated orbital are well preserved.[27] Therefore, the spin of the Eu atom, S = 7/2, is maintained in the crystal.

In the semiclassical approach, the magnetic moment, or spin, of an atom is associated with a circulating electrical current, whose direction and magnitude are described by a vector $\boldsymbol{S}$. Let us inspect the interaction of the incident linearly polarized light with an average Eu atom in the solid, whose spin $\boldsymbol{S}$ makes an angle θ with the direction of light propagation, as depicted in Fig. 1. We express the incident light as a superposition of RCP and LCP, which carry an angular momentum $+\ell$ and $-\ell$, respectively, along the direction of light travel. The angular momentum vector of the incoming RCP or LCP light can be divided into two components, parallel and perpendicular to the vector $\boldsymbol{S}$, as shown in Fig. 1. By symmetry, in a direction perpendicular to $\boldsymbol{S}$, RCP and LCP will induce identical polarizations in magnitude, but in opposite directions, totaling zero. Therefore, birefringence must be associated with the circular polarization light that induces parallel to $\boldsymbol{S}$, which is proportional to the projection of the light angular momenta onto $\boldsymbol{S}$. Hence, when the angle between $\boldsymbol{S}$ and the direction of light travel is increased from zero to θ, the induced polarization is reduced by a factor of $\cos\theta$, i.e.,

$$P_0^{\pm} = N\alpha_{\parallel}^{\pm} E_0 \cos\theta, \tag{5}$$

where $\alpha_{\parallel}^{\pm}$ is the circular electronic polarizability of the solid, when its spins are fully aligned with the direction of light travel ($\theta = 0$ in Fig. 1).

On the other hand, the magnetization projection in the direction of light propagation, M, is given by

$$M = N\mu^{\star}\cos\theta; \tag{6}$$

hence, a comparison between Eqs. (5) and (6) leads to

$$P_0^{\pm} = \frac{M}{\mu^{\star}}\alpha_{\parallel}^{\pm} E_0. \tag{7}$$

Equating (7) and (2) gives

$$\alpha^{\pm} = \frac{M}{M_{\mathrm{SAT}}}\alpha_{\parallel}^{\pm}, \tag{8}$$

where $M_{\mathrm{SAT}} = N\mu^{\star}$ is the saturation magnetization.

Substituting (8) in (4), and using (1), we get

$$\theta_F^{\mathrm{mag}} = \frac{\pi}{\lambda}\frac{N}{\varepsilon_0}\frac{M}{M_{\mathrm{SAT}}}\frac{\alpha_{\parallel}^{-} - \alpha_{\parallel}^{+}}{2n_0}. \tag{9}$$

Equation (9) shows that the contribution from Eu atoms to the FR is proportional to their magnetization, the proportionality coefficient being determined by the polarizability. Because the polarizability is determined by the electronic energy structure, the ratio θ_F/M will remain unchanged as long as the relative position of the electronic energy levels, as well as their occupation, is invariant. In a semiconductor, the essential parameter is the energy gap, E_G, between the valence and the conduction bands. If $k_BT \ll E_G$, the occupation of the electronic energy levels will be unchanged, which gives a measure of the range of temperatures in which θ_F/M is expected to be constant in EuX, except for deviations due to bandgap variations. Thus, θ_F/M behaves in the same fashion as the refractive index of dielectrics, which is also tied to variations of the bandgap.[28,29] As long as the photon energy is within the bandgap, which is the situation considered in this work, contributions from other valence bands will generally be much smaller, due to their excitations being off-resonance with the incident photons, and the central result given by Eq. (9) will remain valid.

The significance of the semiclassical model, with which the proportionality between FR and magnetization was demonstrated as expressed by Eq. (9), based on a simple argument of forced oscillations and symmetry, can be well appreciated if we compare our model to the full quantum mechanical calculation, described in detail in Ref. 19, which requires the use of perturbation theory, Wigner rotations of spins, and statistical averaging. The end result is the same, but the semiclassical model is much simpler and transparent.

V. TEST OF THE SEMICLASSICAL MODEL IN THE MAGNETIC SEMICONDUCTOR EuSe

In Sec. IV, it was argued that in EuX, FR is proportional to the magnetization. In this section, this hypothesis is thoroughly tested using the magnetic semiconductor EuSe. This material was chosen for the test because of its very rich magnetic phase diagram; therefore, by applying a magnetic field and adjusting the temperature, the proportionality between FR and magnetization can be tested in all possible magnetic scenarios.

The EuSe crystalline samples were grown by molecular beam epitaxy (MBE) onto the (111) BaF_2 substrate. Because of the almost perfect lattice constant matching ($a = 6.191$ Å and $a = 6.196$ Å

for EuSe and BaF_2, respectively), the EuSe layer with μm thickness was bulklike and nearly unstrained.[33] The data presented here were obtained on sample no. 1529, whose EuSe epilayer thickness is 2.5 μm. The magnetization was measured using a SQUID magnetometer, which had a magnetic moment resolution better than 10^{-11} Am^2. The FR was measured using a linearly polarized beam from a semiconductor laser as the monochromatic light source and a polarization bridge containing balanced photodetectors. The contribution coming from the substrate to the FR was measured separately, using a substrate piece without the epilayer, and subtracted from the FR produced by the EuSe epilayer.

In fields up to 0.2 T at all temperatures, both the magnetization and the FR angle displayed a linear dependence on B: typical results are shown in Fig. 2(a). It can be seen that the slopes of θ_F and M vary several orders of magnitude with temperature; however, the ratio θ_F/M, obtained from the slopes for $B < 0.2$ T,

$$\frac{\theta_F}{M} = \frac{d\theta_F/dB}{dM/dB}, \tag{10}$$

and shown in Fig. 2(b) for the 4.8–300 K interval, remains constant. The vertical bars represent the estimated experimental error, which increases toward room temperature, when the response from the substrate becomes comparable to that of the epilayer, both in θ_F and in M measurements.

For the photon energy of 1.865 eV, which is in near resonance with the bandgap, θ_F/M increases slightly when the sample is cooled below 20 K. This is explained by the concomitant narrowing of the gap (depicted by the empty circles), which makes the light even closer to resonance with the bandgap, which enhances the FR angle, as explained at the end of this section.

In the temperature interval 4.8–300 K examined so far, EuSe is in the paramagnetic phase, because its Néel temperature is $T_N = 4.75$ K;[9] the magnetic phase diagram of our sample was measured, and it is shown in Fig. 3(a). To investigate θ_F/M in the phases other than the paramagnetic one, the magnetization and FR, at various photon energies, were measured at $T = 1.7$ K as a function of field. At this temperature, the magnetic field drives the EuSe sample through an antiferromagnetic, a ferrimagnetic, and a ferromagnetic phase, as Fig. 3(a) shows (see also Ref. 34). A comparison of the magnetization and FR curves can be seen in Fig. 3(b), both exhibit an almost identical dependence on B; minor differences in the B-dependencies are within the range of the experimental uncertainties. The dependence of θ_F/M on B is shown in Fig. 4(a), for various photon energies. At low fields, θ_F/M remains at the same value measured in the paramagnetic phase up to 300 K.

Increasing the field, θ_F/M increases and tends to a saturation. This process can be understood within the frame of the semiclassical model of Secs. II and IV. When B is increased at $T = 5$K, the EuSe bandgap narrows, as shown in Fig. 4(b), because the applied field imposes ferromagnetic order over a paramagnetic lattice, which lowers the energy of the conduction electrons due to the band-lattice exchange interaction. The dichroic spectrum showing the LCP/RCP splitting was investigated in Ref. 35. A similarly large bandgap redshift of about 100 meV by applying a magnetic field is also observed in YIG,[36] and it is also associated with the

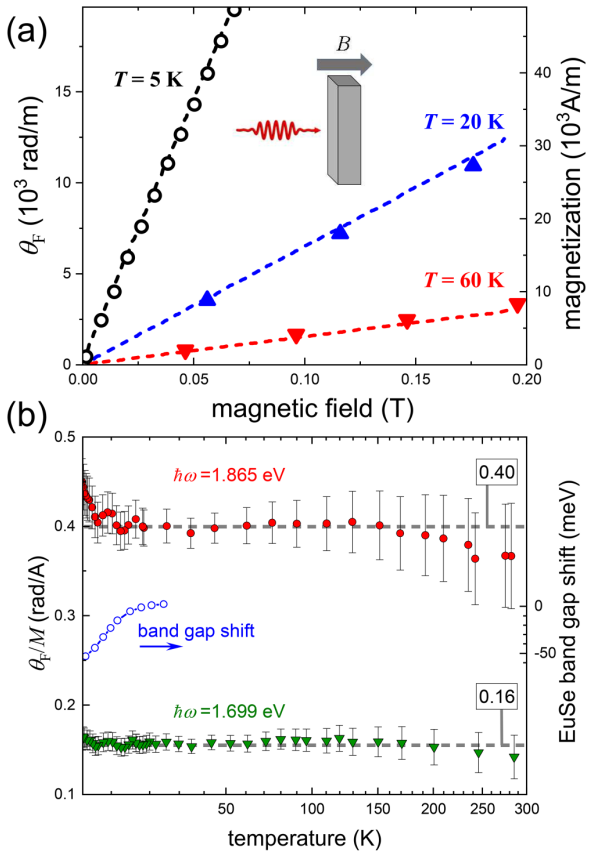

FIG. 2. (a) Lines depict FR, for photons of energy 1.865 eV, while dots represent magnetization, as a function of applied magnetic field, for $T = 5$, 20, and 60 K. The magnetic field was applied perpendicular to the EuSe epitaxial layer. (b) Ratio θ_F/M as a function of temperature for photons with energy 1.865 eV (full circles) and 1.699 eV (triangles). The error bars were estimated at 15% at low temperatures but increase toward room temperature, when the contribution to the epilayer becomes comparable to that of the substrate. Below $T = 20$ K, θ_F/M increases slightly for 1.865 eV, which is explained by the concomitant narrowing of the bandgap, shown by the empty circles, taken from Ref. 30.

conduction band-lattice exchange interaction. As Fig. 4 shows, the bandgap redshift saturates around 2.5 T.[37] The increase of the FR angle with increasing applied magnetic field is because the photon energy of the incident light becomes closer to resonance with the bandgap, which implies that the electronic polarizability increases, as the classical Lorentz model of forced atomic oscillators predicts.

VI. PROPORTIONALITY CONSTANT BETWEEN MAGNETIZATION AND FR IN EUROPIUM CHALCOGENIDES

In Sec. IV, we showed that in EuX, FR is proportional to the magnetization. Here, we go a step forward and determine the

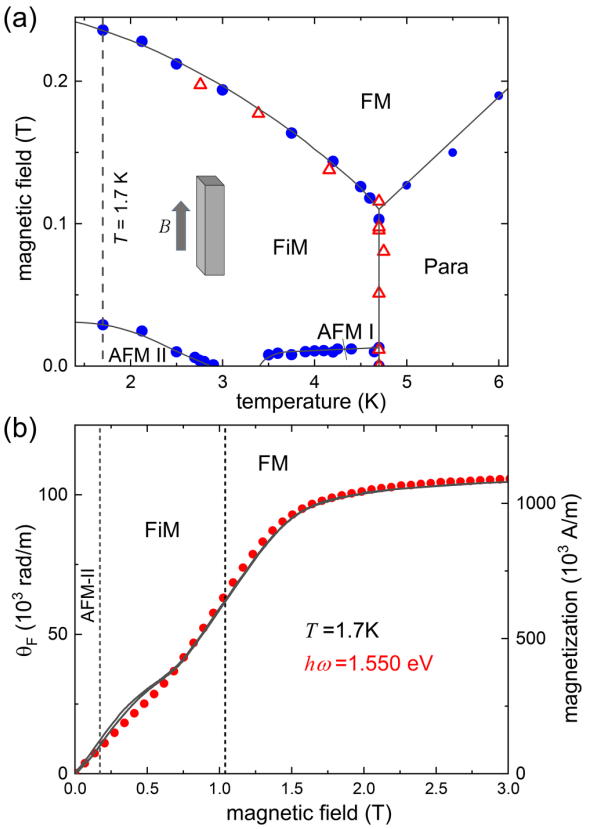

FIG. 3. (a) Magnetic phase diagram of the studied EuSe layer. The full and open dots represent data obtained from M vs B (T = const) and M vs T (B = const) traces, respectively. The magnetic field was applied parallel to the surface of the epitaxial sample. The solid lines are guides to the eye. The dotted line shows that at $T = 1.7$ K, a magnetic field drives EuSe through an antiferromagnetic (AFMII), a ferrimagnetic (FiM), and a ferromagnetic (FM) phase. (b) Magnetization (solid line) and FR at $\hbar\omega = 1.55$ eV (dots), as a function of magnetic field, at $T = 1.7$ K. The magnetic field was applied perpendicular to the surface of the epitaxial sample. When B is applied perpendicular to the layer, the AFMII-FiM and FiM-FM phase boundaries are shifted to $B = 0.17$ T and $B = 1.04$ T, respectively, due to the demagnetization effect.[31] Vertical lines show the boundaries between the magnetic phases indicated.

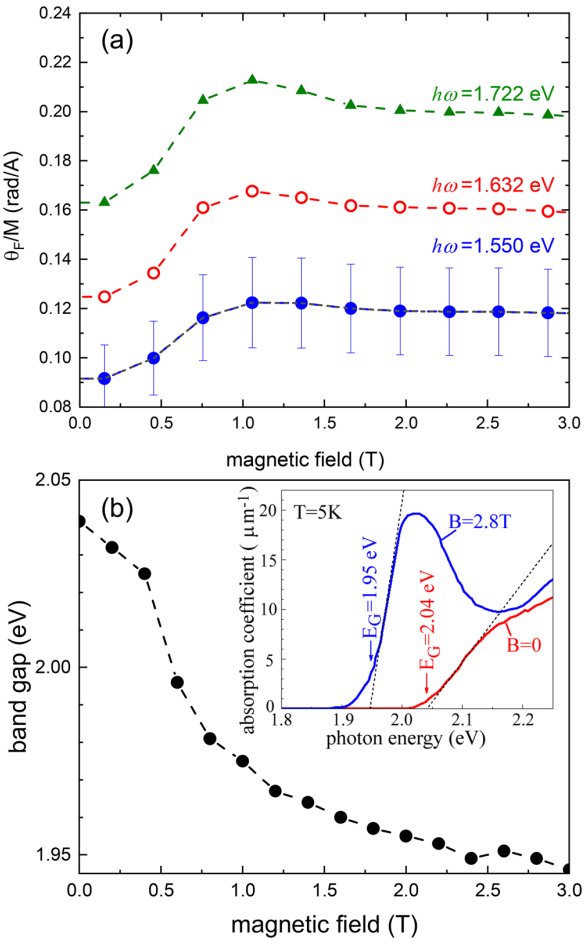

FIG. 4. (a) Ratio of the FR, at the indicated photon energies, to the magnetization, as a function of magnetic field, for $T = 1.7$ K. At low fields, the ratio increases beyond the estimated uncertainty of 15%; (b) EuSe bandgap as a function of B, obtained from optical absorption measurements as shown in the inset. The absorption experiments are detailed in Ref. 32.

proportionality coefficient in EuX, using their well-known specific electronic energy structure, sketched in Fig. 5.[18] First, we shall estimate the weight of the various valence bands to the FR. Using quantum-mechanical time dependent perturbation theory[26] applied to EuTe, it can be shown that[38]

$$\alpha^{\pm} = \frac{1}{2}\sum_{n}\frac{\left|\mu_{gn}^{\pm}\right|^2}{E_{ng} - \hbar\omega}, \tag{11}$$

where $|g\rangle$ represents the ground state of energy E_g, described by an electron in the valence band, $|n\rangle$ represents the excited states of energy E_n, corresponding to an electron in the conduction band, $E_{ng} = E_n - E_g$, and $\mu_{gn}^{\pm}$ is the electric dipole matrix element,

$$\mu_{gn}^{\pm} = -e\langle n|x \pm iy|g\rangle. \tag{12}$$

Equation (11) shows that the coupling through light between the ground and excited electronic states determines the induced polarization current.

In EuTe, when the spins are aligned with the direction of light by the application of a large magnetic field, the band-edge optical absorption becomes strongly dichroic[32,35,39,40] and shows two narrow peaks, one for LCP and another for RCP, split by $\sim 19\lambda_f$,[35] where λ_f is the spin-orbit coupling constant for the Eu^{3+} atom, as sketched on the left of Fig. 5. The circular dichroism is associated with optical transitions between the valence level, $^8S_{7/2}$, formed by the magnetic Eu atoms, into the $5d(t_{2g})$ conduction band. The equal height of the two lines implies that $\left|\mu_{gn}^{+}\right|^2 \sim \left|\mu_{gn}^{-}\right|^2 \sim \mu_{df}^2$. Taking the approximated absorption spectrum into account, (11) leads to

$$\alpha_{\parallel}^{-} \sim \frac{1}{2}\frac{\mu_{df}^2}{E_G - \hbar\omega}, \quad \alpha_{\parallel}^{+} \sim \frac{1}{2}\frac{\mu_{df}^2}{E_G + 19\lambda_f - \hbar\omega}. \tag{13}$$

Substituting (13) in (9), and using (3), we get

$$\theta_F^{\mathrm{mag}} \sim \frac{\pi}{\lambda}\frac{M}{M_{\mathrm{SAT}}}\frac{n_0^2 - 1}{2n_0}\frac{19\lambda_f}{E_G - \hbar\omega}. \tag{14}$$

In obtaining (14), the condition $19\lambda_f \ll E_G - \hbar\omega$ was assumed, which requires the incoming photons to be sufficiently away from resonance with the bandgap.

It must be emphasized, however, that to arrive at (14), we "did not" make any approximation concerning the EuX band-edge electronic energy structure, and we "did not" substitute the energy bands of EuTe by zero width atomic energy levels. We worked within the frame of the full [$^8S_{7/2}$—valence band and $5d(t_{2g})$—conduction band] model, which is specific for EuX and which has successfully described such effects as the continuous evolution of a 500 meV broad featureless absorption band at zero field to a doublet of sharp dichroic lines in high fields,[32,35,39,40] as well as second harmonic generation,[41,42] linear dichroism,[43] and Faraday rotation[19,44] in EuTe and EuSe. We simply exploited the well-known experimental fact that at high fields, when all Eu spins align ferromagnetically, two birefringent narrow lines emerge in the optical absorption threshold of EuX, their width being much less than the bandgap,[35,39,40] which has nothing to do with a substitution of bands by energy levels.

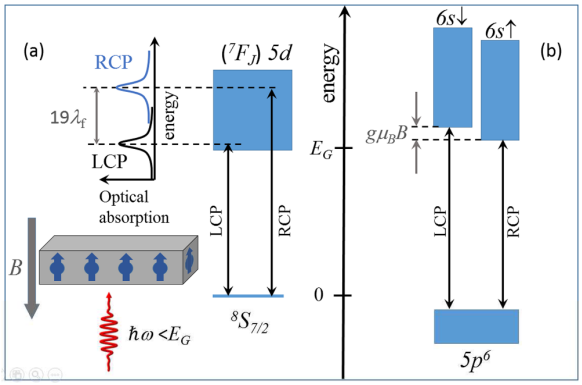

FIG. 5. Electronic levels in EuTe. (a) Under a strong magnetic field, the Eu spins are aligned ferromagnetically, and the absorption spectrum shows a strong magnetic circular dichroism, whereby the RCP and LCP absorption peaks, corresponding to transitions from the Eu atoms in the $S_{7/2}$ state to the $5d(t_{2g})$ conduction band, are split by $\sim 19\lambda_f$, where λ_f is the spin-orbit coupling constant for the Eu^{3+} ion.[35] (b) RCP and LCP optical transitions between the valence band formed by 5*p* orbitals of the Te atoms and a conduction band formed by 6*s* Eu states.[18,30]

Now, we shall inspect the contribution to the FR coming from valence bands generated by completely filled atomic states, whose magnetic moment is zero. In EuTe, just below the $^8S_{7/2}$ valence state, there is a valence band built from $5p^6$ shells of the Te atoms,[18] which can be polarized by the incoming light through the dipole-allowed admixture of empty 6*s* states, as indicated on the right-hand side in Fig. 5. In the absence of a magnetic field, the 5*p*-band will give no birefringence, because optical absorption associated with $5p \rightarrow 6s$ transitions will be identical in position and strength for RCP and LCP. However, when a magnetic field is applied, the RCP and LCP absorption bands are split by the Zeeman energy, $g\mu_B B$. Then, proceeding exactly in the same way as when obtaining (14), the diamagnetic contribution to the FR is found to be

$$\theta_F^{\mathrm{diamag}} \sim -\frac{\pi}{\lambda}\frac{n_1^2 - 1}{4n_1}\frac{g\mu_B B}{E_G - \hbar\omega}, \tag{15}$$

where n_1 is the refractive index associated with the diamagnetic valence band. Equation (15) shows that the diamagnetic FR is proportional to the magnetic field, in stark contrast to the contribution from the magnetic valence band, given by Eq. (14), which is proportional to the magnetization.

Dividing (14) by (15), the relative weight of the diamagnetic FR is found to be

$$\left|\frac{\theta_F^{\mathrm{diamag}}}{\theta_F^{\mathrm{mag}}}\right| \sim \frac{M_{\mathrm{SAT}}}{M}\frac{g\mu_B B}{19\lambda_f}, \tag{16}$$

where $n_0 \sim n_1$ was used. Given that $g\mu_B = 0.116$ meV/T and that $19\lambda_f = 180$ meV,[35] then the diamagnetic FR will generally be much smaller than the magnetic one.

We shall take a step further to investigate in more detail the proportionality coefficient between magnetization and FR. We rewrite Eq. (14) as

$$\frac{\theta_F}{M}\frac{E_G - \hbar\omega}{\hbar\omega} = \mathrm{const}, \tag{17}$$

where the constant is determined by the materials refractive index, spin-orbit coupling constant, and saturation magnetization. Equation (17) was tested by plotting θ_F/M as a function of photon energy, using data taken in a wide temperature and

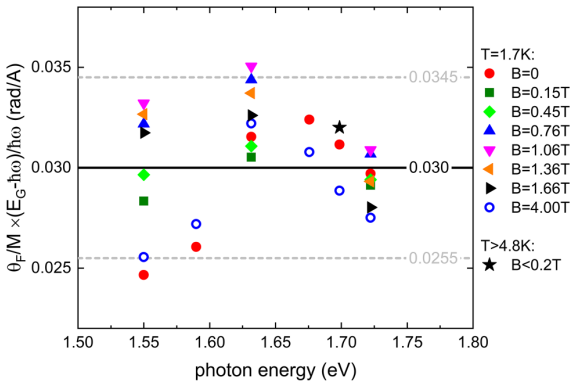

FIG. 6. Measured ratio θ_F/M multiplied by $(E_G - \hbar\omega)/\hbar\omega$, as a function of photon energy, for various magnetic fields at $T = 1.7$ K, and in the 1.7–300 K interval, for fields $B \leq 0.2T$. The thickness of the EuSe epilayer was 2.5 μm. The average is shown by the full line, and a 15% deviation is shown by the dashed lines.

magnetic field range, covering all EuSe magnetic phases, and Fig. 6 shows the result. It can be seen that the data points deviate from the average of 0.03 rad/A by at most 15%, which is the estimated error bar in our experiment, also shown in Fig. 6. The deviation at lower energies is larger, because the FR angle is smaller; hence, the experimental error is larger. This is quite remarkable, because the data shown in Fig. 6 cover a 300 K temperature and a 0–7 magnetic field interval, respectively, where all possible magnetic phases occur, where the ratio θ_F/M changes by an order of magnitude, and where M and θ_F vary several orders of magnitude; nevertheless, (17) remains constant within experimental error. This not only validates our semiclassical model, but it also makes Equation (17) a practical formula to describe θ_F/M in all circumstances, substituting a full complex quantum-mechanical calculation in EuX.

Equation (17) should remain valid for other intrinsic magnetic semiconductors, in which a valence level is formed by strongly localized atomic orbitals with nonzero magnetic moment. For the case of magnetic semiconductors where the top valence band is diamagnetic, FR will be a superposition of one component proportional to the magnetization and another proportional to B. As an example, GdN has a top valence band built from nitrogen $2p$ states,[45] situated above the localized $^8S_{7/2}$ valence state of the Gd rare earth atoms (i.e., the position of the p valence band and of the localized $^8S_{7/2}$ valence level, shown in Fig. 5 for EuTe and EuSe, is inverted in order). The magnetic circular dichroism observed in GdN[46] is an indication that FR will also be connected to the magnetization in this system. However, because in GdN the p valence band forms the bandgap, for below-the-gap FR the diamagnetic contribution may be of the same magnitude as the ferromagnetic one, making a more complicated scenario. An analysis of the relationship between FR and magnetization in GdN and its dependence on the photon energy will require a separate investigation.

VII. CONCLUSION

We developed a semiclassical model to show that in europium chalcogenides, the FR is proportional to the magnetization. The model is based on classical physics concepts only. Our model for FR in the magnetic semiconductors EuX adds to the well-known classical model of FR in a diamagnetic semiconductor, forming a didactic picture of the diversity of the FR in different solids. The model is validated by data taken on EuSe in a large temperature and magnetic field range, covering all possible magnetic phases. Moreover, we provided a formula connecting the Faraday rotation angle, the magnetization, the photon energy, and the semiconductor bandgap, which is a valuable practical solution for the conversion of FR into magnetization, at any temperature and magnetic phase in any member of the EuX family.

ACKNOWLEDGMENTS

This work was funded by CNPq (Project Nos. 307400/2014-0 and 456188/2014-2) and FAPESP (Project No. 2016/24125-5). P.A.U. acknowledges support by the Russian Science Foundation (Project No. 17-12-01314). G.S. acknowledges support by the Austrian Science Fund (Project No. P30960-N27).

REFERENCES

[1]S. A. Crooker, D. D. Awschalom, and N. Samarth, IEEE J. Sel. Top. Quantum Electron **1**, 1082 (1995).
[2]Y. K. Kato, R. C. Myers, A. C. Gossard, and D. D. Awschalom, Science **306**, 1910 (2004).
[3]S. A. Crooker, in *Coherent Spin Dynamics of Carriers and Magnetic Ions in Diluted Magnetic Semiconductors*, Springer Series in Materials Science, Vol. 144, edited by J. Kossut and J. A. Gaj (Springer-Verlag, Berlin, 2010), p. 305.
[4]M. Atatüre, J. Dreiser, A. Badolato, and A. Imamoglu, Nat. Phys. **3**, 101 (2007).
[5]D. D. Awschalom and J. M. Kikkawa, Phys. Today **52**(6), 33 (1999).
[6]A. Greilich, D. R. Yakovlev, A. Shabaev, A. L. Efros, I. A. Yugova, R. Oulton, V. Stavarache, D. Reuter, A. Wieck, and M. Bayer, Science **313**, 341 (2006).
[7]A. B. Henriques, R. C. Cordeiro, P. M. Koenraad, F. W. M. Otten, and M. Bayer, Phys. Rev. B **91**, 081303(R) (2015).
[8]A. Kirilyuk, A. V. Kimel, and T. Rasing, Rev. Mod. Phys. **82**, 2731 (2010).
[9]A. B. Henriques, X. Gratens, P. A. Usachev, V. A. Chitta, and G. Springholz, Phys. Rev. Lett. **120**, 217203 (2018).
[10]O. Madelung, *Introduction to Solid State Theory* (Springer-Verlag, Berlin, 1978), p. 299.
[11]H. Piller, "Faraday rotation," in *Semiconductors and Semimetals* (Elsevier, Amsterdam, 1972), pp. 103–179.
[12]K. Shinagawa, "Faraday and Kerr effects in ferromagnets," in *Magneto-Optics* (Springer, Berlin, 2000), pp. 137–177.
[13]N. Miura, *Physics of Semiconductors in High Magnetic Fields* (Oxford University Press, Oxford, 2008), p. 265.
[14]J. A. Gaj and J. Kossut, *Basic Consequences of sp-d and d-d Interactions in DMS*, Springer Series in Materials Science, Vol. 144, edited by J. Kossut and J. A. Gaj (Springer-Verlag, Berlin, 2010), p. 1.
[15]H. Becquerel, Comptes Rendus **125**, 679 (1897).
[16]A. Sommerfeld, *Optics* (Academic Press, New York, 1954), p. 101.
[17]H. Krenn, W. Herbst, H. Pascher, Y. Ueta, G. Springholz, and G. Bauer, Phys. Rev. B **60**, 8117 (1999).
[18]A. Mauger and C. Godart, Phys. Rep. **141**, 51 (1986).
[19]A. B. Henriques and P. A. Usachev, Phys. Rev. B **96**, 195210 (2017).
[20]Y. R. Shen, Phys. Rev. **133**, A511 (1964).
[21]Y. R. Shen and N. Bloembergen, Phys. Rev. **133**, A515 (1964).

[22]D. U. Bartholomew, J. K. Furdyna, and A. K. Ramdas, Phys. Rev. B **34**, 6943 (1986).
[23]J. C. Maxwell, *A Treatise on Electricity and Magnetism* (Clarendon Press, Oxford, 1873), Vol. 2, Chap. XXI.
[24]C. Kittel, *Introduction to Solid State Physics*, 7th ed. (John Wiley & Sons, New York, 1996), p. 389, formula (22).
[25]R. P. Feynman, R. B. Leighton, and M. L. Sands, *The Feynman Lectures on Physics* (Addison-Wesley, 1963–1965), Vol. 2, Chap. 11, formula (11–8), pp. 11–12.
[26]R. W. Boyd, *Nonlinear Optics* (Academic Press, 2003).
[27]S. Blundell, *Magnetism in Condensed Matter* (Oxford University Press, Oxford, 2001).
[28]P. J. L. Hervé and L. K. J. Vandamme, J. Appl. Phys. **77**, 5476 (1977).
[29]J. Talghader and J. S. Smith, Appl. Phys. Lett. **66**, 335 (1995).
[30]P. Wachter, CRC Crit. Rev. Solid State Sci. **3**, 189 (1972).
[31]S. Blundell, *Magnetism in Condensed Matter* (Oxford University Press, Oxford, 2001), Appendix D, p. 214.
[32]A. B. Henriques, G. D. Galgano, B. L. Diaz, P. H. O. Rappl, and E. Abramof, J. Phys. Condens. Matter **19**, 406234 (2007).
[33]B. Diaz, E. Granado, E. Abramof, P. H. O. Rappl, V. A. Chitta, and A. B. Henriques, Phys. Rev. B **78**, 134423 (2008).
[34]R. T. Lechner, G. Springholz, T. U. Schülli, J. Stangl, T. Schwarzl, and G. Bauer, Phys. Rev. Lett. **94**, 157201 (2005).
[35]A. B. Henriques, A. Wierts, M. A. Manfrini, G. Springholz, P. H. O. Rappl, E. Abramof, and A. Y. Ueta, Phys. Rev. B **72**, 155337 (2005).
[36]R. Vidyasagar, O. A. Santos, J. Holanda, R. O. Cunha, F. L. A. Machado, P. R. T. Ribeiro, A. R. Rodrigues, J. B. S. Mendes, A. Azevedo, and S. M. Rezende, Appl. Phys. Lett. **109**, 122402 (2016).
[37]The bandgap was determined by extrapolating the linear region in the absorption curve to the abscissa, as shown in the inset of Fig. 4(b). Other authors have estimated the bandgap through the photon energy at which the optical transmittance falls to 1% of the transparency region,[47] but this leads to a bandgap dependent on the thickness of the sample; the bandgap is commonly estimated by a Tauc plot,[48] but this does not apply here, because a Tauc plot relies on the parabolic dispersion, which is not the case for EuX, where the $5d(t_{2g})$ conduction band has a tight-binding character.[42,49]
[38]In arriving at (11), we substituted $\alpha^{\pm} = \varepsilon_o \chi^{\pm}/N$ in Eq. (9) of Ref. 19, where χ is the susceptibility.
[39]L. K. Hanamoto, A. B. Henriques, N. F. Oliveira, P. Rappl, E. Abramof, and Y. Ueta, J. Phys. Condens. Matter **16**, 5597 (2004).
[40]A. B. Henriques, M. A. Manfrini, P. H. O. Rappl, and E. Abramof, Phys. Rev. B **77**, 035204 (2008).
[41]B. Kaminski, M. Lafrentz, R. V. Pisarev, D. R. Yakovlev, V. V. Pavlov, V. A. Lukoshkin, A. B. Henriques, G. Springholz, G. Bauer, E. Abramof, P. H. O. Rappl, and M. Bayer, Phys. Rev. Lett. **103**, 057203 (2009).
[42]A. B. Henriques, P. H. O. Rappl, and E. Abramof, Phys. Rev. B **80**, 245206 (2009).
[43]A. B. Henriques, G. D. Galgano, and E. Abramof, J. Phys. Condens. Matter **20**, 255209 (2008).
[44]A. B. Henriques, A. R. Naupa, P. A. Usachev, V. V. Pavlov, P. H. O. Rappl, and E. Abramof, Phys. Rev. B **95**, 045205 (2017).
[45]F. Natali, B. J. Ruck, H. J. Trodahl, D. L. Binh, S. Vezian, B. Damilano, Y. Cordier, F. Semond, and C. Meyer, Phys. Rev. B **87**, 035202 (2013).
[46]H. Yoshitomi, R. Vidyasagar, S. Kitayama, T. Kita, H. Ohta, S. Okubo, Y. Fukuoka, and T. Sakurai, Appl. Phys. Lett. **101**, 122402 (2012).
[47]W. Heiss, R. Kirchschlager, G. Springholz, Z. Chen, M. Debnath, and Y. Oka, Phys. Rev. B **70**, 035209 (2004).
[48]J. Tauc, R. Grigorovici, and A. Vancu, Phys. Stat. Sol. **15**, 627 (1966).
[49]A. Mauger and D. L. Mills, Phys. Rev. B **31**, 8024 (1985).

Appendix D

List of participation in conferences

1) “The 18th Brazilian Workshop on Semiconductor Physics (BWSP-2018)”, Meresias/SP, Brazil, August 13-18, 2017.

2)“International conference on physics of semiconductors (ICPS-2018)”, Montpellier, France, July 29-August 03, 2018.

3)“Encontro de Outono da Sociedade Brasileira de Física (EOSBF-2019)”, Aracaju/SE, Brazil, May 26-31, 2019.

LIGHT INDUCED COHERENT SPIN PRECESSION IN NEGATIVELY CHARGED QUANTUM DOTS

A.R. Naupa[1], C.F.H. Corstjens[1,2], F.W.M. Otten[2], P.M. Koenraad[2] and A.B. Henriques[1]

[1]*Instituto de Física, Universidade de São Paulo, Caixa Postal 66318, 05314-970 São Paulo, Brazil*

[2]*Departament of applied Physics Eindhoven, University of technology, P.O. Box 513, NL-5600 MB Eindhoven, The Netherlands*

ABSTRACT

In an ensemble of quantum dots, the total magnetization is zero because spins in different dots are originally incoherent. However, using ultrashort pulses of light it is possible magnetize the QD ensemble. During the magnetization process, the light creates an intermediate excited state called *trion*, which has an mean lifetime τ. The goal of this work is based on establishing if the use of the time-resolved Faraday rotation technique is a practical method to yield a reliable measure of τ, which usually involve complications during the measurement using traditional methods, related to the contribution of other simultaneously excited states, technical complications separating exciting and emitted light in the resonant case or limitations of using low QD density ($\sim 10^8 cm^{-2}$).

EXPERIMENTAL RESULTS 1

From the photoluminescence spectrum shown in figure 2, it was selected a near resonant wavelength of $\lambda = 880$ nm.

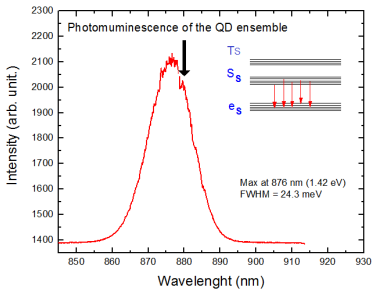

Figure 2. PL spectrum for the (In,Ga)As/GaAs quantum dot ensemble.

With this wavelength, measurements of TRFR were done for different magnetic fields as is shown in figure 3. Using these data, both the phase and amplitude of the photo-induced magnetization precession as a function of the applied magnetic field was fitted with the theoretical expressions found in [1].

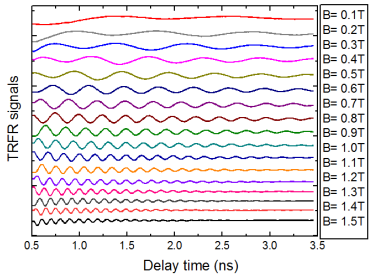

Figure 3. TRFR measurements fitted using theory shown in [1].

Remarkably, the lifetime of the photo-induced trion τ is the one and only adjustable parameter in the fitting of both dependencies. The results present good agreement with theory as is shown in figures 4 and 5, and gives a trion lifetime of $\tau = 0.15 \pm 0.05$ ns .
We compare this result with the estimate of the recombination time obtained using resonant TRDT in the same magnetic field range used in TRFR measurements.

THEORY

The process of light-induced magnetization was recently re-examined in a new quantum mechanical model [1], which describes both the phase and amplitude of the photo-induced magnetization precession as a function of the applied magnetic field. According to this model:

$$M = A \exp\left(\frac{-t}{T_2^*}\right) \cos(\Omega t + \phi) \qquad (1)$$

where the amplitude and phase are:

$$A = \frac{A_0 \Omega \tau}{\sqrt{1 + (\Omega\tau)^2}} \quad and \quad \phi = \frac{\pi}{2} - \arctan(\Omega\tau) \quad (2)$$

with $\Omega = \frac{g_e e B}{2 m_e}$ $T_2^* = \frac{\hbar}{\mu_B \Delta g B}$ A_0 is a constant.

EXPERIMENTAL RESULTS 2

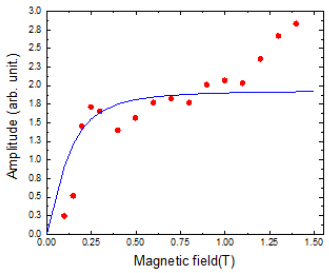

Figure 4. Fitted data of the amplitude of the photo-induced magnetization.

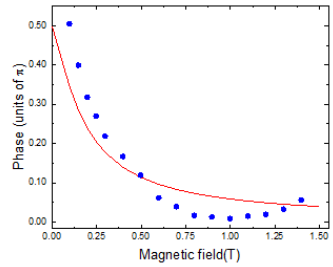

Figure 5. Fitted data of the phase of the photo-induced magnetization.

The TRDT curves present a bi-exponential dynamics which are shown in figure 6 in logarithm scale. From this curve, it is separated the short and long living components of the recombination time as is shown in figure 7.

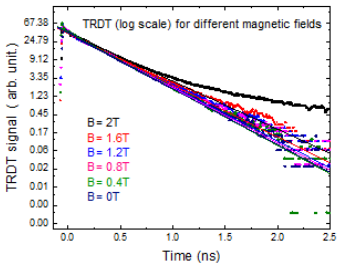

Figure 6. TRDT signals for magnetic fields between 0 T to 2 T in logarithm scale.

EXPERIMENTAL METHODS

We use a (In,Ga)As/GaAs sample containing singly negatively charged dots with QD density ($\sim 10^{10} cm^{-2}$) and fundamental gap of $1,36$ eV. The techniques used were: photoluminescence (PL), time resolved Faraday rotation (TRFR) and time resolved differential transmission (TRDT) for magnetic fields in the range between 0 to 2T at T=5K.

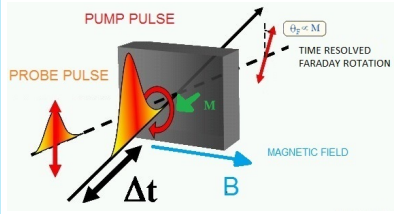

Figure 1. Pump probe Faraday rotation principle.

EXPERIMENTAL RESULTS 3

Fitting these data it is obtained an almost constant short living recombination time value of 0.33 ± 0.01 ns in the range [0T- 1.2T], which is almost twice the trion lifetime found by TRDR. The long living states with lifetime of 1.2 ns appearing for magnetic fields higher than 1.2T is probably associated with dark excitons that result enhanced at high magnetic fields.

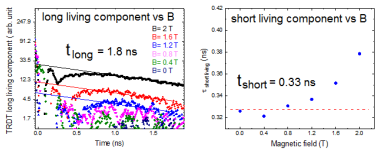

Figure 7. Magnetic field dependence of the short and long living component of the recombination time.

Due to the unavoidable concentration of non-doped and multiple doped QDs in the sample, particles as excitons, and bi-excitons can optically be excited by. The estimative of the trion lifetime by TRDT in this case results inaccessible due to the superposition of the recombination time of the trion and the other species, specially because in general, the trion an exciton have a comparable lifetime.

CONCLUSIONS

The use of the TRFR technique offers a new method to measure the trion lifetime, free of complications related to separating incident and emitted lights in the resonant case or pollution signals related to other excited states, it also offers an exclusive technique to estimate the trion lifetime in QDs samples with high dot density.

REFERENCES

[1] A.B. Henriques, R.C. Cordeiro, P.M. Koenraad, F.W.M.Otten, and M. Bayer, Phys.Rev. B91081303 (2015).

ACKNOWLEDGEMENTS

The financial support by Brazilian agences CNPq and FAPESP (2016/24125-5) is gratefully acknowledged

Photoinduced giant spin polaron parameters in EuTe measured using a SQUID

A.R. Naupa[1], X. Gratens[1], O. Ribeiro Da Fonseca[1], P.H.O Rappl[2], E. Abramof[2], V. Chitta[1] and André Henriques[1]

Abstract n°**11153**

Contacting Author: Alexander Naupa, Email: xander@if.usp.br

INTRODUCTION

In magnetic materials, the induced formation of a region with net magnetic moment called ***magnetic polaron***, was theoretically predicted by de Gennes in his famous paper in 1960 [1], when he anticipated the reorientation of the magnetic moments of the atoms, which create, a non zero magnetization spin ball around one inserted bound electron. The additional electron is introduced by replacing one La^{+3} atom by a Ca^{+2} atom in the antiferromagnetic lanthanum manganite ($LaMnO_3$). The detection of magnetic polarons in *intrinsic* magnetic semiconductors used to require challenging work in the laboratory, as described by Von Molnar in 2009 [2] when he worked with the formation of a magnetic polaron bound to irradiated muons in a EuS sample, observing magnetic polarons composed by four aligned Europium spins with total magnetic moment of around 60 μ_B.

More recently, a proved way to create spin polarons in intrinsic magnetic materials is by the use of photons with energy in resonance with the bandgap as is sketched in figure 1. Photoinduced giant (600 μ_B) and super giant (6000 μ_B) polarons were observed in EuTe and EuSe, respectively. EuTe polarons were detected by using photoluminescence (PL) at T=5 K [3] and by pump-probe Faraday rotation (FR) at higher temperatures (T≈ 140 K) where the PL signals is absent [4].

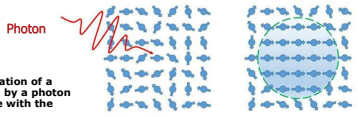

Fig 1. Generation of a spin polaron by a photon in resonance with the bandgap.

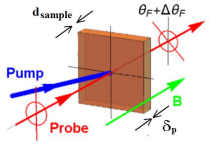

Fig 2. Pump-Probe technique in Faraday geometry to detect photoinduced Faraday rotation, $\Delta\theta_F$, or bulk Faraday rotation, θ_F, in the absence of the pump photon.

Bulk Faraday rotation θ_F and photoinduced Faraday rotation $\Delta\theta_F$ are associated with the bulk magnetization M and the photonduced magnetization ΔM, respectively, by mean of the Verdet constant V, which is temperature independent with value 0.061 [A/m] for EuTe as detailed in [4,5].

$$\theta_F = V\, M\, d_{sample} \quad (1)$$

$$\Delta\theta_F = V\, \Delta M\, \delta_p \quad (2)$$

d_{sample}: sample width

δ_p = pump penetration depth

Photoinduced Faraday rotation by spin polarons

For low concentrations, the polarons are non interacting and form a paramagetic ensemble. Due to the giant magnetic moment of a polaron, the photoinduced magnetization, ΔM, will be described by a Langevin function L(x) = coth(x) - $\frac{1}{x}$ with $x = \frac{\mu_{pol} B_{ap}}{kT}$. By using equation 2 we obtain:

$$\Delta\theta_F(B,T) = \Delta\theta_{FMAX} L(x), \quad (3)$$

where $\Delta\theta_{FMAX} = V\, \Delta M_{MAX}\, \delta_p$ and ΔM_{MAX} is the máximum photoinduced magnetization. Thus, μ_{pol} can be determined by fitting (3) to the experimental data. However, our measurements are made as a function of the *applied* field, whereas the magnetic field entering in (3) is the *internal* field, which acts on the polarons. We therefore need a procedure to determine the internal field.

Determination of the internal field using bulk Faraday rotation

Due to the demagnetization effect, the internal field, B_{int}, is smaller than the applied one, B_a. From ref. [6] for a thin slab and B_a perpendicular to the slab we can write:

$$B_{int} = B_a - \mu_0 M, \quad (4)$$

From (1), we have:

$$M = \frac{\theta_F}{V\, d_{sample}}, \quad (5)$$

Substituing (5) in (4), we obtain:

$$B_{int} = B_a - \frac{\mu_0 \theta_F}{V\, d_{sample}}, \quad (6)$$

At low enough fields, the bulk Faraday rotation θ_F is linear on B_a:

$$\theta_F = B_a\, m(T), \quad (7)$$

where the slope m(T), is a constant, which we measured at each temperature. (See Fig. 3).

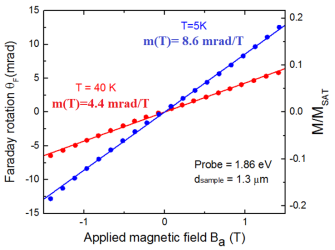

Fig 3. Bulk Faraday rotation curve for T = 5 K (in blue) and T = 40 K (in red).

Thus, substituing (7) in (6), we obtain the ratio $\frac{B_{int}}{B_a}$

$$\frac{B_{int}}{B_a} = 1 - \frac{\mu_0 m(T)}{d_{sample}\, V}, \quad (8)$$

which is a good approximation for B_a < 1 T, as can be seen from figure 3.

Having established the internal field acting on the polaron, we can proceed to fit the experimental data using (3) with μ_{pol}, as the single adjustable parameter.

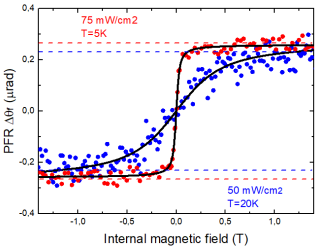

Fig 4. Photoinduced Faraday rotation at T = 5 K (in red) and T=20 K (in blue). The solid line is the fit with equation 3.

As an example, the fitting is shown in Fig 4. for T = 5 K, which yields μ_{pol} = 610 μ_B. Similarly, for T= 20K we obtain yields μ_{pol} = 180 μ_B.
These values are going to be compared with the polaron magnetic moment we get by using the internal field obtained employing a SQUID system, as is explained in the next slide.

Determination of the internal field using SQUID measurements

We measured the magnetic momento of the sample, $m_\perp$ ($m_\parallel$) for B applied perpendicular (parallel) to the surface of the epitaxial layer. By definition we have :

$$m_\perp = \Omega M = \Omega \chi \frac{B_{int}}{\mu_0} \quad (9)$$

$$m_\parallel = \Omega M = \Omega \chi \frac{B_a}{\mu_0} \quad (10)$$

where Ω and χ are the volume and the EuTe magnetic susceptibility, respectively. The internal field equals to the applied one in the later case because of the absents of the demagnetization field as is sketched in figure 5.

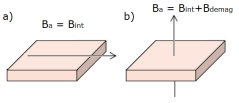

Fig 5. Applied magnetic field parallel (a) and perpendicular (b) to the epitaxial layer of the sample.

We also define the measured magnetic moment as a function of a susceptibility perpendicular (parallel)to the surface of the sample $\chi_\perp$ ($\chi_\parallel$) when we apply a magnetic field B_a:

$$m_\perp = \Omega M_\perp = \Omega \chi_\perp \frac{B_a}{\mu_0} \quad (11)$$

$$m_\parallel = \Omega M_\parallel = \Omega\, \chi_\parallel \frac{B_a}{\mu_0} \quad (12)$$

Therefore, from 11 and 9

$$\chi_\perp = \frac{m_\perp \mu_0}{\Omega B_a} = \frac{\Omega \chi \mu_0 B_{int}}{\Omega \mu_0 B_a} \quad (13)$$

Similarly, from 12 and 10

$$\chi_\parallel = \frac{m_\parallel \mu_0}{\Omega B_a} = \frac{\Omega \chi \mu_0 B_a}{\Omega \mu_0 B_a} \quad (14)$$

Dividing 13 by 14 we get:

$$\frac{\chi_\perp}{\chi_\parallel} = \frac{B_{int}}{B_a} \quad (15)$$

Equation 15 is valid for each temperature when any kind of anisotropy is not considered.
Then, measuring $\chi_\perp$ and $\chi_\parallel$ in the SQUID as a function of the temperature, we obtain the internal field at each temperature as is shown in figure 6. The internal field obtained by Faraday rotation (optical method) is shown as well in the same picture.

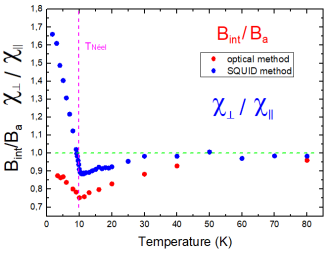

Fig 6. Internal magnetic field as a function of temperature obtained by SQUID measurements (blue). The values obtained by the optical method are plotted in red for comparison.

Below the Néel temperature, T_N = 9,6 K, equation 15 fails, because $\frac{B_{int}}{B_a}$ cannot be larger than unity. This failure is attributed to the anisotropy field, which reduce $\chi_\parallel$ and which was not included in the deduction of 15. Above the Néel temperature $\frac{\chi_\perp}{\chi_\parallel}$ agrees with $\frac{B_{int}}{B_a}$ qualitatively, the difference of about ten percent is attributed to the uncertainty in the experimente. If we fit the PFR data with the internal field obtained by SQUID method for T= 20K the polaron magnetic moment is reduced to 160 μ_B

Bibliography

[1] P. G De Gennes Phys. Rev. 118, 141 (1960)

[2] Vyacheslav G. Storchak, Oleg E. Parfenov, Jess H. Brewer, Peter L. Russo, Scott L. Stubbs, Roger L. Lichti, Dmitry G. Eshchenko, Elvezio Morenzoni, Tel'man G. Aminov, Vladimir P. Zlomanov, Alexander A. Vinokurov, R. L. Kallaher, and Stephan von Molnár, Phys. Rev. B 80, 235203(2009).

[3] A. B. Henriques, G. D. Galgano, E. Abramof, B. Diaz, and P. H. O. Rappl, Appl. Phys. Lett. 99, 091906 (2011).

[4] A. B. Henriques, A. R. Naupa, P. A. Usachev, V. V. Pavlov, P. H. O. Rappl, and E. Abramof, Phys. Rev. B 95, 045205 (2017).

[5] A. B. Henriques and P. A. Usachev Phys. Rev. B 96, 195210 (2017)

[6] S. Blundell, Magnetism in Condensed Matter (Oxford University Press, Oxford, UK, 2001).

Funding:

CAPES

CNPq

FAPESP
FUNDAÇÃO DE AMPARO À PESQUISA DO ESTADO DE SÃO PAULO

[1] *Physics Institute, University of Sao Paulo (USP), Sao Paulo, Brazil*
[2] *National Institute for Space Research (INPE), São José dos Campos, Brazil*

Simple method for the determination of the fast axis of a quarter wave plate

Alexander Naupa
Universidade de São Paulo

Giovanni Decot
Universidade Federal do Espíritu Santo

Andre Henriques
Universidade de São Paulo

Waveplates, also known as retarders, are optical devices that transmit light modifying the polarization state without attenuating the light. They do this by retarding one polarization component (parallel to the so-named slow axis of the waveplate) with respect to the other (parallel to the so-named fast axis of the waveplate), producing a modified polarized state of the exiting light beam.
A simple home-made circular polarizer consists of the sequence of a linear polarizer followed by a quarter wave plate, in which one of the axes of the wave plate is positioned at $+45^\circ$ to the transmitting axes of the linear polarizers. The state of the circular polarization - left or right - depends on which of the axes of wave plate is at $+45^\circ$ to the linear polarizer. In spectroscopic studies, optical selection rules are different for opposite circular polarizations, and it is, therefore, crucial to identify the fast axis of the wave plate in assembling the circular polarizer.
The identification of the fast axis of a quarter-wave plate can be done by using another quarter wave plate with a known fast axis. Here, we present an alternative simple method to identify the fast axis in a wave plate, without the need of a reference wave plate. We exploit the phase shift property of a metallic surface on reflecting light. Using Fresnel equations, we obtain an exact expression for the phase shift between the *senkrecht* and *parallel* rays of the reflected light, as a function of the incidence angle. We use this effect to determine experimentally the fast axis of a quarter-wave plate. Besides being an economic and time-saving solution, our simple experimental setup is an interesting candidate for a didactic laboratory.

Bibliography

[1] Malin, Stuart; Barraclough, David (2000). "Gilbert's De Magnete: An early study of magnetism and electricity". Eos, Transactions American Geophysical Union. 81 (21): 233.

[2] James Clerk Maxwell, "A Dynamical Theory of the Electromagnetic Field", Philosophical Transactions of the Royal Society of London 155, 459–512 (1865).

[3] P. Weiss, Compt. Rend. 143 (1906) p. 1136 – 1139.

[4] L. Néel, Ann. de Physique, 18 (1932) p. 5.

[5] B. Streetman and S. Banerjee, Solid State Electronic Devices. Pearson Education, 6 ed., 2009. 13.

[6] T.D. Ladd, F. Jelezko, R. Laflamme, Y. Nakamura, C. Monroe, Nature 464, 45 (2010).

[7] A Fert et al., Phys. Rev. Lett., Vol.61, p.2472, 1988.

[8] P Grunberg et al., Phys. Rev. B, Vol.39, p.4828, 1989.

[9] Ultrafast optical manipulation of magnetic order Andrei Kirilyuk, Alexey V. Kimel, and Theo Rasing Rev. Mod. Phys. 82, 2731 – Published 22 September 2010.

[10] Kimel, A. V., Kirilyuk, A., Usachev, P. A., Pisarev, R. V., Balbashov, A. M. and Rasing, T. Ultrafast non-thermal control of magnetization by instantaneous photomagnetic pulses. Nature 435, 655-657 (2005).

[11] Landau, L.D.; Lifshitz, E.M. (1935). "Theory of the dispersion of magnetic permeability in ferromagnetic bodies". Phys. Z. Sowjetunion. 8, 153.

[12] T. Gilbert, "A phenomenological theory of damping in ferromagnetic materials," Magnetics, IEEE Transactions on, vol. 40, no. 6, pp. 3443–3449, Nov. 2004.

[13] M. I. Dyakonov (ed.), in Spin Physics in Semiconductors (Springer, Berlin 2008), pp. 35-37.

[14] J.R. Petta, A. C. Johnson, J.M. Taylor, E.A. Laird, A. Yacoby, M.D. Lukin, C.M. Marcus, M.P. Hanson, and A.C. Gossard, Science 309, 2180 (2005).

[15] I.A. Merkulov et al. Phys. Rev. B 65, 205309 (2002).

[16] Greilich, A.; Oulton, R.; Zhukov, E.A.; Yugova, I.A.; Yakovlev, D.R.; Bayer, M.; Shabaev, A.; Efros, Al.L.; Merkulov, I.A.; Stavarache, V.; et al. Phys. Rev. Lett. 2006, 96, 227401:1?227401:4.

[17] S. Varwig, A.Greilich, D.R. Yakovlev, and M. Bayer. Phys. Stat. Sol. B 251:1892, (2014).

[18] A.B. Henriques, R.C. Cordeiro, P.M. Koenraad, F.W.M. Otten, and M. Bayer, Phys. Rev. B 91, 081303 (2015).

[19] A. H. MacDonald, N. Samarth, and P. Schifer. Ferromagnetic semiconductors: moving beyond (Ga,Mn)As. Nature Materials, 4:195?202, (2005).

[20] Dimmock J. O. Optical properties of europium chalcogenides. IBM J. Res. Dev., 14:301,(1970).

[21] J. Philip, A. Punnose, B. I. Kom, K. M. Reddy, S. Layne, J. O. Holmes, B. Satpati, P. R. Leclair, T. S. Santos, and J. S. Moodera,Nat. Mater. 5, 298 (2006).

[22] A. H. MacDonald, P. Schifer, and N. Samarth, Nat. Mater. 4, 195 (2005).

[23] Wachter, P. Handbook on the Physics and Chemistry of Rare Earth, 2nd ed.; CRC Critical Reviews in Solid State Science; North-Holland Publishing Company: 1979; p 189.

[24] Ariponnammal, S.; Natarajan, S. Mod. Phys. Lett. B 2000, 14 (24), 843–848. Kunes, J.; Ku, W.; Pickett, W. E. J. Phys. Soc. Jpn. 2005, 74 (5), 1408.

[25] Sakalle, U. K.; Jha, P. K.; Sanyal, S. P. Bull. Mater. Sci. 2000, 23 (3), 233–235. Kasuya, T. J. Magn. Magn. Mater. 1999, 195 (1), 141–147. Gorlitz, D.; Kotzler, J. Eur. Phys. J., B 1998, 5 (1), 37–43.

[26] P. Wachter. Handbook on the Physics and Chemistry of Rare Earths vol. 1. North-Holland, 1979. (pages 16, 16, 69, 82, 101, 138, 167, 169).

[27] T. Kasuya. Energy spectra of magnetic semiconductors: Eu chalcogenides and nio. Journal of Applied Physics, 41(3):1090?1091, (1970).

[28] L. K. Hanamoto, A. B. Henriques, N. F. Oliveira, P. H. O. Rappl, E. Abramof, and A. Y. Ueta, J. Phys.: Condens.Matter 16, 5597 (2004).

[29] W. Heiss, R. Kirchschlager, G. Springholz, Z. Chen,M. Debnath, and Y. Oka, Phys. Rev. B 70, 035209 (2004).

[30] B. Kaminski, M. Lafrentz, R. V. Pisarev, D. R. Yakovlev, V. V. Pavlov, V. A. Lukoshkin, A. B. Henriques, G. Springholz, G. Bauer, E. Abramof et al., Phys. Rev. Lett. 103, 057203 (2009).

[31] R. R. Subkhangulov, A. B. Henriques, P. H. O. Rappl, E. Abramof, T. Rasing, and A. V. Kimel, Sci. Rep. 4, 4368 (2014).

[32] A. B. Henriques, M. A. Manfrini, P. H. O. Rappl, and E. Abramof. Phys. Rev. B, 77,035204, (2008).

[33] A. B. Henriques, G. D. Galgano, E. Abramof, B. Diaz, and P. H. O. Rappl, Appl. Phys. Lett. 99, 091906 (2011).

[34] T. Kasuya, A. Yanase, and T. Takeda, Solid State Commun. 8,1543 (1970).

[35] E. L. Nagaev, Phys. Status Solidi 145, 11 (1988).

[36] D. D. Awschalom, J. M. Halbout, S. von Molnar, T. Siegrist, and F. Holtzberg, Phys. Rev. Lett. 55, 1128 (1985).

[37] D. D. Awschalom, J. Warnock, and S. von Molnar, Phys. Rev. Lett. 58, 812 (1987).

[38] D. R. Yakovlev and W. Ossau, Introduction to the Physics of Diluted Magnetic Semiconductors, Springer Series in Materials Science Vol. 144 (Springer, Berlin, 2010), pp. 221-262.

[39] A. B. Henriques, G. D. Galgano, E. Abramof, B. Diaz, and P. H. O. Rappl, Appl. Phys. Lett. 99, 091906 (2011).

[40] W. Heiss, R. Kirchschlager, G. Springholz, Z. Chen,M. Debnath, and Y. Oka, Phys. Rev. B 70, 035209 (2004).

[41] A. B. Henriques, F. C. D. Moraes, G. D. Galgano, A. J. Meaney, P. C. M. Christianen, J. C. Maan, E. Abramof, and P. H. O. Rappl, Phys. Rev. B 90, 165202 (2014).

[42] M. Atatüre, J. Dreiser, A. Badolato, A. Högele, K. Karrai, and A.Imamoglu, Science 312, 551 (2006).

[43] P. Dalgarno, J. Smith, J. McFarlane, B. Gerardot, K. Karrai, A. Badolato, P. Petroff and R. Warburton, Phys Rev B 77:245311, (2008).

[44] G. Narvaez, G. Bester, A. Zunger *Title*, Phys rev B 72:245318, (2005)

[45] A. Greilich, R.Oulton, E.A. Zhukov, I.A.Yugova, D.R.Yakovlev, M.Bayer, A.Shabaev, Al.L.Efros, I.A.Merkulov, V.Stavarache, D.Reuter and A.Wieck, Phys. Rev. Lett 96:227401, (2006).

[46] A. B. Henriques, G. D. Galgano, P. H. O. Rappl, and E. Abramof, Phys. Rev. B 93, 201201(R)(2016).

[47] Weiss J. de Physique 6 (1907) pp. 66–690.

[48] B. D. Cullity, C. D. Graham. Introduction to magnetic materials. 2nd Edition. John Wiley and Sons, 2011.

[49] S. Blundell, Magnetism in Condensed Matter (Oxford University Press, New York, 2001), p. 95.

[50] M. Gong, K. Duan, C. F. Li, R. Magri, G. A. Narvaez and L. He, Phys. Rev. B, vol. 77, p. 045326, (2008).

[51] G. D. Galgano, Doctoral thesis, Universidade de sao Paulo, (2012) (Pag 44)

[52] Landolt M. Griessen, R. and H.R. Ott. Solid State Communciations, 9(2219-2223), 1971. (pages 61, 62, 62, 63,63, 64, 138).

[53] G. Güntherodt, P. Wachter, and D. Imboden. Zeitschrift für Physik B Condensed Matter, 12:292?310, (1971).

[54] A. B. Henriques, G. D. Galgano, B. L. Diaz, P. H. O. Rappl, and E. Abramof,J. Phys.: Condens. Matter 19, 406234 (2007).

[55] N. F. O. Jr., S. Foner, and Y. Shapira, Phys. Rev. B 5, 2634 (1972).

[56] W. Heiss, W. Pretchl, and G. Springholz , Appl. Phys, Lett. 78,3484 (2001).

[57] W. Heiss, R. Kirchschlager, G. Springholz, Z. Chen, M. Debnath, and Y. Oka. Phys, Rev. B 70,035209 (2004).

[58] B. Diaz, E. Granado, E. Abramof, P.H.O Rappl, V. A. Chitta, and A.B. Henriques, Phys. Rev. B 78, 134423 (2008).

[59] A. B. Henriques and J. P. Von der Weid, Solid State Commun, 56,571 (1985).

[60] G. D Holah, J.S. Webb, R.B. Dennis, and C.R. Pidgeon, Solid State Commun, 13,209 (1973).

[61] G. Bastard, Wave Mechanics Applied to Semiconductor Heterostructures (Les Editions de Physique, Les Ulis, 1988).

[62] A. Mauger and C. Godart, Phys. Rep. 141, 52 (1986).

[63] L. D. Landau and E. M. Lifshitz, Quantum Mechanics, Non-Relativistic Theory, Course of Theoretical Physics (Addison-Wesley, Reading, 1965), Vol 3, Chap. 10.

[64] A. Mauger and D. L. Mills, Phys. Rev. B 31, 8024 (1985).

[65] J. W. Battles and G. E. Everett, Phys. Rev. B 1, 3021 (1970).

[66] J. M. D. Coey, Magnetism and Magnetic Materials (Cambridge University Press, Cambridge, UK, (2009).

[67] A. B. Henriques, A. Wierts, M. A. Manfrini, G. Springholz, P. H. O. Rappl, E. Abramof, and A. Y. Ueta, Phys. Rev. B 72, 155337 (2005).

[68] C. P. Bean and J. D. Livingston, J. Appl. Phys. 30, S120 (1959).

[69] B. Diaz, E. Granado, E. Abramof, P. H. O. Rappl, V. A. Chitta, and A. B. Henriques, Phys. Rev. B 78, 134423 (2008).

[70] B. Díaz, P.H. O.Rappl, and E.Abramof. Journal of Crystal Growth, 308(1):218- 222, (2007).

[71] N. F. Mott, in Metal-Insulator Transitions, 2nd ed., Springer Series in Materials Science (Taylor and Francis, London, 1990),p. 93.

[72] A. Mauger and C. Godart, Phys. Rep. 141, 51 (1986).

[73] S. Blundell, Magnetism in Condensed Matter (Oxford University Press, Oxford, UK, 2001).

[74] R. T. Lechner, G. Springholz, T. U. Schulli, J. Stangl, T. Schwarzl, and G. Bauer, Phys. Rev. Lett. 94, 157201 (2005).

[75] I. A. Smirnov, Phys. Status Solidi A 14, 363 (1972).

[76] A. Sommerfeld, Optics (Academic Press, New York, 1954) p. 101.

[77] A. B. Henriques, X. Gratens, P. A. Usachev, V. A. Chitta, and G. Springholz, Phys. Rev. Lett. 120, 217203 (2018).

[78] A. Mauger and C. Godart, Phys. Rep. 141, 51 (1986).

[79] A. B. Henriques and P. A. Usachev, Phys. Rev. B 96, 195210 (2017).

[80] R. P. Feynman, R. B. Leighton, and M. L. Sands, The Feynman Lectures on Physics, Vol. 2 (Addison-Wesley, 1963-1965) Chap. 11, p. 11-2, formula (11-8).

[81] C. Kittel, Introduction to solid state physics, seventh ed. (John Wiley and Sons, New York, 1996) p. 389, formula (22).

[82] R. W. Boyd, Nonlinear Optics (Academic Press, 2003).

[83] S. Blundell, Magnetism in condensed matter (Oxford University Press, Oxford, 2001).

[84] P. J. L. Herve and L. K. J. Vandamme, J. Appl. Phys. 77, 5476 (1977).

[85] J. Talghader and J. S. Smith, Appl. Phys. Lett. 66, 335 (1995).

[86] P. Wachter, C R C Critical Reviews in Solid State Sciences 3, 189 (1972).

[87] S. Blundell, Magnetism in condensed matter (Oxford University Press, Oxford, 2001) Appendix D, p. 214.

[88] A. B. Henriques, G. D. Galgano, B. L. Diaz, P. H. O. Rappl, and E. Abramof, J. Phys.: Condens. Matter 19, 406234 (2007).

[89] B. Diaz, E. Granado, E. Abramof, P. H. O. Rappl, V. A. Chitta, and A. B. Henriques, Phys. Rev. B 78, 134423 (2008).

[90] R. T. Lechner, G. Springholz, T. U. Schulli, J. Stangl, T. Schwarzl, and G. Bauer, Phys. Rev. Lett. 94, 157201 (2005).

[91] A. B. Henriques, A. Wierts, M. A. Manfrini, G. Springholz, P. H. O. Rappl, E. Abramof, and A. Y. Ueta, Phys. Rev. B 72, 155337 (2005).

[92] R. Vidyasagar, O. A. Santos, J. Holanda, R. O. Cunha, F. L. A. Machado, P. R. T. Ribeiro, A. R. Rodrigues, J. B. S. Mendes, A. Azevedo, and S. M. Rezende, Appl. Phys. Lett. 109, 122402 (2016).

[93] L. K. Hanamoto, A. B. Henriques, N. F. Oliveira, P. Rappl, E. Abramof, and Y. Ueta, J. Phys.: Condens. Matter 16, 5597 (2004).

[94] A. B. Henriques, M. A. Manfrini, P. H. O. Rappl, and E. Abramof, Phys. Rev. B 77, 035204 (2008).

[95] B. Kaminski, M. Lafrentz, R. V. Pisarev, D. R. Yakovlev, V. V. Pavlov, V. A. Lukoshkin, A. B. Henriques, G. Springholz, G. Bauer, E. Abramof, P. H. O. Rappl, and M. Bayer, Phys. Rev. Lett. 103, 057203 (2009).

[96] A. B. Henriques, P. H. O. Rappl, and E. Abramof, Phys. Rev. B 80, 245206 (2009).

[97] A. B. Henriques, G. D. Galgano, and E. Abramof, J. Phys.: Condens. Matter 20, 255209 (2008).

[98] A. B. Henriques, A. R. Naupa, P. A. Usachev, V. V. Pavlov, P. H. O. Rappl, and E. Abramof, Phys. Rev. B 95, 045205 (2017).

[99] F. Natali, B. J. Ruck, H. J. Trodahl, D. L. Binh, S. Vezian, B. Damilano, Y. Cordier, F. Semond, and C. Meyer, Phys. Rev. B 87, 035202 (2013).

[100] H. Yoshitomi, R. Vidyasagar, S. Kitayama, T. Kita, H. Ohta, S. Okubo, Y. Fukuoka, and T. Sakurai, Appl. Phys. Lett. 101, 122402 (2012).

[101] J. J. Sakurai, San Fu Tuan. Modern Quantum Mechanics: Revised Edition. Pearson Education, 1994.